



HAL
open science

Geoelectrical Signatures of Spreading and Mixing

Alejandro Fernandez Visentini

► **To cite this version:**

Alejandro Fernandez Visentini. Geoelectrical Signatures of Spreading and Mixing. Geophysics [physics.geo-ph]. Université de Lausanne, 2021. English. NNT: . tel-03501047

HAL Id: tel-03501047

<https://hal.science/tel-03501047v1>

Submitted on 17 Apr 2022

HAL is a multi-disciplinary open access archive for the deposit and dissemination of scientific research documents, whether they are published or not. The documents may come from teaching and research institutions in France or abroad, or from public or private research centers.

L'archive ouverte pluridisciplinaire **HAL**, est destinée au dépôt et à la diffusion de documents scientifiques de niveau recherche, publiés ou non, émanant des établissements d'enseignement et de recherche français ou étrangers, des laboratoires publics ou privés.



HAL
open science

Geoelectrical Signatures of Spreading and Mixing

Alejandro Fernandez Visentini

► **To cite this version:**

Alejandro Fernandez Visentini. Geoelectrical Signatures of Spreading and Mixing. Geophysics [physics.geo-ph]. Université de Lausanne, 2021. English. tel-03501047

HAL Id: tel-03501047

<https://hal.archives-ouvertes.fr/tel-03501047>

Submitted on 17 Apr 2022

HAL is a multi-disciplinary open access archive for the deposit and dissemination of scientific research documents, whether they are published or not. The documents may come from teaching and research institutions in France or abroad, or from public or private research centers.

L'archive ouverte pluridisciplinaire **HAL**, est destinée au dépôt et à la diffusion de documents scientifiques de niveau recherche, publiés ou non, émanant des établissements d'enseignement et de recherche français ou étrangers, des laboratoires publics ou privés.

Faculté des géosciences et de l'environnement
Institut des sciences de la Terre

Geoelectrical Signatures of Spreading and Mixing

Thèse de doctorat

Présentée à la
Faculté des géosciences et de l'environnement
Institut des sciences de la Terre
de l'Université de Lausanne
par

Alejandro Fernandez Visentini

Diplôme (M.Sc.) en Géophysique
Université Nationale du La Plata, Argentina
Diplôme (M.Sc.) en Géophysique de Exploration
Université de Paris, France

Jury

Prof. Dr. Marie-Elodie Perga, présidente du jury
Prof. Dr. Niklas Linde, directeur de thèse
Prof. Dr. Kamini Singha, Experte externe
Prof. Dr. Marco Dentz, Expert externe
Prof. Dr. Pietro de Anna, Expert interne

Lausanne, le 20 octobre 2021

IMPRIMATUR

Vu le rapport présenté par le jury d'examen, composé de

Président de la séance publique :	Mme la Professeure Marie-Elodie Perga
Président du colloque :	Mme la Professeure Marie-Elodie Perga
Directeur de thèse :	M. le Professeur Niklas Linde
Expert interne :	M. le Professeur Pietro De Anna
Expert externe :	M. le Professeur Kamini Singha
Expert externe :	M. le Professeur Marco Dentz

Le Doyen de la Faculté des géosciences et de l'environnement autorise l'impression de la thèse de

Monsieur Alejandro FERNANDEZ VISENTINI

Titulaire d'un

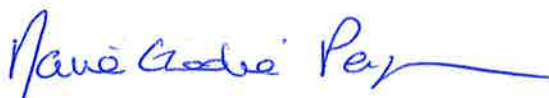
*Master en Géophysique de l'Université de Paris et d'un
Master en Géophysique de l'Université de La Plata, Argentine*

intitulée

GEOELECTRICAL SIGNATURES OF SPREADING AND MIXING

Lausanne, le 16 novembre 2021

Pour le Doyen de la Faculté des géosciences et de
l'environnement



Professeure Marie-Elodie Perga

Acknowledgements

Firstly, I would like to thank my supervisor Dr. Niklas Linde. For mentoring me, by showing me how to work methodically and efficiently, and for encouraging me with great patience to pursue and complete my research goals. Certainly, a successful completion of this thesis work would not have been possible without him.

My special thanks go also to Dr. Pietro de Anna, for providing me the space and expertise to carry out my experiments. During my PhD time our discussions were at times more frequent, at times more sporadic, but always greatly enriching for me. Also, the experimental work would not have been possible without the expert help from Dr. Ludovic Baron, who helped me in setting up the electrical monitoring system used to collect the data.

I would also like to express my sincere gratitude to all the professors that I interacted with through the ENIGMA-ITN network. It has been indeed a real privilege to be part of such an amazing network of scientists. I would like to give my special thanks to Dr. Damien Joungot for his great research advises and uninterested help. My special thanks go also to Drs. Tanguy Le Borgne and Yves Méheust, for welcoming me in Rennes during my two research stays, and for the discussions and thoughtful advices throughout my PhD time. In the same way, I would like to thank Dr. Marco Dentz, for receiving me in Barcelona and for making himself the time to work with me in Geophysics. I would also like to express my gratitude to Dr. Jesús Carrera, for enriching and encouraging discussions at the early stages of my PhD. They were all a great source of inspiration, always there for guiding and encouraging me in good and difficult times of my work.

With great pleasure I also thank all my fellow PhD students and post-docs both at UNIL and within the ENIGMA-ITN that made this journey much more fun and enjoyable. I would like to thank Drs. Nicolas Barbosa, Alexis Shakas, Giulia di Pascuale and Jürg Hunziker, for welcoming when I first arrived at UNIL and for their friendship. My special thanks go also to Dr. Kevin De Vriendt, Gabriel Quiroga, Ayelen Gomez, Alvaro Lopez, Dr. Lara Blazevic, Dr. Santiago Solazzi, Macarena Amaya and Shiran Levy for their friendship. The list continues but in order to avoid missing a name I extend my sincere gratitude to all of the friends without mentioning specific names.

Of course, none of my success would be possible without the loving support from all my family to whom I am eternally grateful. I am also indebted to my partner Pamela for her patience and looking out for me during most of this journey.

This work has received funding from the European Union's Horizon 2020 research and innovation program under the Marie Skłodowska - Curie grant agreement number 722028 (ENIGMA ITN) and from the Swiss National Science Foundation under grant 184574.

Contents

Acknowledgements	i
List of figures	v
List of tables	vii
Abstract	ix
Résumé	xi
1 Introduction	1
1.1 Motivation	1
1.2 Basic theory and modelling tools	3
1.2.1 Groundwater flow and solute transport	3
1.2.2 Solute plume description: spreading and mixing	4
1.2.3 Introduction to the DC geophysical method	5
1.2.4 DC electrical conduction	7
1.2.5 Average electrical conductivity	7
1.2.6 Overview of upscaled electrical conductivity	8
1.3 Translation of σ_{eq} into mean salinity	13
1.4 Milli-fluidic technologies to assess the impact of sub-scale heterogeneity on DC conductivity	15
1.5 Thesis objectives	17
1.6 Thesis outline	18
2 Inferring geostatistical properties of hydraulic conductivity fields from saline tracer tests and equivalent electrical conductivity time-series	19
2.1 Introduction	20
2.2 Governing equations and problem setup	22
2.2.1 Groundwater flow	22
2.2.2 Solute transport	23
2.2.3 DC conduction	24
2.2.4 Numerical implementations and problem setup	25
2.3 Inference problem	28
2.3.1 Bayesian inference framework	28
2.3.2 Posterior density approximation	29
2.3.3 Information measure: Kullback-Leibler divergence	33
2.4 Results	33
2.4.1 Two examples of generated data	34

2.4.2	Test cases	36
2.4.3	Information assessment of data types	37
2.5	Discussion	44
2.5.1	General findings	44
2.5.2	Lessons learned from the three test cases	45
2.5.3	Physical insights and open questions	46
2.5.4	Implications for field-based studies	48
2.6	Conclusions	49
3	Electrical signatures of diffusion-limited mixing: Insights from a milli-fluidic tracer experiment	51
3.1	Introduction	52
3.2	Materials and experimental methods	54
3.2.1	Porous medium design	54
3.2.2	Tracer solutions	55
3.2.3	Flow system	57
3.2.4	Geoelectrical system	58
3.2.5	Image acquisition	58
3.2.6	Image processing	59
3.2.7	Concentration - electrical conductivity calibration	60
3.3	Modelling	60
3.3.1	Electrical modelling	60
3.3.2	Post-processing of electrical resistance time-series	61
3.3.3	Solute diffusion modelling in confined media	63
3.4	Results	64
3.4.1	Fluorimetry-inferred NaCl concentration field	64
3.4.2	Apparent electrical conductivity time-series	68
3.5	Discussion	71
3.5.1	Proof of concept and technical challenges	71
3.5.2	Impact of incomplete mixing and molecular diffusion on time-series of bulk electrical conductivity	73
3.6	Conclusions	82
3.7	Appendices	83
3.7.1	Appendix 3A: Porous system fabrication	83
3.7.2	Appendix 3B: Geoelectrical monitoring system	83
3.7.3	Appendix 3C: Grain mask compilation	84
4	Generalization of Archie's law for heterogeneous and anisotropic salinity fields	85
4.1	Introduction	86
4.2	Theoretical background	88
4.2.1	Groundwater flow and solute transport	88
4.2.2	Spreading and mixing of $c(\mathbf{x}, t)$	88
4.2.3	DC electrical conduction	89
4.2.4	Energy representation of σ_{eq} and the formation factor F	90
4.2.5	Trapped charge and secondary electric field	91

4.2.6	Expressions for the formation factor, electrical tortuosity and cementation exponent	92
4.3	The mixing factor M	94
4.3.1	Analytical expression for the mixing factor M	95
4.4	Numerical tests	98
4.4.1	Validation	99
4.4.2	Anisotropic mixing factors	103
4.4.3	Time-evolving setting	106
4.5	Conclusions and outlook	107
4.6	Appendices	108
4.6.1	Appendix A: Equivalent electrical conductivity for non-isolating matrix	108
5	Conclusions and Outlook	111
5.1	Conclusions	111
5.2	Outlook	114
	Bibliography	128
	Curriculum Vitae	129

List of Figures

1.1	Contaminant plume of size L monitored with the DC geophysical method. Some known current I is injected into the ground from the electrode pair on the left and eight voltages are measured at different distances from both the current source and the target (plume). In this schematic drawing \mathbf{y} represents a point at the scale at which the average electrical conductivity is observed, while \mathbf{x} represents a point at the Darcy scale and \mathbf{x}' represents a point at the pore scale. Adapted from <i>Wood</i> (2009).	6
1.2	Two-dimensional $1\text{ m} \times 1\text{ m}$ heterogeneous multivariate-lognormal electrical conductivity fields organized into (a) layers and (b) lenses. Plots of $\sigma_{\text{eq-y}}$, μ_σ and σ_σ^2 , computed using subdomains of the electrical conductivity fields that have a length of 1 m and varying height y_{obs} starting at $y = 0\text{ m}$ for (c) the layered and (d) lensed fields. The data are normalized by their corresponding values when observed using the full domain's height.	10
1.3	a. Uncoupled hydrogeophysical inversion. b. Coupled hydrogeophysical inversion. The petrophysical transformation takes place (a) after inversion of $\sigma(\mathbf{y})$ and (b) during data forward modelling, respectively.	14
1.4	(a) Summary of typical workflow for electrically- and optically-monitored milli-fluidic tracer tests. The left-sided sequence represents the electrical monitoring workflow and $\sigma_{\text{app}}^{\text{out}_1}$ the observed average electrical conductivity. The right-sided sequence represents the optical monitoring workflow, with $I(\mathbf{x}')$, $c(\mathbf{x}')$, $\sigma(\mathbf{x}')$ and $\sigma_{\text{app}}^{\text{out}_2}$ denoting, respectively, the observed light intensity, inferred concentration and fluid conductivity fields at the pore scale, and calculated average electrical conductivity. (b) (top) Image-inferred $\sigma(\mathbf{x}')$ and (bottom) modulus of the associated (calculated) current density field $\mathbf{J}(\mathbf{x}')$, respectively. Adapted from <i>Jougnot et al.</i> (2018).	16
2.1	Generated sample of size $P = 10^5$ of geostatistical parameters $\mathbf{m} = (\sigma_Y^2, I_y, \lambda)$ drawn from a joint pdf $\pi(\mathbf{m})$. Each realization is used together with an associated \mathbf{R} -realization to create a log-hydraulic conductivity field on which flow and transport simulations are performed.	26
2.2	(a) Weakly heterogeneous hydraulic conductivity field with geostatistical parameters $(\sigma_Y^2, I_y, \lambda) = (0.005, 0.130\text{ m}, 3.179)$. (b) Corresponding steady-state flow field and (c) normalized concentration field at time 10^3 s . (d) Time-series of the horizontal and vertical equivalent electrical conductivity, mass-flux, and mean tracer concentration, denoted σ^H , σ^V , M and μ_c , respectively. The light-blue vertical line, also present in (e), marks the time 10^3 s of the concentration field shown in (c). (e) Time-derivatives of σ^H , σ^V , M and μ_c	34

2.3	(a) Strongly heterogeneous hydraulic conductivity field, defined with geostatistical parameters $(\sigma_Y^2, I_y, \lambda) = (5.111, 0.085 \text{ m}, 1.028)$. (b) Corresponding steady-state flow field and (c) normalized concentration field at time 10^3 s . (d) Time-series of the horizontal and vertical equivalent electrical conductivity, mass-flux, and mean tracer concentration, denoted σ^H, σ^V, M and μ_c , respectively. The light-blue vertical line, also present in (e), marks the time 10^3 s , of the concentration field in (c). (e) Time-derivatives of σ^H, σ^V, M and μ_c . The large peaks exhibited by $\frac{d\sigma^H}{dt}$ and $\frac{dM}{dt}$ approximately coincide with the first arrival of the tracer at the outlet.	35
2.4	(a, d, f) Realizations of log-hydraulic conductivity fields and (b, e, h) associated flow and (c, f, i) concentration fields at time 10^3 s for the three evaluated test cases (a-c) \mathbf{m}_1 , (d-f) \mathbf{m}_2 and (g-i) \mathbf{m}_3 . Note that the locations of high- and low hydraulic conductivity regions are governed by random \mathbf{R} -realizations	37
2.5	Posterior model parameter vector samples of size $S = 500$ obtained by the AARS algorithm for test case $\mathbf{m}_1 = (4.7, 0.06 \text{ m}, 1.5)$ using different datasets as conditioning data. The colored clouds of points represent the samples for datasets (a) \mathbf{d}_H ; (b) \mathbf{d}_V ; (c) \mathbf{d}_M ; (d) \mathbf{d}_{HV} ; (e) \mathbf{d}_{VM} ; (f) \mathbf{d}_{HVM} . The colormap encodes the L_1 distance ρ between simulated and observed data, normalized by the minimum and maximum values of ρ of the test case. The inset plots of (a), (b) and (c) show, respectively, the 50 realizations of time-series σ^H, σ^V and M generated for \mathbf{m}_1 using different \mathbf{R} -realizations. The data considered here for inference are shown by thick-colored curves. The resulting KLD values are given for each dataset.	39
2.6	Marginal posterior PDFs associated to each type of conditioning data $\mathbf{d}_H, \mathbf{d}_V, \mathbf{d}_M, \mathbf{d}_{HV}, \mathbf{d}_{VM}$ and \mathbf{d}_{HVM} for test case $\mathbf{m}_1 = (4.7, 0.06 \text{ m}, 1.5)$. Marginal prior and posterior PDFs corresponding to (a) σ_Y^2 (b) I_y and (c) λ	40
2.7	Posterior model parameter vector samples of size $S = 500$ obtained by the AARS algorithm for test case $\mathbf{m}_2 = (0.80, 0.06 \text{ m}, 10.00)$ using different datasets as conditioning data. The colored clouds of points represent the samples for datasets (a) \mathbf{d}_H ; (b) \mathbf{d}_V ; (c) \mathbf{d}_M ; (d) \mathbf{d}_{HV} ; (e) \mathbf{d}_{VM} ; (f) \mathbf{d}_{HVM} . The colormap encodes the L_1 distance ρ between simulated and observed data, normalized by the minimum and maximum values of ρ of the test case. The inset plots of (a), (b) and (c) show, respectively, the 50 realizations of time-series σ^H, σ^V and M generated for \mathbf{m}_1 using different \mathbf{R} -realizations. The data considered here for inference are shown by thick-colored curves. The resulting KLD values are given for each dataset.	41
2.8	Marginal posterior PDFs associated to each type of conditioning data $\mathbf{d}_H, \mathbf{d}_V, \mathbf{d}_M, \mathbf{d}_{HV}, \mathbf{d}_{VM}$ and \mathbf{d}_{HVM} for test case $\mathbf{m}_2 = (0.80, 0.06 \text{ m}, 10.00)$. Marginal prior and posterior PDFs corresponding to (a) σ_Y^2 (b) I_y and (c) λ	42

2.9	Posterior model parameter vector samples of size $S = 500$ obtained by the AARS algorithm for test case $\mathbf{m}_3 = (4.70, 0.38 \text{ m}, 1.50)$ using different datasets as conditioning data. The colored clouds of points represent the samples for datasets (a) \mathbf{d}_H ; (b) \mathbf{d}_V ; (c) \mathbf{d}_M ; (d) \mathbf{d}_{HV} ; (e) \mathbf{d}_{VM} ; (f) \mathbf{d}_{HVM} . The colormap encodes the L_1 distance ρ between simulated and observed data, normalized by the minimum and maximum values of ρ of the test case. The inset plots of (a), (b) and (c) show, respectively, the 50 realizations of time-series σ^H , σ^V and M generated for \mathbf{m}_1 using different \mathbf{R} -realizations. The data considered here for inference are shown by thick-colored curves. The resulting KLD values are given for each dataset.	43
2.10	Marginal posterior PDFs associated to each type of conditioning data \mathbf{d}_H , \mathbf{d}_V , \mathbf{d}_M , \mathbf{d}_{HV} , \mathbf{d}_{VM} and \mathbf{d}_{HVM} for test case $\mathbf{m}_3 = (4.7, 0.38 \text{ m}, 1.5)$. Marginal prior and posterior PDFs corresponding to (a) σ_Y^2 (b) I_y and (c) λ	44
2.11	Natural logarithm of the absolute value of the current density fields (and their streamlines) resulting from exciting the sample both in the (a-c) horizontal and (d-f) vertical modes. The electrical conductivity distribution is given by the saline concentration fields shown in Figure 2.4, that is, at time 10^3 s for the three evaluated test cases (a, d) \mathbf{m}_1 (column 1), (b, e) \mathbf{m}_2 and (c, f) \mathbf{m}_3	47
3.1	(a) Top schematic view of the flow cell including, from left to right, an inlet chamber, an artificial layered porous medium, and an outlet chamber. The flow direction during the tracer injection is indicated with a pair of blue arrows. The sets of current injection electrodes A_x - B_x (measurement mode M_x) and A_y - B_y (measurement mode M_y), are indicated with red dots and the potential electrodes with yellow dots. (b) Zoom-in of the region indicated by a green rectangle in (a) ($x \in [160, 200]$ and $y \in [52, 72]$ mm) showing the interface separating the top from the middle porous layers, the former saturated with background (grey-colored) and the latter being saturated with fluorescent tracer (white-colored) just after stopping the tracer injection. The radii of the grains and the linear sizes of the pore throats are indicated, respectively, as R_1 and λ_1 , for the top and bottom layer, and as R_2 and λ_2 , for the middle layer.	55
3.2	Fluid electrical conductivity versus bulk electrical conductivity for a homogeneous solute concentration. The measured apparent conductivities are shown as blue dots with the associated regression as a continuous black line. The numerically calculated bulk conductivities are shown as a black dashed line.	62
3.3	Four snapshots of the fluorimetry-inferred NaCl concentration fields corresponding to times (a) $t_1^{\text{NaCl}} = 0$, (b) $t_2^{\text{NaCl}} = 5 \times 10^{-3}$, (c) $t_3^{\text{NaCl}} = 5 \times 10^{-2}$, and (d) $t_4^{\text{NaCl}} = 5 \times 10^{-1}$. The yellow dots indicate the potential electrodes, see Figure 3.1 for convention.	65
3.4	Four snapshots of fluorimetry-inferred and modeled NaCl concentration profiles for times (a) $t_1^{\text{NaCl}} = 0$ (initial conditions for the modeling), (b) $t_2^{\text{NaCl}} = 5 \times 10^{-3}$, (c) $t_3^{\text{NaCl}} = 5 \times 10^{-2}$, and (d) $t_4^{\text{NaCl}} = 5 \times 10^{-1}$	66

- 3.5 (a) y -averaged mean of the fluorimetry-inferred NaCl concentrations as a function of the horizontal coordinate x for times $t_1^{\text{NaCl}} = 0$ (blue solid line), $t_2^{\text{NaCl}} = 5 \times 10^{-3}$ (red dashed line), $t_3^{\text{NaCl}} = 5 \times 10^{-2}$ (green dotted line), and $t_4^{\text{NaCl}} = 5 \times 10^{-1}$ (purple dotted-dashed line). (b) Temporal evolution of the inferred mean concentration over the entire field of view. Note that negative and positive t^{NaCl} represent, respectively, times normalized by advective and diffusion transport time-scales (Subsec. 3.3.3). The grey-colored rectangle highlights the tracer injection period. The blue, red, green and purple-colored dots on the curve indicate the mean concentration field values at times t_1^{NaCl} , t_2^{NaCl} , t_3^{NaCl} and t_4^{NaCl} 68
- 3.6 Measured (dots) and simulated (lines) time-series of apparent electrical conductivity under measurement modes M_x (red and green) and M_y (blue and magenta) for electrode pairs (a) P_3 - P_9 , (b) P_4 - P_5 and (c) P_4 - P_9 . The four vertical black dashed lines mark the times $t_1^{\text{NaCl}} = 0$, $t_2^{\text{NaCl}} = 5 \times 10^{-3}$, $t_3^{\text{NaCl}} = 5 \times 10^{-2}$, and $t_4^{\text{NaCl}} = 5 \times 10^{-1}$, respectively. Negative and positive times represent, respectively, times normalized by advective and diffusion transport time-scales (Subsec. 3.3.3). The gray-colored rectangles highlight the tracer injection period extending over 60s. 70
- 3.7 Apparent electrical conductivity time-series for the electrode pair P_4 - P_9 and measurement mode M_y . Measured time-series (blue dots), simulated time-series with adequate time-scaling of FS concentration images to account for the different diffusion coefficients of FS and NaCl (magenta solid line) as described in section 3.3.3 and without any such time-scaling (black solid line). 72
- 3.8 Simulated apparent electrical conductivity time-series for electrode pair P_3 - P_9 under measurement mode M_y for a cell that has top-bottom and middle layer widths of (a) $w_1 = 6$ mm and $w_1^{\text{middle}} = 62$ mm, (b) $w_2 = 12$ mm and $w_2^{\text{middle}} = 50$ mm (as in the actual experiment) and (c) $w_3 = 18$ mm and $w_3^{\text{middle}} = 38$ mm. The time-series for each w_i are plotted as a function of normalized times t/τ_i , with $\tau_i = w_i^2/D_{\text{NaCl}}$ (defined analogously as $\tau_{\text{ch}}^{\text{NaCl}}$ in sec. 3.3.3). A sketch illustrating the geometry of one of the initial NaCl concentration fields is shown in (c) along with the injection (red dots) and potential (yellow dots) electrodes P_3 and P_9 75
- 3.9 Simulated time-series of (a) total current flowing through the domain and (b) voltage measured between P_3 - P_9 , for chambers located at $d_1 = \infty$ (see the main text) and the three considered initial top and bottom widths of $w_1 = 6$ mm, $w_2 = 12$ mm and $w_3 = 18$ mm. The response associated to w_i ($i = 1, 2, 3$) is plotted as a function of the corresponding normalized t/τ_i (see Fig. 3.8). (c)-(d) Simulated fluid conductivity (tracer concentration) field, normalized by σ_{S_2} , for $w_2 = 12$ mm and $d_1 = \infty$ at (c) $t/\tau_2 = 0$ and (d) $t/\tau_2 = 0.1$. On top of each fluid conductivity field, nine equipotential lines of the electrical potential field for the levels $0.4 + 0.025 \times pV$ ($p = 0, \dots, 8$) are shown for the corresponding conductivity field (red solid lines) and for the case of a homogeneous conductivity field (black dashed lines). The injection electrodes are indicated (red dots) as well as the potential electrodes P_3 and P_9 (yellow dots). 77

3.10	Four snapshots of the image-inferred NaCl concentration field contained in the sub-region defined by the horizontal coordinate range $x \in [140, 175]$ mm at the times (a) $t_1^{\text{NaCl}} = 0$, (b) $t_2^{\text{NaCl}} = 5 \times 10^{-3}$, (c) $t_3^{\text{NaCl}} = 5 \times 10^{-2}$ and (d) $t_4^{\text{NaCl}} = 5 \times 10^{-1}$. The close views shown on top of the full concentration maps correspond to the areas enclosed by the cyan-colored rectangles in the corresponding full maps.	79
3.11	Simulated time-series of the x and y components of the equivalent electrical conductivity tensor, σ_x and σ_y , and computed time-series of the arithmetic and harmonic means σ_A and σ_H over the considered sub-region (Fig. 3.10) of the time-evolving NaCl concentration field.	80
3.12	Scatter plots of the y -component of the equivalent electrical conductivity tensor, σ_y , plotted against (a) the concentration variance $\sigma_c^2(t)$ and (b) the scalar dissipation rate divided by the diffusion coefficient, $\chi(t)/D$	82
4.1	(a-b) Multivariate log-normal fluid conductivity fields, (c-d) secondary electric field in the y -direction and (e-f) trapped charge distributions arising from applying a unit electrical potential drop across the y -direction. The electrical conductivity fields share the same mean value $\mu_{\sigma_w} = 0.1 \text{ Sm}^{-1}$, integral scales $I_y = 0.02 \text{ m}$, $I_x = 10I_y$ and different variances: (a) $\sigma_{\ln\sigma}^2 = 0.5$ and (b) $\sigma_{\ln\sigma}^2 = 1.5$	100
4.2	(solid lines) simulated and predicted equivalent electrical conductivities using (dots) identity of Eq. 4.37 and (stars) energy representation formula (Eq. 4.12) in the (a) x - and (b) y -directions. The underlying conductivity field is multivariate-log-normal with mean $\mu_{\sigma_w} = 0.1 \text{ Sm}^{-1}$ and $I_y = 0.02 \text{ m}$. $\lambda := I_x/I_y$ denotes the anisotropy of the underlying conductivity fields	102
4.3	Contour plots of (dashed) M_x and (solid) M_y as a function of both $\sigma_{\ln\sigma}^2$ and λ computed on multivariate log-normal electrical conductivity fields of fixed mean value $\mu_{\sigma_w} = 0.1 \text{ Sm}^{-1}$ that exhibit connection of (a) conductivity values around the mean value, (b) high conductivity values (connected field) and (c) low conductivity values (disconnected field). Two intersections of the M_x - and M_y -contours are marked with (a) blue (b) red and (c) green dots. Both the contours and dots appearing in (a) are reproduced in (b) and (c) as well with transparency, for reference.	103
4.4	Histograms of secondary electric field appearing when a heterogeneous fluid conductivity field is imposed an electrical potential difference in the (a-c) x -direction and (b-d) y -direction. Two pairs of heterogeneous fluid conductivity fields are considered, having variances (blue histogram) $\sigma_{\ln\sigma}^2 = 0.3$ and (orange histogram) $\sigma_{\ln\sigma}^2 = 3$ and anisotropy factors (first row) $\lambda = 1$ and (second row) $\lambda = 5$. The dashed black line marks the value of -1 V m^{-1}	105
4.5	Solute pulse transported in the positive x -direction at Péclet numbers of (a) 0.1 and (b) 1000.	106
4.6	(a) Spreading of the solute, quantified by Δ_{xx} , (b) mixing of the solute, quantified by χ/D and (c) observed mixing factor in the y -direction, M_y for solute pulse transported at Péclet numbers of (blue) 0.1 and (orange) 1000.	107

List of Tables

2.1	KLDs and mean relative biases of \mathbf{m}_1 for the different conditioning data types. Columns 1 and 2 show the mean μ_{KLD} and standard deviation σ_{KLD} of the KLDs using the ensemble of hydraulic conductivity realizations. Column 3 shows the KLD values for the joint posterior PDFs using one realization of the conditioning data obtained from Figures 2.4a-c and highlighted in Figures 2.5a-c. The subsequent pairs of columns show the marginal KLD values and relative mean biases for the marginal posteriors of each component of \mathbf{m}_1 using this specific realization.	38
2.2	KLDs and mean relative biases of \mathbf{m}_e for the different conditioning data types. Columns 1 and 2 show the mean μ_{KLD} and standard deviation σ_{KLD} of the KLDs using the ensemble of hydraulic conductivity realizations. Column 3 shows the KLD values for the joint posterior PDFs using one realization of the conditioning data obtained from Figures 2.4d-f and highlighted in Figures 2.7a-c. The subsequent pairs of columns show the marginal KLD values and relative mean biases for the marginal posteriors of each component of \mathbf{m}_2 using this specific realization.	40
2.3	KLDs and mean relative biases of \mathbf{m}_s for the different conditioning data types. Columns 1 and 2 show the mean μ_{KLD} and standard deviation σ_{KLD} of the KLDs using the ensemble of hydraulic conductivity realizations. Column 3 shows the KLD values for the joint posterior PDFs using one realization of the conditioning data obtained from Figures 2.4g-i and highlighted in Figures 2.9a-c. The subsequent pairs of columns show the marginal KLD values and relative mean biases for the marginal posteriors of each component of \mathbf{m}_3 using this specific realization.	42
3.1	List of symbols and parameters used throughout the manuscript.	57

Abstract

Effective assessment of the fate of water-soluble contaminants leaked to aquifers is crucial for the management and preservation of groundwater resources. The arrival time of a contaminant plume to a given location depends on its mean velocity and spreading rate, whereas the associated sanitary risk is strongly correlated to the plume's degree of mixing upon its arrival. Mixing in heterogeneous media results from the competition between local-scale diffusion and the spreading of the solute, the latter in turn governed by flow velocity heterogeneity spanning a wide range of spatial scales. As a result, contaminant solute transport unfolds over multiple spatial and temporal scales and is, thus, very challenging to characterize using conventional sparsely-sampled and local hydrological measurement techniques alone. Complementarily, the time-lapse direct-current (DC) geophysical method provides spatially- and temporally-distributed information on equivalent DC electrical conductivity, which is sensitive to the transport of electrically-conductive solutes and carries information on solute heterogeneity below the measurement support scale. Combined with conventional fluid sampling, the DC methodology holds promise as a means to quantitatively characterize the state and evolution of solute spreading and mixing. However, this requires establishing quantitative links between spreading and mixing measures and average DC electrical conductivity under general transport conditions. This calls first for quantification of the uncertainty of electrically-inferred solute transport measures and second for the development of an upscaling framework for predictive purposes. Since both tasks remain largely unresolved, there is a risk for systematic errors in the interpretations. Here, we present numerical, experimental and theoretical investigations aiming at advancing in both directions. Relying on a Bayesian inference framework, we quantify to what extent time-series of the equivalent electrical conductivity tensor observed during tracer tests can constrain geostatistical parameters of hydraulic conductivity fields. We find that the most and least informative data are the flow-aligned component of the tensor and the solute mass breakthrough, respectively. The variance of the field, controlling the spreading rate, is the best constrained parameter for all test cases and data types, followed by the integral scale in the direction perpendicular to the mean flow field. As an experimental contribution, we report on an optically- and electrically-monitored milli-fluidic saline tracer test aimed at understanding electrical signatures of the diffusion-limited mixing of an initially layered tracer distribution. We show that the different diffusion rates of the optical and electrical tracers must be taken into account to reach quantitative agreement between the optically-inferred and measured time-series of equivalent DC electrical conductivity. We find that the electrical data can constrain the initial layers' widths and associated diffusion transport time-scales as well as the degree of mixing of the tracer upon its arrival to the electrode positions. As a theoretical contribution, we introduce a new petrophysical parameter, the mixing factor M , to account for the impact of fluid conductivity heterogeneity below the measurement support scale. When considering anisotropic media, the diagonal components of the M -tensor depends on the variance and anisotropy ratio of heterogeneous conductivity fields, while the nature of the mapping is

affected by the connectivity of the conductivity field. We derive an expression for M , and thus for the equivalent conductivity, in terms of the expected value of the conductivity field fluctuations and the secondary electric field. Then, we study numerically the mapping linking the statistical properties of either field.

Key words: Hydrogeophysics, spreading and mixing, equivalent electrical conductivity, up-scaling, time-lapse DC method

Résumé

Une évaluation quantitative du devenir des contaminants hydrosolubles déversés dans les aquifères est cruciale pour la gestion et la préservation des ressources en eau souterraine. Le temps d'arrivée d'un panache de contaminants à un endroit donné dépend de sa vitesse moyenne et de sa taux de étalement, alors que le risque sanitaire associé est fortement corrélé au degré de mélange du panache à son arrivée. Le mélange dans les milieux hétérogènes résulte de la compétition entre la diffusion à l'échelle locale et l'étalement du soluté, cette dernière étant à son tour régie par l'hétérogénéité de la vitesse d'écoulement sur une large gamme d'échelles spatiales. Par conséquent, le transport de solutés contaminants se déroule sur de multiples échelles spatiales et temporelles et il est donc très difficile de le caractériser en s'appuyant uniquement sur des techniques de mesure hydrologiques locales et à faible échantillonnage. En complément, la méthode géophysique à courant continu fournit des informations réparties dans l'espace et dans le temps sur la conductivité électrique équivalente, qui est sensible au transport des solutés conducteurs d'électricité et fournit des informations sur l'hétérogénéité des solutés sous l'échelle du support de mesure. Combinée à l'échantillonnage conventionnel des fluides, la méthodologie est prometteuse comme moyen de caractériser quantitativement l'état et l'évolution de la propagation et du mélange des solutés. Cependant, cela nécessite d'établir des liens quantitatifs entre les mesures d'étalement et de mélange et la conductivité électrique moyenne dans des conditions générales de transport. Cela nécessite d'abord de quantifier l'incertitude des mesures de transport de solutés déduites électriquement et ensuite de développer un cadre de mise à l'échelle à des fins de prédiction. Comme ces deux tâches restent largement non résolues, il existe un risque d'erreurs systématiques dans les interprétations. Nous présentons ici des études numériques, expérimentales et théoriques visant à faire progresser ces objectifs de recherche. En nous appuyant sur un cadre d'inférence bayésienne, nous quantifions dans quelle mesure les séries temporelles du tenseur de conductivité électrique équivalent observés pendant les essais de traçage peuvent contraindre les paramètres géostatistiques des champs de conductivité hydraulique. Nous constatons que les données les plus et les moins informatives sont respectivement la composante du tenseur alignée sur le flux et la percée de la masse de soluté. La variance du champ, qui contrôle le taux d'étalement, est le paramètre le mieux contraint pour tous les cas d'essai et tous les types de données, suivi par l'échelle intégrale dans la direction perpendiculaire au champ d'écoulement moyen. En guise de contribution expérimentale, nous présentons un essai de traceur salin milli-fluidique contrôlé optiquement et électriquement, visant à comprendre les signatures électriques du mélange limité par la diffusion d'une distribution de traceur initialement stratifiée. Nous montrons que les différents taux de diffusion des traceurs optiques et électriques doivent être pris en compte pour obtenir une correspondance quantitative entre les séries temporelles de conductivité électrique équivalente déduites par voie optique et mesurées. Nous constatons que les données électriques peuvent contraindre les largeurs des couches initiales et les échelles de temps de transport et de diffusion associées, ainsi que le degré de mélange du traceur à son arrivée aux électrodes.

Comme contribution théorique, nous introduisons un nouveau paramètre pétrophysique, le facteur de mélange M , pour tenir compte de l'impact de l'hétérogénéité de la conductivité du fluide sous l'échelle du support de mesure. En considérant les milieux anisotropes, les composantes diagonales du tenseur M dépendent de la variance et du rapport d'anisotropie des champs de conductivité hétérogènes, tandis que la nature de la cartographie est affectée par la connectivité du champ de conductivité. Nous dérivons une expression pour M , et donc pour la conductivité équivalente, en termes de valeur attendue des fluctuations du champ de conductivité et du champ électrique secondaire. Ensuite, nous étudions numériquement la cartographie reliant les propriétés statistiques de l'un ou l'autre champ.

Mots clefs : Hydrogéophysique, étalement et mélange, conductivité électrique équivalente, mise à l'échelle, méthode courant continu répétée dans le temps.

Chapter 1

Introduction

1.1 Motivation

A key component in the management and preservation of groundwater resources is to monitor the fate of aquifer contaminants (e.g., *Houlihan and Botek*, 2016). When a water-soluble contaminant is leaked into groundwater from a localized source, it is transported downstream in the form of a plume, with a center of mass that travels at the mean groundwater flow velocity and, an evolving shape and internal topology that is determined by the sampled velocity field fluctuations with respect to the mean velocity along its path. By deploying fluid sampling instruments along boreholes (e.g., *Maliva*, 2016), breakthrough curve analysis (e.g., *Rubin et al.*, 1997) can provide detailed localized flux-averaged information on the passing plume. This information is nevertheless restricted to the measurement points and is, thus, often insufficient to effectively describe the entire plume; a limitation that is well-established in the literature (e.g., *Western et al.*, 2002; *Butler*, 2005). If the contaminant solute-plume exhibits a significant contrast of electrical conductivity with respect to the in situ groundwater electrical conductivity, then the direct-current (DC) geophysical method can provide a minimally invasive and cost-effective means to constrain the transport of the contaminant.

The usage of the DC geophysical method to complement classical hydrogeological characterization techniques emerged during the 1990's (e.g., *Rubin and Hubbard*, 2005; *Binley et al.*, 2015) within the so-called hydrogeophysical discipline. One of the first attempts to monitor an in-situ contaminant remediation process using the DC method is reported in the field study from *Daily and Ramirez* (1995), where they imaged the temporal evolution of preferential flow paths at the Savannah River Site near Aiken, South Carolina. Another early example is the study from *Slater et al.* (2000), where they used the DC method to monitor a sinking saline body during a controlled tank experiment and introduced the idea of interpreting time-lapse electrical images as a collection of electrical breakthrough curves, in a manner similar to hydrogeological tracer data. This enabled them to perform a qualitative assessment of the spatial distribution of advective-dispersive transport parameters using the DC data. Along this line, more quantitative studies were performed by *Kemna et al.* (2002) and *Binley et al.* (2002). *Kemna et al.* (2002), for instance, provided a field demonstration aiming at retrieving equivalent 1-D stream-tube advective-dispersive transport parameters in the context of 3-D conservative saline transport. Their results were later corroborated

numerically by *Vanderborght et al.* (2005). *Koestel et al.* (2008) inferred the 3-D distribution of solute velocities and dispersivities in a soil column using time-lapse ERT data. A large body of literature dealing with the usage of the DC method to constrain the transport of contaminants has developed over the last three decades (e.g., *Binley et al.*, 2015; *Binley and Slater*, 2020). Over time, the research has moved towards more quantitative goals (*Singha et al.*, 2015), most notably by accounting for spatially and temporal resolution variations of inverted time-lapse DC images (e.g., *Day-Lewis et al.*, 2005; *Singha and Gorelick*, 2006; *Moysey et al.*, 2005a).

The sanitary risk associated with the arrival of a contaminant plume is highly correlated with its maximum contaminant levels (e.g., *Ahuja et al.*, 2014) or, in other words, on the plume's degree of dilution. Plume dilution is achieved through the action of mixing, which is ultimately driven by molecular diffusion, the latter resulting in a net solute flux whenever a solute body presents spatial concentration gradients. Before the plume becomes fully mixed in the direction perpendicular to the flow (i.e, during preasymptotic transport), the plume spreading creates and enhances concentration contrasts. Consequently, mixing in porous media has been defined as flow- or stretched-enhanced molecular diffusion (e.g., *Villermanx*, 2019), implying that there exists a coupling between the flow properties and the dilution rate of contaminants.

Heterogeneity in geologic media appears at a broad range of scales (e.g., *Fetter*, 2018) and solute transport is impacted differently across all the spectrum (e.g., *Berkowitz et al.*, 2006), with the smaller scales notably having a large impact on the mixing of solutes (e.g., *Rolle and Le Borgne*, 2019). Capturing such complex behaviour under field conditions becomes particularly challenging since aquifer characterization is typically feasible only at a single spatial scale associated with the borehole length and spacing (e.g., *Hyndman*, 2016). Developing effective descriptions of solute transport is both a longstanding (e.g., *Matheron and De Marsily*, 1980; *Gelhar and Axness*, 1983; *Haggerty and Gorelick*, 1995; *Berkowitz et al.*, 2006) and active topic of research (e.g., *Dentz et al.*, 2011; *Le Borgne et al.*, 2015; *Comolli et al.*, 2019). One notable development is the multi-rate mass transfer conceptual model (*Haggerty and Gorelick*, 1995), where geologic media is represented as an overlapping continua that store and exchange solute mass with each other at different rates. Among these, the simpler dual domain model (*Coats and Smith*, 1964; *Van Genuchten and Wierenga*, 1976) is probably the most popular one, where media is split into a mobile and an immobile domain; solutes are advected by the flow within the mobile domain while they are exchanged by diffusion with the immobile domain.

A major obstacle is the current lack of practical hydrological methods enabling testing and calibration of such transport models. For instance, conventional hydrogeological sampling do not collect fluid from the immobile portion of the domain directly, but from the mobile pore fluid (e.g., *Singha et al.*, 2007). At the same time, bulk electrical conductivity can sense electrolytic solutes simultaneously from both domains. Solute transport appears particularly well-suited to be characterized using geoelectrical methods that provide spatially- and temporally-distributed information about electrical conductivity and, hence, salinity variations. The DC method has shown potential to constrain the mixing state of solutes. *Singha et al.* (2007) provided field and numerical evidence of the sensitivity of time-lapse DC measurements to dual-domain mass transfer parameters. *Day-Lewis and Singha* (2008) combined the moment-generating equation technique from *Harvey and Gorelick* (1995)

with a modified (two-phase) version of Archie's law (Archie, 1942). Then they proposed a framework that successfully enabled extraction of dual-domain mass transfer parameters of laboratory core-samples, by combining the temporal moments of two types of time-series: the concentration breakthrough curve and time-lapse geoelectrical data, mainly sensitive to the mobile and both portions of the domain, respectively. Briggs *et al.* (2013) calibrates a spatial distribution of dual-domain mass transfer parameters at the Naturita Site, Colorado, by combining fluid and time-lapse DC data.

Still, using the DC method to produce quantitative constraints on solute transport remains a persistent challenge (e.g., Singha *et al.*, 2015). One of the main obstacles lies at the conversion of the observed or inferred DC electrical conductivity distribution at some spatial scale into some measure of the contaminant concentration field, typically in terms of a mean concentration value, by means of a petrophysical relationship. The conversion usually takes place at the (spatially-variable) resolution scale of electrical images that is implicitly assumed to correspond to a Representative Elementary Volume (REV) scale (Hill, 1963) at which the petrophysical relationship is derived. Indeed, the scale at which electrical conductivity is resolved by inversion tends to be large compared to the expected scale of heterogeneity of the salinity field. This leads to spatial fluctuations within the conductivity averaging volume that are not statistically homogeneous (Torquato and Haslach Jr, 2002), for instance, a single solute finger traversing the conductivity averaging volume. These type of sub-resolution features represent non-ergodic fields for which no petrophysical relationship exists, yet they exert a major impact on the observed electrical conductivity (e.g., Jougnot *et al.*, 2018; Visentini *et al.*, 2020, 2021). Archie's relationships remain as the standard petrophysical relationship used to convert average DC electrical conductivity into mean saline concentration (Revil *et al.* (2018)). This choice implies that saline heterogeneity is ignored below the scale of resolution of the electrical conductivity field. Poor recovery of spatial and temporal moments of tracer plumes from electrical monitoring have been systematically reported (e.g., Binley *et al.*, 2002; Singha and Gorelick, 2005; Müller *et al.*, 2010; Doetsch *et al.*, 2012a; Laloy *et al.*, 2012), and is often a consequence of unaccounted saline heterogeneity.

In essence, the DC geophysical method holds much promise to constrain the spreading and mixing state and evolution of solutes below the scale of observed average electrical conductivity in saturated porous media. Yet, the electrical signature of these solute transport processes below the scale of resolution is not accounted for and there is presently no framework to treat them quantitatively. The development of an upscaling framework enabling quantitative prediction of the DC electrical signatures corresponding to sub-scale saline heterogeneity remains a challenging and important research topic. In order to move towards this goal, it is necessary to consider controlled settings where the different heterogeneous features and their DC signature can be assessed. This enables not only to develop conceptual understanding and produce quantitative links for restricted cases of heterogeneity (e.g., statistically homogeneous fields), but also to quantify uncertainties in interpretations where the electrical signature is very challenging or even impossible to upscale (e.g., non-ergodic heterogeneity).

1.2 Basic theory and modelling tools

1.2.1 Groundwater flow and solute transport

In this thesis, we model groundwater flow at the Darcy scale \mathbf{x} (e.g., *Bear*, 1972; *Whitaker*, 2013) and solute transport within an Eulerian framework (e.g., *Rubin*, 2003). Note that we use interchangeably the symbol \mathbf{x} to denote a point and the support scale at which the point is defined (e.g., *Cortis et al.*, 2004).

Water mass conservation at the Darcy point \mathbf{x} is expressed by the continuity equation for the specific discharge $\mathbf{q}(\mathbf{x})$. For steady-state flow and in the absence of flow sources or sinks, it reads:

$$0 = \nabla \cdot \mathbf{q}(\mathbf{x}), \quad (1.1)$$

with " \cdot " denoting the dot product. Darcy's law relates $\mathbf{q}(\mathbf{x})$ with the hydraulic conductivity $K(\mathbf{x})$ and the hydraulic head $h(\mathbf{x})$ via

$$\mathbf{q}(\mathbf{x}) = -K(\mathbf{x})\nabla h(\mathbf{x}). \quad (1.2)$$

Adopting Darcy's law, the groundwater flow equation reads:

$$\nabla K(\mathbf{x})\nabla h(\mathbf{x}) + K(\mathbf{x})\nabla^2 h(\mathbf{x}) = 0. \quad (1.3)$$

Equation 1.3 is solved numerically using the open-source finite-difference solver MODFLOW-2005 (*Harbaugh*, 2005).

Solute mass conservation at the point \mathbf{x} is expressed by the continuity equation for the solute concentration $c(\mathbf{x}, \mathbf{t})$ as:

$$\frac{\partial c(\mathbf{x}, \mathbf{t})}{\partial t} + \nabla \cdot \mathbf{J}_c = 0, \quad (1.4)$$

where the solute flux \mathbf{J}_c is given by advective, $\mathbf{q}(\mathbf{x})c(\mathbf{x}, t)$, and dispersive, $\mathbf{D}(\mathbf{x}) \cdot \nabla c(\mathbf{x}, t)$ components, with $\mathbf{D}(\mathbf{x}) = \lambda_{ij}(\mathbf{x}) + \phi D_m \mathbf{I}$ the hydrodynamic dispersion tensor, accounting for the anisotropic dispersivity $\lambda_{ij}(\mathbf{x})$, caused by velocity fluctuations at smaller scales than \mathbf{x} , and molecular diffusion at the rate ϕD_m . That is:

$$\mathbf{J}_c = \mathbf{q}(\mathbf{x})c(\mathbf{x}, t) - \mathbf{D}(\mathbf{x}) \cdot \nabla c(\mathbf{x}, t). \quad (1.5)$$

Inserting Eq. 1.5 into Eq. 1.4 we obtain the Advection-Dispersion Equation (ADE):

$$\phi \frac{\partial c(\mathbf{x}, \mathbf{t})}{\partial t} + \mathbf{q}(\mathbf{x}) \cdot \nabla c(\mathbf{x}, t) - \nabla [\mathbf{D}(\mathbf{x}) \cdot \nabla c(\mathbf{x}, t)] = 0. \quad (1.6)$$

Equation 1.6 is solved numerically using the groundwater solute transport simulator package MT3D-USGS (*Bedekar et al.*, 2016), assuming constant dispersivity over \mathbf{x} .

1.2.2 Solute plume description: spreading and mixing

The location $\alpha(t)$ of the center of mass of a solute plume observed over some volume V is given by the first spatial moment of $c(\mathbf{x}, t)$:

$$\alpha(t) = \int_V c(\mathbf{x}, t) \mathbf{x} d\mathbf{x}. \quad (1.7)$$

This expression assumes that $c(\mathbf{x}, t)$ is normalized (i.e., it satisfies $\int_V c(\mathbf{x}, t) d\mathbf{x} = 1$). The standard measure of the spread of a solute plume is given by the second spatial moment of $c(\mathbf{x}, t)$ centered at $\alpha(t)$:

$$\Delta_{ij}(t) = \int_V c(\mathbf{x}, t) (\mathbf{x} - \alpha_i(t)) (\mathbf{x} - \alpha_j(t)) d\mathbf{x}. \quad (1.8)$$

The rate of spreading of a solute plume is quantified by the apparent dispersion coefficient $D_{ij}^a(t)$

$$D_{ij}^a(t) = \frac{1}{2} \frac{d\Delta_{ij}}{dt}. \quad (1.9)$$

A common measure of concentration variability is the second statistical moment of $c(\mathbf{x}, t)$, that is, the concentration variance $\sigma_c^2(t)$. Decomposing $c(\mathbf{x}, t)$ into the sum of its mean $\hat{c}(t)$ and fluctuating part $c'(\mathbf{x}, t)$, $\sigma_c^2(t)$ can be expressed as (e.g., Kapoor and Kitanidis, 1998)

$$\sigma_c^2(t) = \int_V c'(\mathbf{x}, t)^2 d\mathbf{x}. \quad (1.10)$$

A measure of the mixing rate of $c(\mathbf{x}, t)$ is given by the scalar dissipation rate (e.g., Pope, 2001):

$$\chi(t) = \int \nabla c'(\mathbf{x}, t) \cdot \mathbf{D} \nabla c'(\mathbf{x}, t) d\mathbf{x}, \quad (1.11)$$

which represents the net solute mass transfer resulting from the presence of concentration gradients and their dissipation by local-scale diffusion (e.g., *Le Borgne et al.*, 2010).

1.2.3 Introduction to the DC geophysical method

The DC geophysical method aims at retrieving information about the spatial distribution of average electrical resistivity in the subsurface. A DC measurement requires two pairs of electrodes: one pair for establishing a known electrical current between two points (can also be lines or surfaces), and the other for measuring the resultant electrical voltage between two other points (e.g., *Keller and Frischknecht*, 1966). The measured resistance (voltage over current) is multiplied by a geometrical factor that accounts for the electrode positions and the probed domain's geometry. The obtained data is termed apparent resistivity (or

conductivity, the inverse of resistivity) and corresponds to the true resistivity if the medium is homogeneous.

The number of electrodes in use depends on the type of application. It is sometimes few, for example, when considering the apparent conductivity of small-scale laboratory core samples (e.g., *Kozlov et al.*, 2012; *Maineult et al.*, 2016; *Ghosh et al.*, 2018), and sometimes hundreds during field experiments (e.g., *Binley et al.*, 2002; *Cassiani et al.*, 2006; *Doetsch et al.*, 2012b). For this latter case, data are collected from electrodes that are typically deployed on either the soil surface or along boreholes. Since the apparent conductivities are sensitive to different parts of the probed volume, they are processed by an inversion procedure yielding a 2- or 3-D image of average electrical conductivity at a given scale of resolution. This process is often referred to as Electrical Resistivity Tomography (ERT).

DC measurements provide average values of electrical conductivity at the scale of the point \mathbf{y} , which for most applications in hydrogeology is greater or equal than to the Darcy scale \mathbf{x} (e.g., *Bear*, 1972) and certainly much greater than the pore scale \mathbf{x}' (see Fig. 1.1). Typically, it is $\mathbf{y} > \mathbf{x}$ during DC field and tank experiments (e.g., *Vanderborgh et al.*, 2005; *Koestel et al.*, 2009), and possibly $\mathbf{y} \sim \mathbf{x}$ for laboratory core-sample measurements or laboratory-based electrically-monitored tracer tests (e.g., *Jougnot et al.*, 2018; *Visentini et al.*, 2021).

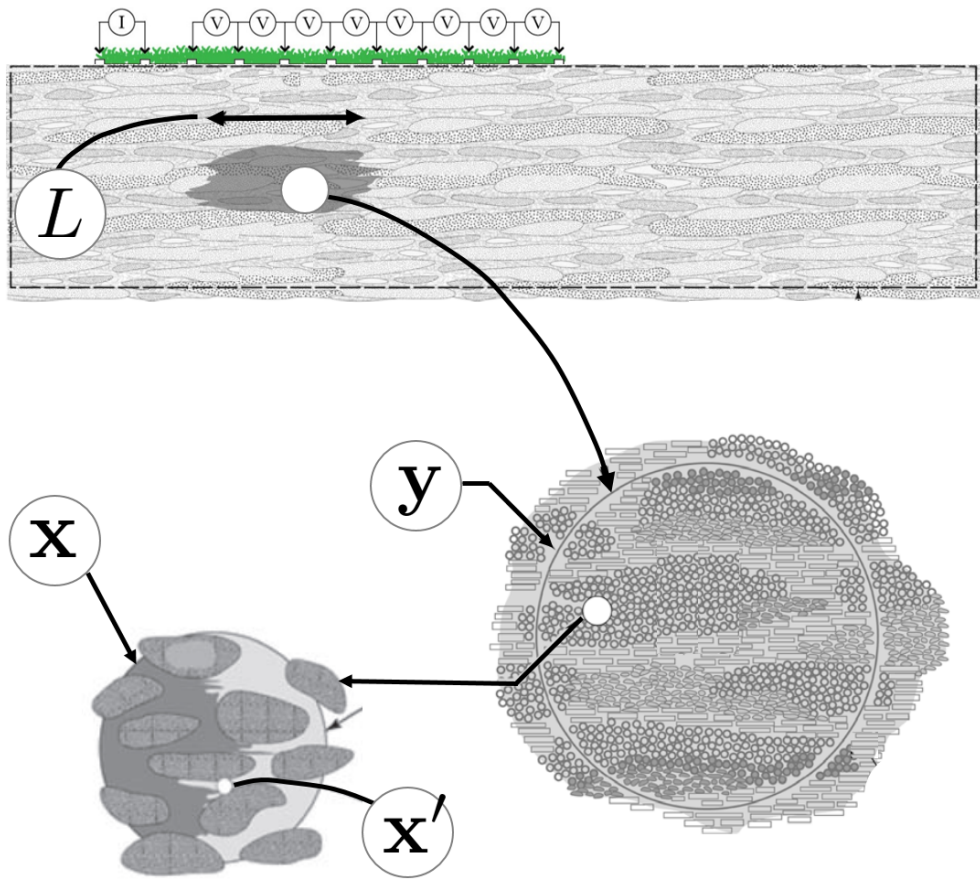


Figure 1.1 – Contaminant plume of size L monitored with the DC geophysical method. Some known current I is injected into the ground from the electrode pair on the left and eight voltages are measured at different distances from both the current source and the target (plume). In this schematic drawing y represents a point at the scale at which the average electrical conductivity is observed, while x represents a point at the Darcy scale and x' represents a point at the pore scale. Adapted from *Wood* (2009).

A DC experiment can be repeated over time to monitor a time-varying system and the measurement protocol will then output time-series of apparent conductivity. Accordingly, if time-lapse ERT is performed, then a collection of time-lapse 2-D or 3-D images of average electrical conductivity is obtained after inversion. See the recent book by *Binley and Slater* (2020) for a comprehensive overview.

1.2.4 DC electrical conduction

Analogously to groundwater flow, the departure point to describe DC electrical conduction is the principle of electric charge conservation, which is expressed by the continuity equation for the macroscopic current density field $\mathbf{J}(\mathbf{x}')$. For steady-state conduction and in the absence of current sources or sinks, the continuity equation reads:

$$\nabla \cdot \mathbf{J}(\mathbf{x}') = 0. \quad (1.12)$$

Ohm's law relates $\mathbf{J}(\mathbf{x}')$ with the electrical conductivity $\sigma(\mathbf{x}')$ and the electric field $\mathbf{E}(\mathbf{x}')$ via the linear relationship $\mathbf{J}(\mathbf{x}') = \sigma(\mathbf{x}')\mathbf{E}(\mathbf{x}')$. Adopting the quasistatic approximation, $\nabla \times \mathbf{E}(\mathbf{x}') = 0$, allows to express $\mathbf{E}(\mathbf{x}') = -\nabla U(\mathbf{x}')$, where $U(\mathbf{x}')$ is the electrical potential. Writing $\mathbf{J}(\mathbf{x}')$ in terms of $U(\mathbf{x}')$ as $\mathbf{J}(\mathbf{x}') = -\sigma(\mathbf{x}')\nabla U(\mathbf{x}')$ and replacing this expression into Eq. 1.12 results in the governing Laplace equation for the electrical potentials:

$$\nabla \sigma(\mathbf{x}')\nabla U(\mathbf{x}') + \sigma(\mathbf{x}')\nabla^2 U(\mathbf{x}') = 0. \quad (1.13)$$

Once the electrical conductivity field $\sigma(\mathbf{x}')$ and boundary conditions for $U(\mathbf{x}')$ are given over the contour of some domain, Eq. 1.13 can be solved for the latter. Since an exact analytical solution of Eq. 1.13 does not exist in general, one often has to rely on numerical methods (e.g., *Rücker et al.*, 2017).

1.2.5 Average electrical conductivity

The average or equivalent electrical conductivity σ_{eq} considered over some support volume V is defined through a volume-averaged Ohm's law as (e.g., *Whitaker*, 2013; *Sanchez-Vila et al.*, 2006)

$$\sigma_{\text{eq}} = \frac{\bar{\mathbf{J}}}{\bar{\mathbf{E}}}, \quad (1.14)$$

where

$$\bar{\mathbf{J}} = \frac{1}{V} \int_V \mathbf{J}(\mathbf{x}') dV, \quad (1.15)$$

and

$$\bar{\mathbf{E}} = \frac{1}{V} \int_V \mathbf{E}(\mathbf{x}') dV. \quad (1.16)$$

An alternative, equivalent definition of σ_{eq} derives from considering energy conservation over V . For simplicity, but without loss of generality, let us assume that V is a cube of side length L . An electrical potential difference ΔU is applied between two opposite faces of the cube, driving an electrical current i . The power dissipated by the sample in the form of Joule's heat is given as $i\Delta U$ which, applying Ohm's law, we can express as $S\Delta U^2$, with S the conductance of the sample, given as $S = \sigma_{\text{eq}}L$. By grouping factors we can express the power in terms of the modulus of the impressed electric field $E_0 = -\Delta U/L$ and σ_{eq} as $-VE_0^2\sigma_{\text{eq}}$. Analogously, the power dissipated locally at the point \mathbf{x}' is given by the dissipation functional $\mathbf{E}(\mathbf{x}') \cdot \mathbf{J}(\mathbf{x}')$. Again, using Ohm's law we can express $\mathbf{E}(\mathbf{x}') \cdot \mathbf{J}(\mathbf{x}') = -\mathbf{E}(\mathbf{x}') \cdot \sigma(\mathbf{x}')\mathbf{E}(\mathbf{x}')$. This quantity, integrated over V , must be identical to $-VE_0^2\sigma_{\text{eq}}$ due to energy conservation. That is:

$$-VE_0^2\sigma_{\text{eq}} = - \int_V \mathbf{E}(\mathbf{x}') \cdot \sigma(\mathbf{x}')\mathbf{E}(\mathbf{x}') dV, \quad (1.17)$$

or,

$$\sigma_{\text{eq}} = \frac{1}{E_0^2 V} \int_V \mathbf{E}(\mathbf{x}') \cdot \sigma(\mathbf{x}')\mathbf{E}(\mathbf{x}') dV, \quad (1.18)$$

which gives the energy representation formula of the equivalent conductivity (e.g., *Johnson et al.*, 1986; *Bernabé and Revil*, 1995). Note that in the context of hydrogeology, such a formulation is also employed for the equivalent hydraulic conductivity (e.g., *Dagan*, 1989), where $\mathbf{E}(\mathbf{x}')$ is replaced by the pressure head gradient field and $\sigma(\mathbf{x}')$ by the hydraulic conductivity field.

1.2.6 Overview of upscaled electrical conductivity

The volume-averaging operations expressed by Eqs. 1.14 or 1.18 make it possible to always obtain σ_{eq} given knowledge of $\sigma(\mathbf{x}')$ and some method to solve Eq. 1.13. However, complete knowledge of $\sigma(\mathbf{x}')$ is not always required to estimate the macroscopic response σ_{eq} , and not possible to attain anyway. What is sought in general, and in hydrogeophysical modelling in particular, is to summarize $\sigma(\mathbf{x}')$ using a few descriptors that, combined under some law or framework, enable prediction of σ_{eq} . In other words, an upscaling procedure for σ_{eq} is sought (e.g., *Wen and Gómez-Hernández*, 1996; *Renard and De Marsily*, 1997; *Sanchez-Vila*

et al., 2006; *Hunt and Sahimi*, 2017). A detailed discussion on the conceptual differences between averaging and upscaling are discussed for instance in *Wood* (2009).

The upscaling operation is tied to the notion of Representative Elementary Volume (REV) (*Hill*, 1963). The averaging volume V is a REV for σ_{eq} if σ_{eq} becomes stationary at V (i.e., σ_{eq} does not change significantly when computed using volumes in the vicinity of V). This implies (i) the existence of structural features of $\sigma(\mathbf{x}')$ that mainly controls the average electrical response and (ii) that these features are sufficiently well-captured at the scale of V (e.g., *Wood*, 2009). More formally, if $\sigma(\mathbf{x}')$ is conceptualized as one realization of a spatial stochastic process then (i) means that the process is statistically homogeneous, that is, its statistical properties (typically mean and covariance) are invariant under translations and (ii) means that $\sigma(\mathbf{x}')$ at the scale of V is ergodic, that is, the statistical properties of the process are sufficiently sampled by that specific single realization (e.g., *Torquato and Haslach Jr*, 2002; *Christakos*, 2012).

There exist only three exact results for electrical (or hydraulic) conductivity upscaling that we are aware of. The first two are given when $\sigma(\mathbf{x}')$ is organized into layers (or laminated) (e.g., *Milton and Sawicki*, 2003) that are parallel or perpendicular to the electrical conductivity measurement direction. For these two cases, σ_{eq} results from averaging $\sigma(\mathbf{x}')$ arithmetically and harmonically, respectively, and the average response can be obtained from knowledge of the conductivity of each layer and the volume fractions occupied by each conductive phase, without knowing, for instance, the ordering of the layers nor the thickness of each of them. The third available exact result for conductivity upscaling is given for 2-D isotropic fields when $\ln \sigma(\mathbf{x}')$ follows an even histogram. In this case, σ_{eq} equates the geometric mean of $\sigma(\mathbf{x}')$ (*Dykhne*, 1971). These examples highlight that conductivity averaging process is non-linear, meaning that it is not constant but depends on $\sigma(\mathbf{x}')$. This introduces a dependence of the (unknown) averaging operator on the observation scale V as well, as different observational volumes capture different heterogeneous features of $\sigma(\mathbf{x}')$.

Since σ_{eq} depends in general on both low- and high-order spatial statistics, as well as the topology (i.e., connectivity) of $\sigma(\mathbf{x}')$, V becomes an REV for σ_{eq} once these 'structural' properties become stationary at V . Capturing sufficiently well such structural features usually requires larger observational volumes compared to, for instance, one-point statistical measures of $\sigma(\mathbf{x}')$, such as its mean μ_c and variance σ_σ^2 (e.g., *Demirel et al.*, 2019; *Koestel et al.*, 2020). Consequently, it usually takes longer to reach a REV (assuming that it exists) for σ_{eq} compared to those measures. In Fig. 1.2 we compare the convergence of σ_{eq} , μ_c and σ_σ^2 as a function of the observational volume, using two heterogeneous fields $\sigma(\mathbf{x}')$ as example, organized into layers (Fig. 1.2a) and lenses (Fig. 1.2b).

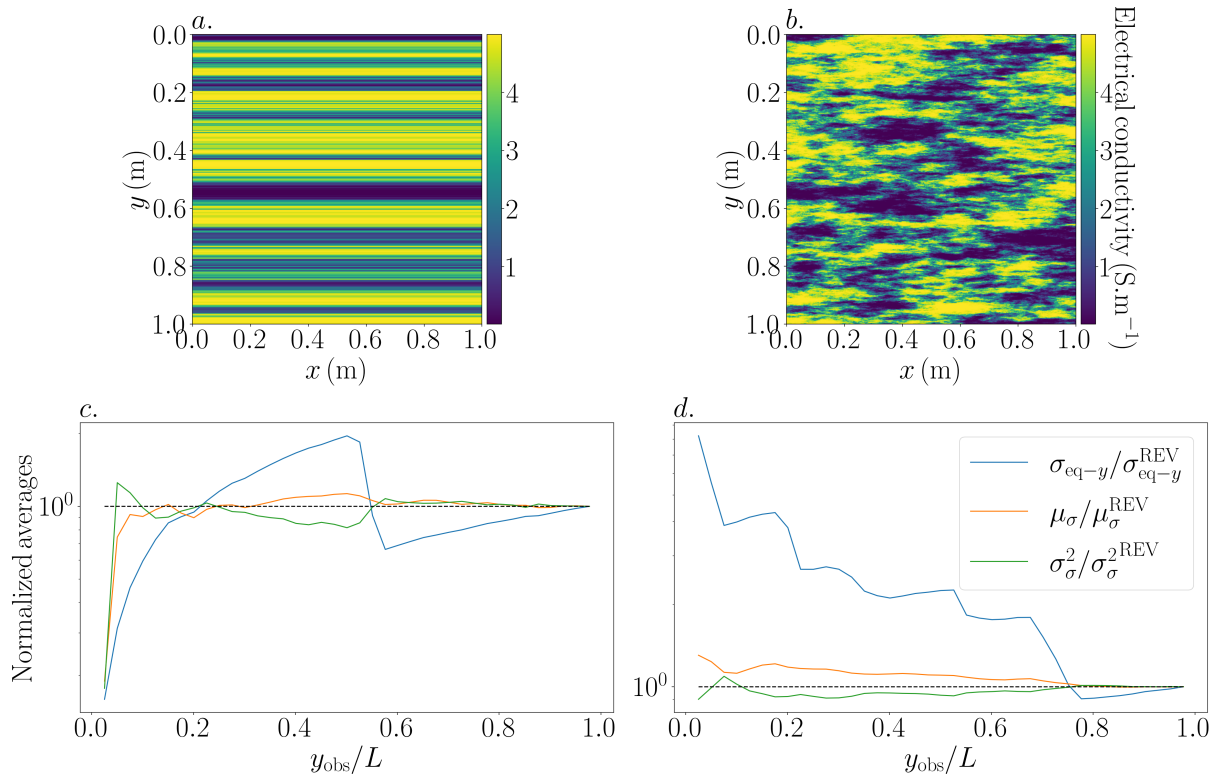


Figure 1.2 – Two-dimensional 1 m \times 1 m heterogeneous multivariate-lognormal electrical conductivity fields organized into (a) layers and (b) lenses. Plots of σ_{eq-y} , μ_σ and σ_σ^2 , computed using subdomains of the electrical conductivity fields that have a length of 1 m and varying height y_{obs} starting at $y = 0$ m for (c) the layered and (d) lensed fields. The data are normalized by their corresponding values when observed using the full domain’s height.

Note that when the conductivity field is perfectly layered, the value of σ_{eq} is strongly controlled by the smaller conductances. Accordingly, the convergence of σ_{eq} becomes highly dependent on how well-sampled such layers are. This can be seen in Fig. 1.2c, where σ_{eq-y} shows an abrupt decrease at $y_{obs} \sim 0.55$ m, that is, after the sampling rectangle incorporates the relatively thick and low conductive layer appearing at that height (Fig. 1.2a).

Fig. 1.2 shows that σ_{eq} converges slower than both μ_σ and σ_σ^2 and, in fact, note σ_{eq} is likely to keep fluctuating if larger domains would be considered. Thus, the considered domains cannot be regarded as REVs for σ_{eq} . In general, there will exist a range of observation scales for which the REV is reached for μ_σ (or σ_σ^2 or other statistical measures of the field) but not for σ_{eq} . This observation becomes relevant in the context of electrically-monitored saline tracer tests, as σ_{eq} , observed at the scale of V , is typically used to infer the mean fluid electrical conductivity at the same scale.

The literature dealing with upscaling methodologies of electrical (or hydraulic) conductivity is vast. Perhaps the most common type of upscaling approaches encountered in the stochastic subsurface hydrology and electrical literature are based on: a perturbative treatment of the constitutive relationship (i.e., Darcy’s or Ohm’s law) (e.g., *Gelhar and Axness, 1983*), the Effective Medium Approximation (EMA) (e.g., *Dagan, 1979; Sen et al., 1981*), and

percolation theory (e.g., *Katz and Thompson*, 1986, 1987). The workflow for each of these families of methodologies is different. In the perturbative approach, most commonly seen for hydraulic conductivity upscaling, the logarithm of the hydraulic conductivity field is decomposed into a mean (constant) and fluctuating part, and the fluctuating part is expanded into power series of the variance of the log-transformed field. By assuming that the fluctuating field has a small amplitude, and using the so-called closure approximations (e.g. *Zhang*, 2001), the average hydraulic conductivity is typically expressed in terms of the geometric mean of the hydraulic conductivity field and a polynomial of the variance of variance of the logarithmically-transformed conductivity (e.g., *Dagan*, 1989; *Zhang*, 2001; *Sanchez-Vila et al.*, 2006). In the EMA-based approaches, the conductivity field is replaced by a fictitious (simplified) medium, for instance an ensemble of spherical or ellipsoidal inclusions of some conductivity that are submerged in a matrix of contrasting conductivity. By making extra assumptions (e.g., the electric field perturbations due to each inclusion do not interact with each other), the average conductivity is expressed in terms of the conductivities, volume fractions and some shape measure of the inclusions (e.g., anisotropy of the ellipsoids) (e.g., *Chelidze and Gueguen*, 1999; *Torquato and Haslach Jr*, 2002; *Choy*, 2015). Among percolation-based approaches, perhaps the most well-suited to deal with continuous fields is the critical path analysis, which assumes that the average electrical response is controlled by the path of least resistance connecting the two sides of the domain sustaining the electrical potential (or pressure head) difference. In its simplest version, the conductance of the sample is obtained as the conductance of the critical path (e.g., *Hunt*, 2001; *Daigle*, 2016; *Hunt and Sahimi*, 2017).

Equivalent conductivity for homogeneous fluid electrical conductivity

For a water-saturated porous medium, σ_{eq} depends on the structural properties of both the pore volume and the fluid electrical conductivity field residing within the pores (e.g., *Revil et al.*, 2018). The starting point of electrical conductivity upscaling in water-saturated porous media is the case when the sample has an insignificantly conductive matrix and no surface conductivity (e.g., *Waxman and Smits*, 1968; *Revil and Glover*, 1998). It is useful at this point to describe the pore space with an indicator function $\Phi(\mathbf{x}')$, which takes values of 0 and 1 in the matrix and pore spaces, respectively, and to define the electrical conductivity field as $\sigma(\mathbf{x}') = \sigma_w(\mathbf{x}')\Phi(\mathbf{x}')$. If we further assume that the fluid electrical conductivity field $\sigma_w(\mathbf{x}')$ is constant and equal to some value σ_f then σ_{eq} can be obtained from dividing σ_f by the formation factor F , a geometrical constant that encodes the electrical effect of the pore space (e.g., *Avellaneda and Torquato*, 1991). Indeed, from Eq. 1.18 we have:

$$\sigma_{eq} = \frac{\sigma_f}{VE_0^2} \int_{V_p} \mathbf{E}(\mathbf{x}') \cdot \mathbf{E}(\mathbf{x}') dV_p, \quad (1.19)$$

or

$$\sigma_{eq} = \frac{\sigma_f}{F}, \quad (1.20)$$

with

$$\frac{1}{F} = \frac{1}{VE_0^2} \int_{V_p} \mathbf{E}(\mathbf{x}') \cdot \mathbf{E}(\mathbf{x}') dV_p, \quad (1.21)$$

where V_p denotes the pore volume. The right-hand side of Eq. 4.15 expresses a weighted average of the pore space, where the weights $\mathbf{E}(\mathbf{x}') \cdot \mathbf{E}(\mathbf{x}')$ correspond to the local dissipated power, divided by the conductivity. The quantity, $1/F$ is a measure of the effective (electrical) porosity participating to electrical conduction (e.g., *Revil and Cathles III*, 1999). Defining F through Eq. 1.21 is meaningful provided that V is a REV for the quantity at its right-hand side (RHS).

Archie's empirical law is given by

$$F = \phi^{-m}, \quad (1.22)$$

where ϕ and m are, respectively, the average porosity and cementation exponent, the latter being inversely related to the connectivity of the pore space (e.g., *Glover*, 2009). Archie's law has been reproduced by *Sen et al.* (1981) using the Differential Effective Medium (DEM) mixing procedure (e.g., *Bruggeman*, 1935), which is one type of EMA-based upscaling approach. *Bussian* (1983) used the DEM to extend the model of *Sen et al.* (1981), allowing the matrix to be conductive. By decomposing $\mathbf{E}(\mathbf{x}')$ into its primary and secondary parts, in Chapter 4 we provide an expression for F in terms of the mean value and variance of the secondary part of the electric field. By allowing the matrix to be conductive, we also provide an expression for σ_{eq} that has the same form as the model proposed empirically by *Glover et al.* (2000), thereby substantiating it theoretically.

Equivalent conductivity for heterogeneous fluid electrical conductivity

If we relax the assumption of homogeneity of $\sigma_w(\mathbf{x}')$ within the pore space, then the total electric field $\mathbf{E}(\mathbf{x}')$ within the sample can be decomposed into three parts: the part of the electric field resulting from the pore space structure given by $\Phi(\mathbf{x}')$, the part of the electric field resulting from the structure of $\sigma_w(\mathbf{x}')$ and the part of the electric field resulting from the interactions between the electric fields arising due to either structure. At present, there is no upscaling framework under such general conditions that enables to predict σ_{eq} . However, research efforts have been made in this direction (e.g. *Singha et al.*, 2007; *Day-Lewis and Singha*, 2008; *Day-Lewis et al.*, 2017). For instance, *Day-Lewis et al.* (2017) produces a model to compute σ_{eq} for samples that exhibit dual porosity and each domain is saturated with fluids of different conductivity σ_{w1} and σ_{w2} (i.e., $\sigma_w(\mathbf{x}')$ exhibits a binary distribution). In their approach, they assign a different formation factor F_1 and F_2 to each domain, they calculate an upscaled value of conductivity for each of them as $\sigma_{eq1} = \sigma_{w1}/F_1$ and $\sigma_{eq2} = \sigma_{w2}/F_2$ and subsequently they input these two average conductivities into the DEM mixing procedure. By applying Archie's law to relate F_1 and F_2 to the average porosity of each domain, the resulting model allows to compute σ_{eq} from knowledge of F_1 , F_2 and the volume fractions of each

conductive phase (see *Day-Lewis et al. (2017)* for details). Note that underlying this model is the assumption of scale separation (e.g., *Adrian et al., 2000; Wood, 2009*). Namely, the scale at which the formation factors are defined is much smaller than the scale at which $\sigma_w(\mathbf{x}')$ fluctuates. This assumption allows neglecting interactions between the electric fields arising due to the structures present in $\Phi(\mathbf{x}')$ and $\sigma_w(\mathbf{x}')$.

In most real settings $\sigma_w(\mathbf{x}')$ is not binary but fluctuates continuously. There is currently no general petrophysical transformation that accounts for the electrical signatures of such variations on σ_{eq} . Suitable candidates for dealing with this problem might be the perturbative upscaling approaches, mentioned before. In Chapter 4 we present an interpretation framework based on extending Archie's law to consider continuous heterogeneity in $\sigma_w(\mathbf{x}')$.

1.3 Translation of σ_{eq} into mean salinity

Typically, the objective of DC-monitored saline tracer tests is to use σ_{eq} , observed at the scale of \mathbf{y} , to constrain the temporal evolution of the mean saline concentration at the same scale. In this context, the heterogeneous pore water electrical conductivity field $\sigma_w(\mathbf{x}')$ originates from the heterogeneous salinity field $c(\mathbf{x}')$, whereby the former and the latter are related by a monotonically increasing relationship (e.g., *Sen and Goode, 1992*).

As was mentioned in Sec. 1.1, the lack of a general petrophysical transformation linking $\sigma_w(\mathbf{x}')$ with σ_{eq} remains a major obstacle to exploit time-lapse DC data quantitatively and in a reliable manner. In order to illustrate this issue, we describe now the two main types of workflows used to exploit DC data in hydrogeological studies (Fig. 1.3). Note that a more exhaustive categorization can be found in *Singha et al. (2015)*, however, the presented categorization serves well to our purposes.

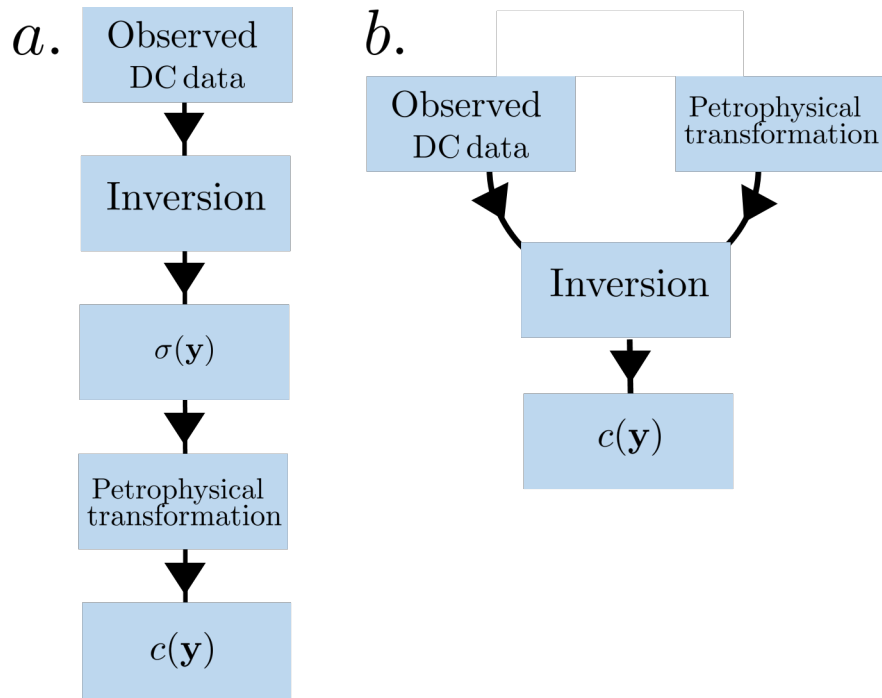


Figure 1.3 – a. Uncoupled hydrogeophysical inversion. b. Coupled hydrogeophysical inversion. The petrophysical transformation takes place (a) after inversion of $\sigma(\mathbf{y})$ and (b) during data forward modelling, respectively.

In the first approach (Fig. 1.3a), called 'uncoupled inversion' (Hinnell *et al.*, 2010) or direct mapping (Linde *et al.*, 2006), the snapshots of bulk electrical conductivity (electrical images), obtained after inversion, are transformed into snapshots of $c(\mathbf{y})$ by means of a petrophysical relationship, the latter applied at the DC modelling discretization scale. The inferred $c(\mathbf{y})$ is either directly used as a final result or to further constrain a hydrological inversion. Due to its simplicity, this is the most commonly applied approach during hydrogeophysical studies (e.g., Singha and Gorelick, 2005; Cassiani *et al.*, 2006; Müller *et al.*, 2010; Doetsch *et al.*, 2012a). In the second approach (Fig. 1.3b), known as coupled hydrogeophysical inversion (Yeh and Šimunek, 2002; Hinnell *et al.*, 2010), apart from the DC data, the full hydrogeological system (i.e., flow and transport) is modelled, and an inversion procedure is applied to obtain snapshots of $c(\mathbf{y})$ directly while inferring the underlying parameters of the hydrogeological system. During this procedure, the petrophysical transformation used to translate $\sigma(\mathbf{y})$ into $c(\mathbf{y})$ occurs during the forward simulation of the data. Since flow and transport forward modelling is necessarily involved, this second approach entails a much higher computational burden, however, it carries a significant advantage. Namely, there is no underlying assumption that the resolution of the electrical images equates the DC model discretization scale, as is often implicitly assumed when transforming electrical images in the uncoupled or direct mapping approaches. Another major advantage is that, the coupled approach ensures mass conservation of the tracer or contaminant being imaged. ERT experiments are typically underdetermined, meaning that the number of pixels in the electrical images to be inverted cannot be constrained uniquely from the collected DC measurements. Consequently, there is almost invariably a need of introducing correlations

between the pixels of the electrical images to stabilize the inversion process (e.g., *Constable et al.*, 1987; *LaBrecque et al.*, 1996), which then result in spatially-varying weighted averages over a much larger volume (e.g., *Friedel*, 2003) than the DC modelling grid elements. Direct naïve conversion of electrical images should be avoided whenever possible (e.g., *Singha et al.*, 2015; *Nussbaumer et al.*, 2019).

Regardless of whether uncoupled or coupled hydrogeophysical inversion approaches are applied, a petrophysical relationship is invariably introduced at some observation scale \mathbf{y} that is either related to the resolution of electrical images (uncoupled) or the DC modelling discretization scale (coupled). This relationship is typically given by Eqs. 1.20 and 1.22 (Archie's relationships), as has been mentioned previously. In order to use Archie's relationships in a meaningful way, that is, allowing to extract an accurate value of mean salinity μ_c by observing σ_{eq} and assuming knowledge of F , it is necessary that $\sigma_w(\mathbf{x}')$ is homogeneous (i.e., the solute is completely mixed) below the scale of \mathbf{y} . In such a special case, $\sigma_w(\mathbf{x}')$ trivially behaves as an additive property and then the observable apparent fluid conductivity σ_f^{app} (obtained as $\sigma_{eq}F$) equates μ_σ . This establishes a bridge between σ_f^{app} and the definition of μ_c , via a simple transformation of μ_σ (e.g., *Sen and Goode* (1992)). However, as $\sigma_w(\mathbf{x}')$ departs from homogeneity (or a layered field), σ_f^{app} becomes in general smaller than μ_σ and then μ_c is no longer directly accessible through σ_f^{app} .

1.4 Milli-fluidic technologies to assess the impact of sub-scale heterogeneity on DC conductivity

During electrically-monitored saline tracer tests within soil-, rock- and sand-columns (e.g., *Koestel et al.*, 2008; *Jougnot et al.*, 2010; *Swanson et al.*, 2012; *Briggs et al.*, 2013; *Swanson et al.*, 2015; *Maineult et al.*, 2016) there are typically two types of collected data: averaged DC electrical conductivity, obtained by placing electrodes on the surface of the sample, and flux-averaged fluid conductivity (or solute concentration) obtained at the outlet of the sample. Depending on the number of DC measurements, time-lapse ERT images (e.g. *Koestel et al.*, 2008) or equivalent conductivity measurements (e.g., *Swanson et al.*, 2015; *Maineult et al.*, 2016) can be considered for interpretation. The latter alternative allows to assess directly the relationship between the temporal evolution of the average DC conductivity and the flux-averaged solute transport behaviour, without having to deal with artefacts from the electrical images. However, given the impact that sub-resolution saline heterogeneity has on averaged DC electrical conductivity, it becomes important to consider experimental settings that give direct access to the conductivity field below the resolution scale of the DC measurements. Along this line, optically-monitored tracer experiments using quasi 2-D micro- or milli-fluidic Hele-Shaw cells allow to monitor the depth-averaged solute concentration field at very high resolutions (e.g., *Kozlov et al.*, 2012; *de Anna et al.*, 2014; *Jiménez-Martínez et al.*, 2015, 2017). Consequently, the possibility of combining optically-monitored milli-fluidic settings with geoelectrical monitoring capabilities becomes very appealing. Note that these types of combined experimental settings require tracers that

create both electrical and optical signals. For this, typically table salt (electrical component) and fluorescein sodium salt (optical component) are dissolved in denatured water.

In Fig. 1.4a we represent a schematic outline of the typical workflow followed during electrically- and optically-monitored tracer tests. After installation and calibration, the electrical monitoring system (a resistivity meter) outputs time-series of apparent electrical conductivity $\sigma_{\text{app}}^{\text{out}_1}$. The optical monitoring system provides time-series of light intensity images $I(\mathbf{x}')$. These data are then transformed into corresponding time-series of depth-averaged 2-D solute concentration fields $c(\mathbf{x}')$, that are in turn converted into time-series of fluid electrical conductivity $\sigma(\mathbf{x}')$. The latter are then used as input to Eq. 1.13 to calculate $\sigma_{\text{app}}^{\text{out}_2}$.

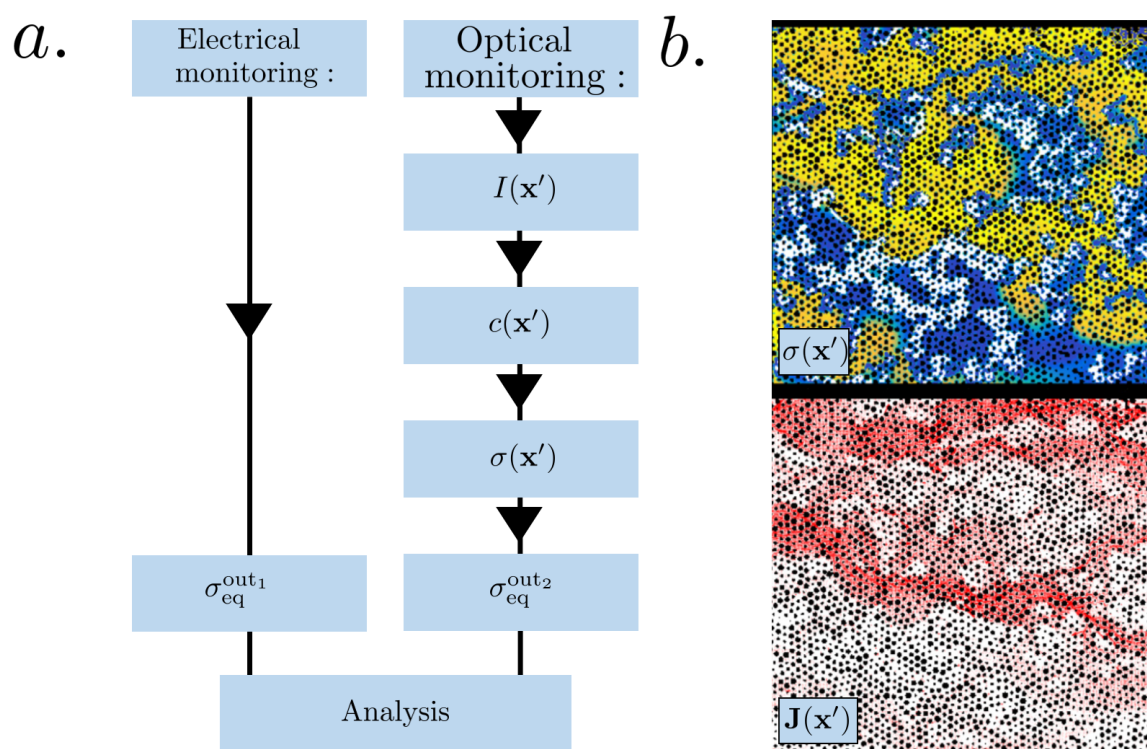


Figure 1.4 – (a) Summary of typical workflow for electrically- and optically-monitored milli-fluidic tracer tests. The left-sided sequence represents the electrical monitoring workflow and $\sigma_{\text{app}}^{\text{out}_1}$ the observed average electrical conductivity. The right-sided sequence represents the optical monitoring workflow, with $I(\mathbf{x}')$, $c(\mathbf{x}')$, $\sigma(\mathbf{x}')$ and $\sigma_{\text{app}}^{\text{out}_2}$ denoting, respectively, the observed light intensity, inferred concentration and fluid conductivity fields at the pore scale, and calculated average electrical conductivity. (b) (top) Image-inferred $\sigma(\mathbf{x}')$ and (bottom) modulus of the associated (calculated) current density field $\mathbf{J}(\mathbf{x}')$, respectively. Adapted from *Jougnot et al. (2018)*.

Fig. 1.4b highlights the impact of the connectivity of the conductivity field $\sigma(\mathbf{x}')$ on the current distribution $\mathbf{J}(\mathbf{x}')$. For instance, note that $\sigma(\mathbf{x}')$ presents large conductivity values on a considerable area of the upper part of the domain. However, $\mathbf{J}(\mathbf{x}')$ has a large amplitude predominantly along two channels that run approximately parallel to the horizontal direction

and are located in the top and middle part of the cell. The region of large $\sigma(\mathbf{x}')$ between the channels is essentially neglected by the current because it is not well connected in the direction of the imposed potential gradient.

It is worth pointing out three aspects of such milli-fluidic experiments. First, the relationship between fluorescein concentration and light intensity is not monotonically increasing. In fact, there exists a threshold concentration value, which depends on the cell thickness, after which the emitted light decreases with fluorescein concentration (e.g., *Imamura and Koizumi*, 1955; *de Anna et al.*, 2014). Consequently, the fluorescein concentration for the tracer must be chosen such that the optical signal is strong enough while remaining at the monotonically-increasing part of the relationship. Second, special care is needed to process the images $I(\mathbf{x}')$, in order to avoid that spurious patterns of light intensity (e.g., some background light) remain and impact the inferred $c(\mathbf{x}')$. Third, since the relationship between light intensity and solute concentration depends on the cell thickness, calibration must account for this. The non-linearity of electrical conductivity averaging makes $\sigma_{\text{app}}^{\text{out}_2}$ very susceptible to errors in the image processing and the $I(\mathbf{x}')-c(\mathbf{x}')$ relationship calibration. These aspects are discussed in *Jougnot et al.* (2018) and *Visentini et al.* (2021). In Chapter 3 we present a study consisting of such an experiment in saturated conditions, where we use a milli-fluidic cell that has a layered distribution of permeability.

1.5 Thesis objectives

The main objective of this thesis is to advance our understanding of how the state and evolution of the spreading and mixing of solutes in saturated porous media impacts equivalent DC electrical conductivity and associated time-series. With this understanding, the ultimate goal is to establish a framework that allows to infer quantitative information on spreading and mixing processes from geoelectrical data.

The overarching research question may be formulated as follows: What statistical information on aquifer and state variables below the scale of equivalent DC electrical conductivity estimates or measurements can be extracted when monitoring the transport of tracers and contaminants? A non exhaustive list of specific questions is:

- What is the value of using static equivalent DC electrical conductivity measurements or estimates?
 - i. To what extent can the equivalent electrical conductivity tensor constrain low- and high-order statistics as well as topological (i.e., connectivity) measures of the conductivity field below the averaging volume? If the field is non-ergodic, how is the uncertainty in those measures propagated to the measured equivalent electrical conductivity ?
 - ii. Since the mixing and spreading state of solutes are one- and two-point statistical measures of the electrical conductivity field (i.e., concentration field variance and spatial variance of the concentration field) then, under which connectivity and regularity conditions of the field is the DC conductivity sensitive to those statistical measures?

- What is the added value of using equivalent time-lapse DC equivalent electrical conductivity compared to static data?
 - iii. To what extent can the time-series of equivalent DC electrical conductivity tensor constrain the first and second-order statistics and topological (i.e., connectivity) measures of underlying hydraulic conductivity fields dictating the transport of the solutes? If the hydraulic conductivity field is non-ergodic, how strong is the dependence of the time-series on the specific realization of the hydraulic conductivity field?
 - iv. Is it possible to exploit time-lapse DC data to gain knowledge on the initial state and temporal evolution of the tracer spreading and its degree of mixing?
- v. How can electrically-monitored milli-fluidic setups be used to gain insight on the electrical signature of small-scale solute mixing processes?

1.6 Thesis outline

We present work that has been published in peer-reviewed journals (Chapters 2 and 3) or will soon be submitted (Chapter 4).

In Chapter 2, we investigate to what extent the time-series of the DC equivalent electrical conductivity tensor and the solute mass breakthrough, observed during a saline tracer test, can constrain the geostatistical parameters of 2-D hydraulic conductivity fields. For doing this, we combine a Bayesian inference framework and the Kullback-Leibler divergence measure, the latter allowing us to make a quantitative assessment of the information content of the data. We select three test cases of hydraulic heterogeneity and compare the performance of the different data types in terms of the test cases and also in terms of the geostatistical parameters. This chapter addresses question iii.

Chapter 3 presents results from a novel experimental setup, combining optical- and electrical-monitoring of a milli-fluidic tracer tests performed using a quasi 2-D artificial porous medium. By measuring electrical conductivity in two perpendicular directions, we investigate electrical signatures associated with the mixing dynamics of a saline tracer initially segregated into layers. We also discuss technical challenges associated with the processing and modelling of the optically-inferred electrical conductivity time-series. This work addresses questions ii, iv and v.

In Chapter 4, we expand Archie's relationships by introducing a new petrophysical parameter, the mixing factor, which accounts for the impact of small-scale heterogeneity of electrical conductivity fields on the equivalent response. Working in 2-D, we investigate to what extent observing the mixing factor in two perpendicular directions permit to constrain the variance and anisotropy of saline conductivity fields. We also derive an analytical expression for the mixing factor that enables us to formulate the problem of electrical conductivity upscaling in terms of the mapping between the statistical properties of heterogeneous conductivity fields and the electric field. As an additional contribution, we derive expressions for the formation factor, cementation exponent and tortuosity in terms of the secondary electric field. This work addresses questions i, ii and iv.

Chapter 5 concludes the thesis and the main findings are summarized. An outlook for future research is also presented.

Chapter 2

Inferring geostatistical properties of hydraulic conductivity fields from saline tracer tests and equivalent electrical conductivity time-series

Alejandro Fernandez Visentini, Niklas Linde, Tanguy Le Borgne and Marco Dentz.

Published¹ in *Advances in Water Resources* and herein slightly adapted to fit the theme of this thesis.

¹Fernandez Visentini, A., Linde, N., Le Borgne, T. and Dentz M. (2020). Inferring geostatistical properties of hydraulic conductivity fields from saline tracer tests and equivalent electrical conductivity time-series. *Advances in Water Resources*, **146**,103758, <https://doi.org/10.1016/j.advwatres.2020.103758>

Abstract

We use Approximate Bayesian Computation and the Kullback-Leibler divergence measure to quantify to what extent horizontal and vertical equivalent electrical conductivity time-series observed during tracer tests constrain the 2-D geostatistical parameters of multivariate Gaussian log-hydraulic conductivity fields. Considering a perfect and known relationship between salinity and electrical conductivity at the point scale, we find that the horizontal equivalent electrical conductivity time-series best constrain the geostatistical properties. The variance, controlling the spreading rate of the solute, is the best constrained geostatistical parameter, followed by the integral scales in the vertical direction. We find that horizontally layered models with moderate to high variance have the best resolved parameters. Since the salinity field at the averaging scale (e.g., the model resolution in tomograms) is typically non-ergodic, our results serve as a starting point for quantifying uncertainty due to small-scale heterogeneity in laboratory-experiments, tomographic results and hydrogeophysical inversions involving DC data.

2.1 Introduction

Time-lapse electrical geophysical methods are popular in hydrogeology (e.g., *Binley et al.*, 2015; *Singha et al.*, 2015)) as they provide non-intrusive means for remote and dense spatio-temporal sampling related to flow and transport processes. Among these, the direct-current (DC) method is cost-effective, easy to employ and probably the most commonly used (*Binley et al.*, 2015). It has been thoroughly assessed through numerical investigations (e.g., *Vanderborgh et al.*, 2005; *Singha and Gorelick*, 2005; *Fowler and Moysey*, 2011), laboratory and controlled tank experiments (e.g., *Slater et al.*, 2000; *Koestel et al.*, 2008; *Jougnot et al.*, 2018), and field investigations (e.g., *Daily et al.*, 1992; *Binley et al.*, 2002; *Singha and Gorelick*, 2005).

DC measurements are generally based on two pairs of electrodes: one pair for establishing a known electrical current between two points, and the other for measuring the resultant electrical voltage between two other points (e.g., *Keller and Frischknecht*, 1966). In the context of time-lapse DC tomographic experiments, the measurement process is repeated using multiple current and voltage electrode pairs at different positions, and the measurement protocol is repeated over time. Such a measurement process is often referred to as time-lapse Electrical Resistivity Tomography (ERT), and it outputs time-series of electrical resistances (voltage over injected current) that in saturated media carry information about the time-evolution of the salinity distribution (e.g., *Lesmes and Friedman*, 2005). The time-lapse ERT method has been applied during conservative saline tracer tests to extract both flow and transport information. Retrieval of hydraulic conductivity from such data is discussed, for example, in *Kemna et al.* (2002) and *Vanderborgh et al.* (2005) and the range of applications span from the calibration of mean hydraulic conductivity values (*Binley et al.*, 2002) to retrieval of the full distribution of hydraulic conductivity (*Pollock and Cirpka*, 2012). Extraction of solute transport parameters has been studied in detail and *Kemna et al.* (2002), for instance, provided a field demonstration of retrieving equivalent 1-D stream-tube advective-dispersive transport parameters in the context of 3-D conservative saline transport, results later corrob-

orated numerically by *Vanderborght et al.* (2005). Also *Koestel et al.* (2008) inferred the 3-D distribution of solute velocities and dispersivities in a soil column using time-lapse ERT data.

Over time, the use of geoelectrical-monitored tracer tests has evolved from qualitative analyses such as saline plume motion detection and geometry delineation (e.g., *Slater et al.*, 2000) to obtain quantitative and spatially-resolved hydrological constraints. Nevertheless, using time-lapse DC data for quantitative hydrogeological purposes remains a persistent challenge (*Singha et al.*, 2015). This challenge is intimately related to the use of time-lapse inversion methodologies that provide resolution-limited time-evolving images of electrical resistivity or conductivity through time (*Singha et al.*, 2015). The most common approach to translate resulting geophysical time-lapse tomograms into salinity distributions rests on two strong assumptions. The first is that there exists a petrophysical relationship, (e.g., *Archie*, 1942), with known spatially-invariant parameters defined at the discretization scale of the tomogram, implying that it corresponds to the Representative Elementary Volume (REV) scale (*Hill*, 1963) of bulk electrical conductivity and, consequently, that the impact of salinity heterogeneity is negligible below this scale. The second assumption is that the resolution of the geophysical tomogram is the same as the model discretization, which is hardly true for any electrical survey. In reality, the tomogram represents spatially-varying weighted averages over a much larger volume (e.g., *Friedel*, 2003). With these two assumptions, temporal differences in time-lapse tomograms can readily be translated into estimates of salinity differences. Unfortunately, this approach typically leads to an underestimation of actual tracer mass with errors often approaching one order of magnitude (e.g., *Binley et al.*, 2002; *Singha and Gorelick*, 2005; *Laloy et al.*, 2012). Research has addressed the second assumption by upscaling the petrophysical relationship to the tomographic resolution using either linearized inverse theory *Day-Lewis et al.* (2005); *Nussbaumer et al.* (2019) or Monte Carlo-based simulation approaches (e.g., *Moysey et al.*, 2005b).

In this work, we are primarily concerned with the first assumption, namely that the impact of salinity variations is negligible below a given scale. To avoid complications inherent to tomographic imaging, we focus here on the case of a time-evolving equivalent electrical conductivity tensor of a 2-D square sample of unit length that is invaded by a saline (i.e., electrically conductive) tracer. In a tomographic setting, this scale can be thought of as the model resolution at a given location of interest. For this case, the equivalent electrical conductivity in a given direction is readily obtained, basically by dividing the electric current with the imposed voltage. The total current is the macroscopic flux of the internal current density field (i.e., the distribution of small-scale currents within the sample) that, for a given internal distribution of local conductivities, is established such that its associated energy loss due to Joule's dissipation, integrated over the domain, is minimized (e.g., *Feynman et al.*, 2011; *Bernabé and Revil*, 1995). This governing principle leads to patterns of current channelling and deflection through and from high and low electrical conductivity zones, respectively, and it governs the time variations of the current density field as the saline tracer invades the sample (e.g., *Li and Oldenburg*, 1991). Accurate prediction of the time-evolution of the equivalent electrical conductivity of the medium, thus, requires accounting for interactions occurring throughout the domain and, given an arbitrarily-shaped time-evolving electrical conductivity field, this remains an open upscaling problem belonging to the family of conductivity upscaling in spatially non-stationary fields (e.g., *Sanchez-Vila et al.*, 2006) and references therein).

The current lack of physically accurate upscaling procedures impedes reliable quantitative analyses of a saline plume's fate from geoelectrical monitoring. For instance, in the most common case where Archie's petrophysical law (Archie, 1942) is used to infer the mean saline concentration within the sample from its equivalent electrical conductivity, the underlying assumption is that the internal electrical conductivity field behaves as an additive property that can be upscaled by taking its arithmetic average. This is only true if the electrical conductivity field is constant or if its distribution is layered and the equivalent electrical conductivity is measured parallel to this layering, corresponding to the upper Wiener bound (e.g., Milton and Sawicki, 2003). In general, since portions of the concentration field are by-passed by the established current patterns, the upper Wiener bound does not apply and this leads to the above-mentioned apparent mass loss as demonstrated, for example, in a recent laboratory study (Jougnot et al., 2018). These issues also impact the performance of many fully-coupled hydrogeophysical inversion approaches and modeling studies that interpret equivalent electrical conductivity time-series using equivalent transport parameters within an advective-dispersive description (e.g., Kemna et al., 2002; Vanderborght et al., 2005; Koestel et al., 2008). On a more positive note, the discussion above also suggests that electrical conductivity time-series at a given scale carry statistical information on the concentration field and its temporal evolution.

Here we investigate to what extent tracer tests associated with time-series of equivalent electrical properties a pre-defined scale can be used to infer geostatistical properties of hydraulic conductivity fields below this scale. This is achieved by considering inference within a Bayesian inference framework (e.g., Gelman et al., 2013; Tarantola, (2005), more specifically through an Approximate Bayesian Computational approach (e.g., Beaumont et al., 2002; Sisson et al., 2018). For comparison purposes, the mass breakthrough curve is also evaluated and its information content is compared to its electrical peers. Using a Bayesian approach allows assessing the information gained on the properties of interest with respect to their assumed prior statistics. We perform our study using a database consisting of 10^5 synthetically-generated equivalent electrical conductivity tensor and mass breakthrough time-series collected during saline tracer tests within a 2-D domain with hydraulic heterogeneity prescribed by multivariate Gaussian fields. We consider advectively-dominated solute transport (i.e., high Péclet numbers), where the concentration field evolution is predominantly determined by the underlying flow field, which in turn depends on the underlying hydraulic conductivity field under the constant applied pressure gradient. In this study, we consider idealized scenarios as it is assumed that there is no spatial variations in petrophysical properties and that the petrophysical relationship is known.

In Section 2 we review the basic governing equations describing groundwater flow, solute transport and electrical conduction together with their numerical implementations. In Section 3 we introduce the inference problem of interest along with the Bayesian inference tools. The main results are presented and discussed in Sections 4 and 5, respectively. Section 6 concludes the paper.

2.2 Governing equations and problem setup

2.2.1 Groundwater flow

For steady-state flow and in the absence of sources or sinks, mass conservation of an incompressible fluid is expressed by the continuity equation for the specific discharge $\mathbf{q}(\mathbf{x})$:

$$\nabla \cdot \mathbf{q}(\mathbf{x}) = 0, \quad (2.1)$$

where $\mathbf{x} = (x, y)^T$ denotes the 2-D position vector and x and y the horizontal and vertical coordinates, respectively. Darcy's law relates $\mathbf{q}(\mathbf{x})$ with the hydraulic conductivity field $K(\mathbf{x})$ and the hydraulic head $h(\mathbf{x})$ via

$$\mathbf{q}(\mathbf{x}) = -K(\mathbf{x})\nabla h(\mathbf{x}). \quad (2.2)$$

Adopting Darcy's law, the groundwater flow equation reads:

$$\nabla K(\mathbf{x})\nabla h(\mathbf{x}) + K(\mathbf{x})\nabla^2 h(\mathbf{x}) = 0. \quad (2.3)$$

It is customary to treat the log-hydraulic conductivity field $Y(\mathbf{x}) (\equiv \ln(K(\mathbf{x})))$ within a geostatistical framework with $Y(\mathbf{x})$ modelled as a second-order spatially-stationary ergodic random function. In this study, we consider multivariate-Gaussian random fields with an exponential covariance structure (e.g., *Rubin*, 2003) with a mean μ_Y and a variance σ_Y^2 . The integral scales of the field are expressed by the integral scale I_y in the vertical direction and an anisotropy factor $\lambda (= I_x/I_y)$. After specifying $K(\mathbf{x})$, the flow field $\mathbf{q}(\mathbf{x})$ is obtained by solving Eq. 4.13 with prescribed boundary conditions (subsection 2.4.2).

2.2.2 Solute transport

The evolution of the concentration field $c(\mathbf{x}, t)$ of a passive tracer being transported within the steady-state flow-field $\mathbf{q}(\mathbf{x})$ can be described within an Eulerian framework using the advection-dispersion equation

$$\theta \frac{\partial c(\mathbf{x}, t)}{\partial t} + \nabla \cdot [(\mathbf{q}(\mathbf{x})c(\mathbf{x}, t) - \theta \mathbf{D} \nabla c(\mathbf{x}, t))] = 0, \quad (2.4)$$

where θ is the porosity and \mathbf{D} is the dispersion tensor. In this study we assume a spatially-constant porosity and dispersion tensor, and furthermore we assume zero dispersivity. In this case and considering Eq. 2.1, Eq. 2.4 simplifies to the advection-diffusion equation with constant coefficients:

$$\theta \frac{\partial c}{\partial t} + \mathbf{q}(\mathbf{x}) \cdot \nabla c - \theta D_m \nabla^2 c = 0, \quad (2.5)$$

where D_m denotes the molecular diffusion coefficient. After solving for $c(\mathbf{x}, t)$, the flux-weighted tracer mass-breakthrough time-series $M(t)$ are defined by

$$M(t) = \frac{\int_{\Gamma_{out}} q_x(\mathbf{x}) c(\mathbf{x}, t) d\mathbf{x}}{\int_{\Gamma_{out}} q_x(\mathbf{x}) d\mathbf{x}}, \quad (2.6)$$

with $q_x(\mathbf{x})$ being the flow-component in the x -direction and Γ_{out} the outflow boundary of the model domain.

2.2.3 DC conduction

Electric charge conservation is in the DC problem expressed by the continuity equation of the current density field $\mathbf{J}(\mathbf{x}, t)$ at time-lapse acquisition time t . In the absence of current sources and net accumulation of electric charge, it takes the following form:

$$\nabla \cdot \mathbf{J}(\mathbf{x}, t) = 0. \quad (2.7)$$

Ohm's law relates $\mathbf{J}(\mathbf{x}, t)$ with the electrical conductivity $\sigma(\mathbf{x}, t)$ and the electric field $\mathbf{E}(\mathbf{x}, t)$ via the linear relationship $\mathbf{J}(\mathbf{x}, t) = \sigma(\mathbf{x}, t)\mathbf{E}(\mathbf{x}, t)$. Adopting the quasistatic approximation, $\nabla \times \mathbf{E}(\mathbf{x}, t) = 0$, allows to express $\mathbf{E}(\mathbf{x}, t) = -\nabla\phi(\mathbf{x}, t)$, where $\phi(\mathbf{x}, t)$ is the electrical potential. Writing $\mathbf{J}(\mathbf{x}, t)$ in terms of $\phi(\mathbf{x}, t)$ as $\mathbf{J}(\mathbf{x}, t) = -\sigma(\mathbf{x}, t)\nabla\phi(\mathbf{x}, t)$ and replacing this expression into Eq. 2.7 results in the governing Laplace equation for the electrical potentials:

$$\nabla\sigma(\mathbf{x}, t)\nabla\phi(\mathbf{x}, t) + \sigma(\mathbf{x}, t)\nabla^2\phi(\mathbf{x}, t) = 0. \quad (2.8)$$

We consider the horizontal and vertical components of the equivalent electrical conductivity tensor time-series of a 2-D square sample of unit length. This implies solving Eq. 2.8 with alternative mixed Dirichlet-Neumann boundary conditions or "excitation modes". For $\sigma^H(t)$ ($\sigma^V(t)$), a constant electrical potential difference $\Delta\phi_H$ ($\Delta\phi_V$) along the horizontal (vertical) direction is imposed, with zero electrical potential gradient along the top and bottom (left and right) boundaries. The resulting electrical potential fields are, respectively, $\phi^H(\mathbf{x}, t)$ and $\phi^V(\mathbf{x}, t)$. The corresponding equivalent electrical conductivity time-series are computed as

$$\sigma^H(t) = \frac{1}{\Delta\phi_H} \int_{\Gamma_y} -\sigma(\mathbf{x}, t)\nabla_x\phi^H(\mathbf{x}, t) d\mathbf{x}, \quad (2.9)$$

and

$$\sigma^V(t) = \frac{1}{\Delta\phi_V} \int_{\Gamma_x} -\sigma(\mathbf{x}, t)\nabla_y\phi^V(\mathbf{x}, t) d\mathbf{x}, \quad (2.10)$$

where the integration paths Γ_y and Γ_x are any two given contours separating the left and right boundaries and the top and bottom boundaries, respectively, and the integrands in each equation is the horizontal or vertical component of the current density field resulting from each excitation mode.

2.2.4 Numerical implementations and problem setup

We create a database of 10^5 time-series of $\sigma^H(t)$, $\sigma^V(t)$ and $M(t)$ that are collected during tracer tests simulated within multivariate Gaussian log-hydraulic conductivity realizations in a square-shaped domain of side length $L = 1$ m discretized into 250×250 elements.

Generation of hydraulic conductivity fields

The log-hydraulic conductivity field realizations $Y(\mathbf{x})$ are generated using the fast circulant embedding technique (see *Dietrich and Newsam (1997)* for details). A given realization depends on the specified geostatistical model parameters and \mathbf{R} ; a 250×250 a random draw from a standard normal distribution. The geostatistical model parameters determine the spatial regularity (smoothness class), while \mathbf{R} determines the locations of high and low log-hydraulic conductivity values relative to the mean value μ_Y of the geostatistical model. Here μ_Y is fixed at -6 while remaining parameters are treated as random variables $\mathbf{m} = (\sigma_Y^2, I_y, \lambda)$ described by a joint probability density function (PDF) $\pi(\mathbf{m})$. The variance σ_Y^2 is randomly drawn from a uniform PDF with support $[0, 5.5]$, the integral scale I_y is drawn from a log-uniform PDF with support $[L/25, L/2]$ m, and the anisotropy factor $\lambda (= I_x/I_y)$ is drawn from a uniform PDF with support $[1, L/I_y]$ (i.e., conditionally on I_y). The discretization implies that heterogeneities obtained with the smallest integral scales are resolved with at least 10 cells in each direction. The log-uniform distribution of I_y is here chosen to favor realizations with finely structured fields. The generated sample of the geostatistical model parameters of size $P = 10^5$ is represented in Figure 2.1. Note that each draw is associated with a unique \mathbf{R} , which together form a log-hydraulic conductivity field realization.

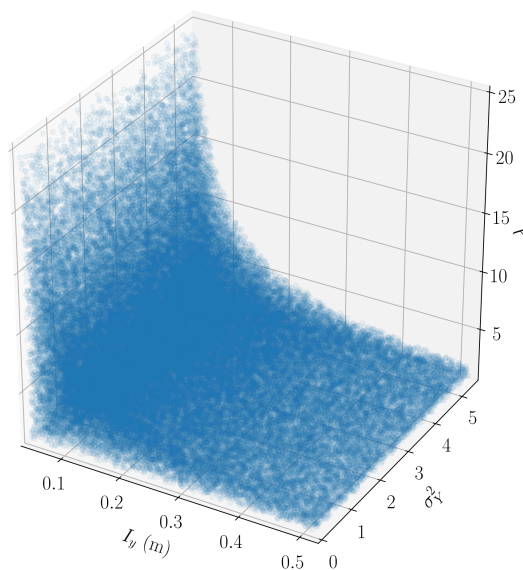


Figure 2.1 – Generated sample of size $P = 10^5$ of geostatistical parameters $\mathbf{m} = (\sigma_Y^2, I_y, \lambda)$ drawn from a joint pdf $\pi(\mathbf{m})$. Each realization is used together with an associated \mathbf{R} -realization to create a log-hydraulic conductivity field on which flow and transport simulations are performed.

Flow simulations

The groundwater flow equation (Eq. 4.13) is solved numerically using the open-source finite-difference solver MODFLOW-2005 (Harbaugh, 2005). The prescribed boundary conditions are a horizontal head gradient of 0.05 inducing flow from left to right and no-flow conditions for the top and bottom boundaries. The head gradient value was chosen such that for a homogeneous field equal to $\exp(\mu_Y)$ the tracer arrival time occurs approximately at half of the simulated time-duration of the tracer experiment. In the simulations, the hydraulic conductivity between two adjacent cells is taken as their harmonic mean. The chosen numerical scheme used to solve the system of linear equations is the preconditioned conjugate gradient method (Hill, 1990).

Transport simulations

The advection-diffusion equation (Eq. 2.5) is solved using the groundwater solute transport simulator package MT3D-USGS (Bedekar et al., 2016). The initial condition is a homogeneous concentration field of 0.01 g l^{-1} and the boundary conditions are: (i) constant concentration of 1 g l^{-1} along the left boundary (ii) no-flux along the top and bottom boundaries and (iii) free-flux along the right boundary. The porosity is assumed constant and equal to 0.3. For the advection term in Eq. 2.5, the third-order Total Variation Diminishing (TVD) approach (Cox and Nishikawa, 1991) is used. The TVD solver was found to be very robust and showed minimal numerical dispersion when benchmarked against planar fronts. Nevertheless, in order to mask the small numerical dispersion, the diffusion coefficient was slightly increased from $D_m = 1.6 \times 10^{-9} \text{ m}^2 \text{ s}^{-1}$ (the standard value for the diffusion coefficient of salt in water) to $D_m = 2 \times 10^{-8} \text{ m}^2 \text{ s}^{-1}$. The latter (larger) value is obtained by fitting the analytical solution for a concentration profile for a step injection in 1-D (e.g., Ogata and Banks, 1961) to a TVD-calculated concentration profile obtained for a homogeneous hydraulic conductivity field equal to μ_Y when the diffusion coefficient is imposed to be the one of salt in water. Each simulated tracer experiment lasts for $4 \times 10^3 \text{ s}$ and during this time period, 400 equidistant samples $c_i(\mathbf{x})$ ($i = 1, \dots, 400$) of the simulated concentration fields are recorded at times $t = (i - 1)\Delta t$, with $\Delta t = 4 \times 10^3 \text{ s} / 400 = 10 \text{ s}$. The injected tracer typically does not fully replace the initial background tracer at the end of the simulation period. This is a consequence of the short simulation time imposed by computational constraints and large low-velocity regions. The mean Péclet number is $\sim 6 \times 10^3$, defined as $Pe = \frac{\bar{u}}{D_m}$, where \bar{u} is the tracer velocity for the constant hydraulic conductivity field.

Electrical simulations

For each sampled concentration field $c_i(\mathbf{x})$, the 2-D square domain is alternatively excited by imposing an electrical potential difference of 1 V with a pair of line electrodes along either the vertical or horizontal boundaries of the sample. The remaining boundaries are prescribed zero electrical potential gradient normal to the boundaries. The resulting electrical potential fields $\phi_i^H(\mathbf{x})$ and $\phi_i^V(\mathbf{x})$ associated to the horizontal and vertical modes, respectively, are computed by numerically solving the Laplace equation (Eq. 2.8) with the finite-element solver module of the Python library pyGIMLi (Rücker et al., 2017). For simplicity, the input electrical conductivity distribution $\sigma_i(\mathbf{x})$, used for solving the boundary-value problems at each time step is assumed to be perfectly and linearly related to the transport simulation

output $c_i(\mathbf{x})$. The resulting normalized dimensionless time-series denoted as σ^H, σ^V and M vary within $[0.01, 1]$. The data generation is summarized by the pseudo-code in Algorithm 1.

Algorithm 1: Data generation procedure

```

for  $j = 1$  to  $10^5$  do
    Draw geostatistical model realization  $\mathbf{m} = (\sigma_Y^2, I_y, \lambda)$  and  $\mathbf{R}$ 

    Generate hydraulic conductivity field  $K(\mathbf{x})$ 

    Simulate steady-state Eulerian flow field  $\mathbf{q}(\mathbf{x})$ 

    for  $i = 1$  to 400 do
        Specify sampling time  $t$  as  $t = (i - 1)\Delta t$ 
        Simulate concentration field  $c_i(\mathbf{x})$ 
        Compute  $M_i, \sigma_i^H$  and  $\sigma_i^V$ 
    end

    Save  $K(\mathbf{x})$ 

    Save concentration field time-series  $\mathbf{C} = [c_1(\mathbf{x}), \dots, c_{400}(\mathbf{x})]$ 

    Save time-series of mass breakthrough  $M = [M_1, \dots, M_{400}]$  and
    electrical conductivity  $\sigma^H = [\sigma_1^H, \dots, \sigma_{400}^H]$  and  $\sigma^V = [\sigma_1^V, \dots, \sigma_{400}^V]$ 
end

```

2.3 Inference problem

We are interested in assessing to what extent the time-series σ^H, σ^V and M may constrain the geostatistical parameters $\mathbf{m} = (\sigma_Y^2, I_y, \lambda)$. We consider the following five combinations of time-series:

$$\begin{aligned}
 \mathbf{d}_H &:= \{\sigma^H\}, \\
 \mathbf{d}_V &:= \{\sigma^V\}, \\
 \mathbf{d}_M &:= \{M\}, \\
 \mathbf{d}_{HV} &:= \{\sigma^H, \sigma^V\}, \\
 \mathbf{d}_{HVM} &:= \{\sigma^H, \sigma^V, M\}.
 \end{aligned}$$

The data vectors $\mathbf{d}_H, \mathbf{d}_V$ and \mathbf{d}_M are used to assess the individual performance of each type of time-series; \mathbf{d}_{HV} is used to evaluate the performance of electrical data alone and \mathbf{d}_{HVM} is

used to evaluate the value of using all the data at the same time. We cast the problem as a Bayesian inference framework as outlined below.

2.3.1 Bayesian inference framework

In a finite-dimensional Bayesian inference framework, a model is described in terms of M random variables with realizations $\mathbf{m} = (m_1, \dots, m_M)$ that can be used as input to a physical forward simulator producing N simulated data $\mathbf{d}^{sim} = \mathcal{F}(\mathbf{m})$ (e.g., *Gelman et al., 2013; Tarantola, (2005)*). The prior probability density function $\pi(\mathbf{m})$ is updated using Bayes' theorem to a posterior probability density function $\pi(\mathbf{m}|\mathbf{d}^{obs})$ after considering the observed data $\mathbf{d}^{obs} = (d_1, \dots, d_N)$ using a likelihood function $\pi(\mathbf{d}^{obs}|\mathbf{m})$. This function evaluates the likelihood of any model realization given and the residual error vector $\mathbf{e} = \mathbf{d}^{obs} - \mathbf{d}^{sim}$ and an assumed underlying observational noise model (e.g., *Tarantola, (2005)*). Bayes' theorem in its unnormalized form reads:

$$\pi(\mathbf{m}|\mathbf{d}^{obs}) \propto \pi(\mathbf{d}^{obs}|\mathbf{m})\pi(\mathbf{m}). \quad (2.11)$$

In our context, the prior is given by the PDF described in subsection 2.4.1 and \mathbf{d}^{obs} is the noise-contaminated output of the forward simulator, $\mathcal{F}(\mathbf{m}_t)$, when evaluated using one of the test cases \mathbf{m}_t described in subsection 2.4.2. For the electrical time-series, $\mathcal{F}(\mathbf{m})$ is formed by the sequential application of the following forward mappings: (i) the realization of the hydraulic conductivity field $K(\mathbf{x})$, (ii) solving the groundwater flow equation (Eq. 4.13), (iii) the advection-diffusion equation (Eq. 2.5), (iv) the Laplace equation (Eq. 2.8) and (v) evaluating the equations defining σ^H (Eq. 2.9) and σ^V (Eq. 2.10).

2.3.2 Posterior density approximation

In Bayesian inference, Monte Carlo (MC) sampling can be used to approximate $\pi(\mathbf{m}|\mathbf{d}^{obs})$ by a MC integration over a finite sample of the sought distribution (e.g., *Mosegaard and Tarantola, 1995; Gelman et al., 2013*). The simplest approach is Acceptance-Rejection Sampling (ARS), which consists of drawing samples \mathbf{m} proportionally to the prior density and accepting them as samples of the posterior density proportionally to their likelihood $\pi(\mathbf{d}^{obs}|\mathbf{m})$. This is an exact sampling method (e.g., *Mosegaard and Tarantola, 1995*) and it can be used off-line using a large ensemble of prior model realizations given that, unlike in a Markov Chain MC (MCMC) sampling method, there is no dependence between the model proposals. Its main disadvantage is that, since the parameter search is unguided (unlike MCMC), the probability of acceptance decreases exponentially with the dimensionality M of the model parameter space. As more dimensions are added to the problem, the ratio of the (hyper)volume of high likelihood values (regions of large acceptance probability), to the total volume of the model space, decreases exponentially to zero (e.g., *Scales, 1996; Curtis and Lomax, 2001*). This so-called curse of dimensionality may result in unrealistically-large prior model samples,

even when addressing only a handful of parameters. In the context of this study, we are interested in only three geostatistical parameters (Subsection 2.1) possibly suggesting that ARS could be a good choice.

However, when the scale of the modelling domain is insufficiently large compared to the integral scales of the field $Y(\mathbf{x})$ under consideration, ergodic conditions are not fulfilled implying a potentially high dependence on \mathbf{R} (Subsection 2.4.1). This high-dimensional variable is different for each realization of $Y(\mathbf{x})$ and it ultimately controls the locations of high- and low hydraulic conductivity regions. Even if we are uninterested in \mathbf{R} as such, it forms part of our data generation process and, thus, it enters the inference problem as a nuisance variable (e.g., *Gelman et al., 2013*) that needs to be accounted for. Consequently, our definition of the forward simulator given above has to be expanded to $\mathcal{F}(\mathbf{m}, \mathbf{R})$. Assuming independence of \mathbf{m} and \mathbf{R} , the actual inference problem to solve reads

$$\pi(\mathbf{m}, \mathbf{R} | \mathbf{d}^{obs}) \propto \pi(\mathbf{d}^{obs} | \mathbf{m}, \mathbf{R}) \pi(\mathbf{m}) \pi(\mathbf{R}). \quad (2.12)$$

To obtain the sought density, we need to marginalize $\pi(\mathbf{m}, \mathbf{R} | \mathbf{d})$ with respect to \mathbf{R} :

$$\pi(\mathbf{m} | \mathbf{d}) = \int \pi(\mathbf{m}, \mathbf{R} | \mathbf{d}) d\mathbf{R}. \quad (2.13)$$

Due to its higher dimensionality (more than 62,500 variables in our examples), the problem expressed by Eq. 2.12 is practically impossible to handle with the formal Bayesian ARS algorithm. For this reason, we resort to an approximate version of the ARS that is outlined in the following subsection.

ABC Acceptance-Rejection Sampling algorithm

The ARS algorithm implemented within an Approximate Bayesian Computational (ABC) framework, labelled Approximate Acceptance-Rejection Sampling (AARS) algorithm from now on, is an approximate sampling method that produces a smooth approximation of $\pi(\mathbf{m} | \mathbf{d})$. The reader is referred to *Sisson et al. (2018)* for an overview on ABC methods. The AARS algorithm requires two additional inputs: (i) a distance metric $\rho(\mathbf{d}^{sim}, \mathbf{d}^{obs})$ for comparing the calculated data with the observed data and (ii) a kernel density function $\mathbf{K}_h(\rho)$ for weighting the distance metric and defining an acceptance probability. Together, they replace the likelihood function.

In our work, the distance metric $\rho(\mathbf{d}^{sim}, \mathbf{d}^{obs})$ is taken as the L_1 -norm:

$$\rho(\mathbf{d}^{sim}, \mathbf{d}^{obs}) = \frac{1}{N} \sum_1^N |\mathbf{d}^{sim} - \mathbf{d}^{obs}| \quad (2.14)$$

and the Kernel density is chosen to be a uniform function:

$$\mathbf{K}_h(\rho) = \begin{cases} 1 & 0 \leq \rho/h \leq 1 \\ 0 & 1 < \rho/h, \end{cases} \quad (2.15)$$

where the acceptance bandwidth h is chosen such that the 0.5th percentile of the distribution of ρ ordered from the lowest to the highest distance are accepted. In our case, this means that $\mathbf{K}_h(\rho)$ accepts the models producing the $S = 500$ lowest distances out of the $K = 10^5$ sampled prior samples.

The AARS algorithm, described in pseudo-code in Algorithm 2, proceeds similarly to the formal ARS algorithm.

Algorithm 2: Approximate Acceptance-Rejection Sampling (AARS) algorithm.

for $k = 1, \dots, P$ **do**

Draw $\mathbf{m}_{(k)}$ from $\pi(\mathbf{m})$ and $\mathbf{R}_{(k)}$ from $\pi(\mathbf{R})$

Generate a data instance $\mathbf{d} = \mathbf{d}^{sim}$ from the underlying unobserved likelihood $\pi(\mathbf{d}^{obs} | \mathbf{d}, \mathbf{m}_{(k)}, \mathbf{R}_{(k)})$

Accept $\mathbf{m}_{(k)}$ with an acceptance probability $AP = \mathbf{K}_h(\rho)$

end

Considering Algorithm 2, it can be noticed that the AARS algorithm draws samples from the joint distribution

$$\pi^{AARS}(\mathbf{m}, \mathbf{R}, \mathbf{d} | \mathbf{d}^{obs}) = \mathbf{K}_h(\rho) \pi(\mathbf{d}^{obs} | \mathbf{d}, \mathbf{m}, \mathbf{R}) \pi(\mathbf{m}) \pi(\mathbf{R}), \quad (2.16)$$

which, when integrated over all generated data instances gives the AARS approximation of the (\mathbf{R} -marginalized) posterior density:

$$\pi^{AARS}(\mathbf{m} | \mathbf{d}^{obs}) = \int \pi^{AARS}(\mathbf{m}, \mathbf{R}, \mathbf{d} | \mathbf{d}^{obs}) d\mathbf{d}; \quad (2.17)$$

or,

$$\pi^{AARS}(\mathbf{m}|\mathbf{d}^{obs}) = \pi(\mathbf{m}) \int \mathbf{K}_h(\rho)\pi(\mathbf{d}^{obs}|\mathbf{d}, \mathbf{m}, \mathbf{R})d\mathbf{d}. \quad (2.18)$$

As pointed out by (Sisson *et al.*, 2018), from Eq. 2.18 the AARS can be interpreted as a formal Bayesian ARS algorithm using an approximated likelihood function that is a Kernel Density Estimation (KDE) of the true likelihood:

$$\pi^{AARS}(\mathbf{d}^{obs}|\mathbf{m}, \mathbf{R}) = \int \mathbf{K}_h(\rho)\pi(\mathbf{d}^{obs}|\mathbf{d}, \mathbf{m}, \mathbf{R})d\mathbf{d}. \quad (2.19)$$

For building the empirical posterior probability densities, we perform KDE over the samples obtained from $\pi^{AARS}(\mathbf{m}|\mathbf{d}^{obs})$. For consistency, the prior PDF (Subsection 2.4.1) is computed by performing KDE over the generated sample of size $P = 10^5$. The KDE approach is described in the following subsection.

Multivariate Kernel Density Estimation (KDE)

Given a sample $\mathbf{X} = \{\mathbf{x}_1, \dots, \mathbf{x}_S\}$ of size S of M -variate random vectors belonging to a common distribution described by the density g , the KDE estimator \hat{g} of g is given by (e.g., *Wand and Jones*, 1994))

$$\hat{g}_{\mathbf{H}}(\mathbf{x}) = \frac{1}{S} \sum_{i=1}^S \mathbf{K}_{\mathbf{H}}(\mathbf{x} - \mathbf{x}_i), \quad (2.20)$$

with the estimator function $\mathbf{K}_{\mathbf{H}}$ defined as:

$$\mathbf{K}_{\mathbf{H}}(\mathbf{x}) = |\mathbf{H}|^{-\frac{1}{2}} K(\mathbf{H}^{-\frac{1}{2}}\mathbf{x}), \quad (2.21)$$

where the kernel function K is a symmetric multivariate density. Furthermore, $|\mathbf{H}|$ is the determinant of the $M \times M$ bandwidth matrix \mathbf{H} , which is symmetric and positive definite in general and, if the M variables are assumed independent, it is diagonal with entries \mathbf{H}_i given as $\sqrt{\mathbf{H}_i} = h\sigma_i$, where h is the bandwidth parameter and σ_i the standard deviation of the i -th component of the random variable.

The estimator of Eq. 2.20 is an average of kernel densities that are centered at the sample points and whose decay is controlled by \mathbf{H} . The particular choice of K does not substantially

influence the performance of the KDE approach, but the choice of the bandwidth h , defining \mathbf{H} (i.e., the tails of K), is a most crucial aspect, given that under- or over-smoothed estimators will be produced if it is taken too small or large, respectively (e.g., *Wand and Jones*, 1994)). In the present work, K is chosen as the standard multivariate normal function

$$\mathbf{K}_{\mathbf{H}}(\mathbf{x}) = (2\pi)^{-\frac{N}{2}} |\mathbf{H}|^{-\frac{1}{2}} \exp\left\{-\frac{1}{2}\mathbf{x}^T \mathbf{H}^{-1} \mathbf{x}\right\}. \quad (2.22)$$

For h , a common choice when dealing with unimodal distributions, as the ones expected in this study, is based on Silverman's rule of thumb (e.g., *Silverman*, 1986):

$$h_s = \frac{4}{M+2} \frac{1}{M+4} d^{-\frac{1}{M+4}}. \quad (2.23)$$

The reliability of the used information measure (Subsection 2.3.3) largely depends on the quality of the input density estimations provided by the KDE approach (e.g., *Budka et al.*, 2011)). Considering the trade-offs pertaining to the choice of h , a manual tuning process was necessary, which resulted in the choice of $h = 0.75h_s$ for the results presented herein.

2.3.3 Information measure: Kullback-Leibler divergence

The degree of knowledge brought by the observed data \mathbf{d}^{obs} pertaining to the geostatistical model parameters is evaluated by comparing our approximation of $\pi(\mathbf{m}|\mathbf{d}^{obs})$ with $\pi(\mathbf{m})$. The Kullback-Leibler divergence (KLD) (*Kullback and Leibler*, 1951), also termed Relative Information Content (*Tarantola*, (2005), is probably the most widely used quantitative measure for comparing PDFs:

$$KLD(\pi(\mathbf{m}|\mathbf{d}^{obs}); \pi(\mathbf{m})) = \int \pi(\mathbf{m}|\mathbf{d}^{obs}) \ln\left(\frac{\pi(\mathbf{m}|\mathbf{d}^{obs})}{\pi(\mathbf{m})}\right) d\mathbf{m}, \quad (2.24)$$

where the base of the logarithm is taken as e , giving the information in units of nats (e.g., *Cover and Thomas*, 2012)). The integration of Eq. 2.10 is performed over the support of the densities and the KLD is finite as the support of $\pi(\mathbf{m}|\mathbf{d}^{obs})$ is contained in the support of $\pi(\mathbf{m})$ (e.g., *Cover and Thomas*, 2012)). The KLD is zero when $\pi(\mathbf{m}|\mathbf{d}^{obs}) \equiv \pi(\mathbf{m})$ (i.e., the data carry no information about the model parameters) and it increases as the posterior becomes more compact with respect to the prior as a consequence of conditioning to the data. Note that when the prior and posterior densities are Gaussian with the same mean, but the standard deviation of the posterior is half the standard deviation of the prior, then the KLD is 0.27 nats.

Since our samples are drawn from approximate posterior densities $\pi^{AARS}(\mathbf{m}|\mathbf{d}^{obs})$ that are KDE (i.e., smoothed) versions of the target densities $\pi(\mathbf{m}|\mathbf{d}^{obs})$ (Eq. 2.18), the chosen AARS approach provides a conservative framework for assessing the information content in terms of the KLD measure, since it is always true that

$$KLD(\pi^{AARS}(\mathbf{m}|\mathbf{d}^{obs});\pi(\mathbf{m})) < KLD(\pi(\mathbf{m}|\mathbf{d}^{obs});\pi(\mathbf{m})), \quad (2.25)$$

which implies that the information content in the considered time-series is at least as large as the estimates obtained by our analysis.

2.4 Results

We first show two examples of generated data for end-member cases of weak and strong hydraulic heterogeneity. Then, we describe the results obtained for different geostatistical parameter value combinations in terms of the KLD and bias measures. In doing so, we discuss results obtained for one \mathbf{R} -realization, as well as ensemble statistics deduced from 50 \mathbf{R} -realizations.

2.4.1 Two examples of generated data

Figure 2.2 shows an example of data obtained for a weakly heterogeneous hydraulic conductivity field with $(\sigma_Y^2, I_y, \lambda) = (0.005, 0.130 \text{ m}, 3.179)$ (Fig. 2.2a), resulting in an approximately constant flow field (Fig. 2.2b). The corresponding concentration field, shown at the sampling time 10^3 s , when the tracer occupies approximately 50% of the model domain, displays an overall planar front (Fig. 2.2c).

The time-series of σ^H and σ^V (Fig. 2.2d) evolve according to the lower and upper Wiener bounds. These upscaling formulas for laminated materials (e.g., *Milton and Sawicki, 2003*) correspond to the harmonic and arithmetic means of the local electrical conductivities, respectively. The arithmetic averaging governing σ^V is manifested by linear scaling with time. In this case, σ^V forms an almost perfect predictor of the mean salinity (μ_c) within the sample. σ^H , on the contrary, strongly underestimates μ_c . For this case, the mean velocity of the tracer front is obtained from the time-derivative of σ^V (Fig. 2.2e), information that is available before the mass-flux (M) time-series shows any response.

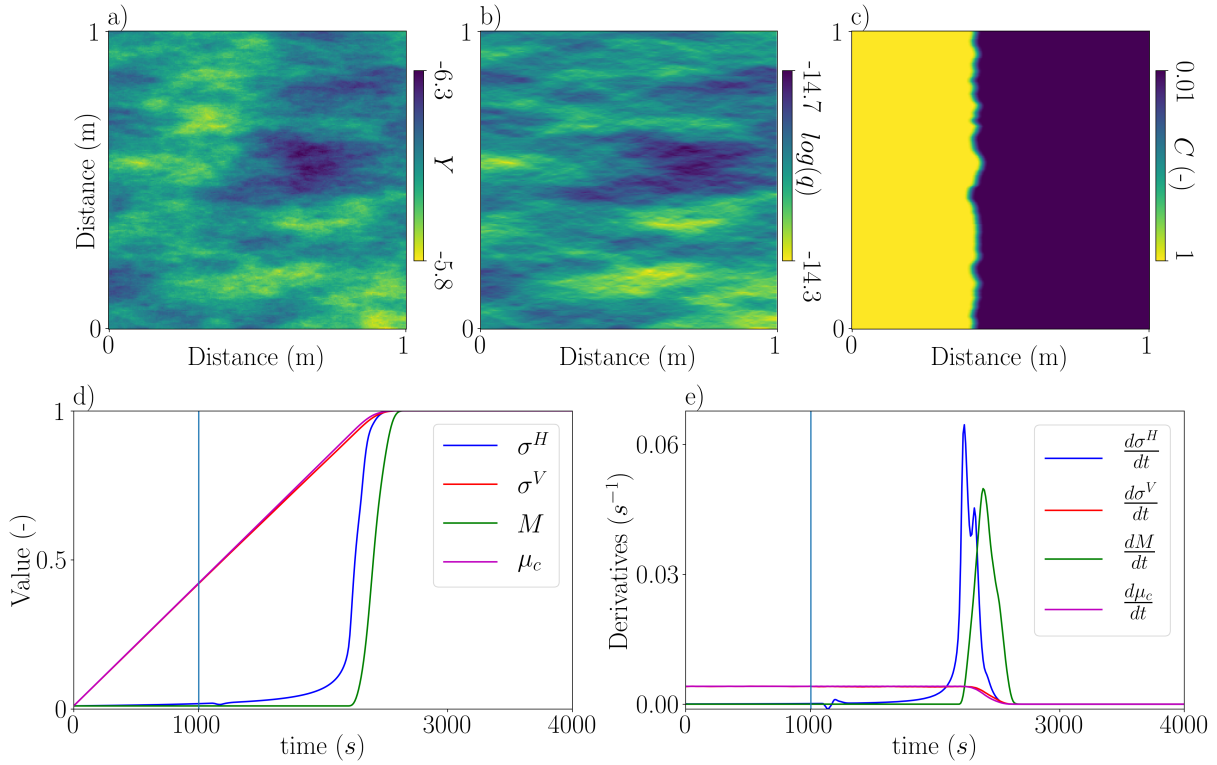


Figure 2.2 – (a) Weakly heterogeneous hydraulic conductivity field with geostatistical parameters $(\sigma_Y^2, I_Y, \lambda) = (0.005, 0.130 \text{ m}, 3.179)$. (b) Corresponding steady-state flow field and (c) normalized concentration field at time 10^3 s . (d) Time-series of the horizontal and vertical equivalent electrical conductivity, mass-flux, and mean tracer concentration, denoted σ^H , σ^V , M and μ_c , respectively. The light-blue vertical line, also present in (e), marks the time 10^3 s of the concentration field shown in (c). (e) Time-derivatives of σ^H , σ^V , M and μ_c .

These easily interpretable results are now contrasted with those obtained for a strongly heterogeneous hydraulic conductivity field, defined with $(\sigma_Y^2, I_Y, \lambda) = (5.111, 0.085 \text{ m}, 1.028)$. The resulting field has small-scale structures and is close to isotropic (Fig. 2.3a). Yet its associated flow field exhibits pronounced channeling (Fig. 2.3b) resulting in a highly heterogeneous concentration field (Fig. 2.3c). Neither σ^H nor σ^V follow any known upscaling law. They both start to vary much earlier than M (Fig. 2.2d), which only reacts when the tracer arrives at the outlet. These early variations are clearly seen in the time-derivatives of the electrical responses (Fig. 2.2e), which are non-zero from the moment the tracer injection starts and exhibit small peaks that are related to internal connection events of the solute that are invisible to M . Both σ^H and M show a steep increase around 10^3 s , and a large peak in their time-derivatives, corresponding to early breakthrough arrival. For this case, μ_c is at early times much larger than all data and is asymptotically approximated by M , followed in order of magnitude by σ^H and σ^V .

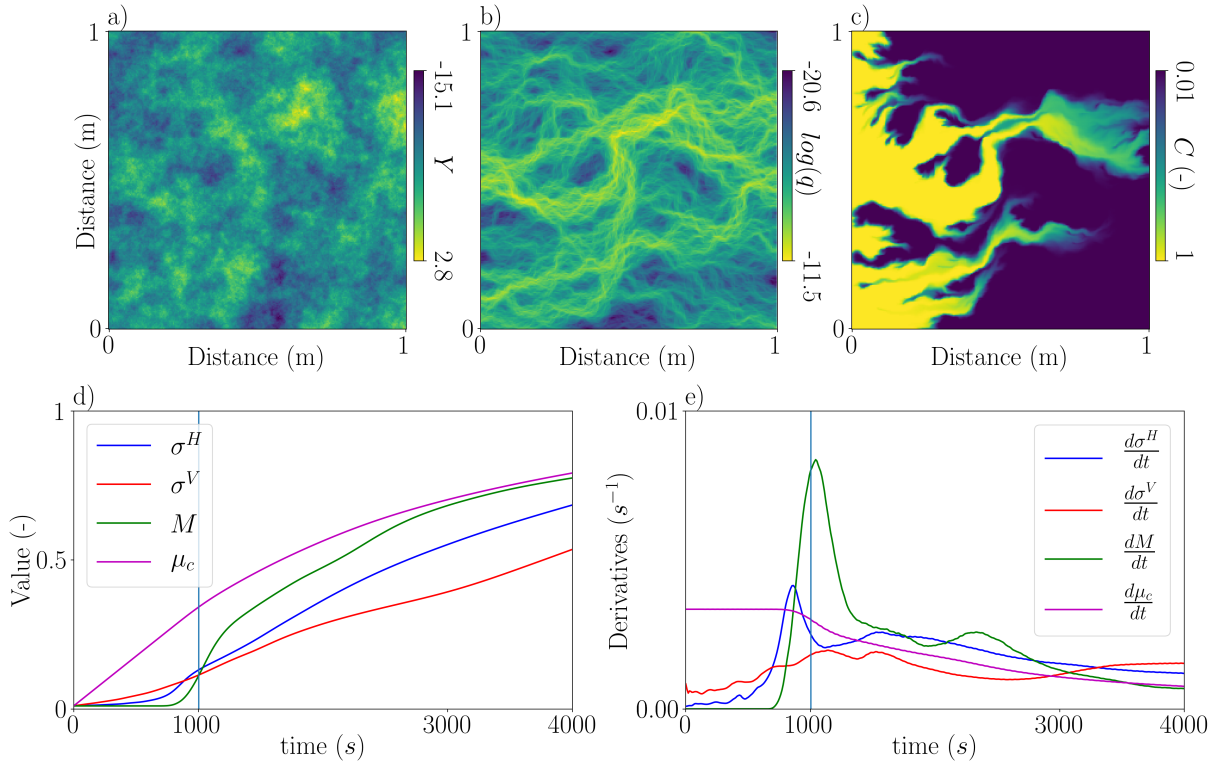


Figure 2.3 – (a) Strongly heterogeneous hydraulic conductivity field, defined with geostatistical parameters $(\sigma_Y^2, I_Y, \lambda) = (5.111, 0.085 \text{ m}, 1.028)$. (b) Corresponding steady-state flow field and (c) normalized concentration field at time 10^3 s. (d) Time-series of the horizontal and vertical equivalent electrical conductivity, mass-flux, and mean tracer concentration, denoted σ^H , σ^V , M and μ_c , respectively. The light-blue vertical line, also present in (e), marks the time 10^3 s, of the concentration field in (c). (e) Time-derivatives of σ^H , σ^V , M and μ_c . The large peaks exhibited by $\frac{d\sigma^H}{dt}$ and $\frac{dM}{dt}$ approximately coincide with the first arrival of the tracer at the outlet.

2.4.2 Test cases

We now apply the Bayesian inference approach using three different combinations of the geostatistical model parameter values:

(i) $\mathbf{m}_1 := (4.70, 0.06 \text{ m}, 1.50)$. This leads to a strongly heterogeneous hydraulic conductivity field that is approximately isotropic and exhibits small structures (Fig. 2.4a).

(ii) $\mathbf{m}_2 := (0.80, 0.06 \text{ m}, 10.00)$. This leads to a mildly-to-moderately heterogeneous field that exhibits a high degree of layering (Fig. 2.4d).

(iii) $\mathbf{m}_3 := (4.70, 0.38 \text{ m}, 1.50)$. This leads to a highly heterogeneous field exhibiting large-scale structures (Fig. 2.4g).

In Figure 2.4, example realizations of generated log-hydraulic conductivity fields for the three test cases are shown together with their corresponding flow and concentration fields.

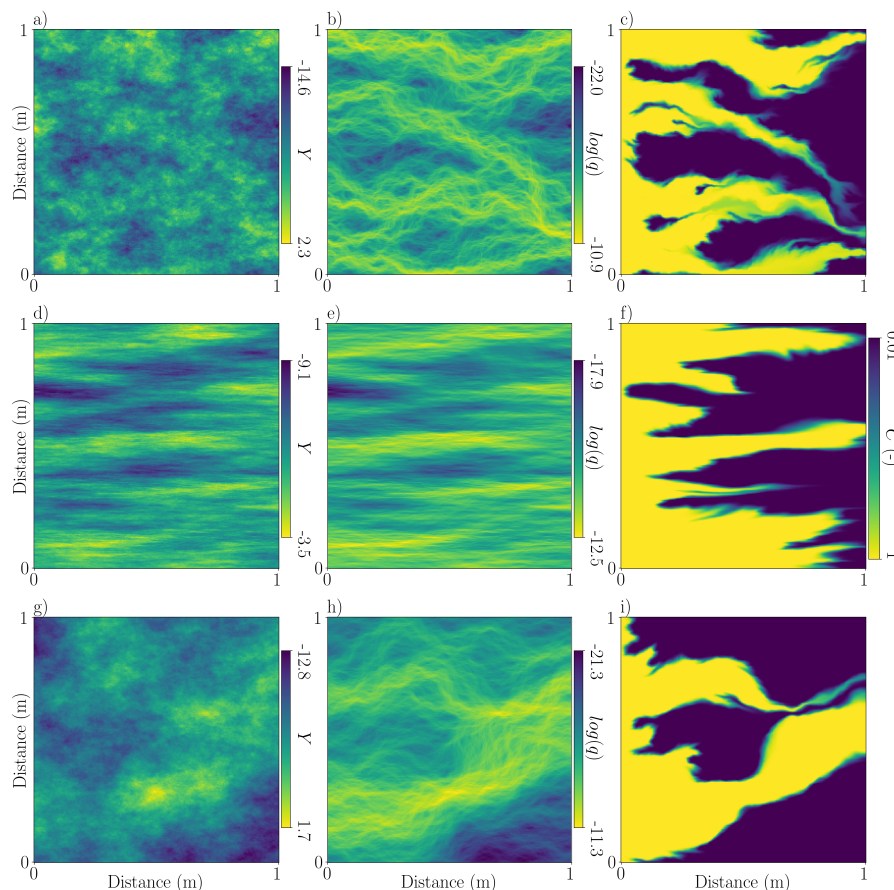


Figure 2.4 – (a, d, f) Realizations of log-hydraulic conductivity fields and (b, e, h) associated flow and (c, f, i) concentration fields at time 10^3 s for the three evaluated test cases (a-c) \mathbf{m}_1 , (d-f) \mathbf{m}_2 and (g-i) \mathbf{m}_3 . Note that the locations of high- and low hydraulic conductivity regions are governed by random \mathbf{R} -realizations

2.4.3 Information assessment of data types

For each test case of the model vector \mathbf{m} , 50 datasets \mathbf{d}_j^{obs} (Section 2.3) are simulated using hydraulic conductivity fields created with different \mathbf{R} -realizations. The forward responses are contaminated with noise having zero mean and a mean deviation of 0.005 representing 50% of the baseline electrical conductivity. The evaluation of the different data types and geostatistical parameter values is considered both in terms of the ensemble of realizations (ensemble performance) and in terms of randomly-picked single realizations (i.e., the fields shown in Fig. 2.4). In addition to the estimated joint posterior PDE, we also consider the

corresponding marginal distributions to evaluate the ability of the data to constrain individual geostatistical parameters. For the marginal analysis, we also consider a relative bias measure, computed as the ratio of the mean bias of the marginal posteriors, with respect to the true values of \mathbf{m} , to the mean bias of the marginal priors with respect to the true values. From now on, we drop the superscript "obs" when referring to the observed conditioning data.

Test case \mathbf{m}_1

Table 2.1 summarizes the results obtained for test case \mathbf{m}_1 .

Table 2.1 – KLDs and mean relative biases of \mathbf{m}_1 for the different conditioning data types. Columns 1 and 2 show the mean μ_{KLD} and standard deviation σ_{KLD} of the KLDs using the ensemble of hydraulic conductivity realizations. Column 3 shows the KLD values for the joint posterior PDFs using one realization of the conditioning data obtained from Figures 2.4a-c and highlighted in Figures 2.5a-c. The subsequent pairs of columns show the marginal KLD values and relative mean biases for the marginal posteriors of each component of \mathbf{m}_1 using this specific realization.

	Ensemble		\mathbf{m}			σ_Y^2		$I_Y(m)$		λ	
	μ_{KLD}	σ_{KLD}	KLD	KLD	Bias	KLD	Bias	KLD	Bias		
\mathbf{d}_H	0.8171	0.1445	0.7351	0.3754	0.5018	0.1418	0.7560	0.0904	0.8525		
\mathbf{d}_V	0.8016	0.1131	0.6418	0.2617	0.6703	0.1021	0.6760	0.0675	1.2163		
\mathbf{d}_M	0.6625	0.1580	0.6973	0.2153	0.8223	0.1771	0.5325	0.0980	1.1271		
\mathbf{d}_{HV}	0.8830	0.1352	0.6937	0.2501	0.6716	0.1536	0.7058	0.0899	0.7971		
\mathbf{d}_{HVM}	0.8712	0.1318	0.6985	0.2386	0.7232	0.1537	0.7189	0.1050	0.7672		

When considering the joint KLDs obtained for the ensemble of realizations, we find that \mathbf{d}_{HV} has the largest mean KLD, closely followed by \mathbf{d}_{HVM} . The least informative data type \mathbf{d}_M has a mean KLD that is $\sim 75\%$ of the one for \mathbf{d}_{HV} , while \mathbf{d}_H and \mathbf{d}_V have values in-between. The KLD standard deviations have similar values among all the data types and represent $\sim 20\%$ of the mean values.

We now turn to the results obtained for the fields in Figures 2.4a-c and the corresponding time-series highlighted in Figures 2.5a-c. For this specific realization, the KLDs span a small range of only $\sim 13\%$. Also, the ordering is different and the most and least informative data sets for this case are \mathbf{d}_H and \mathbf{d}_V , respectively. This illustrates (together with the standard deviations of the KLDs discussed above) the stochastic variations that are inherent under non-ergodic conditions. The variability in the generated data due to variations in the \mathbf{R} -realizations, for a given geostatistical model, is indicated by the insets in Figures 2.5a-c.

The posterior model samples obtained by the AARS algorithm and used for building the empirical posterior PDFs for each type of data are shown in Figure 2.5. The density distribution of these 3-D clouds of points convey a qualitative view of the ability of the different data types to constrain the geostatistical parameters. No eye-catching differences distinguish the different point clouds, reflecting the rather similar values of the associated KLDs.

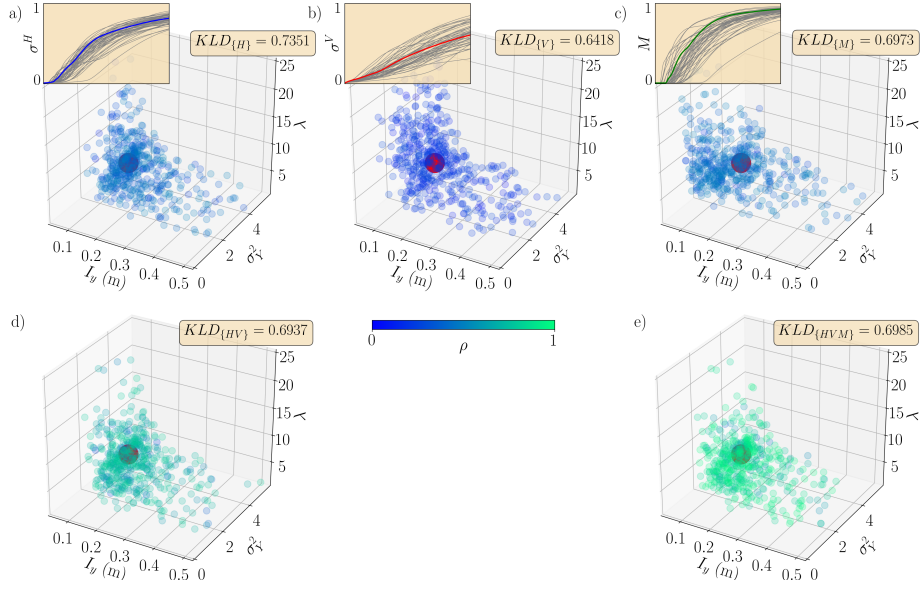


Figure 2.5 – Posterior model parameter vector samples of size $S = 500$ obtained by the AARS algorithm for test case $\mathbf{m}_1 = (4.7, 0.06m, 1.5)$ using different datasets as conditioning data. The colored clouds of points represent the samples for datasets (a) \mathbf{d}_H ; (b) \mathbf{d}_V ; (c) \mathbf{d}_M ; (d) \mathbf{d}_{HV} ; (e) \mathbf{d}_{VM} ; (f) \mathbf{d}_{HVM} . The colormap encodes the L_1 distance ρ between simulated and observed data, normalized by the minimum and maximum values of ρ of the test case. The inset plots of (a), (b) and (c) show, respectively, the 50 realizations of time-series σ^H , σ^V and M generated for \mathbf{m}_1 using different \mathbf{R} -realizations. The data considered here for inference are shown by thick-colored curves. The resulting KLD values are given for each dataset.

The KLDs computed for the marginal posterior PDFs, labelled marginal KLDs from now on, are the largest for σ_Y^2 , followed by I_y and λ , that on average, represent $\sim 50\%$ and $\sim 25\%$ of the KLDs of σ_Y^2 , respectively. We find that σ_Y^2 is best constrained by \mathbf{d}_H , producing the largest marginal KLD and the smallest bias. For this parameter, the poorest performance is achieved by \mathbf{d}_M that has both the smallest marginal KLD and the largest bias. This can be seen in the estimated marginal posterior probability density (Fig. 2.6a) displaying a mass distribution which is the furthest away from the true value $\sigma_Y^2 = 4.70$. For I_y , on the contrary, \mathbf{d}_M features the highest marginal KLD and the smallest bias (Fig. 2.6b). The ability of the data to constrain λ is low (Fig. 2.6c) with \mathbf{d}_{HVM} featuring the highest marginal KLD. The relative mean biases are negatively correlated with the associated KLD measure, showing consistency between the two measures.

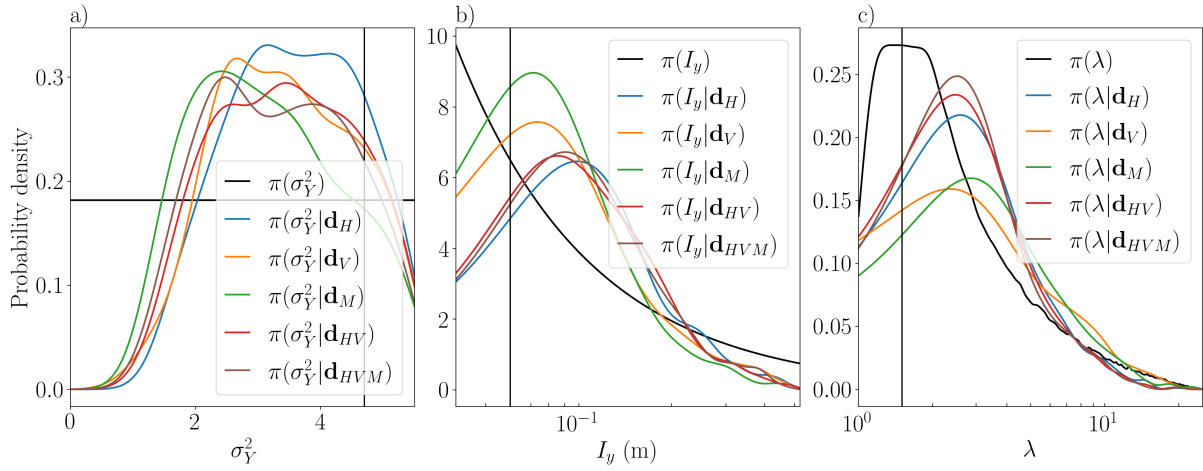


Figure 2.6 – Marginal posterior PDFs associated to each type of conditioning data \mathbf{d}_H , \mathbf{d}_V , \mathbf{d}_M , \mathbf{d}_{HV} , \mathbf{d}_{VM} and \mathbf{d}_{HVM} for test case $\mathbf{m}_1 = (4.7, 0.06 \text{ m}, 1.5)$. Marginal prior and posterior PDFs corresponding to (a) σ_Y^2 (b) I_y and (c) λ .

Test case \mathbf{m}_2

Table 2.2 summarizes the results obtained for test case \mathbf{m}_2 .

Table 2.2 – KLDs and mean relative biases of \mathbf{m}_ϵ for the different conditioning data types. Columns 1 and 2 show the mean μ_{KLD} and standard deviation σ_{KLD} of the KLDs using the ensemble of hydraulic conductivity realizations. Column 3 shows the KLD values for the joint posterior PDFs using one realization of the conditioning data obtained from Figures 2.4d-f and highlighted in Figures 2.7a-c. The subsequent pairs of columns show the marginal KLD values and relative mean biases for the marginal posteriors of each component of \mathbf{m}_2 using this specific realization.

	Ensemble		\mathbf{m}			σ_Y^2		$I_y(\text{m})$		λ	
	μ_{KLD}	σ_{KLD}	KLD	KLD	Bias	KLD	Bias	KLD	Bias		
\mathbf{d}_H	2.1341	0.5027	2.3829	1.3179	0.3687	0.8065	0.0573	0.5979	0.0971		
\mathbf{d}_V	1.4448	0.4425	1.1625	0.7427	0.4359	0.1115	0.6425	0.1003	0.7639		
\mathbf{d}_M	1.3897	0.4768	1.0892	0.4866	0.4889	0.0875	0.6883	0.0952	0.8219		
\mathbf{d}_{HV}	2.1114	0.4465	2.0030	0.9984	0.3019	0.6399	0.1306	0.5412	0.1657		
\mathbf{d}_{HVM}	2.2256	0.4648	2.0741	1.0955	0.2452	0.6158	0.1417	0.4410	0.2640		

When considering the joint posterior KLDs for the ensemble, we find that \mathbf{d}_{HVM} is the most informative dataset followed by \mathbf{d}_H and \mathbf{d}_{HV} . Far behind, featuring mean KLDs that are $\sim 60\%$ of \mathbf{d}_{HVM} , are \mathbf{d}_V and \mathbf{d}_M . Of the individual data sets, we find that \mathbf{d}_H is much more informative than \mathbf{d}_V and \mathbf{d}_M . The standard deviations have similar magnitudes and represent $\sim 20 - 35\%$ of the mean values.

We now consider the results obtained using the time-series (Figures 2.7a-c) obtained from the fields in Figures 2.4d-f. The ranking for the joint KLDs are similar to the ensemble mean

KLDs, except that \mathbf{d}_H performs the best. The point clouds of the posterior samples (Fig. 2.7) clearly shows that \mathbf{d}_H (Fig. 2.7a) constrain the geostatistical model parameters much better than \mathbf{d}_V (Fig. 2.7b) and \mathbf{d}_M (Fig. 2.7c).

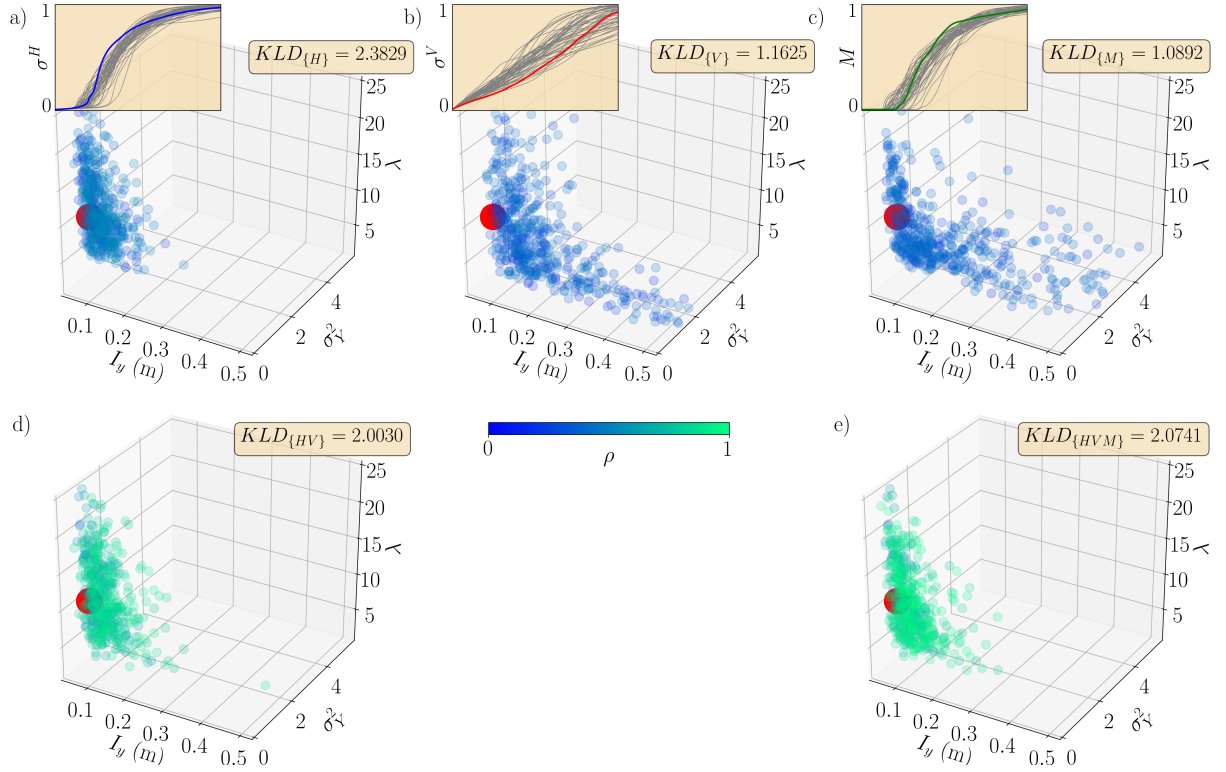


Figure 2.7 – Posterior model parameter vector samples of size $S = 500$ obtained by the AARS algorithm for test case $\mathbf{m}_2 = (0.80, 0.06 \text{ m}, 10.00)$ using different datasets as conditioning data. The colored clouds of points represent the samples for datasets (a) \mathbf{d}_H ; (b) \mathbf{d}_V ; (c) \mathbf{d}_M ; (d) \mathbf{d}_{HV} ; (e) \mathbf{d}_{VM} ; (f) \mathbf{d}_{HVM} . The colormap encodes the L_1 distance ρ between simulated and observed data, normalized by the minimum and maximum values of ρ of the test case. The inset plots of (a), (b) and (c) show, respectively, the 50 realizations of time-series σ^H , σ^V and M generated for \mathbf{m}_1 using different \mathbf{R} -realizations. The data considered here for inference are shown by thick-colored curves. The resulting KLD values are given for each dataset.

The marginal KLDs are again the largest for σ_Y^2 , followed by those of I_y and λ . We find that σ_Y^2 is the most constrained by \mathbf{d}_H and the least constrained by \mathbf{d}_M as reflected by their marginal KLDs and the compactness of their posterior PDFs (Fig. 2.8a). All the marginal PDFs for σ_Y^2 exhibit a small bias towards larger variances, with the smallest and largest biases exhibited for \mathbf{d}_{HVM} and \mathbf{d}_M , respectively. For I_y , the marginal KLD associated with \mathbf{d}_H is well-above the others (Fig. 2.8b). The secondmost and thirdmost best performing data set for this parameter are \mathbf{d}_{HV} and \mathbf{d}_{HVM} , while \mathbf{d}_M performs the poorest. The marginal KLDs and biases for λ (Fig. 2.8b) follow the ranking of I_y . For this test case \mathbf{m}_2 , the data better constrain the geostatistical parameters than for test case \mathbf{m}_1 as reflected by generally much larger KLD values.

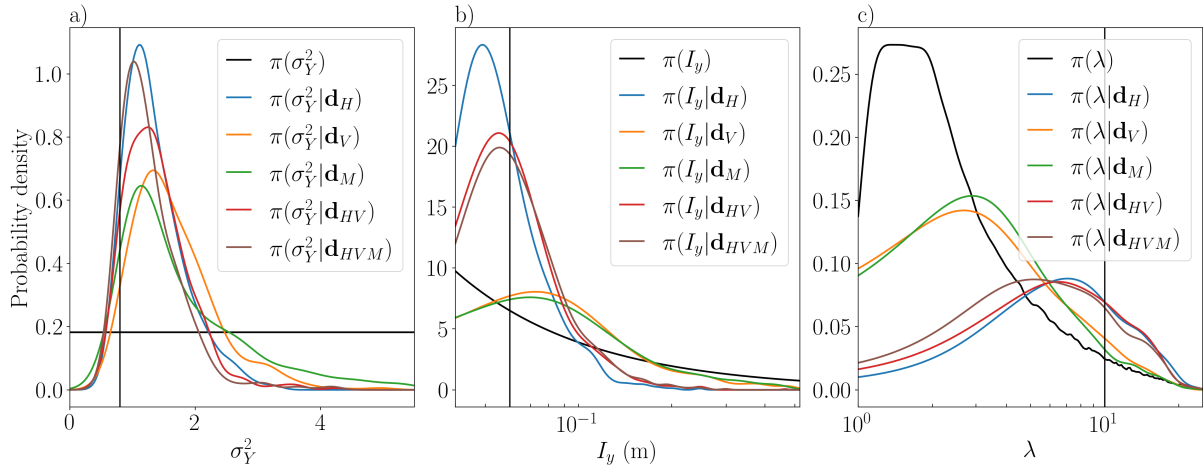


Figure 2.8 – Marginal posterior PDFs associated to each type of conditioning data \mathbf{d}_H , \mathbf{d}_V , \mathbf{d}_M , \mathbf{d}_{HV} , \mathbf{d}_{VM} and \mathbf{d}_{HVM} for test case $\mathbf{m}_2 = (0.80, 0.06 \text{ m}, 10.00)$. Marginal prior and posterior PDFs corresponding to (a) σ_Y^2 (b) I_y and (c) λ .

Test case \mathbf{m}_3

Table 2.3 summarizes the performance of the different datasets for test case \mathbf{m}_3 .

Table 2.3 – KLDs and mean relative biases of \mathbf{m}_3 for the different conditioning data types. Columns 1 and 2 show the mean μ_{KLD} and standard deviation σ_{KLD} of the KLDs using the ensemble of hydraulic conductivity realizations. Column 3 shows the KLD values for the joint posterior PDFs using one realization of the conditioning data obtained from Figures 2.4g-i and highlighted in Figures 2.9a-c. The subsequent pairs of columns show the marginal KLD values and relative mean biases for the marginal posteriors of each component of \mathbf{m}_3 using this specific realization.

	Ensemble		\mathbf{m}			σ_Y^2		$I_y(m)$		λ	
	μ_{KLD}	σ_{KLD}	KLD	KLD	Bias	KLD	Bias	KLD	Bias		
\mathbf{d}_H	1.1845	0.3195	1.0166	0.4818	0.3098	0.2681	0.6388	0.2031	0.3962		
\mathbf{d}_V	1.0565	0.3313	0.7459	0.3046	0.6171	0.0488	0.9635	0.0356	1.0166		
\mathbf{d}_M	0.8413	0.2798	0.6205	0.2019	0.7347	0.1949	0.6983	0.1296	0.5169		
\mathbf{d}_{HV}	1.3462	0.3491	1.0123	0.4491	0.4202	0.2680	0.6577	0.2054	0.4002		
\mathbf{d}_{HVM}	1.2932	0.3100	1.0068	0.4200	0.4429	0.2915	0.6164	0.2245	0.3647		

Considering the ensemble statistics of the joint posterior KLDs, we find that \mathbf{d}_{HV} has the largest mean KLD, closely followed by \mathbf{d}_{HVM} and \mathbf{d}_H . Again, \mathbf{d}_M features the smallest mean KLD with a values that is $\sim 63\%$ of that for \mathbf{d}_{HV} . The standard deviations are varying within $\sim 15\%$ and represent $\sim 25\%$ of the mean values.

We now consider the results from the data time-series (Figures 2.9a-c) obtained from the fields in Figures 2.4g-i. The joint KLD for \mathbf{d}_H is the largest closely followed by \mathbf{d}_{HV} and \mathbf{d}_{HVM} . Their KLDs are $\sim 30\%$ higher than the others. The point clouds of posterior model

realizations (Fig. 2.9) are rather similar, but the results obtained from \mathbf{d}_H (Fig. 2.9a) are more compact compared to \mathbf{d}_V and \mathbf{d}_M . For instance there is minimal scatter in the λ -direction (c.f., Fig. 2.9b) and the high σ_Y^2 is better constrained (c.f. Fig. 2.9c).

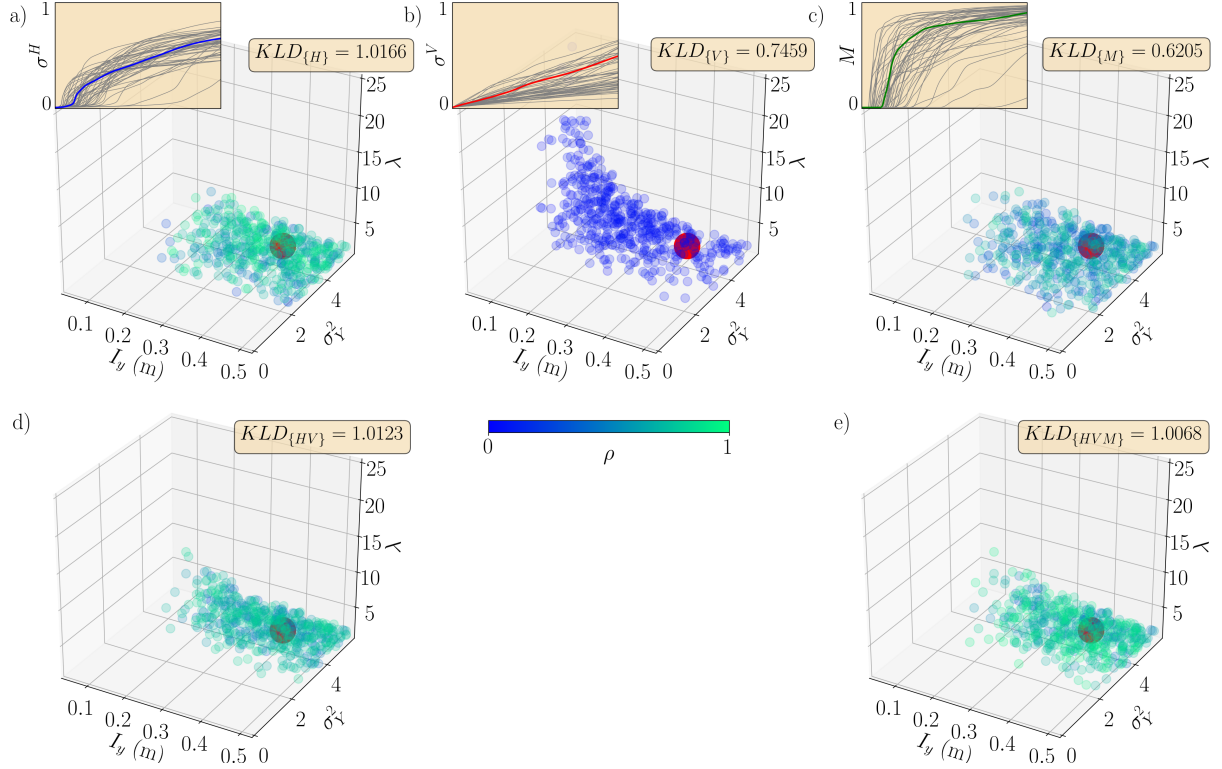


Figure 2.9 – Posterior model parameter vector samples of size $S = 500$ obtained by the AARS algorithm for test case $\mathbf{m}_3 = (4.70, 0.38 \text{ m}, 1.50)$ using different datasets as conditioning data. The colored clouds of points represent the samples for datasets (a) \mathbf{d}_H ; (b) \mathbf{d}_V ; (c) \mathbf{d}_M ; (d) \mathbf{d}_{HV} ; (e) \mathbf{d}_{VM} ; (f) \mathbf{d}_{HVM} . The colormap encodes the L_1 distance ρ between simulated and observed data, normalized by the minimum and maximum values of ρ of the test case. The inset plots of (a), (b) and (c) show, respectively, the 50 realizations of time-series σ^H , σ^V and M generated for \mathbf{m}_1 using different \mathbf{R} -realizations. The data considered here for inference are shown by thick-colored curves. The resulting KLD values are given for each dataset.

The marginal KLDs are again the highest for σ_Y^2 followed by I_y and λ . The relative mean biases show a similar trend, being smallest for σ_Y^2 . The marginal probability densities for σ_Y^2 (Fig. 2.10a) show that \mathbf{d}_H best constrain this parameter, followed by \mathbf{d}_{HV} and \mathbf{d}_{HVM} . The marginal KLD for \mathbf{d}_H are only $\sim 10\%$ larger than for \mathbf{d}_{HV} and \mathbf{d}_{HVM} , but its bias is 30% lower. Note also that \mathbf{d}_M is strongly biased towards too low σ_Y^2 . For I_y and λ , both KLDs and biases indicate that \mathbf{d}_H , \mathbf{d}_{HV} and \mathbf{d}_{HVM} are the most informative, while \mathbf{d}_V has the poorest performance.

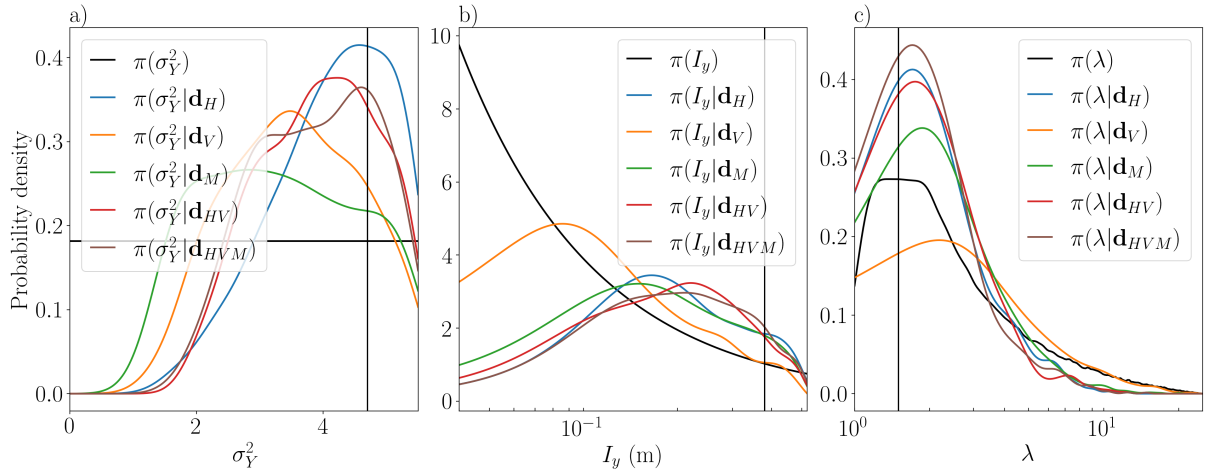


Figure 2.10 – Marginal posterior PDFs associated to each type of conditioning data \mathbf{d}_H , \mathbf{d}_V , \mathbf{d}_M , \mathbf{d}_{HV} , \mathbf{d}_{VM} and \mathbf{d}_{HVM} for test case $\mathbf{m}_3 = (4.7, 0.38 \text{ m}, 1.5)$. Marginal prior and posterior PDFs corresponding to (a) σ_Y^2 (b) I_y and (c) λ .

2.5 Discussion

2.5.1 General findings

The absolute values of the computed KLDs and biases are dependent on the choices made when approximating the posterior probability densities (Subsection 2.2), such as the width of the acceptance kernel of the AARS algorithm (Algorithm 2) and the bandwidth of the kernel density function used to represent the probability densities. For this reason, we focus our discussion below on relative differences between datasets and test cases. We first summarize the main results that apply to all test cases before discussing the test cases one-by-one. After this, we discuss broader implications of this research.

Considering the ensemble statistics of 50 hydraulic conductivity realizations for each test case, we find that the information content of \mathbf{d}_H measured by the KLD is higher than \mathbf{d}_V , which in turn is higher than \mathbf{d}_M for the three test cases considered: \mathbf{m}_1 (Table 2.1), \mathbf{m}_2 (Table 2.2) and \mathbf{m}_3 (Table 2.3). The added value of combining different data types (\mathbf{d}_{HV} and \mathbf{d}_{HVM}) is generally found to be comparatively low. When considering individual hydraulic conductivity realizations and associated fields (Figure 2.4), we generally obtain relative rankings of the different data types that are consistent with those of the ensemble means. Given that we consider non-ergodic model domains, the actual locations of high- and low hydraulic conductivities governed by the nuisance variable \mathbf{R} plays an important role in the data-generating process. Its impact is manifested by the comparatively high standard deviations of the KLD estimates (Tables 2.1-3) and in the variability of the generated time-series (Figs. 2.5a-c, 2.7a-c and 2.9a-c). Despite this inherent stochastic variability, we consistently find that the best constrained parameter is σ_Y^2 , followed by I_y and λ . The individual test cases are discussed in detail below.

2.5.2 Lessons learned from the three test cases

Test case \mathbf{m}_1 features a highly heterogeneous field $K(\mathbf{x})$ with relatively small structures (Fig. 2.4a), for which one could possibly assume that ergodic conditions are fulfilled and consequently that the geostatistical parameters are well-represented within the modelling domain, yet it corresponds to the least-constrained test case. Indeed, the \mathbf{R} -realization plays here a very important role, implying a rather weak mapping from the time-series to the geostatistical parameters of interest. To understand this, note first that $\{\sigma^H\}$ and $\{\sigma^V\}$ are only sensitive to the underlying geostatistical parameters through the solute spreading patterns that these parameters induce. Indeed, the electrical responses result from optimal current patterns established throughout the highly non-ergodic and time-evolving distribution of local concentrations (i.e., conductivities) that are, in turn, driven by the flow field $\mathbf{q}(\mathbf{x})$. As in the example in Figure 2.2, the hydraulic conductivity field $K(\mathbf{x})$ has small-scale structures and is close to isotropic (Fig. 2.4a) but its associated flow field $\mathbf{q}(\mathbf{x})$ exhibits pronounced channeling (Fig. 2.4b). This tendency of the flow field to concentrate in preferential flow channels for high σ_Y^2 is well-known (e.g., *Cvetkovic et al.*, 1996). Hence, an ergodic $K(\mathbf{x})$ is no guarantee of well-sensed geostatistical parameters when using geoelectrically monitored saline tracer tests. Nevertheless, compared to the prior, the estimated marginal posterior densities suggest that the geostatistical model that needs a comparatively high σ_Y^2 (Fig. 2.6a) and very small or high I_y (Fig 2.6b) are unlikely.

Test case \mathbf{m}_2 corresponds to a layered distribution of hydraulic conductivity with a moderate σ_Y^2 . The KLDs (Table 2.2), and consequently the constraining nature of the time-series, are much higher than for test cases \mathbf{m}_1 (Table 2.1) and \mathbf{m}_3 (Table 2.3). For \mathbf{m}_2 , the smallest variations between the \mathbf{R} -realizations are observed (Figs. 2.7a-c) since the actual location of the flow channels is of secondary importance in the data-generating process. The hydraulic conductivity field (Figs. 2.4d) and its associated flow field (Fig. 2.4e) are visually more similar to each other than for \mathbf{m}_1 . This is a consequence of the large anisotropy factor imposing horizontally continuous structures within which the flow-field channels are naturally developed. Both $\{\sigma^H\}$ and $\{M\}$ are highly sensitive to the arrival of horizontal connections that are established by the solute when it arrives to the outlet. Considering the marginal KLDs, we find that high and low σ_Y^2 -values are incompatible with the data (Fig. 2.8a), as is large I_y . For this test case \mathbf{m}_2 , λ is particularly interesting as its true value is high and, therefore, of low prior probability (Fig. 2.8c). We see a strong ability of all time-series including $\{\sigma^H\}$ to constrain this parameter.

Test case \mathbf{m}_3 is a highly heterogeneous test case that distinguishes itself from \mathbf{m}_1 by its larger I_y . A consequence of the resulting larger structures is that the generated data vary widely between the different hydraulic conductivity realizations (see insets in Figs. 2.9a-c). Yet the KLDs (Table 2.3) are higher than for test case \mathbf{m}_1 . Considering the marginal posterior PDFs, all datasets indicate that the underlying geostatistical model has a high σ_Y^2 (Fig. 2.10a), at least a moderately high I_y (Fig. 2.10b) and that the field is close to isotropic (Fig. 2.10c).

2.5.3 Physical insights and open questions

In our idealized numerical investigation, we found consistently that geoelectrical data performed better than mass breakthrough data in constraining the geostatistical parameters. This is a consequence of the fact that, for a given geostatistical model, the actual positioning of high- and low hydraulic conductivity fields, governed by the nuisance variable \mathbf{R} , has a larger impact on the mass breakthrough data than on the geoelectrical data (e.g., compare the insets in Figs. 2.9a-c). We understand this as a consequence of the local flux-averaged nature of the tracer breakthrough, compared to the more integrative non-linear volume-averaging of the electrical responses over the concentration field. Additionally, since $\{M\}$ is only sensitive to the time-evolution of the solute concentration field at the outlet, it cannot determine the causality of the arrival times, that is, if they originate from large horizontal correlation scales or from high variance, for instance.

We also found that $\{\sigma^H\}$ always has a higher constraining power than $\{\sigma^V\}$. This can be understood by noting that $\{\sigma^H\}$ is sensitive to electrical conduction paths created by the concentration field in the flow direction, leading to a very strong sensitivity to tracer arrivals at the outlet (e.g., Fig. 2.2e, or the generally steep slopes in the generated time-series in the insets of Figs. 2.5a, 2.7a and 2.9a). In Figure 2.12 we plot the generated current density distributions determining $\{\sigma^H\}$ and $\{\sigma^V\}$ for the concentration fields shown in Figs. 2.4c, 2.4f and 2.4j. We see that for $\{\sigma^H\}$ (Figs. 2.12a-c) the support of the current density field (i.e. the regions of high current flow) is almost coincident with the area occupied by the invading tracer driven by the flow-field. This does not occur for $\{\sigma^V\}$ (Figs. 2.12d-f), indicating why $\{\sigma^H\}$ is more informative than $\{\sigma^V\}$. Clearly, $\{\sigma^V\}$ results from current patterns that are mainly constrained by vertical connection bottlenecks that become more common further away from the inlet region. This can be appreciated by the high density of current field streamlines observed at the inlet regions in Figs. 2.11d, 2.11e and 2.11f. This suggests that the main ability of $\{\sigma^V\}$ to sense the geostatistical parameters is through its sensitivity to the trailing end of the tracer front. Again, it is the connectivity-aspect of the electrical data that is at play.

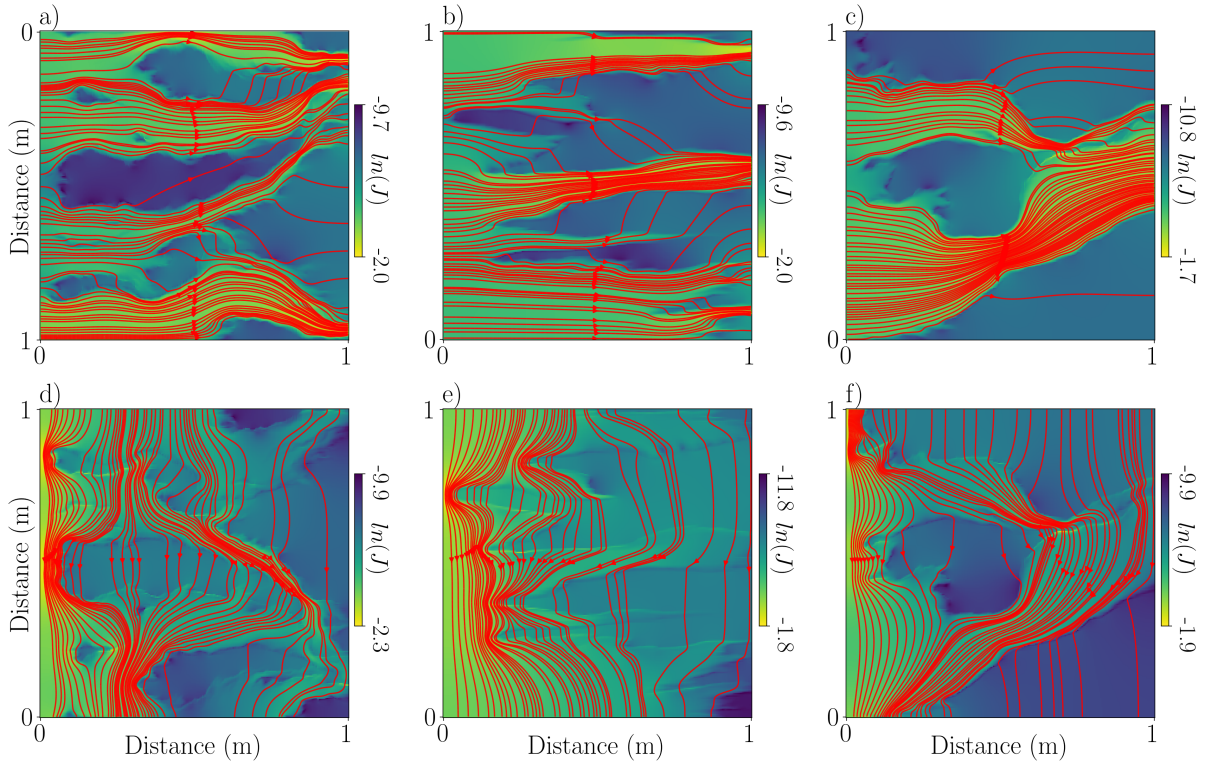


Figure 2.11 – Natural logarithm of the absolute value of the current density fields (and their streamlines) resulting from exciting the sample both in the (a-c) horizontal and (d-f) vertical modes. The electrical conductivity distribution is given by the saline concentration fields shown in Figure 2.4, that is, at time 10^3 s for the three evaluated test cases (a, d) \mathbf{m}_1 (column 1), (b, e) \mathbf{m}_2 and (c, f) \mathbf{m}_3 .

Our results also suggest a strong dependence on the injection type. For a pulse injection, we expect $\{\sigma^H\}$ to be much less informative, compared to the present continuous injection case, as there will be no horizontal connections of salinity to sense. That is, the connectivity created by establishing a continuous concentration field across the domain is very helpful for electrical-based inference of geostatistical properties from tracer tests.

For all test cases, we find that σ_Y^2 is the best constrained parameter. This is explained by the fact that σ_Y^2 controls the spreading rate of the solute (e.g., *Gelhar and Axness, 1983*) and is, thus, a first-order feature of the time-series. It will determine the time-spacing or pace of occurrence of the horizontal connection events as sensed particularly well by $\{\sigma^H\}$. However, also the trailing part of the tracer field as sensed by $\{\sigma^V\}$ is affected by σ_Y^2 .

One open question is to what extent the electrical data can constrain mixing and spreading. Intuitively, there should be a strong sensitivity to the spreading width as σ^H is highly sensitive to the front of the tracer plume and σ^V to its end. Since solute spreading ultimately controls solute mixing (e.g., *Villiermaux, 2019*), the high sensitivity of the electrical data to the former indicates that these data are able to at least quantify the mixing potential of the solute (e.g., *de Dreuzy et al., 2012*). This will be the topic of future research. Furthermore, the equivalent electrical conductivity tensor time-series is determined by the time-evolution of

the concentration field, which in turn is driven by the flow-field. This suggests that the electrical data might be more strongly related with the flow-field than the geostatistical model of log-hydraulic conductivity. In the future, we plan to study the geoelectrical sensitivity to flow-field descriptors (e.g., *Koponen et al.*, 1996; *Englert et al.*, 2006). Similarly, we would like to relate the electrical data to concentration field descriptors. However, as the concentration field is time-variant, this is more challenging to summarize than the steady-state flow field. One possibility is to relate it to the spatial distribution of localized temporal moments of the solute concentration field (*Cirpka and Kitanidis*, 2000).

2.5.4 Implications for field-based studies

Our work has several implications for field-based and laboratory-based electrical time-lapse monitoring of tracer tests. The first is that ignoring significant tracer-concentration heterogeneity below a given scale will tend to underestimate mass when interpreting tomograms (Fig. 2.3d) and bias inferred transport parameters when performing a fully-coupled hydrogeophysical inversion. This can be circumvented through appropriate geostatistics-based time-lapse hydrogeophysical inversions (e.g., *Kowalsky et al.*, 2005) provided that overly simple model parameterizations are avoided (*Hinnell et al.*, 2010). Furthermore, we demonstrate for non-ergodic situations, common to many hydrogeophysically-monitored tracer tests, that both the locations of high- and low hydraulic conductivities (in our case controlled by \mathbf{R}) and the geostatistical model have a strong impact on the measured data, suggesting that inversion approaches should attempt to constrain both of these aspects (*Laloy et al.*, 2015). Our results suggest that for a well-designed time-lapse experiment, it might be possible to infer geostatistical parameters with relatively few measurement configurations, that is, without the need to actually resolve the tracer plume. Indeed, all the inferences performed in this study are based on upscaled equivalent values at the scale of the experiment. Another implication is that strong geoelectrical responses are mainly linked to preferential current pathways that in clay free formations are dependent on a near-continuous high-salinity region between the current electrodes. This suggests that continuous (compared to pulse) injections are preferable and that it could be beneficial to favor measurement configurations with one of the current electrodes located in the tracer source region (i.e., in the pit in which injection is performed or in a packed-off injection interval in a borehole). It also suggests that using push-pull technology for electrode installations, thereby allowing for more of a 3-D localization of electrodes without associated borehole effects (*Doetsch et al.*, 2010) and costly boreholes, could enable improved imaging by allowing the tracer to arrive to the electrodes (*Pidlisecky et al.*, 2006). Furthermore, unaccounted saline tracer heterogeneity should lead to anisotropic behavior at larger scales. For instance, when interpreting crosshole time-lapse data with two boreholes using so-called AB-MN configurations (current and potential electrodes in different boreholes) leading to mainly vertical current patterns or AM-BN configurations (one current and potential electrode in each borehole) leading to mainly horizontal current patterns (*Bing and Greenhalgh*, 2001), then it might be essential to account for anisotropy in the inversion to avoid inversion artifacts (*Herwanger et al.*, 2004). Furthermore, we expect that any inferred upscaled anisotropy measures such as anisotropy factors could guide the interpretation about the spatial organization of the concentration field below the resolution scale of the resulting tomograms (e.g., different behaviors of $\{\sigma^H\}$ and $\{\sigma^V\}$ in Fig. 2.3d).

2.6 Conclusions

We use Approximate Bayesian Computation to assess to what extent equivalent electrical conductivity time-series associated with tracer tests constrain geostatistical parameters governing small-scale structure. We consider an idealized set-up in which local concentration and electrical conductivity is linearly and perfectly correlated, implying that the results correspond to a best-case scenario. By considering three different geostatistical test models and ensemble statistics of 50 corresponding hydraulic conductivity field realizations, we find that $\{\sigma^H\}$ is the most informative data type, followed by $\{\sigma^V\}$ and $\{M\}$. The added value of combining different time-series is comparatively low. We further find that σ_Y^2 is the best-constrained geostatistical parameter followed by I_Y and λ . The geostatistical parameters are the best constrained when considering data generated with a large λ . Ignoring concentration heterogeneity (i.e., assuming well-mixed conditions below a given scale) leads to underestimated solute mass when interpreting electrical data. This is a consequence of non-linear averaging and suggests that hydrogeophysical data interpretations and coupled hydrogeophysical inversions need to consider highly resolved hydraulic conductivity, fluid flow, concentration and electrical simulations in order to avoid biased results. Casting the inference problem within a geostatistical framework decreases the number of electrical configurations needed to constrain the geostatistical parameters. Since the electrical data are primarily sensitive to the presence (or not) of a connected high-concentration field between current electrodes, we recommend experimental setups favoring continuous tracer injections including measurement configurations with one electrode located within the tracer injection area.

Chapter 3

Electrical signatures of diffusion-limited mixing: Insights from a milli-fluidic tracer experiment

Alejandro Fernandez Visentini, Pietro de Anna, Damien Jougnot, Tanguy Le Borgne, Yves Méheust and Niklas Linde.

Published¹ in *Transport in Porous Media* and herein slightly adapted to fit the format of this thesis.

¹Fernandez Visentini, A., de Anna, P., Jougnot, D., Le Borgne, T., Méheust, Y. and Linde, N. (2021). Electrical signatures of diffusion-limited mixing: Insights from a milli-fluidic tracer experiment. *Transport in Porous Media*, **146**, <https://doi.org/10.1007/s11242-021-01607-0>

Abstract

We investigate how diffusion-limited mixing of a layered solute concentration distribution within a porous medium impacts bulk electrical conductivity. To do so, we perform a millifluidic tracer test by injecting a fluorescent and electrically conductive tracer in a quasi two-dimensional (2D) and water-saturated porous medium. High resolution optical- and geoelectrical monitoring of the tracer is achieved by using a fluorimetry technique and equipping the flow cell with a resistivity meter, respectively. We find that optical and geoelectrical outputs can be related by a temporal re-scaling that accounts for the different diffusion rates of the optical and electrical tracers. Mixing-driven perturbations of the electrical equipotential field lines cause apparent electrical conductivity time-series, measured perpendicularly to the layering, to peak at times that are in agreement with the diffusion transport time-scale associated with the layer width. Numerical simulations highlight high sensitivity of such electrical data to the layers' degree of mixing and their distance to the injection electrodes. Furthermore, the electrical data correlate well with time-series of two commonly used solute mixing descriptors: the concentration variance and the scalar dissipation rate.

3.1 Introduction

Time-lapse direct-current (DC) geophysical data acquired during saline tracer tests in porous media can provide constraints, both in the field and in the laboratory, on the temporal evolution of solute mixing processes. DC electrical resistance data are typically acquired using electrode configurations consisting of two electrode pairs: one to drive a known electrical current between two positions (points, along lines or across surfaces depending on application) and another to measure the voltage difference between two other positions (e.g., *Keller and Frischknecht*, 1966). When considering the injected current and the measurement geometry, these voltages are readily transformed into apparent resistivities. The number of electrode configurations used are sometimes few, for example when considering the equivalent electrical conductivity (inverse of resistivity) tensor of small-scale laboratory core samples (e.g., *Maineult et al.*, 2016; *Ghosh et al.*, 2018), and sometimes large (hundreds or many thousands) for field experiments aiming at inferring the spatial distribution of bulk electrical resistivity; a process often referred to as Electrical Resistivity Tomography (ERT). When applied in time-lapse mode, DC measurements are repeated over time to produce time-series of apparent resistivities. See the recent book by *Binley and Slater* (2020) for a comprehensive overview.

The bulk electrical conductivity of a fluid-saturated porous medium, with an insignificantly conductive matrix, depends on the porosity and non-linearly on the fluid electrical conductivity field $\sigma(\mathbf{x})$ within the pore space (e.g., *Torquato and Haslach Jr*, 2002; *Milton and Sawicki*, 2003). During DC-monitored saline tracer tests, the interstitial fluid electrical conductivity field $\sigma(\mathbf{x})$ originates from the heterogeneous and time-dependent saline concentration field $c(\mathbf{x})$, whereby $\sigma(\mathbf{x})$ and $c(\mathbf{x})$ are related by a monotonically-increasing relationship (e.g., *Sen and Goode*, 1992).

Time-lapse DC data have been routinely acquired during conservative saline tracer tests to retrieve solute transport parameters. Examples include the calibration of advective-dispersive transport models (e.g., *Kemna et al.*, 2002; *Vanderborght et al.*, 2005; *Koestel et al.*, 2008) highlighting the ability to constrain the spreading state and dynamics of solutes, which in turn have a strong impact on their mixing rate (e.g., *Dentz et al.*, 2011; *Villermanx*, 2019). They have also been used to calibrate dual-domain transport models (e.g., *Singha et al.*, 2007; *Day-Lewis et al.*, 2017), thereby, highlighting the sensitivity of DC conductivity to incomplete mixing. Regardless of context, there is always an implicit or explicit reliance on a petrophysical relationship linking the salinity field to the bulk electrical conductivity at some scale. Almost all petrophysical relationships (e.g., Archie's law (*Archie*, 1942)) ignore heterogeneity in fluid conductivity below the scale at which the petrophysical relationship is applied. This not only leads to biased estimates of mean saline concentrations (see the well-documented problem of apparent mass loss in, for instance, *Singha and Gorelick* (2005)), but it also neglects potentially-valuable information pertaining to mixing and spreading. Indeed, recent numerical modelling has demonstrated that equivalent electrical conductivity time-series can constrain geostatistical models of log-hydraulic conductivity fields (*Visentini et al.*, 2020).

Advancing our understanding of how tracer heterogeneity affects bulk electrical conductivity is necessary to obtain quantitative and robust spreading and mixing-related measures of the salinity field from geoelectrical data. Theoretical work on upscaling is needed, but also well-controlled experiments with simultaneous monitoring of upscaled electrical conductivities of porous medium samples together with highly-resolved imaging of concentration fields. Optically-monitored tracer tests (e.g., *Willingham et al.*, 2008; *de Anna et al.*, 2014; *Jiménez-Martínez et al.*, 2015, 2017)) with geoelectrical monitoring (e.g., *Kozlov et al.*, 2012; *Jougnot et al.*, 2018; *Izumoto et al.*, 2020) provides a suitable framework for such experiments. For example, *Kozlov et al.* (2012) used a micro-model sample filled with brine, oil and air to highlight the percolation-driven response of bulk electrical conductivity. Another study by *Jougnot et al.* (2018) considered advectively-dominated solute transport in saturated and unsaturated conditions to demonstrate that the apparent loss of mass that commonly plagues hydrogeophysical investigations is, at least partly, a consequence of assuming complete mixing (i.e., a constant salinity) below the averaging scale.

Milli-fluidic experiments combining optical- and electrical monitoring are challenging and few such studies have been performed to date. Errors in electrical monitoring and modelling, in the inferred time-evolving concentration field or in the concentration-conductivity relationship may lead to misleading findings. The strong connectivity-dependence of the salinity field on the electrical response places higher demands on the concentration imaging than in purely hydrological experiments (e.g., *Willingham et al.*, 2008; *de Anna et al.*, 2014; *Jiménez-Martínez et al.*, 2015, 2017). Consequently, there is a need for comparatively simple experiments covering well-known processes that can be used to ensure consistency in all aspects of the experimental setup, processing and modelling.

Here, we investigate the impact of diffusion-limited solute mixing on the temporal evolution of bulk electrical conductivity in a quasi two-dimensional (2-D) saturated porous medium. To this end, we have developed a milli-fluidic cell which allows monitoring the transport of a saline and fluorescent tracer both optically and electrically. High resolution optical

monitoring of the time-evolving 2-D (depth-averaged) solute concentration field is achieved by a fluorimetric technique combined with careful calibration to link light intensity with solute concentration. The resulting time-series of 2D concentration fields are used to predict the associated spatial distribution of local electrical conductivities. These are then used to predict the apparent conductivities under various configurations of current injection and voltage measurements. Direct electrical measurements of apparent conductivities are also carried out, by equipping the flow cell with a resistivity meter. The porous medium consists of three regions with two contrasting permeabilities, one region of higher permeability being sandwiched across the medium's width between two identical regions of lower permeability. We investigate the electrical signature of diffusive mass transfer from the high permeability region to the others.

The article is organized as follows. In Section 3.2, the materials and methods used for performing the experiment are described, including the tracer test procedure, the millifluidic, geoelectrical and optical acquisition setups, along with the fluorimetry technique and associated image processing workflow. In Section 3.3, we provide a summary of the implemented modelling approaches to simulate DC-conductivity and solute diffusion. In Sections 3.4 and 3.5, the main results are presented and discussed, respectively. Section 3.6 concludes the paper.

3.2 Materials and experimental methods

3.2.1 Porous medium design

We consider a Polydimethylsiloxane (PDMS) flow cell with length $L = 590$ mm, width $w = 74$ mm and height $h = 0.4$ mm that contains a hexagonal lattice of length $L_{\text{PM}} = 330$ mm formed by impermeable cylindrical pillars, representing the grains of a porous medium (black disks in Fig. 3.1a). We designed the porous system as three regular networks of pillars: as shown in Figure 3.1b, the top and bottom networks are characterized by radii $R_1 = 0.50$ mm and spacing (pore throats) of $\lambda_1 = 0.20$ mm, while the middle one by $R_2 = 2$ mm and $\lambda_2 = 0.70$ mm. The porosity is $\phi = 0.35$ and the pore volume is 3.42 ml. For flow regimes characterized by low Reynolds number ($Re = \lambda v / \nu$, ν being the average fluid velocity and ν its kinematic viscosity), the fluid motion is controlled by the confinement scale λ , as described by the Kozeny-Carman formulae (e.g., *Bear*, 1972): each region's (layer from now on) permeability is proportional to λ^2 , thus, the permeability contrast between the layers is 16. This induces a temporal scale separation of the same amount (16) in the advective transport for the middle layer compared to the top-bottom layers. Details on the cell construction are given in Appendix 3A. In Table 3.1 we include a summary of the parameters used to describe the flow and porous medium geometry.

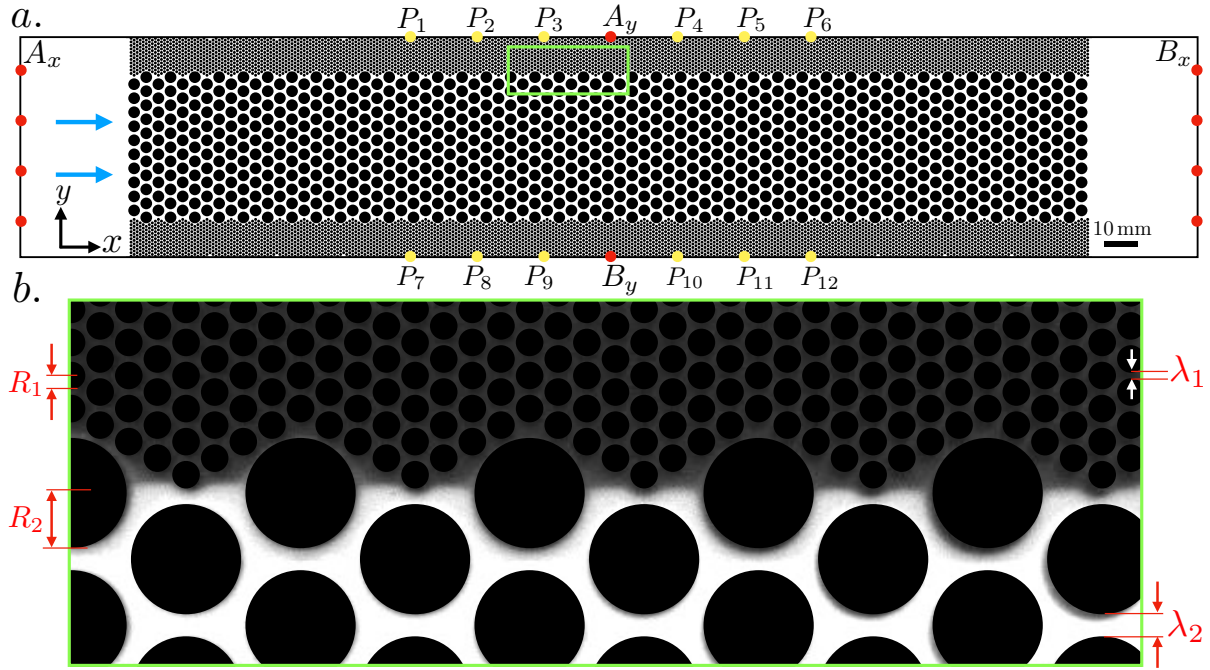


Figure 3.1 – (a) Top schematic view of the flow cell including, from left to right, an inlet chamber, an artificial layered porous medium, and an outlet chamber. The flow direction during the tracer injection is indicated with a pair of blue arrows. The sets of current injection electrodes A_x - B_x (measurement mode M_x) and A_y - B_y (measurement mode M_y), are indicated with red dots and the potential electrodes with yellow dots. (b) Zoom-in of the region indicated by a green rectangle in (a) ($x \in [160, 200]$ and $y \in [52, 72]$ mm) showing the interface separating the top from the middle porous layers, the former saturated with background (grey-colored) and the latter being saturated with fluorescent tracer (white-colored) just after stopping the tracer injection. The radii of the grains and the linear sizes of the pore throats are indicated, respectively, as R_1 and λ_1 , for the top and bottom layer, and as R_2 and λ_2 , for the middle layer.

3.2.2 Tracer solutions

We used a water-soluble tracer that is optically detectable and electrically conductive. We prepared two mixtures of distilled water containing a fluorescent tracer (FS), fluorescein sodium salt, Sigma-Aldrich, and sodium chloride (SC). Solution 1 has FS and NaCl concentrations of 0.001 and 0.015 g/l, respectively, and is used to saturate the cell before injecting the tracer Solution 2, which has FS and NaCl concentrations of 0.01 and 0.15 g/l. Solution 1 is obtained by diluting Solution 2 by a factor 15.

The FS concentration is measured with the optical method described in Subsection 3.2.5. It serves as a proxy for the concentration of SC, which is used to create high-enough contrast between the electrical conductivities of the background and tracer mixtures (e.g., *Jougnot et al.*, 2018). The FS molecule is about 3 times larger than the NaCl molecule, which results in a factor of ~ 3.8 between the diffusion coefficients of the salts, with $D_{FS} \sim 0.42 \times 10^{-9} \text{ m}^2 \text{ s}^{-1}$

and $D_{\text{NaCl}} \sim 1.6 \times 10^{-9} \text{ m}^2 \text{ s}^{-1}$ (e.g., *Casalini et al.*, 2011). Such a factor also applies to the ratio between the salts' ionic mobility, which combined with the considered 1:15 concentration ratio results in the FS contributing ~ 57 times less to the fluid's electrical conductivity than the NaCl (e.g., *Lesmes and Friedman*, 2005).

To conclude, note that after injecting Solution 2 some gravity-induced stratification in the water density may arise within the cell, parallel to the x - y plane. However, the considered small cell thickness is likely to prevent the development of a very pronounced vertical concentration profile. Moreover, given that our measurements of bulk electrical conductivity utilize electrodes that traverse the cell's height entirely (see Subsec. 3.2.4), tracer mass (fluid conductivity) that is segregated into parallel layers is volume-averaged the same as if no segregation occurred, that is, arithmetically, which leaves the bulk conductivity of the sample unchanged.

Table 3.1 – List of symbols and parameters used throughout the manuscript.

Symbols and parameters	Description
<i>Porous medium</i>	
$L = 590$, $w = 74$ and $h = 0.4$. $L_{PM} = 330$ (mm)	Length, width and height of the flow cell. Length of the porous medium
$R_1 = 0.50$ and $R_2 = 2.00$. $\lambda_1 = 0.20$ and $\lambda_2 = 0.70$ (mm)	Cylindrical pillars radii corresponding to the top and bottom, and middle networks, respectively. Idem for the pore throats lengths
$w_{ch} = 12$. $w_{middle} = 50$ (mm)	Top and bottom low-permeability layer widths. Middle high-permeability layer width
<i>Tracer solutions</i>	
$D_{FS} \sim 0.42 \times 10^{-9}$ and $D_{NaCl} \sim 1.6 \times 10^{-9}$ ($m^2 s^{-1}$)	Diffusion coefficients of fluorescein and sodium chloride, the two used tracers
$\sigma_{S_1} = 0.0218$ and $\sigma_{S_2} = 0.2728$ ($S m^{-1}$)	Electrical conductivity of Solution 1 and Solution 2, used as tracer and background, respectively
<i>Electrical monitoring</i>	
$\{A_x, B_x\}$ and $\{A_y, B_y\}$	Current electrode sets for the horizontal and vertical measurement modes, respectively, M_x and M_y
<i>Time parameters</i>	
$t_{ch}^{NaCl} = 127300$ and $\tau_v = 33$ (s)	Diffusive and advective transport time-scales associated with, respectively, w_{ch} and L_{PM}
t^{NaCl}	Temporal coordinate used to present the results, defined in terms of t_{ch}^{SC} and τ_v

3.2.3 Flow system

Solution 2 is injected from a 60ml syringe that is pushed by a syringe pump (Harvard Apparatus PHD 22/2000 Series). In order to ensure full saturation within the flow cell, it is initially lifted from the outlet side and fixed at a nearly vertical position with the inlet side at the bottom. The air is pushed out by slowly injecting (heavier) carbon dioxide (CO_2) from the inlet during approximately one hour. After flushing with CO_2 , 52 pore volumes of Solution 1 are slowly injected within a period of 48 hours allowing the trapped CO_2 bubbles to diffuse into the liquid and flush away. Once the flow cell is fully saturated with Solution 1, the experiment starts at $t = 0$ s and Solution 2 is injected at a volumetric flow rate $Q = 0.1 \text{ ml s}^{-1}$, that

yields a mean advective velocity of $v \sim 10 \text{ mm s}^{-1}$, until $t_{\text{stop}} = 60 \text{ s}$. This injection time was chosen to saturate the middle more permeable porous layer with the injected tracer, while leaving the top and bottom layers predominantly filled with Solution 1 (see Fig. 3.1b). After stopping the injection, the tracer is left to diffuse through the cell for 4 days. During the experiment, a full set of electrical measurements are made every 24 s while the FS concentration is measured optically, as described in Subsection 3.2.5.

3.2.4 Geoelectrical system

Since we expect electrical anisotropy at the sample scale, we measure the apparent electrical conductivity both along the x - and y -directions. To do so, we inject every 12 s a voltage square wave of $\Delta V = 1 \text{ V}$ amplitude and 12 s period (see Appendix 3B for details) alternatively either through the sets of injection electrodes A_x - B_x or through the set A_y - B_y (see Fig. 3.1a). These two injection modes are denoted M_x and M_y , respectively, and we collect measurements of: (i) the total electric currents i_x and i_y flowing between either set of injection electrodes, stored as $I_x(t)$ and $I_y(t)$, and (ii) the resulting voltages between each of the eleven potential electrodes P_i ($i = 2, \dots, 12$) and the reference electrode P_1 . These potential electrodes are distributed along the boundary of the porous medium (see Fig. 3.1a). Invoking the superposition principle, the voltage between any two given electrodes P_i and P_j are obtained by subtracting the voltage measured between P_j and P_1 from the one measured between P_i and P_1 . This allows us to construct 66 voltage-difference time-series for each injection mode, collectively grouped as the columns of the corresponding arrays $\mathbf{V}_x(t)$ and $\mathbf{V}_y(t)$. Finally, the resistance time-series corresponding to M_x and M_y are obtained as $\mathbf{R}_x(t) = \mathbf{V}_x(t)/I_x(t)$ and $\mathbf{R}_y(t) = \mathbf{V}_y(t)/I_y(t)$, respectively, and contain data sampled every 24 s.

The current injection and measurement protocols are interfaced with the datalogger Campbell Micrologger CR3000, which executes all operations. To establish electrical contacts with the cell, we use stainless steel cylindrical electrodes of 1 mm diameter that are inserted through the PDMS such that they are in contact with the fluid at the designated locations.

3.2.5 Image acquisition

The concentration field of the FS within the flow cell is optically measured, from the intensity of the light emitted by the tracer when excited (e.g., *de Anna et al.*, 2014; *Jiménez-Martínez et al.*, 2015, 2017; *Jougnot et al.*, 2018). Fluorescein sodium salt emits light around $\lambda_{\text{em}} = 521 \text{ nm}$ when excited by light at $\lambda_{\text{ex}} = 494 \text{ nm}$ (e.g., *Sjöback et al.*, 1995; *de Anna et al.*, 2014). To reduce tracer bleaching occurring during its exposition (e.g., *Imamura and Koizumi*, 1955), we use a flash lamp, placed about 60 cm above the cell, that is activated by an electronic signal (transistor–transistor logic gate, TTL) triggered by a computer through the open-source software Micromanager, the latter also controlling a CCD camera (Ximea, MD120MU-SY), placed 85 cm below the cell. The flash lamp is combined with a parabolic umbrella with a reflective internal surface focusing the emitted light towards the flow cell and the camera below it. Moreover, a translucent white sheet nylon covering the open side of the umbrella helps to homogenize the light over the flow cell. The experiment takes place in a darkroom to avoid any light disturbance. The camera exposure time is set to 0.4 s: as soon a picture

acquisition is triggered, the controlling software triggers the flash that lasts for a few tens of ms. A band pass optical filter (LEE 126 Mauve) is placed between the flash lamp and the flow cell to illuminate it with light having wavelengths below 500nm. Also, a band pass optical filter (Edmund Optics 520 nm CWL, 10 nm Bandwidth) is placed in front of the camera to only allow light in the window [510 – 530] nm to reach its sensor.

The camera records gray-scale light intensity images of 2832×4244 pixels with intensities ranging from 0 to 255 (8-bit pixel depth camera). The size of each pixel corresponds to 0.06 mm, which implies that the pore throats of the finely-grained layers are resolved with 3 pixels. The collected time-series of light intensity images, $I(x, y, t)$, consists of 2334 pictures sampled as follows: (i) 90 every 2s; then (ii) 490 every 60s and then (iii) 1889 every 600s. This sampling scheme follows the decaying dynamics of our tracer test: fastest at the beginning and slowing down in time.

Note that x -, y - and t interchangeably denote discrete spatial and temporal indices, used for describing the experiment, or continuous coordinates. We prefer such a loose notation for reasons of simplicity and because their meaning are facilitated by context.

3.2.6 Image processing

To obtain concentration images, we first build a binary image, a so-called pore space mask, containing the spatial distribution of the pore space and grains in terms of a 2D indicator function that takes values of 1 inside the pores and 0 elsewhere (see Appendix 3C for details on its compilation). Second, we transform $I(x, y, t)$ into time-series of FS concentration fields, $c(x, y, t)$ using a calibrated relationship. To establish this relationship, we collected a series of 6 pictures $I_c^i(x, y)$ ($i = 1, \dots, 6$) of the flow cell when it was uniformly saturated with 6 corresponding solutions having FS concentrations C^i ($i = 1, \dots, 6$) of 0.00100 (corresponding to Solution 1), 0.00195, 0.00300, 0.00500, 0.00833 and 0.01500 g/l (corresponding to Solution 2). These solutions are obtained by successive dilution of Solution 2 until Solution 1 is obtained. The concentrations follow approximately a log-equidistant distribution and are slowly injected over successive periods of ~ 36 h in an increasing order of concentration, using 52 pore volumes for each of them to ensure uniform concentration fields. After, both $I_c^i(x, y)$ and $I(x, y, t)$ are registered (e.g., Brown, 1992) using the grain mask as reference, in order to ensure that (x, y) represents the same position within the flow cell for any image. Such a procedure, combined with the fact that both the camera and flow cell are fixed to an aluminum solid structure during the whole duration of the experiment and calibration, allows us to employ a pixel-by-pixel transform of the acquired light intensity $I(x, y, t)$ into the concentration field $c(x, y, t)$. We use a local Piecewise Cubic Hermite Interpolating Polynomial on the calibration data $I_c^i(x, y) - C^i$.

3.2.7 Concentration - electrical conductivity calibration

We calibrate an empirical relationship between concentration and fluid electrical conductivity, in order to transform $c(x, y, t)$ into the electrical conductivity field $\sigma(x, y, t)$. To do so, we rely on electrical conductivity measurements of the calibration solutions C^i , using the WTW ProfiLine Cond 3310 portable conductivity meter. This yields conductivity values of $\sigma_{S_1} = 0.0218$ and $\sigma_{S_2} = 0.2728 \text{ S m}^{-1}$ for Solution 1 and 2, respectively, giving $\sigma_{S_2}/\sigma_{S_1} = 12.51$.

3.3 Modelling

3.3.1 Electrical modelling

Once the time-series $\sigma(x, y, t)$ have been obtained, they are used as inputs to the governing Laplace equation

$$\nabla \cdot (\sigma \nabla \phi) = 0, \quad (3.1)$$

where ϕ is the electrical potential. Equation 3.1 is solved with the finite-element solver module of the open-source Python library pyGIMLi (*Rücker et al., 2017*), using mixed Dirichlet-Neumann boundary conditions corresponding to the two injection modes. For both cases, following conductivity measurements performed on the PDMS material, the grain mask is assigned a conductivity of 10^{-9} S m^{-1} . Additional simulations (not included in the manuscript) were performed using different values for the grain mask conductivity, the latter ranging between 10^{-6} S m^{-1} and $10^{-10} \text{ S m}^{-1}$. No noticeable differences were observed between these tests. For M_x , values of 1 and 0V are imposed for ϕ , respectively, at the positions of the current electrodes A_x (left) and B_x (right) (Fig. 3.1), respectively, and no-flux conditions are imposed on the remaining boundaries. For M_y , values of 1 and 0V are imposed, respectively, at the positions of A_y and B_y , and a no-flux condition is imposed on the remainder of the cell's perimeter. This yields a pair of time-series of electrical potential fields $\phi_{M_x}(x, y, t)$ and $\phi_{M_y}(x, y, t)$, corresponding to each injection mode, sampled at the positions of the potential electrodes P_i ($i = 1, \dots, 12$) from which 66 voltage time-series are obtained (see Subsection 3.2.4). They are grouped into the arrays $\mathbf{V}_x^{\text{sim}}(t)$ and $\mathbf{V}_y^{\text{sim}}(t)$. From the corresponding simulated time-series of electrical current, $\mathbf{I}_x^{\text{sim}}(t)$ and $\mathbf{I}_y^{\text{sim}}(t)$, the simulated resistance time-series are obtained as $\mathbf{R}_x^{\text{sim}}(t) = \mathbf{V}_x^{\text{sim}}(t)/\mathbf{I}_x^{\text{sim}}(t)$ and $\mathbf{R}_y^{\text{sim}}(t) = \mathbf{V}_y^{\text{sim}}(t)/\mathbf{I}_y^{\text{sim}}(t)$.

The camera images $I(x, y, t)$ and, hence, the resulting concentration estimates $c(x, y, t)$ include neither the inlet nor the outlet chambers. Three modeling scenarios including these chambers were used to assess their influence on the electrical resistance time-series. First, we assumed the chambers to be filled with Solution 1 (background conductivity). Second, we considered the chambers to be filled with Solution 2 (injected tracer conductivity). Third, we assumed that the inlet chamber was filled with Solution 2 and the outlet chamber with

Solution 1. Considering both measurement modes M_x and M_y , the observed discrepancies were below 0.8%.

3.3.2 Post-processing of electrical resistance time-series

The observed (simulated) electrical resistance time-series $\mathbf{R}_x(t)$ and $\mathbf{R}_y(t)$ ($\mathbf{R}_x^{\text{sim}}(t)$ and $\mathbf{R}_y^{\text{sim}}(t)$) are transformed into corresponding time-series of apparent conductivities $\Sigma_{M_x}(t)$ and $\Sigma_{M_y}(t)$ ($\Sigma_{M_x}^{\text{sim}}(t)$ and $\Sigma_{M_y}^{\text{sim}}(t)$), by, first, multiplying the columns of the resistance arrays with the corresponding 66 geometrical factors, that account for the measurement and sample geometry in a homogeneous medium (hence the term "apparent") (e.g., *Keller and Frischknecht*, 1966), and, second, inverting element-wise the resulting arrays. The geometrical factors are obtained by numerical simulations following a procedure similar to that of *Jougnot et al.* (2010): briefly, a resistance value is simulated using a domain of the same dimensions of the experimental cell but having unit porosity (i.e., without grains) and saturated with a known value of fluid resistivity. For such setting, since, by definition, the apparent resistivity equates the input fluid resistivity, the corresponding geometrical factor is obtained by dividing the latter by the simulated resistance. This has to be repeated for each measurement configuration

The simulated time-series $\Sigma_{M_x}^{\text{sim}}(t)$ and $\Sigma_{M_y}^{\text{sim}}(t)$ are calculated on a 2-D geometry that implicitly assumes a 1 m-thick third dimension. Consequently, they are multiplied by the ratio of the cell's nominal thickness to 1 m, that is, $4 \cdot 10^{-4}$, in order to make them comparable with the measured time-series $\Sigma_{M_x}(t)$ and $\Sigma_{M_y}(t)$.

We now consider the bulk electrical conductivity (Fig. 3.2) calculated using the potential electrode pair P_1 - P_6 and the horizontal injection mode M_x for 12 different solute concentrations (including those of Solution 1 and 2). The data plot on a linear log-log plot and extrapolation to zero fluid conductivity suggests a negligibly small bulk electrical conductivity under those conditions. This confirms that the PDMS pillars are electrical insulators and that all electrical conduction takes place in the liquid phase (i.e., no measurable surface conductivity). Thus, we can use Archie's linear relationship (*Archie*, 1942) to relate the electrical conductivity of the homogeneous interstitial fluid, σ_{fluid} , to that of the porous medium, σ_{PM} , by

$$\sigma_{\text{PM}} = \frac{\sigma_{\text{fluid}}}{F}, \quad (3.2)$$

with F the formation factor. Note that F is constant and the same in all sub-regions (or similar) within the artificial porous medium, given that both the network's porosity and geometry (i.e., its topology) are spatially invariant by design. The regression line has a slope of 1/3.34, which yields an empirical formation factor $F_{\text{data}} = 3.34$. On the other hand, simulated values of apparent conductivity, obtained using the cell model for the same measurement device and set of fluid conductivities, plot on a slightly different linear log-log plot (see dashed line in Fig. 3.2), yielding a theoretical formation factor $F_{\text{sim}} = 4.82$.

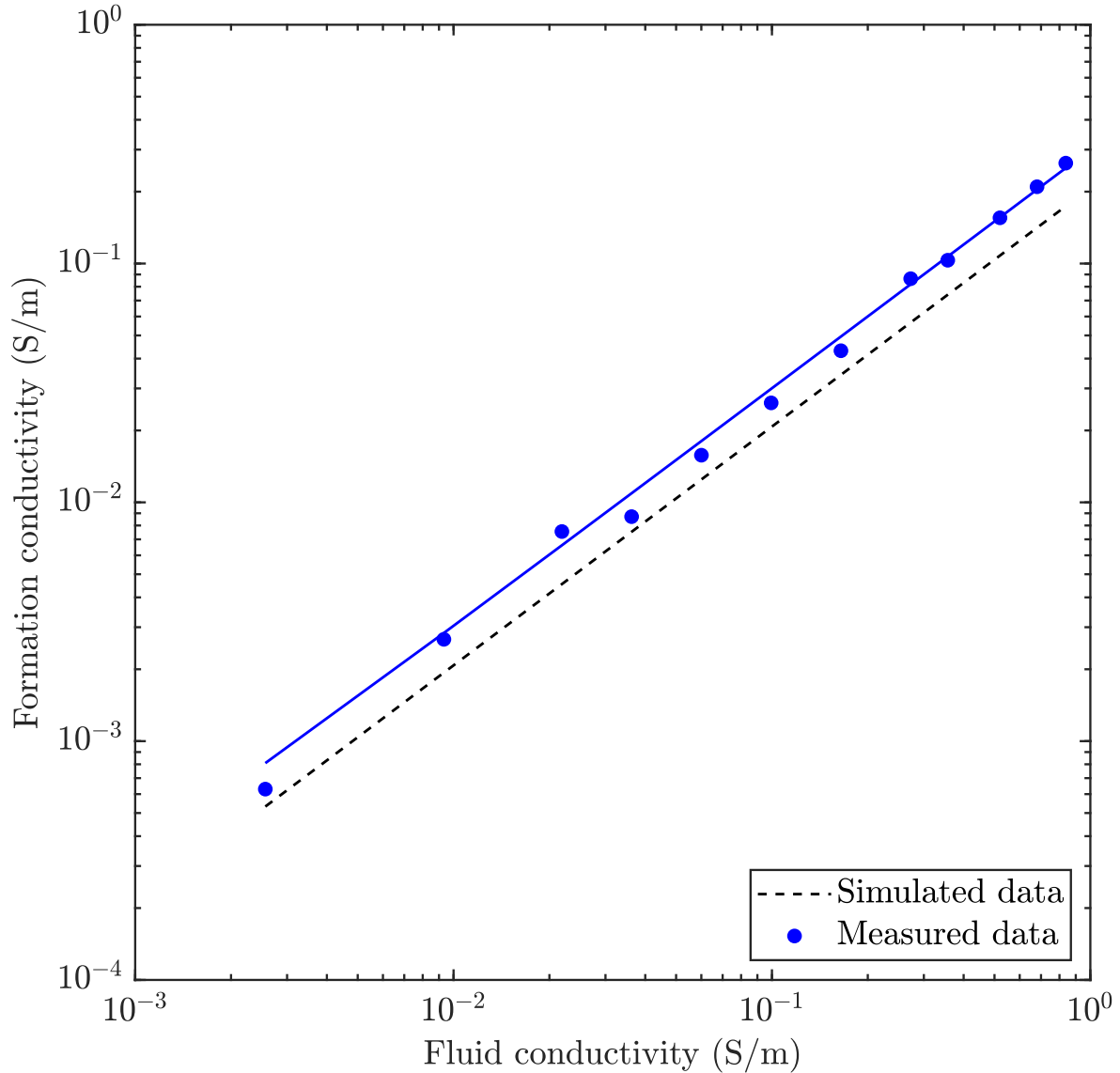


Figure 3.2 – Fluid electrical conductivity versus bulk electrical conductivity for a homogeneous solute concentration. The measured apparent conductivities are shown as blue dots with the associated regression as a continuous black line. The numerically calculated bulk conductivities are shown as a black dashed line.

In order to ensure that $F_{\text{data}} = F_{\text{sim}}$, and discarding the possibility of surface conductivity (see paragraph above), an effective cell thickness of 0.57 mm is finally used (instead of the cell's nominal thickness of 0.4 mm) when normalizing the simulated data. A slightly different (larger) cell thickness is to be expected if there were small errors during the porous system fabrication (see Appendix 3A). Indeed, anomalously deep cylindrical pillars could result from an imperfect drilling operation when compiling the stainless-steel mould. Also, some slight thickness variations (increments) may arise if the PDMS plate was not sandwiched perfectly flat between the acrylic plates, that is, with a slight topography.

3.3.3 Solute diffusion modelling in confined media

In order to model diffusion within our experimental cell after tracer injection, we adopt an Eulerian standpoint and consider the diffusion equation in both 1- and 2-D. The 1-D model is used as a comparison tool against our observed concentration profiles (see Fig. 3.4) whereas the 2-D model is used for the numerical investigation presented in Subsection 5.2.

For 1-D diffusion, we consider a confined domain of length $L = \infty$ and width $w = 74$ mm, subjected to homogeneous Neumann (i.e., impermeable walls) boundary conditions. Prescribing an initial condition $f(\hat{y})$ (with $\hat{y} = y - w/2$), that is, a y -oriented concentration profile after stopping the injection, the corresponding boundary-value problem admits the following closed-form solution in terms of a Fourier cosine representation (e.g., *Balluffi et al.*, 2005):

$$c(\hat{y}, t) = \sum_{n=0}^{\infty} b_n \cos(\pi n \hat{y}) \exp\left\{-\frac{n^2 \pi^2 D t}{w^2}\right\}, \quad (3.3)$$

where D is the diffusion coefficient and the weights b_n are the Fourier coefficients of the series, given by

$$b_n = \frac{2}{L} \int_0^L f(\hat{y}') \cos(\pi n \hat{y}') d\hat{y}'. \quad (3.4)$$

For 2-D diffusion, we consider a confined domain of length $L = 590$ mm and width $w = 74$ mm (as in the experimental cell, Subsec. 3.2.1), with a no-flux condition along all the boundaries. Different initial conditions for the modelled NaCl concentration field are considered (Subsec. 3.5.2) and the resulting boundary-value problem is numerically solved using the finite difference implementation included within the groundwater solute transport simulator package MT3D-USGS (*Bedekar et al.*, 2016).

Characteristic transport time-scales within the cell

We consider characteristic diffusive $\tau_{\text{ch}}^{\text{NaCl}}$ and advective τ_v transport time-scales for the NaCl associated with, respectively, the length scales (i) $w_{\text{ch}} = 12$ mm corresponding to the width of the top and bottom low-permeability layers and (ii) L_{PM} corresponding the porous medium x -length. These are defined as $\tau_{\text{ch}}^{\text{NaCl}} = w_{\text{ch}}^2 / D_{\text{NaCl}}^{\text{eff}} \sim 127300$ s (~ 16 h) and $\tau_v = L_{\text{PM}} / v \sim 33$ s. Note that we have replaced the bulk diffusion coefficient D_{NaCl} by the effective diffusion coefficient $D_{\text{NaCl}}^{\text{eff}} = D_{\text{NaCl}} / \sqrt{2}$ to account for the tortuosity of the porous medium (e.g., *Bear*, 1972). The smaller effective diffusion rate is a consequence of the solute needing to travel a longer path in order to circumvent the grains.

Time handling

Since the measured apparent electrical conductivity time-series $\Sigma_{M_x}(t)$ and $\Sigma_{M_y}(t)$ are predominantly sensitive to the NaCl concentration field, we present such data as a function of t^{NaCl} , a temporal coordinate defined as a function of t as:

$$t^{\text{NaCl}} = \begin{cases} (t - t_{\text{stop}})/\tau_\nu & 0 \leq t \leq t_{\text{stop}} \\ (t - t_{\text{stop}})/\tau_{\text{ch}}^{\text{NaCl}} & t > t_{\text{stop}}, \end{cases} \quad (3.5)$$

where t_{stop} refers to the end of the tracer injection (Subsec. 3.2.3) and τ_ν and $\tau_{\text{ch}}^{\text{NaCl}}$ have been defined in and Subsection 3.3.3. The origin is established at t_{stop} as the main interest lies in times after injection has stopped. With this convention, negative and positive t^{NaCl} represent, respectively, times normalized by advective and diffusion transport time-scales. The FS sensed by the optical measurements diffuses ~ 3.8 times slower (Subsec. 3.2.2) than the NaCl sensed by the DC data. Thus, to make geoelectrical and image-based outputs comparable, we will present the latter as a function of $t^{\text{NaCl}}/3.8$ for $t^{\text{NaCl}} > 0$. This implies that our 4-day experiment provides us with fluorimetry-inferred NaCl concentration fields over $4/3.8$ days.

3.4 Results

We now analyze the data obtained during the tracer test. First, we consider the fluorimetry-inferred NaCl concentration field (Subsec. 3.1) using four snapshot examples. Then, we present measured apparent electrical conductivity time-series and compare them with simulations.

3.4.1 Fluorimetry-inferred NaCl concentration field

Snapshots of the fluorimetry-inferred NaCl concentration field are shown for the following t^{NaCl} times (Subsec. 3.3.3): $t_1^{\text{NaCl}} = 0$ (Fig. 3.3a), that is, just after the tracer injection has been stopped; $t_2^{\text{NaCl}} = 5 \times 10^{-3}$ (Fig. 3.3b) and $t_3^{\text{NaCl}} = 5 \times 10^{-2}$ (Fig. 3.3c), approximate times at which the apparent electrical conductivity data show, respectively, an accelerated growth rate and a local maximum (Subsec. 3.4.2); and $t_4^{\text{NaCl}} = 5 \times 10^{-1}$ (Fig. 3.3d), that is, close to the latest available fluorimetry-inferred NaCl concentration field.

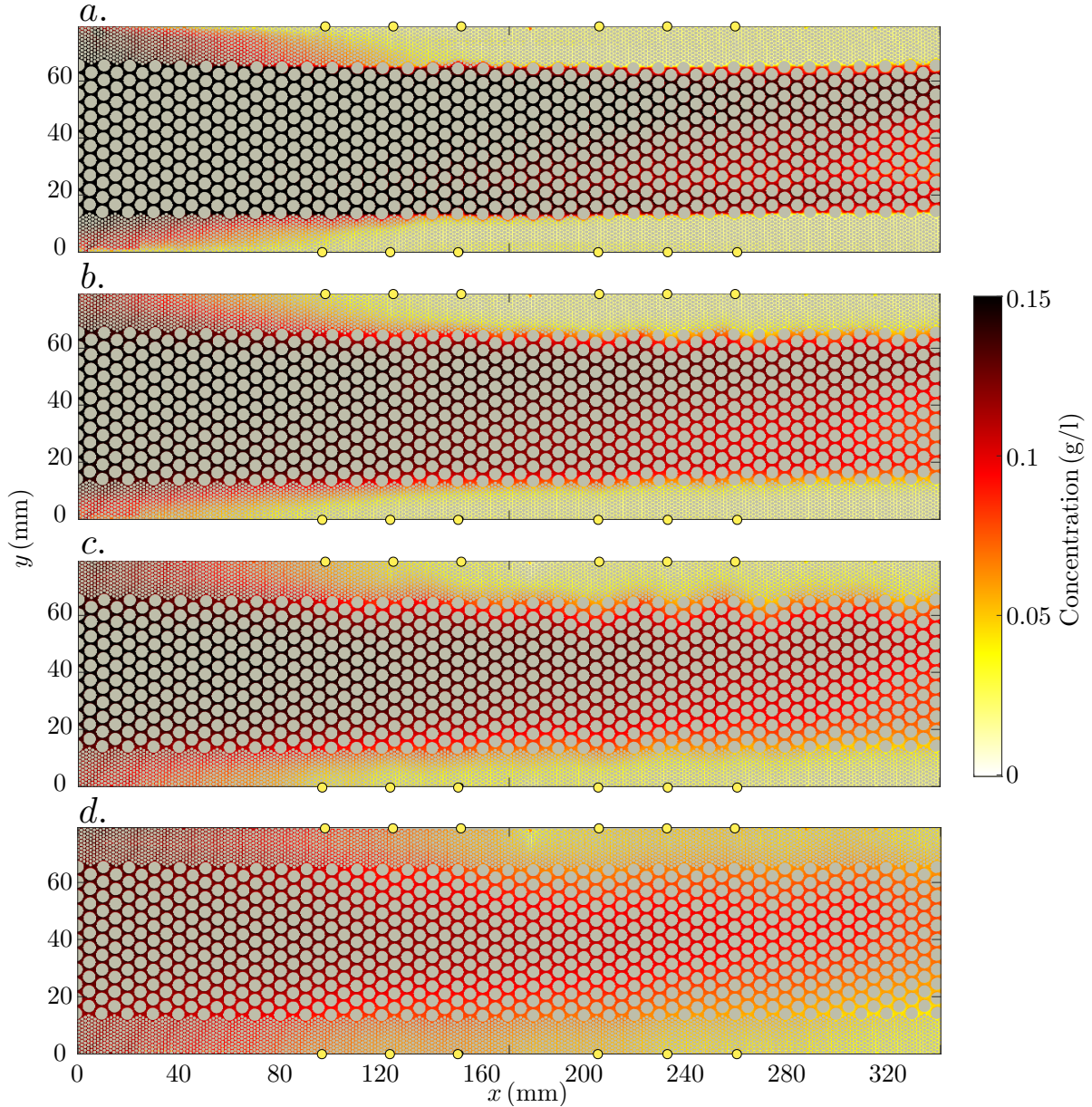


Figure 3.3 – Four snapshots of the fluorimetry-inferred NaCl concentration fields corresponding to times (a) $t_1^{\text{NaCl}} = 0$, (b) $t_2^{\text{NaCl}} = 5 \times 10^{-3}$, (c) $t_3^{\text{NaCl}} = 5 \times 10^{-2}$, and (d) $t_4^{\text{NaCl}} = 5 \times 10^{-1}$. The yellow dots indicate the potential electrodes, see Figure 3.1 for convention.

For t_1^{NaCl} and $x > 160$ mm (Fig. 3.3a), there is a sharp concentration gradient along the y -direction, marking the boundaries between the layers (see also the zoom in Fig. 3.1b). The high permeability middle layer does not exhibit a perfectly homogeneous concentration distribution as evidenced by lower values in the middle. We attribute this to slight thickness variations in the inlet chamber, also seen in *Jougnot et al.* (2018). For $x < 160$ mm, the tracer has slightly invaded the low permeability layers up to the x -locations of P_2 and P_8 (3.1a). For t_2^{NaCl} and t_3^{NaCl} (Figs. 3.3b and 3.3c), the initially sharp concentration gradient along the

y -direction is decreased. At the last considered time (t_4^{NaCl} , Fig. 3.3d), the NaCl concentration field has achieved a much higher degree of homogeneity in comparison to t_1^{NaCl} .

Snapshots of y -oriented fluorimetry-inferred NaCl mean concentration profiles for the times considered above are shown in Figure 3.4. These are obtained by x -averaging the 2-D concentration field within the horizontal coordinate range $x \in [140, 175]$ mm. Additionally, we present analytically computed NaCl concentration profiles (Equation 3.3) assuming a 1D domain. This is done for the same width w as that of our porous medium, but also for a ten times larger width, to mimic an unconfined domain. As initial condition, we consider the first snapshot of the x -averaged concentration profile (note the perfect match between the modelled and observed concentration profiles for t_1^{NaCl}).

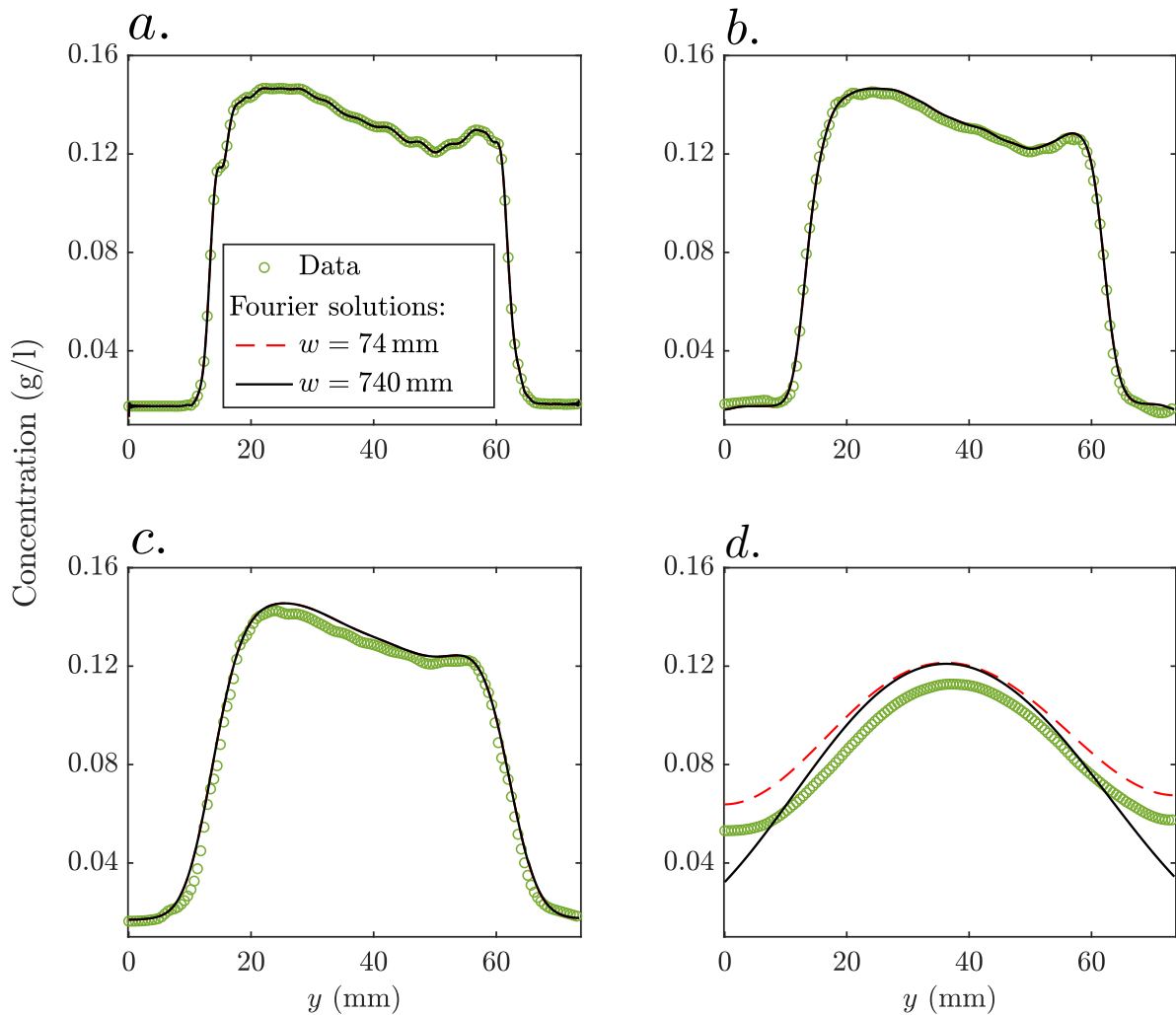


Figure 3.4 – Four snapshots of fluorimetry-inferred and modeled NaCl concentration profiles for times (a) $t_1^{\text{NaCl}} = 0$ (initial conditions for the modeling), (b) $t_2^{\text{NaCl}} = 5 \times 10^{-3}$, (c) $t_3^{\text{NaCl}} = 5 \times 10^{-2}$, and (d) $t_4^{\text{NaCl}} = 5 \times 10^{-1}$.

The concentration profile at t_1^{NaCl} (end of the injection) is not a perfect step function but it features a non-flat topography in its central part (Fig. 3.4a). This is caused by an imperfect tracer injection pattern, as mentioned before (see description of Fig. 3.3). At t_2^{NaCl} (Fig. 3.4b), a small degree of smoothing has occurred, along with a slight amplitude decay ($\sim 2\%$) of the observed concentration profile with respect to the analytically calculated profiles. At t_3^{NaCl} (Fig. 3.4c), the smoothing, as well as the magnitude decay of the observed data, are more pronounced (with an average of $\sim 4\%$ within the central part), the latter indicating an ongoing loss of solute mass from the computational range $x \in [140, 175]$ which is not accounted for in the 1D solutions. At t_4^{FS} (Fig. 3.4d), the NaCl profiles display a much higher degree of homogeneity compared with the situation at t_1^{NaCl} . Particularly, a considerable amount of NaCl mass has been brought by diffusion to the low permeability layers. The shapes of the observed and analytical solution for the confined domain (i.e., $w = 74 \text{ mm}$) are very similar, although the magnitude of the former is $\sim 9\%$ smaller than that of the latter. As expected, the analytical solution for the unconfined solution (i.e., $w = 740 \text{ mm}$) underestimates concentrations in the vicinity of the boundaries of the domain.

In Figure 3.5, y -averaged concentration profiles are plotted as a function of x for the same four times. The longitudinal profile at t_1^{NaCl} (blue solid line in Fig. 3.5) shows a decreasing trend from left to right. The ratio of mean concentration in the inlet to the outlet is ~ 1.8 . This is mainly due to the invasion of the tracer along the low permeability channels in the inlet region, and by the incomplete tracer saturation of the middle high permeability layer in the outlet region (Fig. 3.3a). At t_2^{NaCl} (red dashed line in Fig. 3.5), the ratio of inlet to outlet concentrations has been slightly reduced to ~ 1.75 , suggesting that the mass imbalance along the x -direction is being mitigated by the action of x -directed mass transport by molecular diffusion. At the subsequent times t_3^{NaCl} and t_4^{NaCl} (respectively, green dotted and purple dotted-dashed lines in Fig. 3.5), the ratios decrease further to 1.7 and 1.5, respectively. Note also that the curves in Figure 3.5 as a whole exhibit a downward shift with time, indicating that the total FS mass within the field of view, from which the NaCl concentrations are derived, has decreased either due to photo-bleaching or horizontal mass transport. The mean concentration, calculated by integrating the concentration field over the entire field of view, decreases throughout the experiment from 0.11 to 0.09 g/l (inset in Figure 3.5), suggesting an apparent loss of tracer mass. This issue is discussed in Subsection 3.5.1.

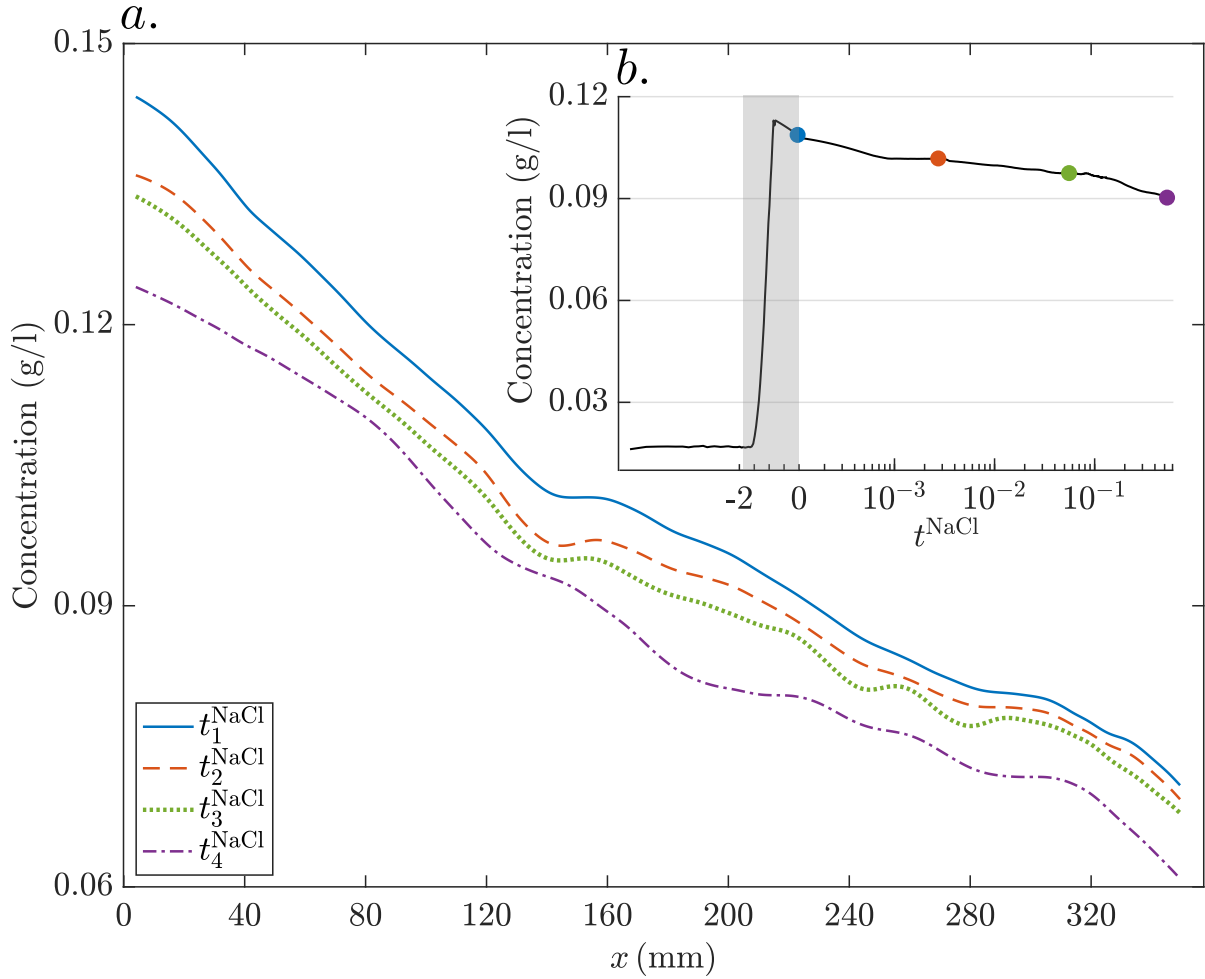


Figure 3.5 – (a) y -averaged mean of the fluorimetry-inferred NaCl concentrations as a function of the horizontal coordinate x for times $t_1^{\text{NaCl}} = 0$ (blue solid line), $t_2^{\text{NaCl}} = 5 \times 10^{-3}$ (red dashed line), $t_3^{\text{NaCl}} = 5 \times 10^{-2}$ (green dotted line), and $t_4^{\text{NaCl}} = 5 \times 10^{-1}$ (purple dotted-dashed line). (b) Temporal evolution of the inferred mean concentration over the entire field of view. Note that negative and positive t^{NaCl} represent, respectively, times normalized by advective and diffusion transport time-scales (Subsec. 3.3.3). The grey-colored rectangle highlights the tracer injection period. The blue, red, green and purple-colored dots on the curve indicate the mean concentration field values at times t_1^{NaCl} , t_2^{NaCl} , t_3^{NaCl} and t_4^{NaCl} .

3.4.2 Apparent electrical conductivity time-series

We consider three potential electrode pairs having different relative orientations with respect to the predominant direction of diffusive mass transport (i.e., the y -direction). The chosen pairs are located close to the cell's center with respect to the x -direction in order to have a minimal influence from the inlet and outlet chambers. The electrode pair P_3 - P_9 measures a voltage in a direction that is aligned with the y -direction, P_4 - P_5 in a direction aligned with the x -direction and P_4 - P_9 along a diagonal line that crosses the cell's center (see Fig. 3.1a for details concerning the electrode positions).

For the electrode pair P_3 - P_9 (Fig. 3.6a), only the time-series corresponding to the measurement mode M_y are plotted as the geometrical factor for measurement mode M_x is above 5000 m, which leads to highly unreliable apparent conductivities. Before the tracer injection period (highlighted by the gray-colored rectangle in Figs. 3.6a-c), the system is initialized and some electrical data is collected. For times $-1.8 \leq t^{\text{NaCl}} \leq -1.25$ the tracer injection has started but Solution 2 is still saturating the inlet chamber (i.e, no tracer invasion into the porous medium) and the measured apparent conductivity (blue scatter in Fig. 3.6a) is approximately constant and equal to $\sim 0.07 \text{ S m}^{-1}$. As the tracer invades the porous medium ($-1.25 \leq t^{\text{NaCl}} \leq 0$), the measured response shows a sharp increase by ~ 5.5 times the baseline apparent conductivity. After the injection is stopped, a smooth trend of increasing values are seen until $t_3^{\text{NaCl}} = 5 \times 10^{-2}$ when the apparent electrical conductivity is $\sim 25\%$ higher than the value at the end of the injection (at $t^{\text{NaCl}} = 0$). Subsequently, the apparent conductivities decrease slowly. The simulated apparent electrical conductivity time-series (magenta solid line) agrees well with the measured data although there is an overestimation of $\sim 7\%$ for $-1.25 \leq t^{\text{NaCl}} \leq 0$. Also, the simulated data start to increasingly underestimate the data for $t^{\text{NaCl}} > t_2^{\text{NaCl}}$ reaching a maximal discrepancy of $\sim 5\%$ by t_4^{NaCl} .

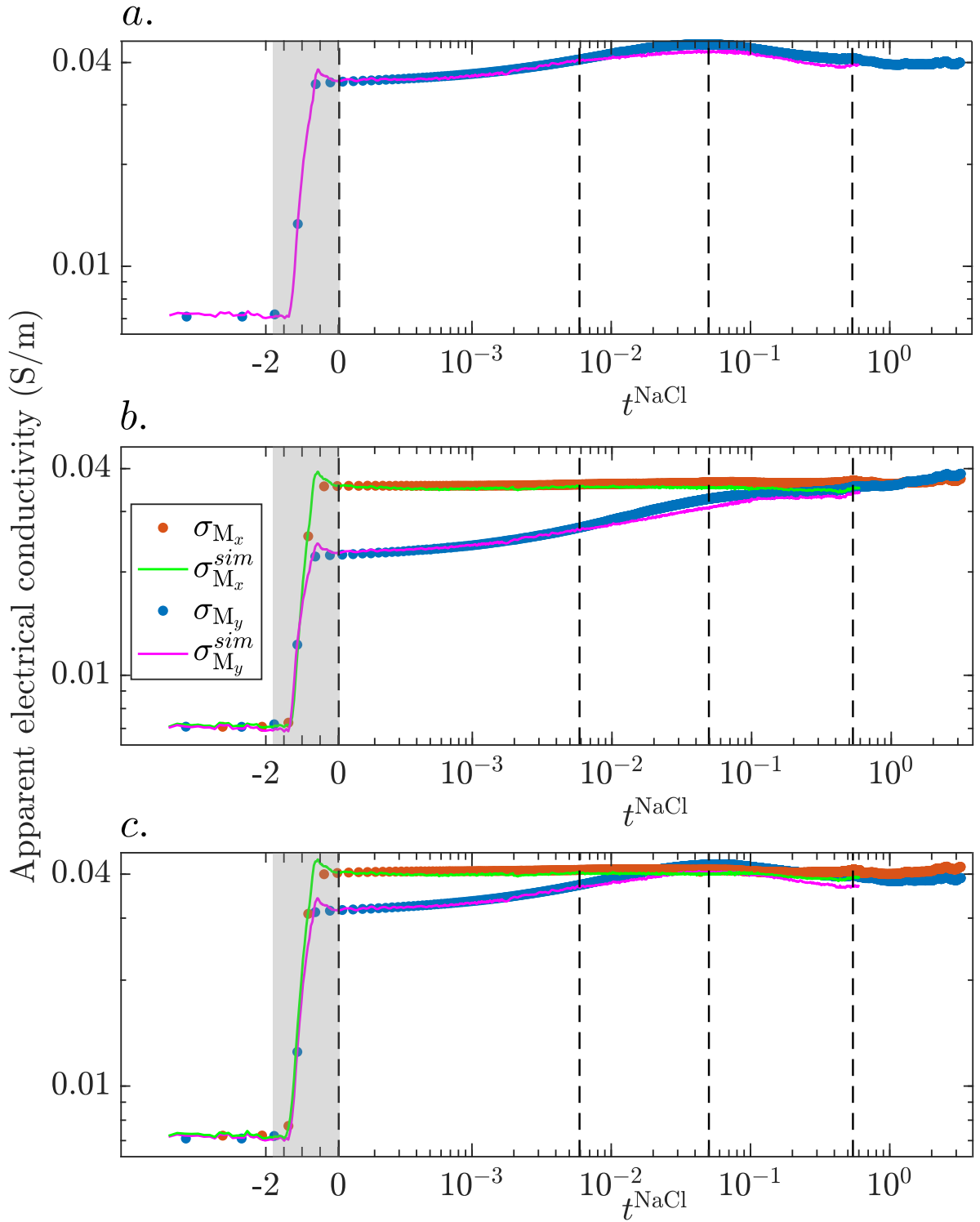


Figure 3.6 – Measured (dots) and simulated (lines) time-series of apparent electrical conductivity under measurement modes M_x (red and green) and M_y (blue and magenta) for electrode pairs (a) P_3 - P_9 , (b) P_4 - P_5 and (c) P_4 - P_9 . The four vertical black dashed lines mark the times $t_1^{\text{NaCl}} = 0$, $t_2^{\text{NaCl}} = 5 \times 10^{-3}$, $t_3^{\text{NaCl}} = 5 \times 10^{-2}$, and $t_4^{\text{NaCl}} = 5 \times 10^{-1}$, respectively. Negative and positive times represent, respectively, times normalized by advective and diffusion transport time-scales (Subsec. 3.3.3). The gray-colored rectangles highlight the tracer injection period extending over 60 s.

For electrode pair P_4 - P_5 (Fig. 3.6b), the measured apparent conductivity time-series for injection configuration M_y shows a different behavior compared to P_3 - P_9 . First, the tracer invasion leads only to an apparent conductivity increase of ~ 3 times the baseline value. Second, the positive growth rate spans the full duration of the experiment with a decreased rate from $t^{\text{NaCl}} > t_3^{\text{NaCl}}$. The simulated responses fit the data well, except for small over- and underestimations for times $-1.25 \leq t^{\text{NaCl}} \leq 0$ and $t^{\text{NaCl}} > t_2^{\text{NaCl}}$, respectively. Excepting the injection phase, the simulated response remains within 5.5% of the measured data. The measured apparent conductivity time-series for injection configuration M_x shows a larger increase when the tracer invades the porous medium (~ 5 times the baseline conductivity), and remains approximately constant during the rest of the experiment. The level of agreement of the simulated response with the measured data for M_x shows a similar behaviour of over- and underestimation for the aforementioned time-periods. Apart from the overestimation during tracer injection ($\sim 7\%$), the simulated responses remain within 4% of the measured data.

The voltage time-series measured between P_4 - P_9 for injection mode M_y (Fig. 3.6c) behaves overall rather similarly to that of electrode pair P_3 - P_9 (Fig. 3.6a). Around its maximum value, the apparent conductivity surpasses the one of M_x . For both injection modes, the simulated time-series show a very good agreement with the measurements, except for some over- and underestimation at early (i.e., $-1.25 \leq t^{\text{NaCl}} \leq 0$ during the tracer injection) and late (i.e., $t^{\text{NaCl}} > t_2^{\text{NaCl}}$) times, respectively. As for P_4 - P_5 , the apparent conductivity time-series for M_x show more sensitivity to the tracer invasion than M_y and remains rather flat afterwards.

3.5 Discussion

3.5.1 Proof of concept and technical challenges

We have performed an electrically- and optically-monitored milli-fluidic tracer test by injecting a solution of FS and NaCl in an artificial porous medium made of PDMS. Two key assumptions behind our approach are that: (i) the electrical conductivity time-series determined by the time-evolving NaCl concentration field can be modelled using the observed time-evolving FS concentration field by a suitable temporal and amplitude re-scaling; (ii) the PDMS material represents a porous medium that is quasi 2D, rigid and with negligible surface conductivity. In the following, we examine these two assumptions.

The simulated apparent conductivity time-series for electrode pair P_3 - P_9 and injection type M_y are plotted in Figure 3.7 with and without temporal rescaling (see section 3.3.3). This clearly highlights that simulated and observed data are best compared after accounting for the different diffusion coefficients of FS and NaCl salts.

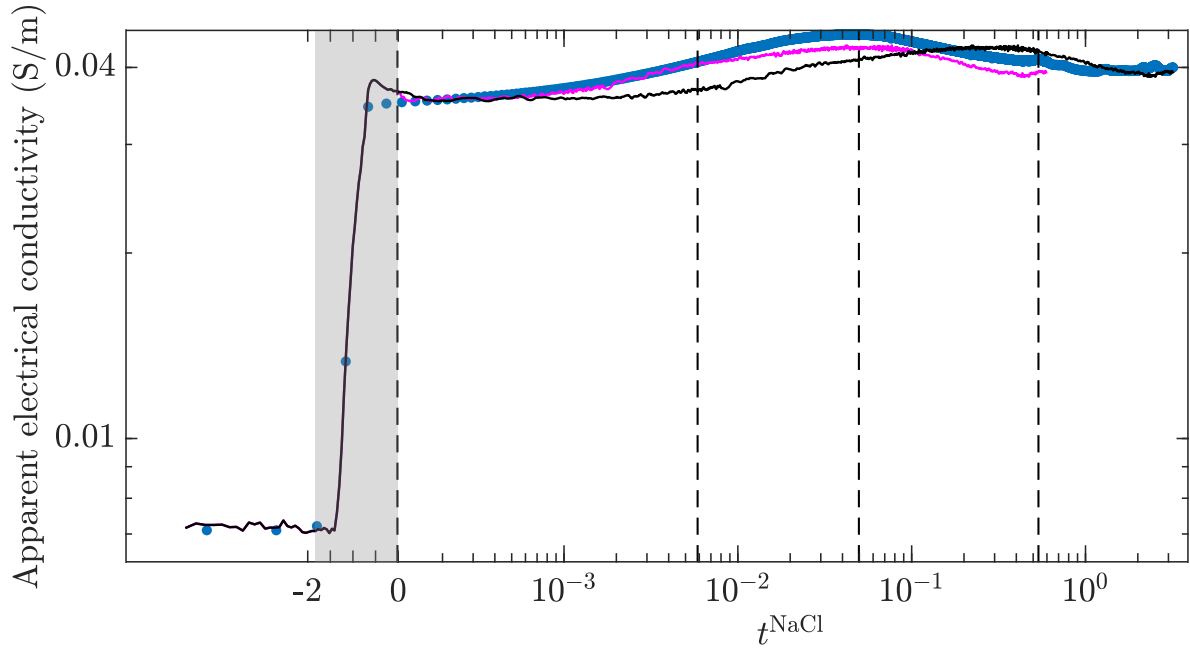


Figure 3.7 – Apparent electrical conductivity time-series for the electrode pair P_4 - P_9 and measurement mode M_y . Measured time-series (blue dots), simulated time-series with adequate time-scaling of FS concentration images to account for the different diffusion coefficients of FS and NaCl (magenta solid line) as described in section 3.3.3 and without any such time-scaling (black solid line).

The absence of advection after injection ($t^{\text{NaCl}} > 0$) implies that the diffusion coefficient D acts as a multiplicative constant in the governing transport equation (i.e., the diffusion equation). Thus, a ratio $D_{\text{NaCl}}/D_{\text{FS}} > 1$ can be compensated by a change of variables in the temporal coordinate such that the history of the unobserved NaCl concentration field is obtained from the time-compressed history of the observed FS concentration field. A previous study (Jougnot *et al.*, 2018) implicitly assumed that the diffusion coefficients of both salts are equal, but this is only defensible when working at high Péclet numbers. One workaround at intermediate Péclet numbers is to design experiments for which the non-dimensional advection-diffusion equations for the FS and NaCl salts have the same Péclet number. To this aim, the salts would need to be advected by flow fields having different mean flow velocities \bar{v} differing by the ratio $D_{\text{FS}}/D_{\text{NaCl}}$. That is, one experiment with FS and another with NaCl are carried out while ensuring the same \bar{v}/D ratio.

On the one hand, the measured apparent electrical conductivity time-series appear rather insensitive to the observed apparent mass loss in the inferred concentration fields (Fig. 3.5). This insensitivity is particularly apparent for measurement mode M_x , for which the observed responses are close to flat after stopping the injection (Fig. 3.6b,c). Given the approximately (x -parallel) layered distribution of tracer concentration, the bulk electrical conductivity is mainly sensitive to the arithmetic mean of the conductivities computed along y -oriented profiles and thus, mixing along y is expected to leave the time-series unmodified, provided that mass is conserved. On the other hand, the simulated data are impacted by the apparent

mass loss in the inferred concentration fields, leading to an increasing underestimation of the observed data with time $t^{\text{NaCl}} > t_2^{\text{NaCl}}$. This growing inconsistency in time between observed and simulated data may indicate a small, but non-negligible, degree of FS photobleaching (e.g., *Imamura and Koizumi*, 1955) leading to apparent FS mass loss. This occurred despite that we tried to decrease such effects using a flash lamp to diminish the exposure time of the tracer. The measured electrical data are mainly sensitive to the NaCl concentration and is, thus, basically insensitive to FS photobleaching.

Concerning the suitability of PDMS for this type of experiments, we highlight possible issues related to the tracer injection. At times $-1.25 \leq t^{\text{NaCl}} \leq 0$ we see that the simulated electrical responses overestimate the observed time-series of apparent electrical conductivity (Figs. 3.6a-c). We attribute this discrepancy to two possible PDMS-related sources of error. First, the slight flexibility of the acrylic plates used for sandwiching the PDMS (see 3.7.1) may have led to a slight inflation of the PDMS cell during injection, due to the applied pressure. In our calibration procedure and data processing, we assumed a rigid cell and thus a time-invariant cell thickness. For the considered range of FS concentrations, the light intensity is an exponentially increasing function of both the concentration but also the cell thickness (e.g., *de Anna et al.*, 2014), implying that such an inflation could be misinterpreted as a slight increase in the concentration. Note that the measured conductivities should also be impacted by this effect, as they increase linearly with the height of the porous medium sample. However, the power-law dependence of concentration on light intensity, makes the fluorimetry data much more susceptible. Another possible error source during the injection period is optical effects appearing when the fluorescent tracer is invading the cell from left to right. During this period, the tracer acts as a moving light source that generates rapidly-changing patterns of light diffractions within the translucent PDMS material. Such patterns are manifested as secondary sources of light that might perturb the concentration estimates. In our calibration procedure, we are unable to account for such effects as a homogeneous distribution of the fluorescent tracer is assumed. Lastly, we confirm that the PDMS material has negligible surface conductivity.

3.5.2 Impact of incomplete mixing and molecular diffusion on time-series of bulk electrical conductivity

Time-series of apparent electrical conductivity

The increased growth rate (or acceleration) of the measured conductivity time-series at $\sim t_2^{\text{NaCl}}$ (Figs. 3.6a-c) suggests that diffusion has started to enhance the tracer connectivity by transporting mass from the middle high permeability layer towards the top and bottom low permeability layers of the porous medium (see modelled NaCl concentration profile in Fig. 3.4b). The maxima present in all responses at $\sim t_3^{\text{NaCl}}$ (Figs. 3.6a-c) suggest that at this moment the amount of NaCl mass brought by diffusion towards the sides is large enough to create a well-connected vertical path for the electrical current. Note that the responses reach their maxima ~ 20 times before the characteristic diffusive transport time-scale $\tau_{\text{ch}}^{\text{NaCl}}$. This is simply a consequence of the presence of the impermeable boundaries located at $y = 0$ and $y = 74$ mm that increase the homogenization rate (see Fig. 3.4d). Indeed, since our initial tracer front is separated by a distance w_{ch} from a wall, a representative time-scale for such

confined situation is expected to be 10 to 50 times smaller than the used $\tau_{\text{ch}}^{\text{NaCl}}$ (e.g., *Hamada et al.*, 2020).

In the following, we use numerical simulations to gain insights on the impacts of incomplete mixing and small-scale diffusion on the time-series of apparent electrical conductivity under injection mode M_y , using electrode pair P_3 - P_9 as example. We examine different time-series resulting from monitoring solute plumes evolving from different initial widths and lengths until reaching complete mixing. Note that the considered initial conditions, inspired by the NaCl concentration field at t_1^{NaCl} in the experiment (see the inset in Fig. 3.8c for a representation of the initial NaCl concentration field) might represent a solute finger situated at the boundary of a field- or large-scale solute plume. Along that line, the bulk electrical conductivity of the sample can be associated to the upscaled value conductivity for that location impacting ERT data during a field-scale experiment. Then, our analysis may provide insight on the ability of ERT data to capture the mixing state and dynamics at the boundaries of field-scale solute plume bodies.

We simulate the electrical conductivity time-series following the procedure described in Subsection 3.3.1, but also the time-evolving NaCl concentration field (Subsec. 3.3.3), used as input for the conductivity field time-series in Equation 3.1. The modelling domain has unit porosity and the same dimensions as the experimental flow cell (see 3.2.1). Three different sets of initial conditions are considered, defined by the widths of the top and bottom layers, which are $w_1 = 6$ mm, $w_2 = 12$ mm and $w_3 = 18$ mm. Since the modelling domain has the same height as the experimental flow cell, the associated middle layer widths w_i^{middle} ($= 74 \text{ mm} - 2 \times w_i$) are $w_1^{\text{middle}} = 62$ mm, $w_2^{\text{middle}} = 50$ mm and $w_3^{\text{middle}} = 38$ mm. For each set we place rectangular and identical chambers to the left and right sides of the domain, which are saturated with tracer (as the middle layer) and background (as the top-bottom layers) fluid, respectively (as in the experiment). In turn, for each layer width w_i we vary the chambers' sizes such that the left chamber has six different distances to the electrode pair P_3 - P_9 . These distances are $d_1 = \infty$ (1-D or layered NaCl concentration field), $d_2 = 4 \times w_i$, $d_3 = 2 \times w_i$, $d_4 = 1 \times w_i$ and $d_6 = 0.5 \times w_i$. To sum up, we simulate eighteen electrically monitored tracer tests, grouped into three sets of initial conditions that are determined by the top-bottom and middle layer widths, which in turn comprise six different cases each, defined by the different chamber sizes. We run the transport simulations for 8 days (twice the time of the actual experiment) in order to ensure influence of the chambers for all the considered values of d_j . The tracer and background fluids are chosen to have electrical conductivities of $\sigma_{S_1} = 0.0218$ and $\sigma_{S_2} = 0.2728 \text{ S.m}^{-1}$, respectively (Subsec. 3.2.7). Lastly, note that in the actual experiment, we had $w = w_2$ ($\equiv w_{\text{ch}}$, Subsec. 3.3.3), $w^{\text{middle}} = w_2^{\text{middle}}$ and $d = 12 \times w_2$.

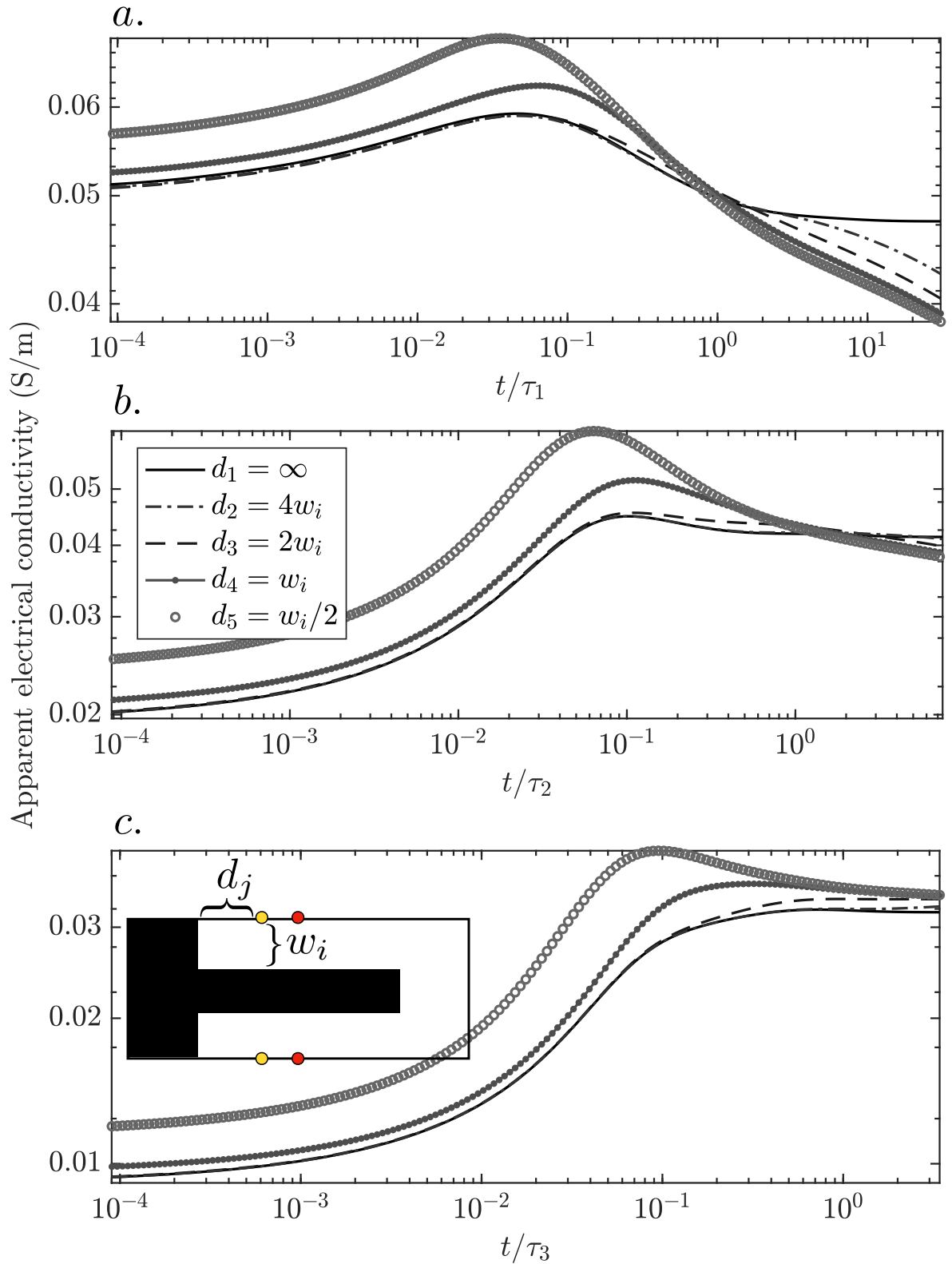


Figure 3.8 – Simulated apparent electrical conductivity time-series for electrode pair P_3 - P_9 under measurement mode M_y for a cell that has top-bottom and middle layer widths of (a) $w_1 = 6$ mm and $w_1^{\text{middle}} = 62$ mm, (b) $w_2 = 12$ mm and $w_2^{\text{middle}} = 50$ mm (as in the actual experiment) and (c) $w_3 = 18$ mm and $w_3^{\text{middle}} = 38$ mm. The time-series for each w_i are plotted as a function of normalized times t/τ_i , with $\tau_i = w_i^2/D_{\text{NaCl}}$ (defined analogously as $\tau_{\text{ch}}^{\text{NaCl}}$ in sec. 3.3.3). A sketch illustrating the geometry of one of the initial NaCl concentration fields is shown in (c) along with the injection (red dots) and potential (yellow dots) electrodes P_3 and P_9 .

For w_1 (Fig. 3.8a), the apparent electrical conductivity time-series shows higher values at intermediate times (unmixed tracer) compared to late times (mixed tracer) for all d_j . This may appear counter-intuitive when considering $d_1 = \infty$ as diffusion along y increases the total current flowing through the sample (Fig. 3.9a) by connecting the top and bottom injection electrodes. This "overshoot" in apparent conductivity occurs by virtue of the perturbation of the electrical potential field, generated by the presence of the (horizontal) conductive tracer front, which modifies the voltage $P_3 - P_9$. At an interface separating media of different conductivity, the tangential component of the electric field and the normal component of the current density field are continuous. These boundary conditions imply that the current density field lines, perpendicular to the equipotential lines, are refracted when the former cross the boundary between two bodies of different conductivity (e.g., *Feynman et al.*, 2011). Such lines bend away from (towards to) the concentration gradient direction when they enter (exit) a more conductive body. In our setting, this is manifested in the electrical potential field as an overall compression of its equipotential lines (Fig. 3.9c). In particular, the compression of such lines along the x -direction leads to a decrease in the measured voltage (Fig. 3.9b), that translates into an increase in apparent electrical conductivity.

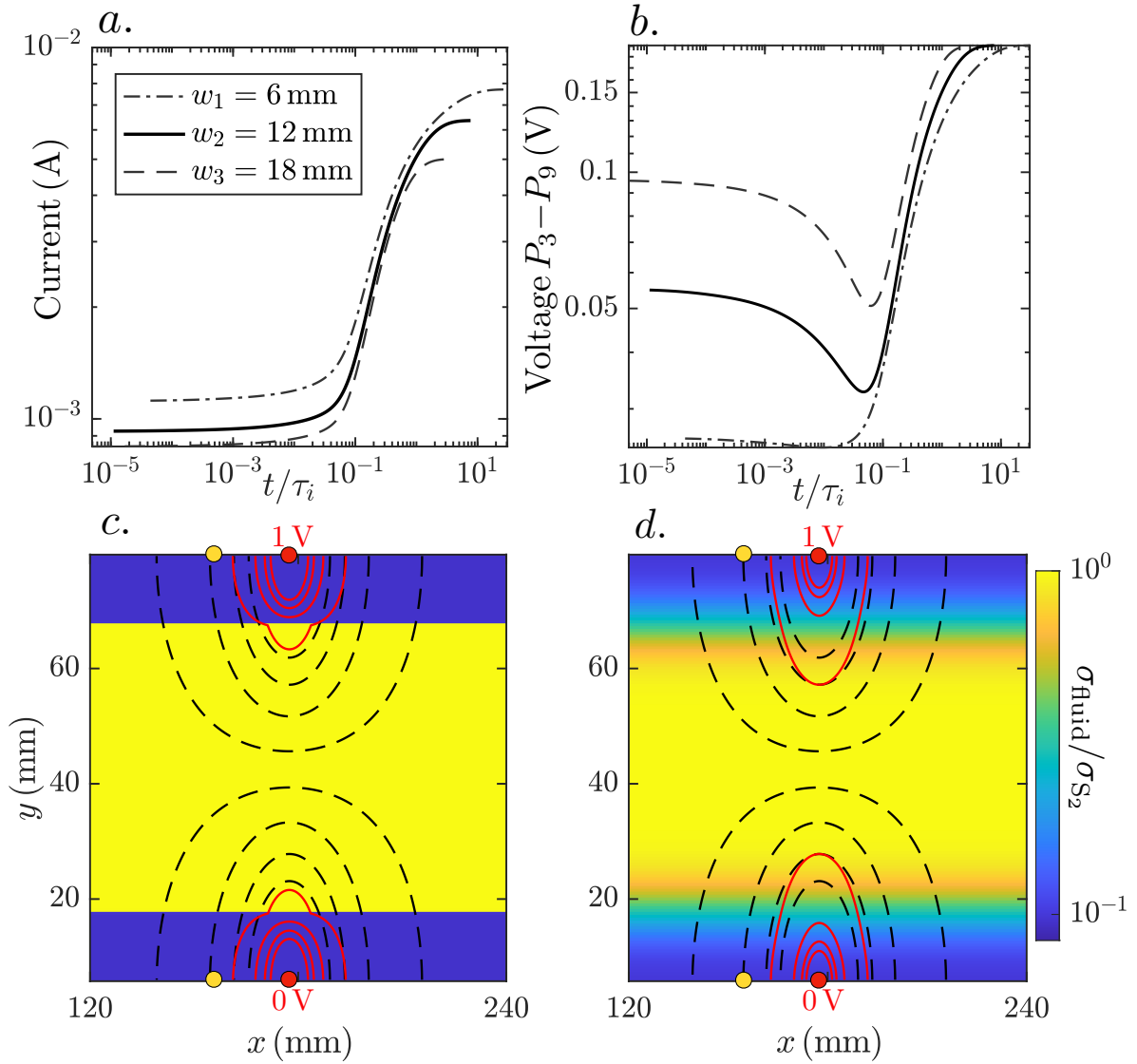


Figure 3.9 – Simulated time-series of (a) total current flowing through the domain and (b) voltage measured between P_3 - P_9 , for chambers located at $d_1 = \infty$ (see the main text) and the three considered initial top and bottom widths of $w_1 = 6$ mm, $w_2 = 12$ mm and $w_3 = 18$ mm. The response associated to w_i ($i = 1, 2, 3$) is plotted as a function of the corresponding normalized t/τ_i (see Fig. 3.8). (c)-(d) Simulated fluid conductivity (tracer concentration) field, normalized by σ_{S_2} , for $w_2 = 12$ mm and $d_1 = \infty$ at (c) $t/\tau_2 = 0$ and (d) $t/\tau_2 = 0.1$. On top of each fluid conductivity field, nine equipotential lines of the electrical potential field for the levels $0.4 + 0.025 \times pV$ ($p = 0, \dots, 8$) are shown for the corresponding conductivity field (red solid lines) and for the case of a homogeneous conductivity field (black dashed lines). The injection electrodes are indicated (red dots) as well as the potential electrodes P_3 and P_9 (yellow dots).

For $d_j \geq w_1$ ($j = 1, \dots, 4$), the time-series are maximized at $t/\tau_1 \sim 0.1$. As described above, the tracer arrival by diffusion leads to further compression of the equipotential lines along x (compare equipotential lines of Figs. 3.9c-d), which leads to a minimum of the voltage time-

series (Fig. 3.9b), that in turn is manifested as a maximum in the conductivity time-series. The situation is different for $d_5 (< w_1)$, for which the left chamber is closer to P_3 - P_9 than the initial tracer front. Consequently, the time-series is maximized due to the (earlier) arrival of the tracer from the chamber.

For w_2 , the starting values of the apparent conductivities are smaller than the final ones. Correspondingly, the voltage measurement from P_3 - P_9 starts at a larger value when compared to the case for w_1 . Additionally, note that for $t/\tau_2 \sim 3.7$, which corresponds to 4 days, that is, the duration of the actual experiment, the apparent electrical conductivity time-series for d_2 show only a negligible difference compared to the data for the 1-D case. Considering that for the PDMS cell, the chambers are located much farther apart than d_2 , this indicates that for the experiment, the impact of diffusion from the chambers is negligible.

For w_3 , the starting values of the apparent conductivities are again smaller than the final ones, although the difference is more marked than for w_2 . Also, note the absence of a clear maximum occurring around t/τ_3 . For larger w_i , the tracer arrives more mixed to the electrodes at $t/\tau_i \sim 0.1$. Consequently, the associated perturbation of the electrical potential is less marked, hence, the less pronounced signature.

The simultaneous dependence of the time-series of apparent electrical conductivity on both the current and the voltage time-series (as illustrated by the supporting Fig. 3.9) make such data difficult to interpret (e.g., Jung *et al.*, 2009). However, it also makes such time-lapse data potentially more informative on the temporal evolution of the spatial organization of the tracer. An example is their sensitivity to the tracer arrival at the diffusion transport time-scale for a confined sample. Also, the ratio of the initial to terminal values of apparent conductivity is sensitive to the distance of the tracer front to the injection electrodes. In order to effectively exploit this information, it is necessary to develop a framework that quantitatively link solute transport-driven conductivity variations with perturbations of the electrical potential field. This will be the topic of future research.

Time-series of the equivalent electrical conductivity tensor

We examine now the impact of the mixing of an initially layered concentration distribution on the time-series of the equivalent electrical conductivity tensor $\underline{\underline{\sigma}}$. We simulate the latter using as input fluid conductivity fields derived from the fluorimetry-inferred NaCl concentration fields (as for Section 3.4). However, we take a subregion of the images, from which four snapshots are shown in Figure 3.10, in order to work with conductivity fields which are the closest possible to layered.

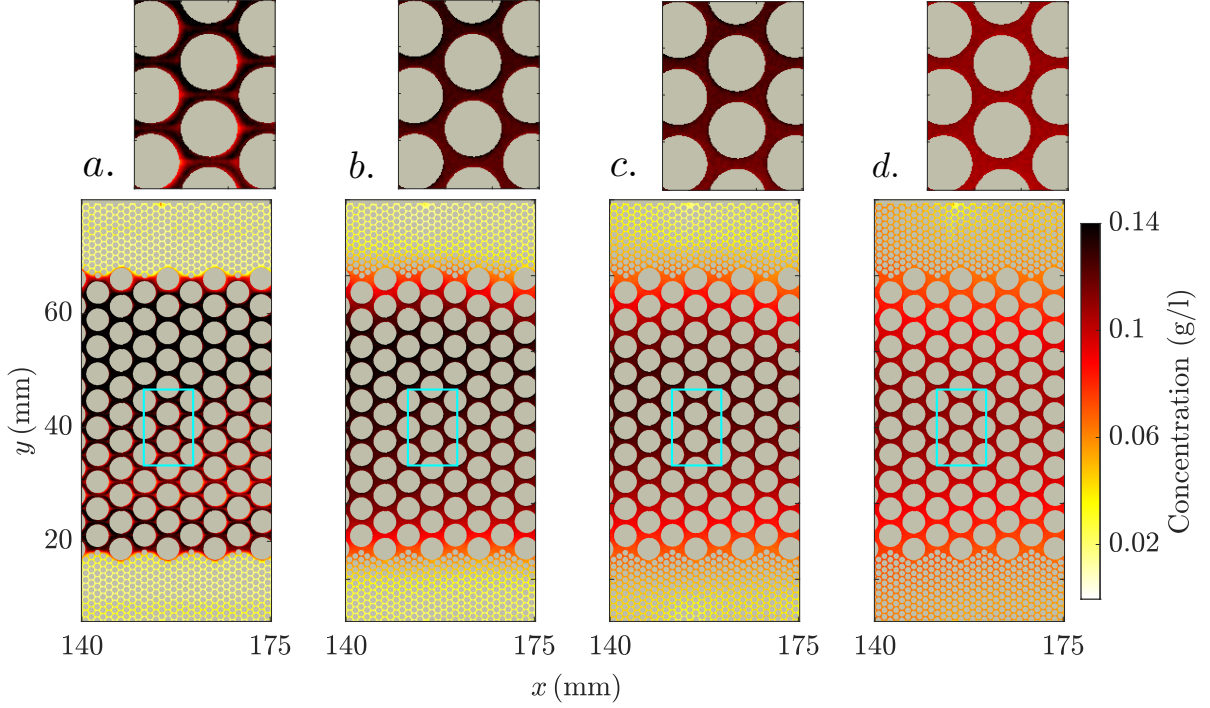


Figure 3.10 – Four snapshots of the image-inferred NaCl concentration field contained in the sub-region defined by the horizontal coordinate range $x \in [140, 175]$ mm at the times (a) $t_1^{\text{NaCl}} = 0$, (b) $t_2^{\text{NaCl}} = 5 \times 10^{-3}$, (c) $t_3^{\text{NaCl}} = 5 \times 10^{-2}$ and (d) $t_4^{\text{NaCl}} = 5 \times 10^{-1}$. The close views shown on top of the full concentration maps correspond to the areas enclosed by the cyan-colored rectangles in the corresponding full maps.

We compute numerically the electrical potential as described in Subsection 3.3.1. However, we now excite the sample using line electrodes along the left and right (top and bottom) boundaries of the cell, respectively, for computing the x - and y components of $\underline{\underline{\sigma}}$, denoted by σ_x and σ_y . As usual, for each excitation mode, a no-flux condition is imposed to the electrical potential along the other boundaries. Due to the x -oriented layering, the spatial coordinate system given by (x, y) is oriented along the principal directions of $\underline{\underline{\sigma}}$, implying that σ_x and σ_y are its only non-zero entries. For reference, we also compute the time-series of the Wiener bounds of the domain, that is, the harmonic σ_H and arithmetic σ_A means of the conductivity fields, divided by the (spatially constant) formation factor F ($:= F_{\text{sim}}$, Subsec. 3.3.2):

$$\sigma_H = \frac{1}{F} \frac{N}{\sum_{n=1}^N \frac{1}{\sigma_{\text{fluid}}^i}}, \quad (3.6)$$

and

$$\sigma_A = \frac{1}{F} \frac{1}{N} \sum_{n=1}^N \sigma_{\text{fluid}}^i, \quad (3.7)$$

where N and σ_{fluid}^i denote, respectively, the number of pixels and the value of the fluid conductivity for pixel i . The computed time-series are shown in Figure 3.11.

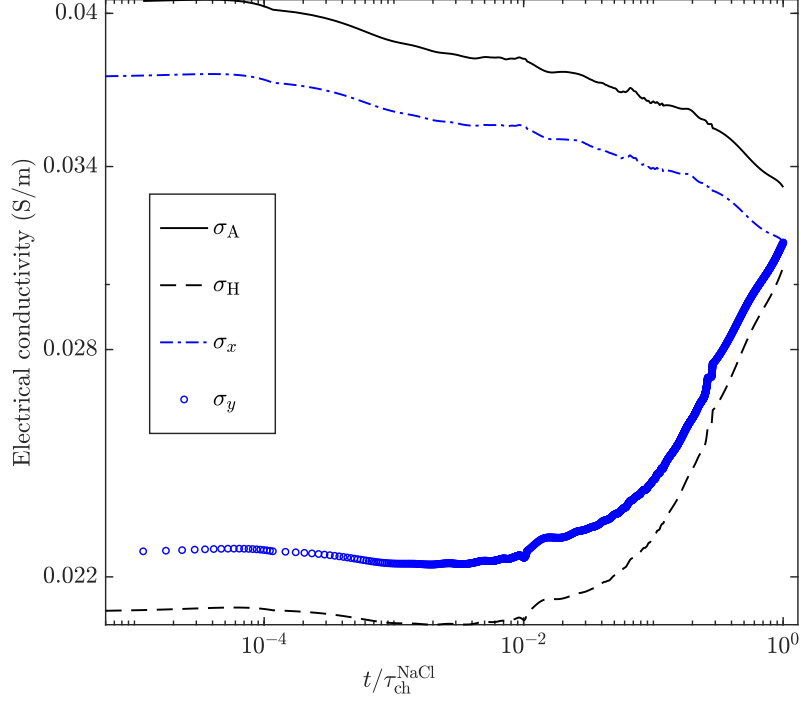


Figure 3.11 – Simulated time-series of the x and y components of the equivalent electrical conductivity tensor, σ_x and σ_y , and computed time-series of the arithmetic and harmonic means σ_A and σ_H over the considered sub-region (Fig. 3.10) of the time-evolving NaCl concentration field.

The x -oriented layered tracer distribution results in qualitative behaviours of σ_x and σ_y that are very close to those of σ_A and σ_H , respectively. The discrepancies between σ_x and σ_A , and between σ_y and σ_H indicate that the tracer distribution within the sub-sector is not perfectly layered (i.e., 1-D), as discussed previously. Note again the decay over time of σ_A (and σ_x), indicative of apparent tracer mass loss within the considered sub-region (see Fig. 3.5 and Subsec. 3.5.1). By the end of the experiment, σ_x and σ_y collapse at $\sim 0.03 \text{ S.m}^{-1}$ before the tracer has completely mixed (evidenced by the remaining separation between σ_A and σ_H at late times). At this point, the steep slopes of the conductivity time-series suggest that σ_y would surpass σ_x if longer times would have been considered. This is a consequence of the x -oriented gradient (see Fig. 3.5). Again, this is possible since the concentration distribution is not perfectly layered.

The time-evolution of the mean tracer concentration within the sample could be estimated from Archie's law (Eq. 3.2), by inputting either σ_x or σ_y as the formation conductivity. However, when using such approach, apparent loss of mass is to be expected as soon as the tracer is not completely mixed within the sampled volume (Jougnot et al., 2018; Visentini et al., 2020). Note that we refer here to a common problem arising during hydrogeophysical experiments, and not to the previously mentioned (optical) apparent tracer mass loss (occurring likely due to FS photobleaching, as discussed in Subsection 3.5.1). When compared against σ_A (i.e., the mean fluid electrical conductivity that is directly related to the mean tracer concentration), they yield solute mass recoveries of 92 and 60% at early times. It is clear that the more aligned

the layering and conductivity measurement directions are, the better. These considerations may become relevant for anisotropic ERT experiments for which spatial distributions of both σ_x and σ_y are recovered, instead of just distributions of bulk (scalar) electrical conductivity values (e.g., *Herwanger et al.*, 2004).

The time-series for σ_y shows an overall increase over time and no maximum at $t/\tau_{\text{ch}}^{\text{NaCl}} \sim 0.1$ as described in Subsection 3.5.2. With line electrodes in a layered 2-D media, the potential lines are straight. Consequently, sensitivity to the temporal evolution of electrical potential perturbations is less evident, although it may still be captured by differentiating the time-series with respect to time (see *Visentini et al.* (2020)).

Finally, we explore the relationship between the time-series of σ_y and the temporal evolution of two common descriptors characterizing the degree of mixing: the concentration variance σ_c^2 and the scalar dissipation rate χ (e.g., *Le Borgne et al.*, 2010). The latter is defined as

$$\chi = \int d\mathbf{x} \nabla c^T D \nabla c. \quad (3.8)$$

In Figures 3.12a-b, scatter plots of σ_y versus $\sigma_c^2(t)$ and $\chi(t)/D$ demonstrate strong negative correlations. We attribute the higher variability in Figure 3.12b to noise in the image-recovered concentration gradient field rather than to variability in the relationship itself. Establishing quantitative links between statistical descriptors of the mixing state of the solute such as the concentration variance and the scalar dissipation rate with the time-evolution of the electrical conductivity is the topic of ongoing research.

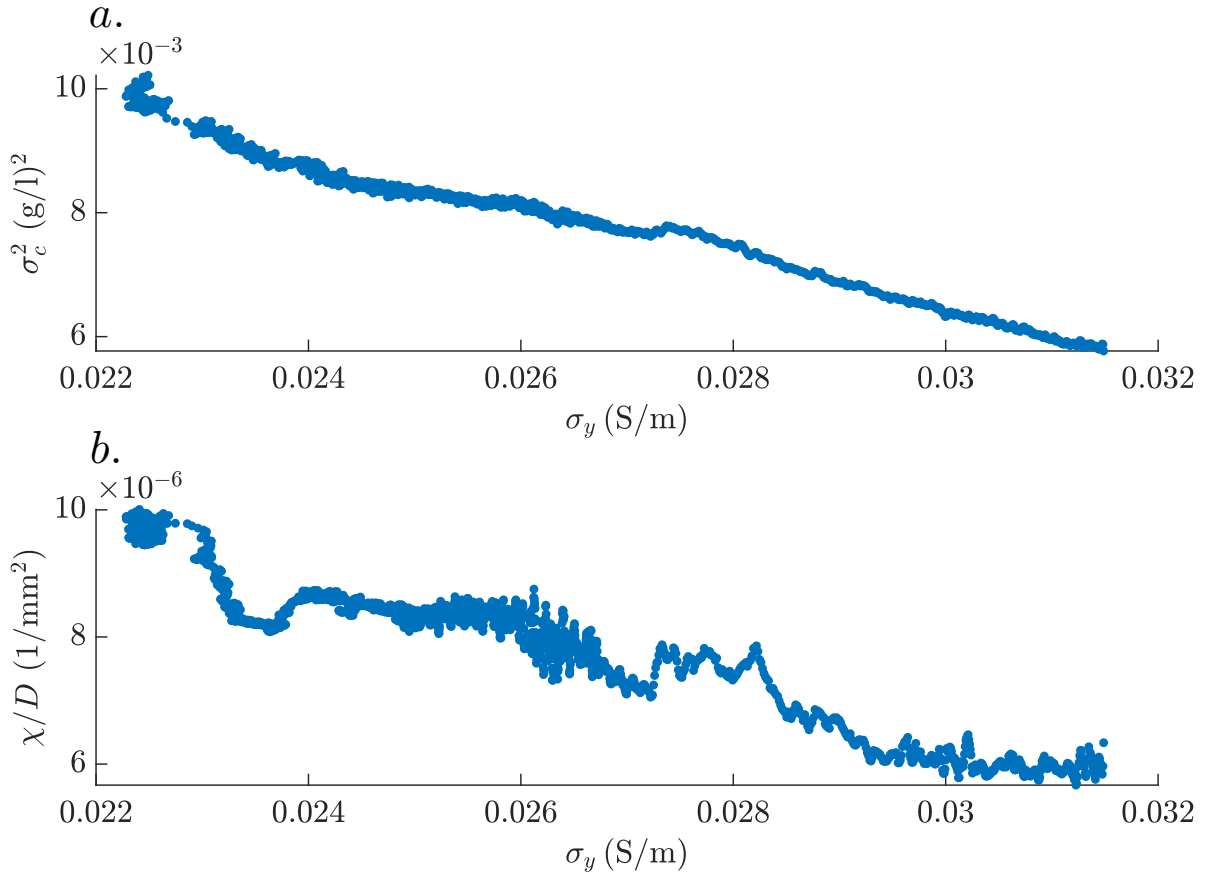


Figure 3.12 – Scatter plots of the y -component of the equivalent electrical conductivity tensor, σ_y , plotted against (a) the concentration variance $\sigma_c^2(t)$ and (b) the scalar dissipation rate divided by the diffusion coefficient, $\chi(t)/D$.

3.6 Conclusions

We have performed an optically- and electrically-monitored milli-fluidic tracer test to study the electrical signatures of diffusion-limited mixing of an initially-layered tracer distribution. We have confirmed that fluorimetry- and geoelectrically-inferred time-series of apparent electrical conductivity can, in a diffusion-dominated environment, be related by a temporal re-scaling that accounts for the ratio of ~ 3.8 between the FS (optical) and NaCl (electrical) tracer diffusion coefficients. After this correction, we find that the observed and simulated apparent electrical conductivities are in strong agreement and demonstrate high sensitivity to the initial tracer invasion and subsequent diffusion. Particularly, the apparent electrical conductivity time-series measured perpendicularly to the concentration gradient are consistently maximized at times that are in agreement with the NaCl diffusion transport time-scale associated with the layer width in confined media. Numerical simulations confirm this and indicate high sensitivity of the electrical data to the layers' degree of mixing and their distance to the injection electrodes. The time-evolving equivalent electrical conductivity in the direction of layering is strongly anti-correlated to two common solute mixing descriptors:

the concentration variance and the scalar dissipation rate. In summary, our study provides a proof of concept for a novel experimental approach while pointing towards interesting avenues for establishing quantitative links between the mixing dynamics of the solute and time-series of electrical responses.

Data availability and material

The data collected during the experiment presented is publicly available in Zenodo .

3.7 Appendices

3.7.1 Appendix 3A: Porous system fabrication

The porous network is mechanically-drilled into a stainless steel rectangular plate with 0.4 mm depth. A PDMS solution and curing agent (9:1 ratio) are then poured into the mold and left to cure at room temperature during ~ 48 hours. Subsequently, the solid PDMS is detached from the mold and placed between two 2 cm-thick transparent acrylic plates and the sandwich is tightened using mechanical clumps. Prior to assembling, the acrylic plate that is placed in contact with the positive reliefs of the cell is covered with a thin film of the same PDMS solution and both the reliefs and the film are radiated with plasma (e.g., *Xiong et al.*, 2014) in order to ensure a high degree of cohesion of the cell.

3.7.2 Appendix 3B: Geoelectrical monitoring system

The geoelectrical monitoring system consists of two injection circuits and one measurement circuit, all operated using the Campbell Micrologger CR3000. The system is electrically connected to the flow cell using stainless steel cylindrical electrodes of diameter 1 mm that are pinched into the PDMS along the cell's contour (Fig. 3.1) through holes in the top acrylic plate.

The injection circuits, connected to the cell using the sets of injection electrodes A_x-B_x or A_y-B_y , are full resistive bridges comprising (i) a voltage source of amplitude 1 V, connected in series with (ii) a bridge resistor of resistance $26700\Omega \pm 1\%$, (iii) the flow cell, which is the time-varying resistance of interest and (iv) another bridge resistor identical to the first one. These circuits are alternatively activated using a voltage switch relay, controlled by a logic port of the CR3000, to apply a voltage square wave of period 12 s formed by 4 cycles of 3 s each with the following sequence: 1 V, 0 V, -1 V and 1 V. This injection protocol alternating the polarity of the signal, standard for geoelectrical monitoring applications, is used to prevent cumulative electrode polarization and correct for possible electrode drift.

The measurement circuit consists of 13 high impedance differential voltage measurement channels that collect data for each injection mode. The voltage measurements are performed using the CR3000 "VoltDiff" instruction with (i) signal integration over 3 ms, in order to remove 60 Hz noise, and (ii) polarity reversal, in order to remove any voltage offset coming

from the datalogger circuitry. The CR3000 needs ~ 0.65 s to perform the 13 measurements. The recorded voltages are obtained by averaging the measured voltage during the positive and negative excitation cycles mentioned above. The individual measurements for each cycle are taken 2.3 s after initiating each current injection to allow the recorded signal to stabilize.

3.7.3 Appendix 3C: Grain mask compilation

We binarize a light intensity image that displays a high intensity contrast between the pore space and the solid phase; it is obtained by saturating the medium with Solution 2. We use a spatially-variable binarization threshold value obtained from Otsu's thresholding algorithm (*Otsu*, 1979) within subwindows of 20×20 pixels. A local thresholding is preferred due to the spatially-varying light intensities. The binarization distorts the shape of the originally circular grains somewhat. To avoid this, the binary image is used to locate the centroids of all the (distorted) grains. They are then replaced by circular disks of required size. In this way, known internal distances within the lattice are preserved.

Chapter 4

Generalization of Archie's relationship to heterogeneous and anisotropic salinity fields

Alejandro Fernandez Visentini, Niklas Linde.

In preparation for submission to *a peer-reviewed journal*.

Abstract

We expand Archie’s relationship by introducing a new petrophysical parameter, the mixing factor M , which accounts for the impact of small-scale saline heterogeneity on the equivalent electrical conductivity tensor. We investigate to what extent the M -tensor can constrain the variance, anisotropy factor and connectivity of 2-D multivariate-lognormal electrical conductivity fields. By observing the two components of the tensor one can univocally determine the variance and anisotropy ratio of the field, provided that the mean value and the connectivity of the latter is known. By invoking scale separation between pore-scale and saline heterogeneity and energy conservation arguments, we arrive at an identity that expresses the components of M in terms of the expected value of the product of the conductivity field fluctuations and the secondary electric field arising in response to this heterogeneity. This narrows the problem of predicting M to gaining knowledge of the latter relationship. We further find that the secondary electric fields are log-normally distributed for all the considered cases of heterogeneity and connectivity. By calibrating numerical relationships between the parameters describing the probability density function of the conductivity and secondary electric fields, one could potentially build an upscaling approach that requires as input only the parameters describing the statistics of the conductivity field.

4.1 Introduction

The direct-current (DC) geophysical method is regularly used to retrieve the spatial distribution of the electrical resistivity. DC data are typically acquired using combinations of electrode pairs: one to drive a known electrical current between two positions and another to measure the voltage between two other positions (e.g., *Keller and Frischknecht, 1966; Binley and Slater, 2020*). The resistance (measured voltage over injected current) is then multiplied by a geometrical factor to remove the influence of the measurement geometry, yielding an apparent electrical resistivity. In this study, we consider such measurements using sheet electrodes (line electrodes) over a 3-D (2-D) sample. In this specific measurement configuration, the resulting apparent conductivity (inverse of apparent resistivity) is then the equivalent electrical conductivity of the sample (e.g. *Sanchez-Vila et al., 2006*). In actual field settings, multiple current and electrode pairs are used to obtain many hundreds or thousands of apparent resistivities that are subsequently used to derive electrical resistivity images at a given spatial resolution. This process is often referred to as Electrical Resistivity Tomography (ERT) or time-lapse ERT, when repeating the measurement sequence to study dynamic phenomena.

The equivalent electrical conductivity σ_{eq} of composite media at a given scale depends in general on both low- and high-order spatial statistics as well as the connectivity of the conductive phases at smaller scales; these features are often collectively referred to as the microstructural properties of the composite medium (e.g., *Torquato and Haslach Jr, 2002; Milton and Sawicki, 2003*). In particular, for a fluid-saturated porous medium having an isolating matrix material, σ_{eq} is in general impacted by the microstructure of both the pore space and $\sigma_w(\mathbf{x})$, the heterogeneous fluid electrical conductivity field residing within the

pores. When $\sigma_w(\mathbf{x})$ is constant in the pore space, then σ_{eq} is solely influenced by the pore space fraction and geometry, as expressed by empirical Archie's law (Archie, 1942).

When considering a saline tracer test in a porous medium, $\sigma_w(\mathbf{x})$ originates from a heterogeneous and time-evolving saline concentration field $c(\mathbf{x})$, whereby $\sigma_w(\mathbf{x})$ and $c(\mathbf{x})$ are related by a monotonically-increasing relationship (e.g., Sen and Goode, 1992). Since this implies that the time-series of σ_{eq} carry information about the time-evolution of $c(\mathbf{x})$, time-lapse ERT has been routinely applied to constrain the transport of saline bodies (e.g., Binley et al., 2015). For example, time-lapse ERT has proven effective to constrain the evolving position and approximate shape of saline plumes (e.g., Slater et al., 2000), and it has also shown success to constrain advective-dispersive (e.g., Kemna et al., 2002; Vanderborght et al., 2005; Koestel et al., 2008), as well as dual-domain transport parameters (e.g., Singha et al., 2007; Day-Lewis and Singha, 2008). Archie's law (Archie, 1942) remains the basis for the conversion of σ_{eq} data or inverted electrical images into salinity (e.g., Revil et al., 2018). When relying on Archie's law it is tacitly assumed that $\sigma_w(\mathbf{x})$ is homogeneous below the scale at which the petrophysical relationship is applied. Such homogeneity of $\sigma_w(\mathbf{x})$ (i.e., fully-mixed salinity field $c(\mathbf{x})$) is unlikely during a tracer test, and operating under such an assumption contributes to a poor recovery of spatial and temporal moments of tracer plumes estimated from electrical monitoring (e.g., (Singha and Gorelick, 2005; Müller et al., 2010; Doetsch et al., 2012a; Laloy et al., 2012)). Furthermore, this assumption implies that any potentially valuable information contained in σ_{eq} pertaining to the microstructure of $c(\mathbf{x})$ is lost. Indeed, these type of aggregation errors occurring when treating environmental systems as homogeneous below a given scale of observation are ubiquitous and seldom treated (e.g., Kirchner, 2016; Shakas and Linde, 2017).

In the present contribution, we propose a new interpretation framework to assess the impact of heterogeneous $\sigma_w(\mathbf{x})$ on σ_{eq} . We introduce a new petrophysical parameter, the mixing factor M , which quantifies the departure of σ_{eq} from its (maximum) value occurring given when $\sigma_w(\mathbf{x})$ is homogeneous. In doing so, we seek to remove interpretation bias associated with aggregation and also explore the constraining power of σ_{eq} pertaining to microstructural and connectivity properties of $\sigma_w(\mathbf{x})$. We investigate how the M -tensor can constrain the variance, anisotropy factor and connectivity type of 2-D multivariate-lognormal electrical conductivity fields. We consider different connectivities using the transformation by Zinn and Harvey (2003). We observe unique mapping between from the two components of the M -tensor to the variance and anisotropy ratio of the conductivity field. When considering different connectivities, we observe that the mapping is modified in ways that depend on the geostatistical properties of the underlying field. Further, by decomposing the electric field into its primary and secondary parts and assuming that the fluctuations of $\sigma_w(\mathbf{x})$ around its mean occur at scales that are large compared to the Representative Elementary Volume (REV) (Hill, 1963) of F , we can relate the M -components with the expected value of the product of the conductivity field fluctuations and the secondary electric field, in the measurement direction. This identity highlights the non-linearity of the DC conductivity averaging, that is, the dependence of M on the heterogeneity of $\sigma_w(\mathbf{x})$, contrary to Archie's linear dependence on a constant fluid conductivity. It provides also a framework that reduces the problem of predicting M to the problem of how to gain knowledge of the joint probability density field of the conductivity field fluctuations and the secondary electrical field. We explore the statistical distributions of the secondary electric fields and find that they are log-normally distributed

for all considered field variances, anisotropy ratios and connectivities. This research is work in progress and has as its ultimate goals to build an upscaling approach that requires only the parameters of the probability density function of the electrical conductivity field to predict M .

In Section 4.2 we review the governing equations of DC electrical conduction, the energy representation of σ_{eq} that leads to the formal definition of the formation factor F and the origin of secondary electric fields. In Section 4.3 we introduce the mixing factor M and derive an expression for it. The main results of the numerical tests are presented and discussed in Section 4.4. Section 4.5 concludes the paper and highlights the next steps for this research.

4.2 Theoretical background

4.2.1 Groundwater flow and solute transport

For steady-state flow and in the absence of sources or sinks, the continuity equation for the specific discharge $\mathbf{q}(\mathbf{x})$ at the Darcy scale reads:

$$0 = \nabla \cdot \mathbf{q}(\mathbf{x}). \quad (4.1)$$

Adopting Darcy's law,

$$\mathbf{q}(\mathbf{x}) = -K(\mathbf{x})\nabla h(\mathbf{x}), \quad (4.2)$$

$\mathbf{q}(\mathbf{x})$ is related with the hydraulic conductivity $K(\mathbf{x})$ and the hydraulic head $h(\mathbf{x})$. Then, the groundwater flow equation reads:

$$\nabla K(\mathbf{x})\nabla h(\mathbf{x}) + K(\mathbf{x})\nabla^2 h(\mathbf{x}) = 0. \quad (4.3)$$

Equation 4.3 is solved numerically using the open-source finite-difference solver MODFLOW-2005 (*Harbaugh, 2005*).

We model solute transport within an Eulerian framework using the Advection-Dispersion Equation (ADE):

$$\phi \frac{\partial c(\mathbf{x}, t)}{\partial t} + \mathbf{q}(\mathbf{x}) \cdot \nabla c(\mathbf{x}, t) - \nabla [\mathbf{D}(\mathbf{x}) \cdot \nabla c(\mathbf{x}, t)] = 0. \quad (4.4)$$

Equation 4.4 is solved numerically using the groundwater solute transport simulator package MT3D-USGS (*Bedekar et al., 2016*), assuming constant dispersivity over \mathbf{x} .

4.2.2 Spreading and mixing of $c(\mathbf{x}, t)$

The location $\alpha(t)$ of the centre of mass of a solute plume observed over some volume V is given by the first spatial moment of $c(\mathbf{x}, t)$:

$$\alpha(t) = \int_V c(\mathbf{x}, t) \mathbf{x} d\mathbf{x}, \quad (4.5)$$

assuming that $c(\mathbf{x}, t)$ is normalized (i.e., it satisfies $\int_V c(\mathbf{x}, t) d\mathbf{x} = 1$). The spread of a solute plume around its centre of mass is given by the second spatial moment of $c(\mathbf{x}, t)$ centred at $\alpha(t)$:

$$\Delta_{ij}(t) = \int_V c(\mathbf{x}, t) (\mathbf{x} - \alpha_i(t)) (\mathbf{x} - \alpha_j(t)) d\mathbf{x}. \quad (4.6)$$

The scalar dissipation rate $\chi(t)$ (e.g., *Pope, 2001*),

$$\chi(t) = \nabla c'(\mathbf{x}, t) \cdot \mathbf{D} \nabla c'(\mathbf{x}, t) d\mathbf{x}, \quad (4.7)$$

quantifies the net mass transfer resulting from the presence of concentration gradients and local-scale diffusion.

4.2.3 DC electrical conduction

For steady-state DC conduction, and in the absence of current sources or sinks, the principle of electric charge conservation is expressed by the continuity equation for the current density field $\mathbf{J}(\mathbf{x})$ at the pore scale as follows:

$$\nabla \cdot \mathbf{J}(\mathbf{x}) = 0. \quad (4.8)$$

Ohm's law relates $\mathbf{J}(\mathbf{x})$ with the electrical conductivity $\sigma(\mathbf{x})$ and the electric field $\mathbf{E}(\mathbf{x})$ via the linear relationship $\mathbf{J}(\mathbf{x}) = \sigma(\mathbf{x})\mathbf{E}(\mathbf{x})$. Adopting the quasistatic approximation, $\nabla \times \mathbf{E}(\mathbf{x}) = 0$, allows to express $\mathbf{E}(\mathbf{x}) = -\nabla U(\mathbf{x})$, where $U(\mathbf{x})$ is the electrical potential. Writing $\mathbf{J}(\mathbf{x})$ in terms of $U(\mathbf{x})$ as $\mathbf{J}(\mathbf{x}) = -\sigma(\mathbf{x})\nabla U(\mathbf{x})$ and replacing this expression into Eq. 4.8 results in the governing Laplace equation for the electrical potentials:

$$\nabla \sigma(\mathbf{x}) \nabla U(\mathbf{x}) + \sigma(\mathbf{x}) \nabla^2 U(\mathbf{x}) = 0. \quad (4.9)$$

Once the electrical conductivity field (ECF) $\sigma(\mathbf{x})$ and boundary conditions for $U(\mathbf{x})$ are given, Eq. 4.9 can be solved for the latter.

The equivalent (or block-averaged) electrical conductivity (EEC) $\overline{\overline{\sigma}}_{\text{eq}}$ of the considered domain at a given scale can be defined through an averaged Ohm's law over its volume V (e.g., (Sanchez-Vila et al., 2006)):

$$\overline{\mathbf{J}} = -\overline{\overline{\sigma}}_{\text{eq}} \int_V \nabla U(\mathbf{x}) dV. \quad (4.10)$$

For media that behaves anisotropically at the scale of V , $\overline{\overline{\sigma}}_{\text{eq}}$ is in general a 3×3 second-rank tensor. If the conductivity measurement direction is coincident with the principal directions of the medium, then the tensor becomes diagonal. We will assume that we are in such a setting and continue the exposition of the theory focusing on some component of $\overline{\overline{\sigma}}_{\text{eq}}$, denoted σ_{eq} for short.

4.2.4 Energy representation of σ_{eq} and the formation factor F

Let us consider a cubic-shaped and water-saturated porous medium sample with pore volume V_p and average porosity $\phi = V_p/V$. The spatial distributions of the matrix and pore spaces are given by the indicator function $\Phi(\mathbf{x})$, which takes values of 0 and 1 in the former and the latter cases, respectively. The matrix material is assumed to be an electrical insulator and the pore space is filled with a heterogeneous solution consisting of some mass m of salt dissolved in denaturated water, which results in a saline concentration field $c(\mathbf{x})$ with mean value $\mu_c = m/V_p$. Further, $c(\mathbf{x})$ induces a (spatially-variable) scalar fluid electrical conductivity field $\sigma_w(\mathbf{x})$ (e.g., Sen and Goode, 1992) of mean value μ_{σ_w} within the pore space. The conductivity field of the sample can be expressed as $\sigma(\mathbf{x}) = \sigma_w(\mathbf{x})\Phi(\mathbf{x})$. Assume we cover two opposite faces of the cube with a pair of sheet electrodes, to impose an electrical potential difference ΔU along the x -direction. This drives an electrical current i , which results from integrating the flux of $\mathbf{J}(\mathbf{x})$ across any surface separating the injection electrodes. The power dissipated by the sample in the form of Joule's heat is given by $i\Delta U$. Applying Ohm's law we can express it as $S\Delta U^2$, with S the conductance of the sample, in turn given as $S = \sigma_{\text{eq}}L$, where L is the side length of the cube. We can express the power in terms of the modulus of the impressed electric field \mathbf{E}_0 , $E_0 \equiv -\Delta U/L$ and σ_{eq} as $-VE_0^2\sigma_{\text{eq}}$. Analogously, the power dissipated locally at the point \mathbf{x} is given by the dissipation functional $\mathbf{E}(\mathbf{x}) \cdot \mathbf{J}(\mathbf{x})$. Using Ohm's law, we can express $\mathbf{E}(\mathbf{x}) \cdot \mathbf{J}(\mathbf{x}) = -\mathbf{E}(\mathbf{x}) \cdot \sigma(\mathbf{x})\mathbf{E}(\mathbf{x})$. This quantity, integrated over V_p , must be identical to $-VE_0^2\sigma_{\text{eq}}$ due to energy conservation. That is:

$$-VE_0^2\sigma_{\text{eq}} = - \int_{V_p} \mathbf{E}(\mathbf{x}) \cdot \sigma(\mathbf{x})\mathbf{E}(\mathbf{x}) dV_p, \quad (4.11)$$

or,

$$\sigma_{\text{eq}} = \frac{1}{E_0^2 V} \int_{V_p} \mathbf{E}(\mathbf{x}) \cdot \sigma(\mathbf{x}) \mathbf{E}(\mathbf{x}) dV_p, \quad (4.12)$$

which gives the energy representation formula of the equivalent conductivity (e.g., *Bernabé and Revil, 1995*).

In the simplest case, $\sigma_w(\mathbf{x})$ is constant within the pore space and equal to some value μ_{σ_w} . We then have:

$$\sigma_{\text{eq}} = \frac{\mu_{\sigma_w}}{V E_0^2} \int_{V_p} \mathbf{E}(\mathbf{x}) \cdot \mathbf{E}(\mathbf{x}) dV_p, \quad (4.13)$$

or

$$\sigma_{\text{eq}} = \frac{\mu_{\sigma_w}}{F}, \quad (4.14)$$

with the proportionality constant $\frac{1}{F}$,

$$\frac{1}{F} = \frac{1}{V E_0^2} \int_{V_p} \mathbf{E}(\mathbf{x}) \cdot \mathbf{E}(\mathbf{x}) dV_p, \quad (4.15)$$

recognized as the inverse of the formation factor F (e.g., *Avellaneda and Torquato, 1991*). The right-hand side (RHS) of Eq. 4.15 expresses a weighted average of the pore space, where the weights $\mathbf{E}(\mathbf{x}) \cdot \mathbf{E}(\mathbf{x})$ correspond to the local dissipated power, divided by the conductivity. Note that $1/F$ represents the effective (electrical) porosity participating in the electrical conduction (e.g., *Revil and Cathles III, 1999*) and so it encodes the relationship between the spatial distribution of the pore space $\phi(\mathbf{x})$ and σ_{eq} . The definition of F through Eq. 4.15 assumes that $\sigma_w(\mathbf{x})$ is constant, that the conductivity of grains and grain-water interfaces are negligible (e.g., *Bussian, 1983*), and the quantity at RHS of the latter is stationary at V_p (i.e., it does not change significantly when considering volumes in the vicinity of V_p). In other words, V_p must be a Representative Elementary Volume (REV) for that quantity. This requires that $\phi(\mathbf{x})$ is statistically homogeneous (e.g., *Torquato and Haslach Jr, 2002*) when viewed at the scale of V_p . Note that F is an intrinsic material property that is independent of the pore space fluid.

4.2.5 Trapped charge and secondary electric field

At any point within the porous sample, the electric field \mathbf{E} can be separated into primary \mathbf{E}_0 and secondary $\mathbf{E}_{s\phi}(\mathbf{x})$ parts. The source for the secondary or scattering field $\mathbf{E}_{s\phi}(\mathbf{x})$ is a conduction (free) trapped charge density $\rho_{free}(\mathbf{x})$ appearing whenever the impressed field \mathbf{E}_0 has a parallel component to the conductivity gradient field $\nabla\sigma(\mathbf{x})$. It is given by (e.g., *Feynman et al.*, 2011; *Kaufman*, 1985) as

$$\rho_{free}(\mathbf{x}) = -\varepsilon \frac{\nabla\sigma(\mathbf{x}) \cdot \mathbf{E}(\mathbf{x})}{\sigma(\mathbf{x})}, \quad (4.16)$$

where ε is the electrical permittivity. If $\sigma_w(\mathbf{x})$ is constant within the pore space then $\nabla\sigma(\mathbf{x})$, and thus $\rho_{free}(\mathbf{x})$, takes non-zero values only at the grain-fluid interface. Note that $\rho_{free}(\mathbf{x})$ adopts a distribution such that the net effect of $\mathbf{E}_{s\phi}(\mathbf{x})$ is that of reducing the total power dissipated by the sample, leading to a reduction of σ_{eq} . Consequently, a value of F larger than unity is the consequence of a non-zero $\mathbf{E}_{s\phi}(\mathbf{x})$.

4.2.6 Expressions for the formation factor, electrical tortuosity and cementation exponent

Decomposing the electric field into its primary and secondary parts, we can express F in terms of the first and second statistical moments of $\mathbf{E}_{s\phi}(\mathbf{x})$. By replacing $\mathbf{E}(\mathbf{x})$ in Eq. 4.15 by $\mathbf{E}_0 + \mathbf{E}_{s\phi}(\mathbf{x})$ we get:

$$\begin{aligned} \frac{1}{F} &= \frac{1}{VE_0^2} \int_{V_p} \mathbf{E}_0 \cdot \mathbf{E}_0 + 2\mathbf{E}_0 \cdot \mathbf{E}_{s\phi} + \mathbf{E}_{s\phi} \cdot \mathbf{E}_{s\phi} dV_p \\ &= \frac{\phi}{E_0^2} \left[E_0^2 + \frac{2}{V_p} \int_{V_p} \mathbf{E}_0 \cdot \mathbf{E}_{s\phi} dV_p + \frac{1}{V_p} \int_{V_p} \mathbf{E}_{s\phi} \cdot \mathbf{E}_{s\phi} dV_p \right]. \end{aligned} \quad (4.17)$$

Expanding component-wise the products in the integrands of Eq. 4.17 and recalling that the y -component of \mathbf{E}_0 is zero, we have

$$\frac{1}{F} = \frac{\phi}{E_0^2} \left[E_0^2 + \frac{2E_0}{V_p} \int_{V_p} E_{s\phi x} dV_p + \frac{1}{V_p} \int_{V_p} E_{s\phi x}^2 dV_p + \frac{1}{V_p} \int_{V_p} E_{s\phi y}^2 dV_p + \frac{1}{V_p} \int_{V_p} E_{s\phi z}^2 dV_p \right], \quad (4.18)$$

where $E_{s\phi x}$, $E_{s\phi y}$ and $E_{s\phi z}$ denote the x -, y - and z -components of $\mathbf{E}_{s\phi}$, respectively. By definition, the first integral of Eq. 4.18 is the mean value $\mu_{E_{s\phi x}}$ of $E_{s\phi x}$ within the pore space. The remaining integrals correspond to the sum of the squared means $\mu_{E_{s\phi x}}^2$ ($\mu_{E_{s\phi y}}^2$ and $\mu_{E_{s\phi z}}^2$) and variances $\sigma_{E_{s\phi x}}^2$ ($\sigma_{E_{s\phi y}}^2$ and $\sigma_{E_{s\phi z}}^2$) of $E_{s\phi x}$ ($E_{s\phi y}$ and $E_{s\phi z}$), computed over the pore space.

Note that since $\mathbf{E}_{s\phi}(\mathbf{x})$ is considered only within the pore space, where the amplitude of the total field is always smaller than that of the impressed field, $\mu_{E_{s\phi x}}$ needs to be a negative quantity. Further, $\mu_{E_{s\phi y}}$ and $\mu_{E_{s\phi z}}$ are identically zero. Finally, we arrive at the following expression for F :

$$\frac{1}{F} = \frac{\phi}{E_0^2} \left[(\mu_{E_{s\phi x}} + E_0)^2 + \sigma_{E_{s\phi x}}^2 + \sigma_{E_{s\phi y}}^2 + \sigma_{E_{s\phi z}}^2 \right]. \quad (4.19)$$

Note that we consider conductivity measurements in the x -direction, but analogous expressions can be obtained for the y - and z -directions. For anisotropic media, $\mathbf{E}_{s\phi}$ and, thus, $1/F$, will change depending on the direction of \mathbf{E}_0 . Given some value within $(0, 1)$ for the mean porosity ϕ , $E_{s\phi x}$ varies within $(-E_0, 0)$, depending on the spatial structure of the pore volume. In particular, it is identically $-E_0$ when the porous structure is arranged into layers that are perpendicular to the conductivity measurement direction. In such case, $\mu_{E_{s\phi x}}$ and $\sigma_{E_{s\phi}}^2$ ($:= \sigma_{E_{s\phi x}}^2 + \sigma_{E_{s\phi y}}^2 + \sigma_{E_{s\phi z}}^2$) are equal to $-E_0$ and zero, respectively. If the layers are parallel to the conductivity measurement direction then $E_{s\phi x}$, $\mu_{E_{s\phi x}}$ and $\sigma_{E_{s\phi}}^2$ are all equal to zero. In Appendix 4.6.1 we derive an expression similar to Eq. 4.19 but for a non-isolating matrix.

As a corollary, we make two observations. The first one is that Eq. 4.19 provides an alternative (physical) definition for the electrical tortuosity τ_e . Since (e.g., *Ghanbarian et al.*, 2013)

$$\tau_e = \phi F, \quad (4.20)$$

we have that

$$\tau_e = \frac{1}{1 - \frac{(\mu_{E_{s\phi x}} + E_0)^2 + \sigma_{E_{s\phi}}^2}{E_0^2}}. \quad (4.21)$$

It is clear that $\mu_{E_{s\phi x}}$ and $\sigma_{E_{s\phi}}^2$ are correlated in general. For instance, as $\mu_{E_{s\phi x}}$ approaches zero (i.e., no secondary field), so does $\sigma_{E_{s\phi}}^2$.

As a second observation, we can invoke Archie's law (*Archie*, 1942)

$$\frac{1}{F} = \phi^m, \quad (4.22)$$

to also provide an alternative expression for the cementation exponent m , in terms of $\mu_{E_s\phi x}^2$ and $\sigma_{E_s\phi}^2$. By combining Eqs. 4.19 and 4.22, we have that

$$1 - \frac{(\mu_{E_s\phi x} + E_0)^2 + \sigma_{E_s\phi}^2}{E_0^2} = \phi^{m-1}, \quad (4.23)$$

and thus by solving for m we obtain:

$$m = \frac{\ln \left[1 - \frac{(\mu_{E_s\phi x} + E_0)^2 + \sigma_{E_s\phi}^2}{E_0^2} \right]}{\ln [\phi]} + 1. \quad (4.24)$$

Eq. 4.24 predicts values of m within $[1, \infty)$ which is consistent with the theoretical minimum bound for this parameter. That is, $m = 1$ or $m \rightarrow \infty$ when the matrix space is organized into layers that are parallel or perpendicular to the conductivity measurement directions, respectively.

4.3 The mixing factor M

In the context of electrically-monitored saline tracer tests in a medium exhibiting negligible surface conductivity, the typical approach (e.g., *Kemna et al.*, 2002; *Singha and Gorelick*, 2005; *Cassiani et al.*, 2006; *Müller et al.*, 2010) is to rely on Equation 4.14 to estimate the mean saline concentration μ_c within the sample, by measuring or inferring σ_{eq} and assuming knowledge of F . This approach is only meaningful when the saline field is homogeneous (i.e., completely mixed) or exhibits lamination parallel to the conductivity measurement direction. In these situations, the interstitial fluid electrical conductivity trivially behaves as an additive property and then the observable apparent fluid conductivity σ_f^{app} (obtained as $\sigma_{eq}F$) equates μ_{σ_w} . This establishes a link between σ_f^{app} and μ_c , via a simple transformation (e.g., *Sen and Goode*, 1992). However, as $\sigma_w(\mathbf{x})$ departs from homogeneity (or a layered field), σ_f^{app} becomes smaller than μ_{σ_w} and then μ_c is no longer directly accessible through σ_f^{app} . Consequently, it is in practice difficult to assign a clear meaning to σ_f^{app} , except when making the strong assumption that deviations from homogeneity have a negligible effect.

We introduce M , a conductivity reduction factor due to heterogeneity in $\sigma(\mathbf{x})$ within the pore space. We call M the (solute) mixing factor and we define M as:

$$M = \frac{\mu_{\sigma_w}}{\sigma_f^{app}}. \quad (4.25)$$

Here, $M \in [1, \infty)$ quantifies the departure of σ_f^{app} from its maximum possible value μ_{σ_w} , and it evolves in response to evolution of $c(\mathbf{x})$, which in turn is governed by the spreading and mixing dynamics of the solute. In analogy to $1/F$, $1/M$ can be seen as an effective fraction of tracer mass participating in electrical conduction. Thus, F accounts for the pore structure of the medium whereas M accounts for the structure of $\sigma_w(\mathbf{x})$, and hence $c(\mathbf{x})$, within the porous volume. For the time-being, we only consider a given time instance and omit any explicit reference to time t .

Let us assume that $\Phi(\mathbf{x})$ exhibits heterogeneity at scales which are small compared to those in $\sigma_w(\mathbf{x})$. This argument is known as scale separation in the upscaling literature (e.g., *Adrian et al.*, 2000; *Wood*, 2009), and it allows us to decouple the impact on σ_{eq} coming from heterogeneity in either $\Phi(\mathbf{x})$ (captured by F) and $\sigma_w(\mathbf{x})$ (captured by M). Furthermore, if we assume that F is constant in space and $\sigma_w(\mathbf{x})$ is an ergodic field at the scale of the conductivity averaging, then, using M , we can express σ_{eq} as:

$$\sigma_{\text{eq}} = \frac{\mu_{\sigma_w}}{FM}. \quad (4.26)$$

Eq. 4.26 can be viewed as a generalization of Archie's linear relationship to account for heterogeneous $\sigma_w(\mathbf{x})$.

4.3.1 Analytical expression for the mixing factor M

In order to gain physical insights regarding how a heterogeneous fluid conductivity field $\sigma_w(\mathbf{x})$ impacts σ_{eq} , we arrive to an identity for M in terms of the secondary electric field arising due to fluctuations of $\sigma_w(\mathbf{x})$ around its mean value μ_{σ_w} .

It is convenient to replace σ_f^{app} by $\sigma_{\text{eq}}F$ as then we can express M as:

$$\begin{aligned} M &= \frac{\mu_{\sigma_w}}{\sigma_{\text{eq}}F} \\ &= \frac{\sigma_A}{\sigma_{\text{eq}}} \end{aligned} \quad (4.27)$$

where $\sigma_A = \mu_{\sigma_w}/F$ designates the equivalent electrical conductivity of the sample when $\sigma_w(\mathbf{x})$ is homogeneous within the porous space and σ_f^{app} equates μ_{σ_w} .

Replacing σ_{eq} by its energy representation (Eq. 4.12), we have:

$$M = \frac{\sigma_A E_0^2 V}{\int_{V_p} \mathbf{E}_{\text{eq}}(\mathbf{x}) \cdot \sigma(\mathbf{x}) \mathbf{E}_{\text{eq}}(\mathbf{x}) dV_p} \quad (4.28)$$

where $\mathbf{E}_{\text{eq}}(\mathbf{x})$ denotes the electric field within the sample in the presence of heterogeneous $\sigma_w(\mathbf{x})$.

We now decompose both $\mathbf{E}_{\text{eq}}(\mathbf{x})$ and $\sigma_w(\mathbf{x})$ into their mean and fluctuating part, that is, $\mathbf{E}_{\text{eq}}(\mathbf{x}) = \mathbf{E}_0 + \mathbf{E}_s(\mathbf{x})$ and $\sigma_w(\mathbf{x}) = \mu_{\sigma_w} + \sigma'_w(\mathbf{x})$. Under the scale separation argument invoked in Subsection 4.3 we can assume that the secondary fields arising due to the structures present in $\Phi(\mathbf{x})$ and $\sigma_w(\mathbf{x})$ do not interact. That is, we can invoke linearity of the responses, meaning that $\mathbf{E}_s(\mathbf{x})$ can be expressed as $\mathbf{E}_s(\mathbf{x}) = \mathbf{E}_{s\phi}(\mathbf{x}) + \mathbf{E}_{sc}(\mathbf{x})$, where $\mathbf{E}_{s\phi}(\mathbf{x})$ is solely produced by the structures of $\phi(\mathbf{x})$ and $\mathbf{E}_{sc}(\mathbf{x})$ is solely produced by the structures of $\sigma_w(\mathbf{x})$. Since F is constant, so is $\mathbf{E}_{s\phi}$ and we write the total field more conveniently as $\mathbf{E}_{\text{eq}}(\mathbf{x}) = \mathbf{E}_A + \mathbf{E}_{sc}(\mathbf{x})$, where \mathbf{E}_A ($= \mathbf{E}_0 + \mathbf{E}_{s\phi}$) is constant and represents the electric field when $\sigma_w(\mathbf{x})$ is homogeneous. Then, we can express the denominator in Eq. 4.28 as:

$$\int_{V_p} \mathbf{E}_{\text{eq}}(\mathbf{x}) \cdot \sigma(\mathbf{x}) \mathbf{E}_{\text{eq}}(\mathbf{x}) dV_p = \int_{V_p} \mu_{\sigma_w} \left[\mathbf{E}_A \cdot \mathbf{E}_A + 2\mathbf{E}_A \cdot \mathbf{E}_{sc}(\mathbf{x}) + \mathbf{E}_{sc}(\mathbf{x}) \cdot \mathbf{E}_{sc}(\mathbf{x}) \right] \\ + \sigma'_w \mathbf{E}_A \cdot \mathbf{E}_A + 2\sigma'_w \mathbf{E}_A \cdot \mathbf{E}_{sc}(\mathbf{x}) + \sigma'_w \mathbf{E}_{sc}(\mathbf{x}) \cdot \mathbf{E}_{sc}(\mathbf{x}) dV_p. \quad (4.29)$$

Without loss of generality we assume that \mathbf{E}_A is parallel to the x -direction. By expanding the dot products in Eq. 4.29 component-wise it is straightforward to see that the second and fourth terms of the right-hand side (RHS), each of them integrated over V_p , vanish exactly. This is a consequence of the fact that both $\mathbf{E}_{sc}(\mathbf{x})$ and σ' have zero mean. Consequently, Eq. 4.29 reduces to:

$$\int_{V_p} \mathbf{E}_{\text{eq}}(\mathbf{x}) \cdot \sigma(\mathbf{x}) \mathbf{E}_{\text{eq}}(\mathbf{x}) dV_p = \int_{V_p} \mu_{\sigma_w} \mathbf{E}_A \cdot \mathbf{E}_A dV_p \\ + \int_{V_p} \mu_{\sigma_w} \mathbf{E}_{sc}(\mathbf{x}) \cdot \mathbf{E}_{sc}(\mathbf{x}) dV_p + \int_{V_p} 2\sigma'_w(\mathbf{x}) \mathbf{E}_A \cdot \mathbf{E}_{sc}(\mathbf{x}) dV_p + \int_{V_p} \sigma'_w(\mathbf{x}) \mathbf{E}_{sc}(\mathbf{x}) \cdot \mathbf{E}_{sc}(\mathbf{x}) dV_p \quad (4.30)$$

The second, third and fourth terms of the RHS of Eq. 4.23 are related. By expressing the current density $\mathbf{J}_{\text{eq}}(\mathbf{x})$ as the sum of its mean and fluctuating parts, respectively \mathbf{J}_A and $\mathbf{J}_{sc}(\mathbf{x})$, and applying Ohm's law we have

$$\mathbf{J}_A + \mathbf{J}_{sc}(\mathbf{x}) = \left[\mu_{\sigma_w} + \sigma'_w(\mathbf{x}) \right] \left[\mathbf{E}_A + \mathbf{E}_{sc}(\mathbf{x}) \right]. \quad (4.31)$$

Multiplying Eq. 4.31 by $\mathbf{E}_A + \mathbf{E}_{sc}(\mathbf{x})$, integrating over V_p and distributing products, we obtain:

$$\begin{aligned} & \int_{V_p} \mathbf{E}_A \cdot \mathbf{J}_A + \mathbf{E}_A \cdot \mathbf{J}_{sc}(\mathbf{x}) + \mathbf{E}_{sc}(\mathbf{x}) \cdot \mathbf{J}_A + \mathbf{E}_{sc}(\mathbf{x}) \cdot \mathbf{J}_{sc}(\mathbf{x}) dV_p = \\ & \int_{V_p} \mu_{\sigma_w} \mathbf{E}_A \cdot \mathbf{E}_A + \sigma'_w(\mathbf{x}) \mathbf{E}_A \cdot \mathbf{E}_A + \mu_{\sigma_w} \mathbf{E}_A \cdot \mathbf{E}_{sc}(\mathbf{x}) + \sigma'_w(\mathbf{x}) \mathbf{E}_{sc}(\mathbf{x}) \cdot \mathbf{E}_A \\ & + \mu_{\sigma_w} \mathbf{E}_A \cdot \mathbf{E}_{sc}(\mathbf{x}) + \mu_{\sigma_w} \mathbf{E}_{sc}(\mathbf{x}) \cdot \mathbf{E}_{sc}(\mathbf{x}) + \sigma'_w(\mathbf{x}) \mathbf{E}_A \cdot \mathbf{E}_{sc}(\mathbf{x}) + \sigma'_w(\mathbf{x}) \mathbf{E}_{sc}(\mathbf{x}) \mathbf{E}_{sc}(\mathbf{x}) dV_p. \end{aligned} \quad (4.32)$$

Note that Eq. 4.32 is simply an identity for the dissipated power in the sample in terms of the mean and fluctuating electric and current density fields, using Ohm's law to express the latter. We consider now the different terms of the LHS and RHS of Eq. 4.32, each of them integrated over V_p . By definition, the first term of the LHS is the total power dissipated by the sample, and it equals the sum of the first and second terms on the RHS. This implies that the remaining terms of the LHS must be equal to zero. Again, by recalling that \mathbf{E}_A is aligned with the x -direction and $\mathbf{E}_{sc}(\mathbf{x})$ has zero mean, the third, and fifth terms of the RHS vanish exactly. This gives:

$$0 = \int_{V_p} \mu_{\sigma_w} \mathbf{E}_{sc}(\mathbf{x}) \cdot \mathbf{E}_{sc}(\mathbf{x}) dV_p + \int_{V_p} \sigma'_w(\mathbf{x}) \mathbf{E}_{sc}(\mathbf{x}) \cdot \mathbf{E}_A(\mathbf{x}) + \sigma'_w(\mathbf{x}) \mathbf{E}_{sc}(\mathbf{x}) \cdot \mathbf{E}_{sc}(\mathbf{x}) dV_p. \quad (4.33)$$

Using the identity of Eq. 4.33, we replace the second and fourth terms of the RHS of Eq.4.30 and then express

$$\int_{V_p} \mathbf{E}_{eq}(\mathbf{x}) \cdot \sigma(\mathbf{x}) \mathbf{E}_{eq}(\mathbf{x}) dV_p = \int_{V_p} \mu_{\sigma_w} \mathbf{E}_A \cdot \mathbf{E}_A dV_p + \int_{V_p} \sigma'_w(\mathbf{x}) \mathbf{E}_{sc}(\mathbf{x}) \cdot \mathbf{E}_A(\mathbf{x}) dV_p. \quad (4.34)$$

Then, we can write $1/M$ as

$$\frac{1}{M} = \frac{\int_{V_p} \mu_{\sigma_w} \mathbf{E}_A \cdot \mathbf{E}_A dV_p + \int_{V_p} \sigma'_w(\mathbf{x}) \mathbf{E}_{sc}(\mathbf{x}) \cdot \mathbf{E}_A(\mathbf{x}) dV_p}{\sigma_A E_0^2 V}, \quad (4.35)$$

or,

$$\frac{1}{M} = 1 + \frac{F\phi}{\mu_{\sigma} E_0^2 V_p} \int_{V_p} \sigma'_w(\mathbf{x}) E_{scx}(\mathbf{x}) dV_p, \quad (4.36)$$

where $E_{\text{scx}}(\mathbf{x})$ denotes the x -component of $\mathbf{E}_{\text{sc}}(\mathbf{x})$.

Note that M depends on the fluid conductivity field, thereby highlighting the non-linearity of conductivity averaging in the presence of heterogeneous $\sigma_w(\mathbf{x})$. We can use the relationship given by Eq. 4.36 to replace it in Eq. 4.26 and then express the equivalent conductivity σ_{eq} as:

$$\sigma_{\text{eq}} = \frac{\mu_{\sigma_w}}{F} + \frac{\phi}{E_0^2 V_p} \int_{V_p} \sigma'_w(\mathbf{x}) E_{\text{scx}}(\mathbf{x}) dV_p. \quad (4.37)$$

Eq. 4.37 expresses σ_{eq} in terms of the mean value of the product of $\sigma'_w(\mathbf{x})$ with $E_{\text{scx}}(\mathbf{x})$. The utility of Eq. 4.37 is that it narrows the problem of predicting σ_{eq} to gaining knowledge on the mapping between the statistical properties of $\sigma'_w(\mathbf{x})$ and $E_{\text{scx}}(\mathbf{x})$.

Finally, if $\sigma_w(\mathbf{x})$ renders the sample electrically anisotropic, then both the equivalent electrical conductivity and the mixing factor become tensors $\overline{\overline{\sigma}}_{\text{eq}}$ and $\overline{\overline{M}}$, respectively, and we can write Eq. 4.37 more generally as:

$$\overline{\overline{\sigma}}_{\text{eq}} = \frac{\mu_{\sigma_w}}{F} \overline{\overline{M}}^{-1}. \quad (4.38)$$

Assuming that the anisotropy is aligned with the x - y - and z -directions, we can express Eq. 4.37 as

$$\overline{\overline{\sigma}}_{\text{eq}} = \frac{\mu_{\sigma_w}}{F} \mathbf{I} + \frac{\phi}{E_0^2 V_p} \begin{bmatrix} \int_{V_p} \sigma'_w(\mathbf{x}) E_{\text{scx}}(\mathbf{x}) dV_p & 0 & 0 \\ 0 & \int_{V_p} \sigma'_w(\mathbf{x}) E_{\text{scy}}(\mathbf{x}) dV_p & 0 \\ 0 & 0 & \int_{V_p} \sigma'_w(\mathbf{x}) E_{\text{scz}}(\mathbf{x}) dV_p \end{bmatrix} \quad (4.39)$$

where $E_{\text{scy}}(\mathbf{x})$ and $E_{\text{scz}}(\mathbf{x})$ denote the components of the secondary electric field in the y - and z -conductivity measurement directions, respectively.

In what follows, we study the relationship between $\overline{\overline{M}}$ and the degree of heterogeneity, spatial correlation and connectivity of 2-D heterogeneous conductivity fields.

4.4 Numerical tests

We simulate the pair of equivalent electrical conductivities, σ_x^{eq} and σ_y^{eq} of a 2-D rectangular domain of length $L = 10$ m and height $h = 1$ m, containing heterogeneous fluid electrical conductivity fields. We assign to the domain a constant porosity $\Phi = 0.2$ and cementation exponent $m = 1.43$, which yields a formation factor $F = 10$. Based on Eq. 4.39 we study numerically the behaviour of \overline{M} and the secondary electric field in response to the degree of heterogeneity and spatial (statistical) correlation of the electrical conductivity fields. We model the later using one realization of a multivariate-lognormal field, completely defined by its mean μ_{σ_w} , variance of the log-transformed field $\sigma_{\ln\sigma}^2$ and covariance model (e.g., *Rubin*, 2003). Fixing μ_{σ_w} at 0.1 S m^{-1} , then the field heterogeneity and its degree of spatial correlation are considered, respectively, via $\sigma_{\ln\sigma}^2$, varying within $[0, 2]$, and an anisotropic exponential covariance model that is aligned with the x - and y -directions (longitudinal and latitudinal, respectively). The corresponding integral scales in each direction, I_x and I_y , vary within $I_x \in [I_y, 10I_y]$, with $I_y = 0.02$ m. These values ensure to always have at least 50 integral scales in each direction. In order to consider connectivity, we use the histogram mapping by *Zinn and Harvey* (2003) that gives us in addition poorly and highly connected fields.

4.4.1 Validation

We first illustrate the appearance of trapped charge and the consequent secondary electric field.

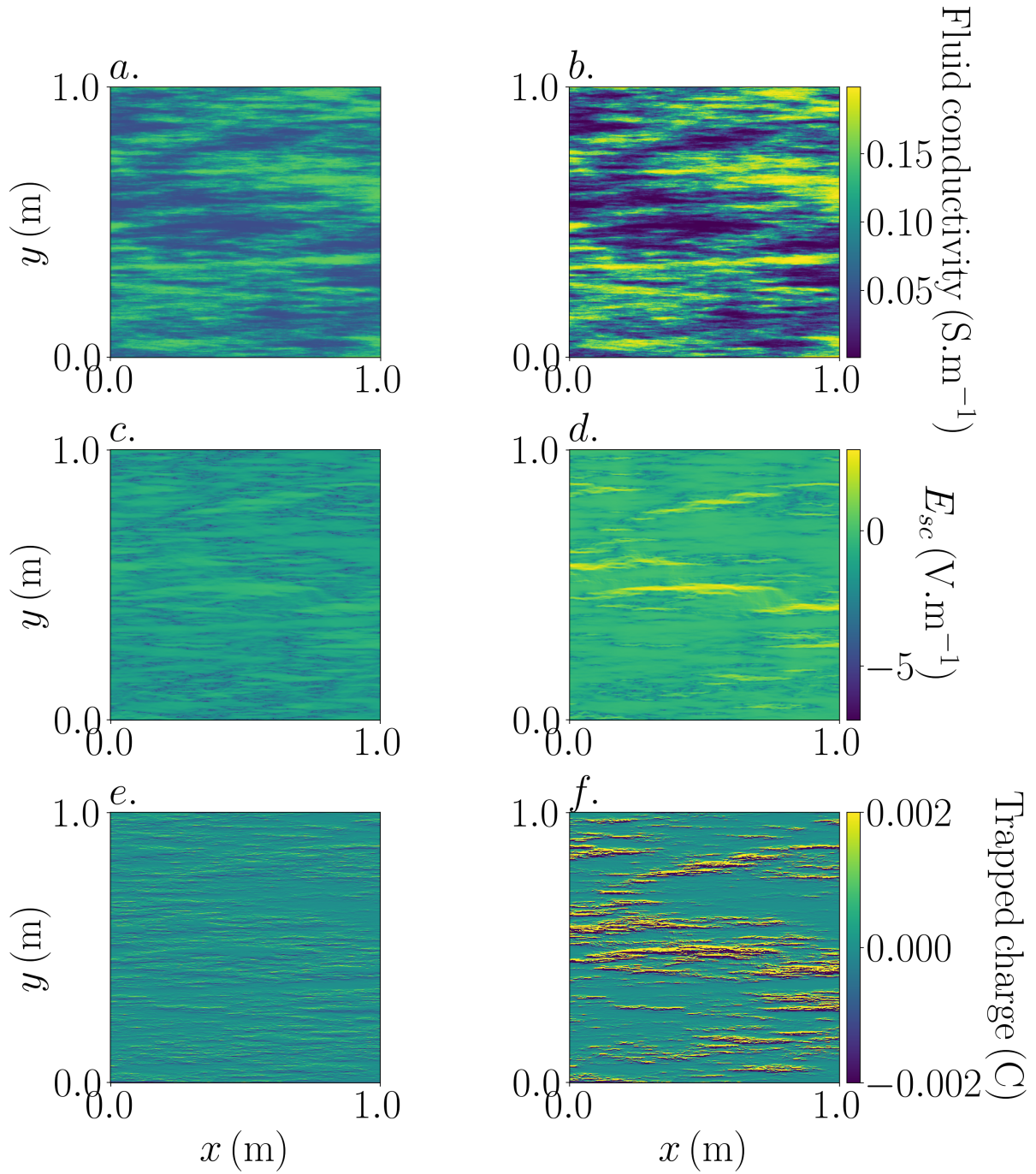


Figure 4.1 – (a-b) Multivariate log-normal fluid conductivity fields, (c-d) secondary electric field in the y -direction and (e-f) trapped charge distributions arising from applying a unit electrical potential drop across the y -direction. The electrical conductivity fields share the same mean value $\mu_{\sigma_w} = 0.1 \text{ S.m}^{-1}$, integral scales $I_y = 0.02 \text{ m}$, $I_x = 10I_y$ and different variances: (a) $\sigma_{\ln\sigma}^2 = 0.5$ and (b) $\sigma_{\ln\sigma}^2 = 1.5$.

We consider two heterogeneous fluid conductivity fields originated from the same random seed, sharing the mean and integral scales but having a low (Fig. 4.1a) and high (4.1b)

variance. For the low variance field, the associated secondary electric field exhibits a small amplitude (Fig. 4.1c) compared to the field associated with the high variance case (Figs. 4.1d). The same can be observed for the associated trapped charge density distributions appearing at conductivity gradients that are not perpendicular to the applied electric field. For the low variance field, the trapped charge (Figs. 4.1e) is much less compared to the case where the variance is higher (Figs. 4.1f).

We present now some numerical examples validating Eq. 4.37. Figure 4.2a (Fig. 4.2b) shows plots of simulated σ_{eqx} (σ_{eqy}) and predicted, using the derived expression Eq. 4.37 and the energy representation formula (Eq. 4.29). The agreement between the simulated and predicted mixing factors diminishes with the variance. However, note that both Eq. 4.37 and Eq. 4.12 yield similar levels of agreement. Thus, given that Eq. 4.12 is always valid, this suggests that the observed errors are related to numerical issues in the computation of the primary and secondary electric fields in the presence of conductivity contrasts. For the x -direction (Fig. 4.2a), the responses agree within 2% and 9% for $\lambda = 1$ and 5, respectively, for the maximum tested variance of the log-transformed conductivity field $\sigma_{\ln\sigma} = 3$. For the y -direction (Fig. 4.2b) the level of agreement for the maximum variances decreases to 15% and 8% for $\lambda = 1$ and 5, respectively.

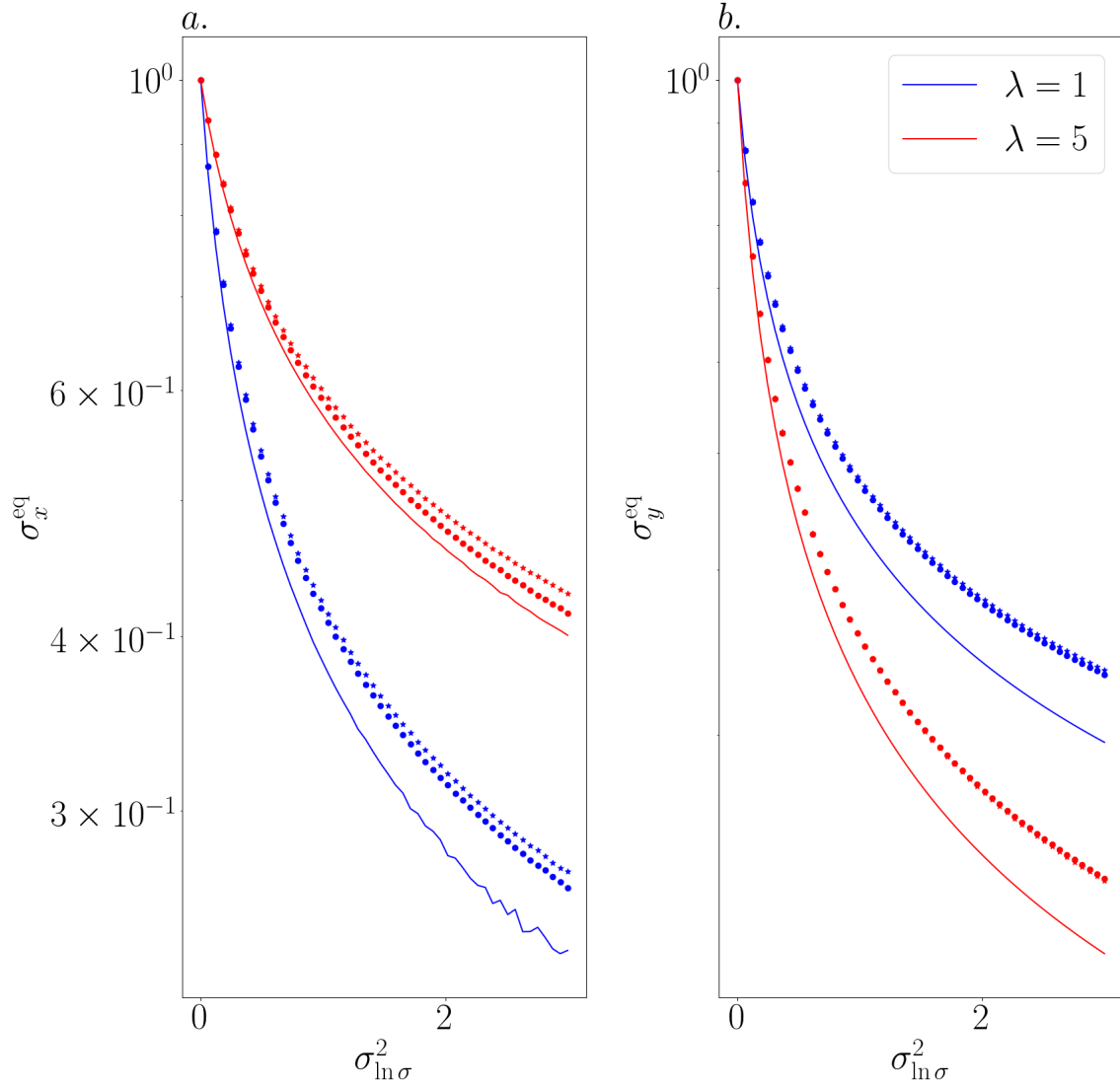


Figure 4.2 – (solid lines) simulated and predicted equivalent electrical conductivities using (dots) identity of Eq. 4.37 and (stars) energy representation formula (Eq. 4.12) in the (a) x - and (b) y -directions. The underlying conductivity field is multivariate- log-normal with mean $\mu_{\sigma_w} = 0.1 \text{ S m}^{-1}$ and $I_y = 0.02 \text{ m}$. $\lambda := I_x/I_y$ denotes the anisotropy of the underlying conductivity fields

4.4.2 Anisotropic mixing factors

We analyse now the behaviour of M_x and M_y as a function of $\sigma_{\ln\sigma}^2$ and λ and the connectivity of the heterogeneous electrical conductivity fields.

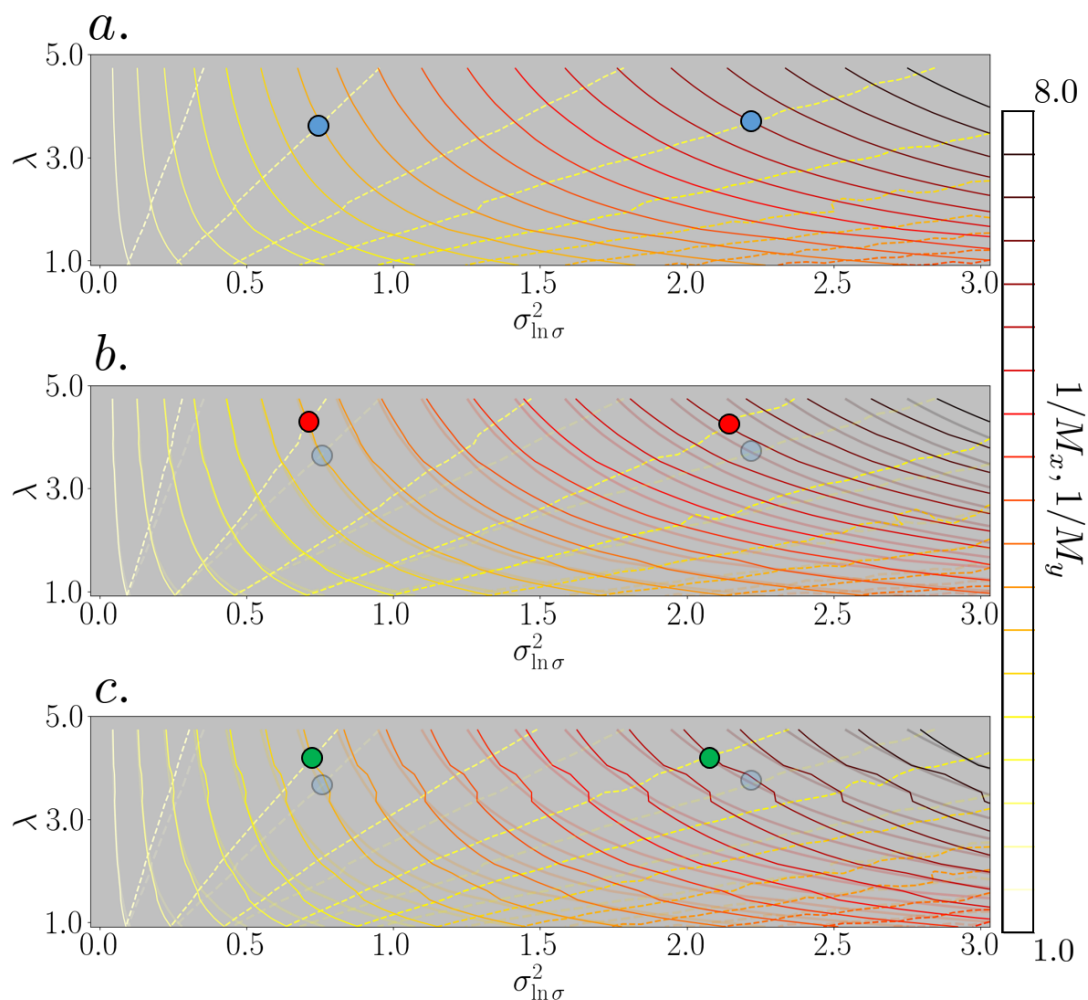


Figure 4.3 – Contour plots of (dashed) M_x and (solid) M_y as a function of both $\sigma_{\ln\sigma}^2$ and λ computed on multivariate log-normal electrical conductivity fields of fixed mean value $\mu_{\sigma_w} = 0.1 \text{ S m}^{-1}$ that exhibit connection of (a) conductivity values around the mean value, (b) high conductivity values (connected field) and (c) low conductivity values (disconnected field). Two intersections of the M_x - and M_y -contours are marked with (a) blue (b) red and (c) green dots. Both the contours and dots appearing in (a) are reproduced in (b) and (c) as well with transparency, for reference.

The mixing factors M_x and M_y increase with the variance of the electrical conductivity fields $\sigma_{\ln\sigma}^2$ (Fig. 4.3), with M_x decreasing with λ whereas M_y increases with this parameter. This is because as λ increases, the conduction pathways along the x -direction become less

tortuous (decrease of M_x) and the opposite occurs for the conduction pathways along the y -direction, that is, they become more tortuous (increase of M_y). A given pair of M_x - and M_y -values maps univocally to some set $[\sigma_{\ln\sigma}^2, \lambda]$, as seen by the intersection of the M_x - and M_y -contours. When the larger conductivity values of the underlying electrical conductivity field are connected, the mapping is modified (Fig. 4.3b), mainly due to a displacement of the M_x -contours towards regions of larger $\sigma_{\ln\sigma}^2$ and λ -values, indicating an overall increase of M_x (and thus decrease of σ_x^{eq}). The same behaviour is observed when the smaller conductivity values are connected (Fig. 4.3c).

The identity expressed by Eq. 4.37 indicates that the equivalent electrical conductivity is entirely described by the statistics of the electrical conductivity field fluctuations $\sigma'_w(\mathbf{x})$ and the secondary electric field E_s in the conductivity measurement direction. Given the prescribed log-normal statistics for $\sigma'_w(\mathbf{x})$, we consider the histograms of E_{s-x} and E_{s-y} (i.e., when the sample is excited in the x - and y -directions, respectively) as a function of both $\sigma_{\ln\sigma}^2$ and λ .

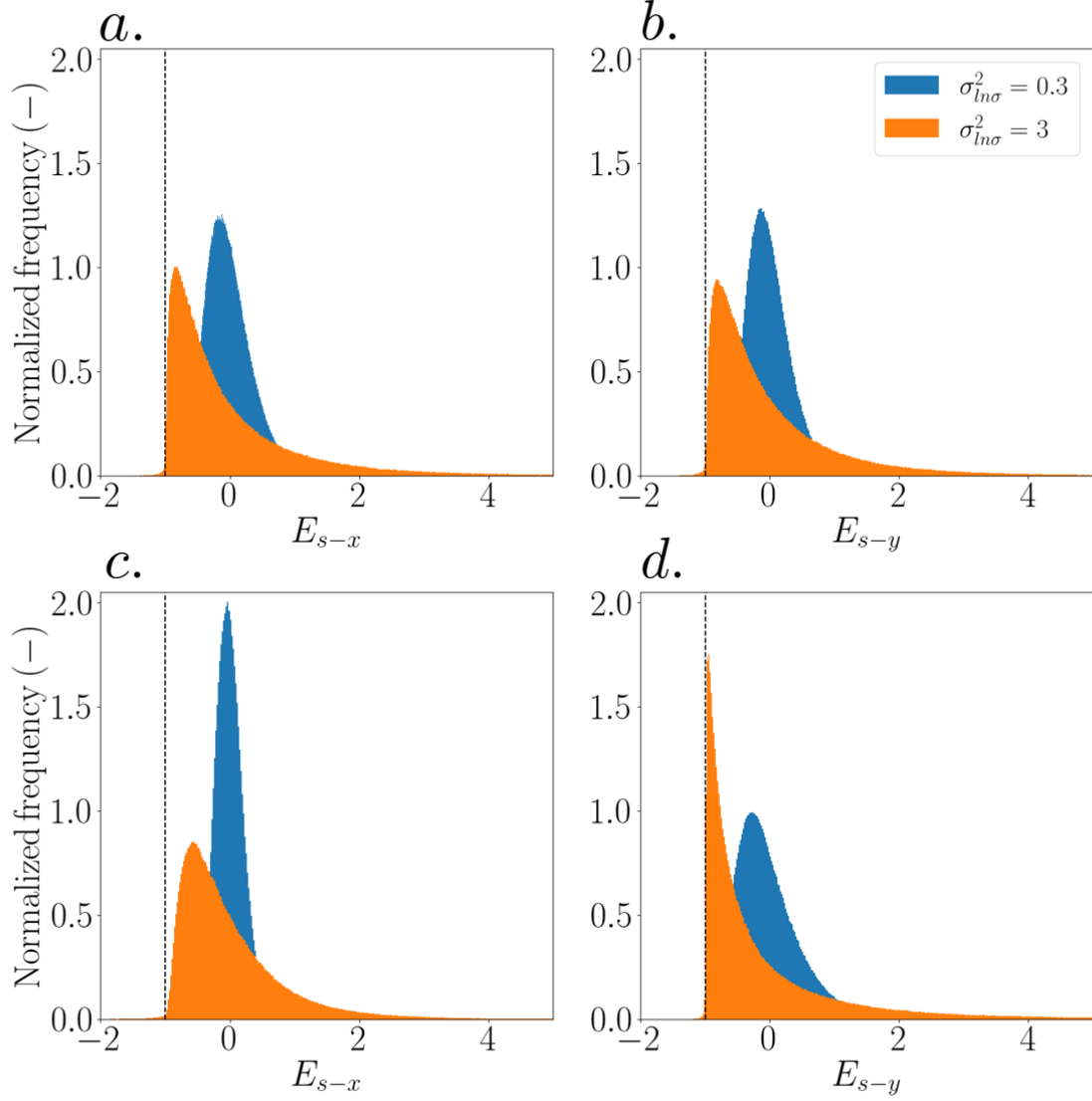


Figure 4.4 – Histograms of secondary electric field appearing when a heterogeneous fluid conductivity field is imposed an electrical potential difference in the (a-c) x -direction and (b-d) y -direction. Two pairs of heterogeneous fluid conductivity fields are considered, having variances (blue histogram) $\sigma_{\ln\sigma}^2 = 0.3$ and (orange histogram) $\sigma_{\ln\sigma}^2 = 3$ and anisotropy factors (first row) $\lambda = 1$ and (second row) $\lambda = 5$. The dashed black line marks the value of -1 V m^{-1} .

For the x -component and $\lambda = 1$ (Fig. 4.4a), as $\sigma_{\ln\sigma}^2$ increases, the histogram of E_{s-x} leans towards the asymptotic value of -1 V m^{-1} . This value is the amplitude of the impressed primary electric field and thus represents a minimum bound for the secondary electric field, due to energy conservation. Yet, note that there are some E_{s-x} -values smaller than the asymptote, thereby, highlighting the numerical issues mentioned in Subsec. 4.4.1. For the y -component and $\lambda = 1$ (Fig. 4.4b), E_{s-y} is identically distributed to E_{s-x} since the conductivity field is isotropic. When $\lambda = 5$, a given value for $\sigma_{\ln\sigma}^2$ induces smaller amplitudes for E_{s-x}

(Fig. 4.4c) compared to the isotropic case. The opposite behaviour is observed for E_{s-y} (Fig. 4.4d) that shows larger amplitudes.

For all the considered cases, the histograms seem to follow a three-parameter log-normal distribution, with the third parameter (or shift parameter) being the amplitude of the impressed field -1 V m^{-1} . This results remain to be confirmed through proper statistical testing.

4.4.3 Time-evolving setting

We consider now the temporal evolution of M_y for fluid conductivity fields that evolve from a pulse injection and are transported at (Fig. 4.5a) low and (Fig. 4.5b) high Péclet numbers.

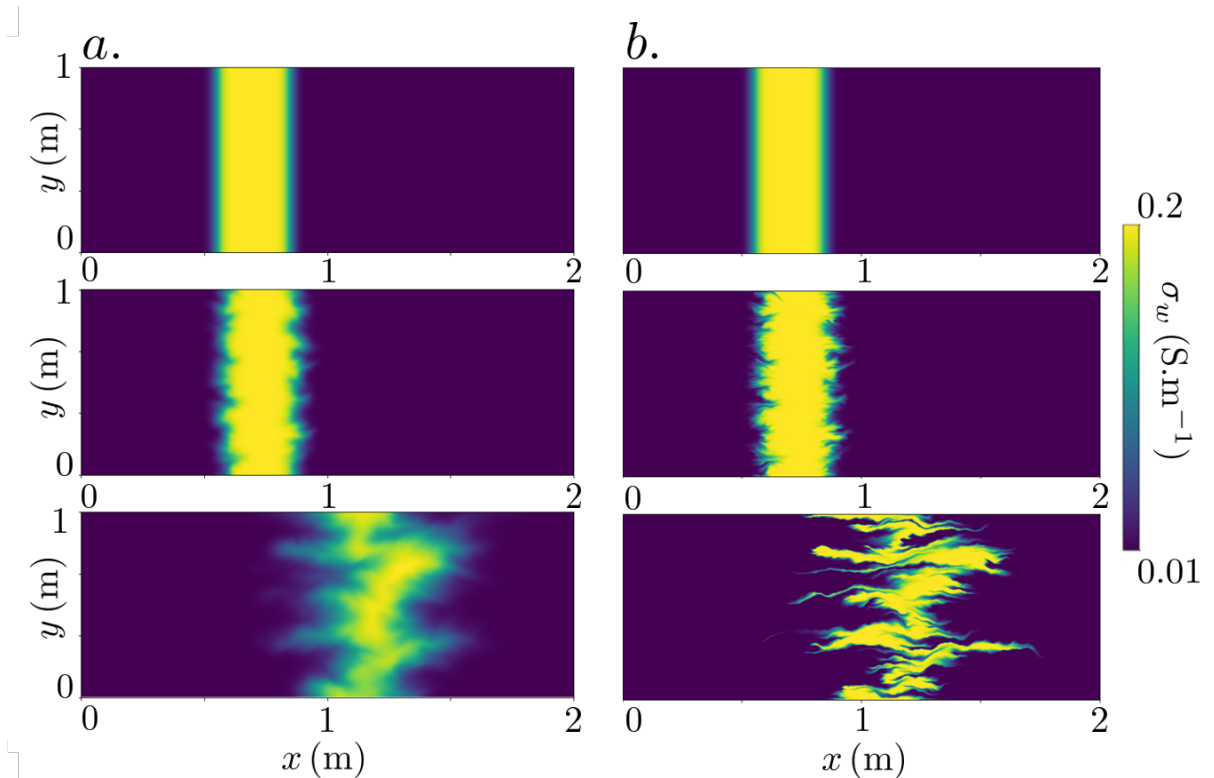


Figure 4.5 – Solute pulse transported in the positive x -direction at Péclet numbers of (a) 0.1 and (b) 1000.

It is observed that the spreading of the solute in the x -direction, Δ_{xx} (Eq. 4.6) is almost identical for the different Péclet numbers (Fig. 4.6a), however the mixing evolution, quantified by the scalar dissipation rate χ (Eq.4.7) divided by the diffusion coefficient D , χ/D , is much more marked for the high Péclet number (Fig. 4.6b). Accordingly, M_y evolves differently for both cases of transport (Fig. 4.6c), reflecting its sensitivity to mixing. However, note that the time-series of M_y corresponding to the high Péclet number case is not very sensitive to the mixing evolution for times before $\sim 2000 \text{ s}$. Also, by $t \sim 2 \times 10^4 \text{ s}$, when χ/D starts to decrease

over time for the low Péclet number case, the time-series of M_y corresponding to that case do not show a decreasing trend.

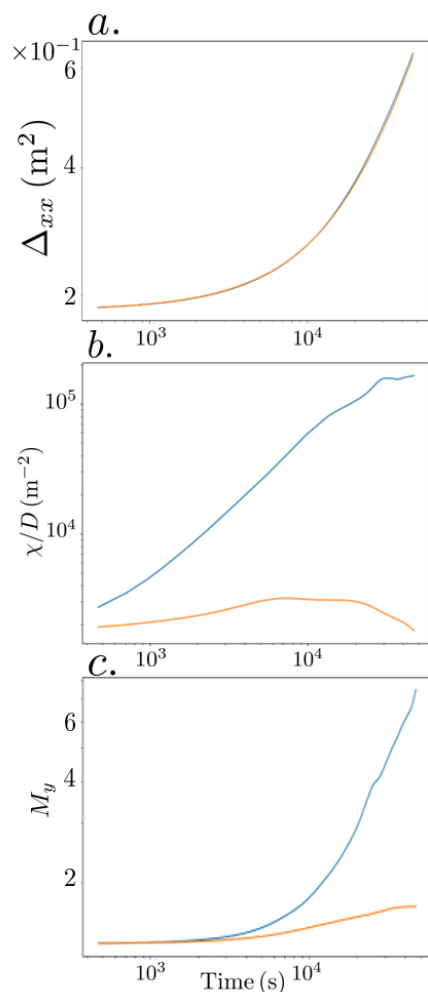


Figure 4.6 – (a) Spreading of the solute, quantified by Δ_{xx} , (b) mixing of the solute, quantified by χ/D and (c) observed mixing factor in the y -direction, M_y for solute pulse transported at Péclet numbers of (blue) 0.1 and (orange) 1000.

4.5 Conclusions and outlook

We have introduced a new petrophysical parameter, the mixing factor M , to interpret the impact of sub-resolution saline heterogeneity on the equivalent electrical conductivity tensor. We assessed how the observed equivalent electrical conductivity tensor, or mixing factor tensor within our framework, can constrain the variance, anisotropy and connectivity degree of ergodic 2-D multivariate-lognormal electrical conductivity fields. We observe that the two components of the mixing factor tensor map univocally to the variance and anisotropy ratio of the field with the mapping being modified by the connectivity degree of the field in a non-homogeneous manner, that is, dependent on the geostatistical properties of the

underlying field. Furthermore, based on a primary-secondary decomposition of the electric and conductivity fields we arrive at an identity that expresses the components of the mixing factor in terms of the expected value of the product of the conductivity field fluctuations and the secondary electric field component that is parallel to the conductivity measurement direction. We expect that numerical issues related to the computation of electric fields in the presence of conductivity contrasts are compromising the presented results. The main advantage of the derived expression is that it narrows the problem of predicting equivalent conductivity to gaining knowledge of the mapping between the statistics of the electrical conductivity field fluctuations and those of the secondary electric field. Along this line, we explore the statistical distributions of the secondary electric fields and we find that they are log-normally distributed for all the cases. Considering a time-lapse setting, we observe high sensitivity of the electrical data to differentiate between the spreading and mixing of the fluid conductivity field.

This study remains to be further developed. First, we will continue exploring the statistical properties of the secondary electric field in a static setting. Specifically, we will consider electrical conductivity fields following different statistical distributions to assess how they map to the corresponding distribution of the secondary electric field. Then, we will attempt to calibrate numerical relationships between the variance and anisotropy factor describing the fluid conductivity field and the variance and spatial correlation of the secondary electric field. By advancing the knowledge concerning such mapping, the goal is to use the above-mentioned identity to upscale electrical conductivity by using as input information the geostatistical descriptors of the fluid electrical conductivity. Second, we will continue working with the time-lapse setting where solutes are transported within a mass conservative system with the mixing factors evolve over time. We will start considering the temporal evolution of the mapping between the statistics of conductivity field and the secondary electric field under diffusion limited transport. Within this transport scenario, given that the mixing rate depends on the length scale of the structures (e.g., the layer widths in a layered solute concentration field), it is expected that the observed time-series of mixing factors permit not only to extract the anisotropy degree of the field but also to inform on an absolute measure of its structure, for instance, the integral scale in the y -direction. After we will continue the analysis including advection from (i) layered flow velocity fields and (ii) completely random velocity fields.

4.6 Appendices

4.6.1 Appendix A: Equivalent electrical conductivity for non-isolating matrix

In order to consider the case of a non-isolating matrix in our derivation we need to consider Eq. 4.12 but integrating over the entire sample volume V (instead of V_p) and split the

integration volume into the pore and solid matrix volumes, V_p and V_M , respectively, with $V = V_p + V_M$. We then have:

$$\sigma_{eq} = \frac{\mu_{\sigma_w}}{VE_0^2} \int_{V_p} \mathbf{E}(\mathbf{x}) \cdot \mathbf{E}(\mathbf{x}) dV_p + \frac{\sigma_M}{E_0^2} \int_{V_M} \mathbf{E}(\mathbf{x}) \cdot \mathbf{E}(\mathbf{x}) dV_M, \quad (4.40)$$

where σ_M denotes the conductivity of the solid matrix. Proceeding similarly as before, we arrive at the following expression for σ_{eq} resulting from two conductive phases:

$$\sigma_{eq} = \mu_{\sigma_w} \phi \left[\frac{(\mu_{E_{s\phi x}^p} + E_0)^2 + \sigma_{E_{s\phi}^p}^2}{E_0^2} \right] + \sigma_M (1 - \phi) \left[\frac{(\mu_{E_{s\phi x}^M} + E_0)^2 + \sigma_{E_{s\phi}^M}^2}{E_0^2} \right], \quad (4.41)$$

with $E_{s\phi}^p$ and $E_{s\phi}^M$ denoting the secondary fields in the pore and matrix spaces, respectively, and $\sigma_{E_{s\phi}^p}^2 := \sigma_{E_{s\phi x}^p}^2 + \sigma_{E_{s\phi y}^p}^2 + \sigma_{E_{s\phi z}^p}^2$ and $\sigma_{E_{s\phi}^M}^2 := \sigma_{E_{s\phi x}^M}^2 + \sigma_{E_{s\phi y}^M}^2 + \sigma_{E_{s\phi z}^M}^2$.

Both $\mu_{E_{s\phi x}^p}$ and $\mu_{E_{s\phi x}^M}$ depend on the values of μ_{σ_w} and σ_M . Thus, the two terms of Eq. 4.41 are not independent, implying that there is no assumption of conductive phases acting in parallel, as is customary in petrophysical models relying on the high-salinity limit used to account for surface conduction phenomena (e.g., *Revil et al.*, 2018). Equation 4.41 has the same form as the two-phase conductivity model proposed by *Glover et al.* (2000). Analogously to the one-phase conductive model, we can derive expressions for the cementation exponents corresponding to the solid and water phase, proposed by *Glover et al.* (2000), in terms of $\mu_{E_{s\phi x}^p}$ and $\mu_{E_{s\phi x}^M}$.

Chapter 5

Conclusions and Outlook

Solute transport unfolds over multiple spatial and temporal scales. Conventional hydrogeological monitoring techniques alone are insufficient to capture all its complexity, mainly because they provide information only at sparsely distributed locations near borehole wells. At the same time, the direct-current (DC) geophysical method provides spatially-distributed information on equivalent electrical conductivity, which is sensitive to the presence of electrically-conductive tracers and carries information on tracer heterogeneity below the electrical conductivity averaging scale. Thus, such data holds promise as a means to quantitatively characterize the state and evolution of the spreading and mixing of solutes. However, at present, no upscaling framework exists that links statistical measures of the tracer concentration field and their temporal evolution with equivalent DC electrical conductivity under general conditions. Furthermore, sub-resolution tracer heterogeneity is seldom considered in hydrogeophysical studies and there are no uncertainty quantification related to it, leading to systematic errors in the interpretations. The challenging nature of this problem makes it necessary to consider controlled settings and tools allowing the electrical signatures related to different transport scenarios to be assessed separately. In this thesis, we presented theoretical and experimental advances on the use of equivalent DC electrical conductivity and associated time-series to constrain tracer heterogeneity and its evolution under advective- and diffusive-dominated transport scenarios.

In the following, we critically discuss the results and conclusions of the research presented in Chapters 2, 3 and 4.

5.1 Conclusions

In Chapter 2, we investigate synthetic electrically-monitored saline tracer tests performed on heterogeneous hydraulic conductivity fields. The study is performed under continuous tracer injection and advective-dominated transport. It is aimed to explore how the spreading of solutes impacts the temporal evolution of the equivalent electrical conductivity and what can be learned by observing the latter. We rely on a Bayesian inference framework to quantify how well the time-series of the equivalent electrical conductivity tensor and mass breakthrough can constrain the variance and integral scales of multivariate Gaussian log-hydraulic conductivity fields. We focused the analysis on three test cases of hydraulic

heterogeneity, namely, fields having either small or large isotropic structures, or fields exhibiting fine layering parallel to the mean flow direction. We found that for all test cases and data types, the variance of the fields, controlling the spreading rate of the solute, is the best-constrained parameter, followed by the integral scales in the perpendicular and parallel directions to the flow, respectively. We also observed that the mean flow-aligned component of the electrical conductivity tensor consistently performs the best as conditioning data, followed by the perpendicular component and the solute breakthrough ranking third. We note that the parallel component is sensitive to the continuous paths created by the tracer, that is, to the tracer arrivals at the outlet, whereas the perpendicular component is mainly constrained by connection bottlenecks that tend to form away from the outlet region. At the same time, the integrative nature of the electrical responses makes both components more informative than the solute mass breakthrough, which is only directly sensitive to what happens at the outlet of the domain. We point out that the constraining nature of the data is assessed using both single and an ensemble of realizations of the hydraulic conductivity fields. The performance of the electrical data appears less sensitive to the specific field realization compared to the mass breakthrough, and this is again attributed to its integrating aspect. Regarding differences between the test cases, the layered field is the best constrained setting.

One main limitation of the study presented in Chapter 2 is that we consider a known and spatially-constant petrophysical relationship. In real settings this is probably not the case and, thus, it is necessary to consider petrophysical heterogeneity within the conductivity averaging volume, for instance, a spatially-variable formation factor. The superiority of time-lapse geoelectrical data over mass breakthrough, observed in our study, remains to be tested under such heterogeneous petrophysical conditions. Furthermore, laboratory-based experiments and extensions to 3-D media would be logical extensions to this study.

In Chapter 3, we report on an optically- and electrically monitored milli-fluidic laboratory tracer test aimed at (i) testing a novel experimental setup and (ii) gaining conceptual understanding of the electrical signatures of the diffusion-limited mixing of an initially layered tracer distribution. On the experimental side, we find that when working at low and intermediate Péclet numbers, the different diffusion rates of the optical (fluorescein) and electrical (table salt; NaCl) tracers must be accounted for before reaching quantitative agreement between the optically-inferred and measured time-series of equivalent DC electrical conductivity. This aspect is not considered in, for instance *Jougnot et al. (2018)*, thereby highlighting the importance of considering separately different transport scenarios. We observe that electrical conductivity time-series measured using point electrodes aligned perpendicularly to the concentration gradient are consistently maximal at times corresponding to the salt diffusion transport time-scale associated with the layer width of our confined cell. We confirm this experimental finding with numerical simulations and find that these time-series can also be used to constrain the initial layer widths and the degree of mixing of the tracer upon arrival to the measurement electrode positions. We interpret this sensitivity in terms of the simultaneous dependence of the time-series to both the net current flowing through the domain and temporal variations in the electrical potential field. These discriminative features disappear when using line electrodes as the imposed electrical potential field is more constrained due to the electrode geometry. For the case of line electrodes, we find that the time-evolving equivalent electrical conductivity in the direction of layering is strongly

anti-correlated to two common solute mixing descriptors: the concentration variance and the scalar dissipation rate.

We point out two technical challenges concerning the laboratory study presented in Chapter 3. First, the differences in the diffusion coefficients for the optical and electrical tracers could easily be addressed in our diffusion-limited setting by a simple re-scaling of the times for either data; a consequence of the linear dependence of the diffusion equation on the diffusion coefficient. However, as advection becomes more relevant, such linearity does not hold anymore. A possible workaround would be to perform separate experiments for each salt, such that it experiences the same Péclet number at each time. To ensure this, the two mean flow velocities in each experiment need to be chosen such that their ratio equates the ratio of the diffusion coefficients of the salts. A second aspect to consider during long experiments is fluorescein photobleaching, which during our experiment impacted the image-inferred apparent conductivity time-series but not the measured ones, leading to an increasing disagreement between the measured and simulated electrical responses over time. In our experiment we tried to decrease photobleaching by using a flash lamp that diminished the exposure time of the optical tracer. In addition, it is important to keep as reference a fluorescein-saturated chamber, that is isolated from the tracer test but receives the same light exposure over time. We stress that the non-linearity of the electrical conductivity averaging makes it highly sensitive to eventual errors present during the collection and processing of the optical data.

In Chapter 4 we introduce a new petrophysical parameter, the mixing factor M , which accounts for the impact of fluid conductivity heterogeneity below the averaging volume. We first investigate how the M -tensor can be used to constrain the degree of heterogeneity, small-scale structure and connectivity of log-normally distributed fluid conductivity fields. We find that the M -tensor maps univocally to the variance and anisotropy ratio of conductivity fields and that the mapping is impacted by the connectivity of the field. By assuming that the REV of the formation factor F is much smaller than the spatial fluctuations of the fluid conductivity field, we use a decomposition of the electric field in its primary and secondary components to arrive at an identity for M depending solely on the expected value of the product of the fluid conductivity field fluctuations and the secondary electric field. This expression allows us to attack the problem of electrical conductivity upscaling by studying the mapping between the geostatistical properties of either field. We observe that the secondary electric fields are log-normally distributed for all considered cases of heterogeneity. Considering a time-lapse setting, we observe high sensitivity of the time-series of M to the mixing degree of the solute.

We point out two limitations and challenges related with the framework presented in Chapter 4. First, surface conductivity is not considered. However, by relying on the usual assumption that surface conductivity acts in parallel with bulk fluid conductivity, we expect the corresponding expansion to be straightforward. Second, it is assumed that solute mass is known and conserved within the sample. This enables us to attribute temporal variations of the conductivity solely to the evolution of the structure of the conductivity field. Expanding the definition of M for non-conservative systems remains to be explored.

Below, we discuss a number of related expansions of the present work that we believe are of significant interest.

5.2 Outlook

Time-series of equivalent electrical conductivity collected during tracer tests are strongly dependent on the time-evolution of the concentration field, which in turn is driven by the flow-field. Thus, such data might be more strongly related with heterogeneity in the flow-field rather than with hydraulic conductivity. This suggests that the research presented in Chapter 2 could be expanded by considering geoelectrical sensitivity to geostatistical parameters or tortuosity (e.g., *Koponen et al.*, 1996; *Englert et al.*, 2006) of flow-field descriptors. For this, we can for instance combine a Bayesian inference framework with a method producing flow-fields with prescribed geostatistics. Regarding the inference framework, in Chapter 2 we used Approximate Bayesian Computation (e.g., *Sisson et al.*, 2018), however we could use instead the correlated pseudo-marginal method (*Deligiannidis et al.*, 2018), which enables us to assess the impact of the specific random realization of the field on the data. For generating the flow-fields, the method by *Kraichnan* (1970) appears well-suited. In turn, as a next step, we could relate the electrical data to concentration field descriptors. However, as the concentration field is time-variant, it is more challenging to summarize than the steady-state flow field. Spatial distributions of localized temporal moments (*Cirpka and Kitanidis*, 2000) are one possibility to summarize time-series of solute concentration fields. The ultimate goal is to estimate the uncertainty associated with electrically-inferred geostatistical or topological descriptors of all the fields involved in the flow and transport forward modelling chain.

Electrically-monitored milli-fluidic tracer tests represent an appealing framework to (i) test existing transport models and associated electrical conductivity upscaling frameworks and (ii) gain conceptual insights. For instance, using milli-fluidic cells exhibiting dual porosity appear to be an interesting way forward to assess the sensitivity of electrical data to dual-domain mass transfer parameters and to shed light on the electrical signatures arising from multi-rate mass transfer models. The permeability and boundary conditions of the milli-fluidic cell can also be adapted to reproduce specific hydrogeological settings, for instance, a coastal aquifer. Also, the usage of reactive tracers remains to be explored as well. For instance, the average electrical response could be linked to the reactive front properties (e.g., *Ghosh et al.*, 2018), which can be controlled using different permeability distributions for the milli-fluidic cell. The resulting electrical potential field is very sensitive to the connectivity of the tracer between the current injection electrodes. Such sensitivity can mask mixing-induced signals. The self-potential method (e.g., *Revil and Jardani*, 2013) has shown potential to constrain the transport of saline tracers (e.g., *Straface and De Biase*, 2013; *MacAllister et al.*, 2018), thereby, suggesting that combining milli-fluidic experiments with self-potential measurements seems worth to explore.

The research presented in Chapter 4 remains to be further developed. First, there is a need for a systematic assessment of the mapping between the statistical properties of fluid conductivity and secondary electric fields in both static and time-lapse settings. Specifically, we will consider electrical conductivity fields following different statistical distributions to assess how they map to the corresponding distribution of the secondary electric field. By calibrating numerical relationships between the variance and anisotropy factor describing the fluid conductivity field on the one hand and the variance and spatial correlation of the secondary electric field on the other hand, the goal is to produce an upscaling approach

for electrical conductivity based on the mixing factor presented in Chapter 4. Within the time-lapse setting, it is expected that the observed time-series of mixing factors permit not only to extract the anisotropy of the saline field but also to gain insights into its structure, for instance, the integral scales.

As the objectives of electrically-monitored tracer tests become more quantitative and ambitious, it appears necessary to define the targeted quantities more precisely. The current paradigm is based on relating equivalent electrical conductivity with mean salinity at some scale by means of a petrophysical relationship. Sophisticated approaches have been developed around this aim, for instance, by targeting moments of the solute plume (*Laloy et al.*, 2012). However, based on the research presented in Chapter 4, an alternative could be to perform inversion of the charge density distribution induced by the concentration field gradient. This approach is explored in *Li and Oldenburg* (1991, 1992) but has not been pursued further in hydrogeophysics. The relationship between charge density and conductivity gradients depends on the local electric field, so the non-linearity of the electrical conductivity averaging would still be present. For instance, a given conductivity gradient will accumulate more or less charge depending on whether it is located at a connection bottleneck or not. Then, translation of charge density into mean values of conductivity (or salinity) gradient would remain a non-trivial task. However, the approach seems worth to be explored as solute plume heterogeneity would be directly targeted. Along this line, provided that tracer heterogeneity induces a change in the volumetric chargeability (*Seigel*, 1959) of the medium, the application of the Induced Polarization method (e.g., *Oldenburg and Li*, 1994; *Ahmed et al.*, 2019) could be considered as a natural complementary extension of the DC method for mixing characterization.

One important limitation of the presented line of research is that equivalent electrical conductivity is mostly impacted by the connectivity degree of the tracer, while its sensitivity to one- and two-point statistical measures of solute concentration fields, directly related to common spreading and mixing measures, appears rather to be a second-order factor controlling the average electrical response. Then, an underlying (and open) research question is, how is the interplay between the connectivity degree of the tracer and the sensitivity of the electrical data to its degree of solute spreading and mixing? For instance, the mixing of the solute is very-well captured by the electrical data when it connects the injection electrodes. However, it is largely invisible if the transport occurs perpendicularly to the conductivity measurement direction. This is highlighted in Chapter 3. Certainly, an upscaling framework linking small-scale tracer heterogeneity with average electrical data is likely to depend on connectivity descriptors (e.g., *Renard and Allard*, 2013) of the tracer concentration field. Along this line, percolation-based approaches could be a way forward for cases of very strong salinity heterogeneity. However, the task becomes challenging because connectivity, while being an intuitive notion, is not very-well defined in the literature. Thus, there is a need of identifying a robust measure of connectivity for continuous fields and to relate it with transport-relevant properties.

Bibliography

- Adrian, R., K. Christensen, and Z.-C. Liu (2000), Analysis and interpretation of instantaneous turbulent velocity fields, *Experiments in Fluids*, 29(3), 275–290.
- Ahmed, A. S., A. Revil, and L. Gross (2019), Multiscale induced polarization tomography in hydrogeophysics: A new approach, *Advances in Water Resources*, 134, 103,451.
- Ahuja, S., M. C. Larsen, J. L. Eimers, C. L. Patterson, S. Sengupta, and J. L. Schnoor (2014), *Comprehensive Water Quality and Purification*, Elsevier Amsterdam.
- Archie, G. E. (1942), The electrical resistivity log as an aid in determining some reservoir characteristics, *Transactions of the AIME*, 146(01), 54–62, doi:10.2118/942054-G.
- Avellaneda, M., and S. Torquato (1991), Rigorous link between fluid permeability, electrical conductivity, and relaxation times for transport in porous media, *Physics of Fluids A: Fluid Dynamics*, 3(11), 2529–2540.
- Balluffi, R. W., S. M. Allen, and W. C. Carter (2005), *Kinetics of Materials*, John Wiley & Sons.
- Bear, J. (1972), *Dynamics of Fluids in Porous Media*, Dover Publications.
- Beaumont, M. A., W. Zhang, and D. J. Balding (2002), Approximate Bayesian Computation in Population Genetics, *Genetics*, 162(4), 2025–2035.
- Bedekar, V., E. D. Morway, C. D. Langevin, and M. J. Tonkin (2016), MT3D-USGS version 1: A US Geological Survey release of MT3DMS updated with new and expanded transport capabilities for use with MODFLOW, *Tech. rep.*, US Geological Survey, doi:10.3133/tm6A53.
- Berkowitz, B., A. Cortis, M. Dentz, and H. Scher (2006), Modeling non-Fickian transport in geological formations as a continuous time random walk, *Reviews of Geophysics*, 44(2).
- Bernabé, Y., and A. Revil (1995), Pore-scale heterogeneity, energy dissipation and the transport properties of rocks, *Geophysical Research Letters*, 22(12), 1529–1532, doi:10.1029/95GL01418.
- Bing, Z., and S. Greenhalgh (2001), Cross-hole resistivity tomography using different electrode configurations, *Geophysical Prospecting*, 48(5), 887–912, doi:10.1046/j.1365-2478.2000.00220.x.
- Binley, A., and L. Slater (2020), *Resistivity and Induced polarization: Theory and Applications to the Near Surface earth*, Cambridge University Press.

- Binley, A., G. Cassiani, R. Middleton, and P. Winship (2002), Vadose zone flow model parameterisation using cross-borehole radar and resistivity imaging, *Journal of Hydrology*, 267(3-4), 147–159, doi:10.1016/S0022-1694(02)00146-4.
- Binley, A., S. S. Hubbard, J. A. Huisman, A. Revil, D. A. Robinson, K. Singha, and L. D. Slater (2015), The emergence of hydrogeophysics for improved understanding of subsurface processes over multiple scales, *Water Resources Research*, 51(6), 3837–3866, doi:10.1002/2015WR017016.
- Briggs, M. A., F. D. Day-Lewis, J. B. Ong, G. P. Curtis, and J. W. Lane (2013), Simultaneous estimation of local-scale and flow path-scale dual-domain mass transfer parameters using geoelectrical monitoring, *Water Resources Research*, 49(9), 5615–5630, doi:10.1002/wrcr.20397.
- Brown, L. G. (1992), A survey of image registration techniques, *ACM Computing Surveys (CSUR)*, 24(4), 325–376.
- Bruggeman, V. D. (1935), Berechnung verschiedener physikalischer konstanten von heterogenen substanzen. i. dielektrizitätskonstanten und leitfähigkeiten der mischkörper aus isotropen substanzen, *Annalen der Physik*, 416(7), 636–664.
- Budka, M., B. Gabrys, and K. Musial (2011), On accuracy of pdf divergence estimators and their applicability to representative data sampling, *Entropy*, 13(7), 1229–1266, doi:10.3390/e13071229.
- Bussian, A. (1983), Electrical conductance in a porous medium, *Geophysics*, 48(9), 1258–1268.
- Butler, J. J. (2005), Hydrogeological methods for estimation of spatial variations in hydraulic conductivity, in *Hydrogeophysics*, pp. 23–58, Springer.
- Casalini, T., M. Salvalaglio, G. Perale, M. Masi, and C. Cavallotti (2011), Diffusion and aggregation of sodium fluorescein in aqueous solutions, *The Journal of Physical Chemistry B*, 115(44), 12,896–12,904.
- Cassiani, G., V. Bruno, A. Villa, N. Fusi, and A. M. Binley (2006), A saline trace test monitored via time-lapse surface electrical resistivity tomography, *Journal of Applied Geophysics*, 59(3), 244–259, doi:10.1016/j.jappgeo.2005.10.007.
- Chelidze, T., and Y. Gueguen (1999), Electrical spectroscopy of porous rocks: a review—i. theoretical models, *Geophysical Journal International*, 137(1), 1–15.
- Choy, T. C. (2015), *Effective Medium Theory: Principles and Applications*, vol. 165, Oxford University Press.
- Christakos, G. (2012), *Random Field Models in Earth Sciences*, Courier Corporation.
- Cirpka, O. A., and P. K. Kitanidis (2000), Characterization of mixing and dilution in heterogeneous aquifers by means of local temporal moments, *Water Resources Research*, 36(5), 1221–1236, doi:10.1029/1999WR900354.

- Coats, K., and B. Smith (1964), Dead-end pore volume and dispersion in porous media, *Society of Petroleum Engineers Journal*, 4(01), 73–84.
- Comolli, A., V. Hakoun, and M. Dentz (2019), Mechanisms, upscaling, and prediction of anomalous dispersion in heterogeneous porous media, *Water Resources Research*, 55(10), 8197–8222.
- Constable, S. C., R. L. Parker, and C. G. Constable (1987), Occam's inversion: A practical algorithm for generating smooth models from electromagnetic sounding data, *Geophysics*, 52(3), 289–300.
- Cortis, A., C. Gallo, H. Scher, and B. Berkowitz (2004), Numerical simulation of non-Fickian transport in geological formations with multiple-scale heterogeneities, *Water Resources Research*, 40(4).
- Cover, T. M., and J. A. Thomas (2012), *Elements of Information Theory*, John Wiley & Sons.
- Cox, R. A., and T. Nishikawa (1991), A new total variation diminishing scheme for the solution of advective-dominant solute transport, *Water Resources Research*, 27(10), 2645–2654, doi:10.1029/91WR01746.
- Curtis, A., and A. Lomax (2001), Prior information, sampling distributions, and the curse of dimensionality, *Geophysics*, 66(2), 372–378, doi:10.1190/1.1444928.
- Cvetkovic, V., H. Cheng, and X.-H. Wen (1996), Analysis of nonlinear effects on tracer migration in heterogeneous aquifers using Lagrangian travel time statistics, *Water Resources Research*, 32(6), 1671–1680, doi:10.1029/96WR00278.
- Dagan, G. (1979), Models of groundwater flow in statistically homogeneous porous formations, *Water Resources Research*, 15(1), 47–63.
- Dagan, G. (1989), *Flow and Transport in Porous Formations*, Springer-Verlag Berlin Heidelberg.
- Daigle, H. (2016), Application of critical path analysis for permeability prediction in natural porous media, *Advances in Water Resources*, 96, 43–54.
- Daily, W., and A. Ramirez (1995), Electrical resistance tomography during in-situ trichloroethylene remediation at the savannah river site, *Journal of Applied Geophysics*, 33(4), 239–249.
- Daily, W., A. Ramirez, D. LaBrecque, and J. Nitao (1992), Electrical resistivity tomography of vadose water movement, *Water Resources Research*, 28(5), 1429–1442, doi:10.1029/91WR03087.
- Day-Lewis, F., N. Linde, R. Haggerty, K. Singha, and M. A. Briggs (2017), Pore network modeling of the electrical signature of solute transport in dual-domain media, *Geophysical Research Letters*, 44(10), 4908–4916, doi:10.1002/2017GL073326.
- Day-Lewis, F. D., and K. Singha (2008), Geoelectrical inference of mass transfer parameters using temporal moments, *Water Resources Research*, 44(5), doi:10.1029/2007WR006750.

- Day-Lewis, F. D., K. Singha, and A. M. Binley (2005), Applying petrophysical models to radar travel time and electrical resistivity tomograms: Resolution-dependent limitations, *Journal of Geophysical Research: Solid Earth*, 110(B8), doi:10.1029/2004JB003569.
- de Anna, P. d., J. Jimenez-Martinez, H. Tabuteau, R. Turuban, T. Le Borgne, M. Derrien, and Y. Méheust (2014), Mixing and reaction kinetics in porous media: An experimental pore scale quantification, *Environmental Science & Technology*, 48(1), 508–516.
- de Dreuzy, J.-R., J. Carrera, M. Dentz, and T. Le Borgne (2012), Time evolution of mixing in heterogeneous porous media, *Water Resources Research*, 48(6), doi:10.1029/2011WR011360.
- Deligiannidis, G., A. Doucet, and M. K. Pitt (2018), The correlated pseudomarginal method, *Journal of the Royal Statistical Society: Series B (Statistical Methodology)*, 80(5), 839–870.
- Demirel, S., J. Irving, and D. Roubinet (2019), Comparison of rev size and tensor characteristics for the electrical and hydraulic conductivities in fractured rock, *Geophysical Journal International*, 216(3), 1953–1973.
- Dentz, M., T. Le Borgne, A. Englert, and B. Bijeljic (2011), Mixing, spreading and reaction in heterogeneous media: A brief review, *Journal of Contaminant Hydrology*, 120, 1–17.
- Dietrich, C. R., and G. N. Newsam (1997), Fast and exact simulation of stationary Gaussian processes through circulant embedding of the covariance matrix, *SIAM J. Scientific Computing*, 18, 1088–1107, doi:10.1137/S1064827592240555.
- Doetsch, J., N. Linde, T. Vogt, A. Binley, and A. G. Green (2012a), Imaging and quantifying salt-tracer transport in a riparian groundwater system by means of 3-D ERT monitoring, *Geophysics*, 77(5), B207–B218, doi:10.1190/geo2012-0046.1.
- Doetsch, J., N. Linde, M. Pessognelli, A. G. Green, and T. Günther (2012b), Constraining 3-D electrical resistance tomography with GPR reflection data for improved aquifer characterization, *Journal of Applied Geophysics*, 78, 68–76, doi:10.1016/j.jappgeo.2011.04.008.
- Doetsch, J. A., I. Coscia, S. Greenhalgh, N. Linde, A. Green, and T. Günther (2010), The borehole-fluid effect in electrical resistivity imaging, *Geophysics*, 75(4), F107–F114, doi:10.1190/1.3467824.
- Dykhne, A. (1971), Conductivity of a two-dimensional two-phase system, *Sov. Phys. JETP*, 32(1), 63–65.
- Englert, A., J. Vanderborght, and H. Vereecken (2006), Prediction of velocity statistics in three-dimensional multi-Gaussian hydraulic conductivity fields, *Water Resources Research*, 42(3), doi:10.1029/2005WR004014.
- Fetter, C. W. (2018), *Applied Hydrogeology*, Waveland Press.
- Feynman, R. P., R. B. Leighton, and M. Sands (2011), *The Feynman Lectures on Physics, Vol. I: The New Millennium Edition: Mainly Mechanics, Radiation, and Heat*, vol. 1, Basic Books.

- Fowler, D. E., and S. M. Moysey (2011), Estimation of aquifer transport parameters from resistivity monitoring data within a coupled inversion framework, *Journal of Hydrology*, 409(1-2), 545–554, doi:10.1016/j.jhydrol.2011.08.063.
- Friedel, S. (2003), Resolution, stability and efficiency of resistivity tomography estimated from a generalized inverse approach, *Geophysical Journal International*, 153(2), 305–316, doi:10.1046/j.1365-246X.2003.01890.x.
- Gelhar, L. W., and C. L. Axness (1983), Three-dimensional stochastic analysis of macrodispersion in aquifers, *Water Resources Research*, 19(1), 161–180, doi:10.1029/WR019i001p00161.
- Gelman, A., J. B. Carlin, H. S. Stern, D. B. Dunson, A. Vehtari, and D. B. Rubin (2013), *Bayesian Data Analysis*, CRC Press.
- Ghanbarian, B., A. G. Hunt, R. P. Ewing, and M. Sahimi (2013), Tortuosity in porous media: a critical review, *Soil Science Society of America Journal*, 77(5), 1461–1477.
- Ghosh, U., T. Borgne, D. Jougnot, N. Linde, and Y. Méheust (2018), Geoelectrical signatures of reactive mixing: a theoretical assessment, *Geophysical Research Letters*, 45(8), 3489–3498.
- Glover, P. (2009), What is the cementation exponent? A new interpretation, *The Leading Edge*, 28(1), 82–85.
- Glover, P. W., M. J. Hole, and J. Pous (2000), A modified Archie's law for two conducting phases, *Earth and Planetary Science Letters*, 180(3-4), 369–383.
- Haggerty, R., and S. M. Gorelick (1995), Multiple-rate mass transfer for modeling diffusion and surface reactions in media with pore-scale heterogeneity, *Water Resources Research*, 31(10), 2383–2400.
- Hamada, M., L. Cueto-Felgueroso, and P. de Anna (2020), Diffusion limited mixing in confined media, *Physical Review Fluids*, 5(12), 124,502.
- Harbaugh, A. W. (2005), *MODFLOW-2005, the US Geological Survey modular ground-water model: the ground-water flow process*, US Department of the Interior, US Geological Survey Reston, VA, doi:10.3133/tm6A16.
- Harvey, C. F., and S. M. Gorelick (1995), Temporal moment-generating equations: Modeling transport and mass transfer in heterogeneous aquifers, *Water Resources Research*, 31(8), 1895–1911.
- Herwanger, J., C. Pain, A. Binley, C. De Oliveira, and M. Worthington (2004), Anisotropic resistivity tomography, *Geophysical Journal International*, 158(2), 409–425, doi:10.1111/j.1365-246X.2004.02314.x.
- Hill, M. C. (1990), Solving groundwater flow problems by conjugate-gradient methods and the strongly implicit procedure, *Water Resources Research*, 26(9), 1961–1969, doi:10.1029/WR026i009p01961.
- Hill, R. (1963), Elastic properties of reinforced solids: some theoretical principles, *Journal of the Mechanics and Physics of Solids*, 11(5), 357–372, doi:10.1016/0022-5096(63)90036-X.

- Hinnell, A., T. Ferré, J. Vrugt, J. Huisman, S. Moysey, J. Rings, and M. Kowalsky (2010), Improved extraction of hydrologic information from geophysical data through coupled hydrogeophysical inversion, *Water Resources Research*, 46(4), doi:10.1029/2008WR007060.
- Houlihan, M. E., and P. J. Botek (2016), Groundwater Monitoring, in *The Handbook of Groundwater Engineering*, pp. 841–876, CRC Press.
- Hunt, A. (2001), Applications of percolation theory to porous media with distributed local conductances, *Advances in Water Resources*, 24(3-4), 279–307.
- Hunt, A. G., and M. Sahimi (2017), Flow, transport, and reaction in porous media: Percolation scaling, critical-path analysis, and effective medium approximation, *Reviews of Geophysics*, 55(4), 993–1078.
- Hyndman, D. W. (2016), Geophysical and tracer characterization methods, in *The Handbook of Groundwater Engineering*, pp. 935–956, CRC Press.
- Imamura, M., and M. Koizumi (1955), Irreversible photobleaching of the solution of fluorescent dyes. i. kinetic studies on the primary process, *Bulletin of the Chemical Society of Japan*, 28(2), 117–124.
- Izumoto, S., J. A. Huisman, Y. Wu, and H. Vereecken (2020), Effect of solute concentration on the spectral induced polarization response of calcite precipitation, *Geophysical Journal International*, 220(2), 1187–1196.
- Jiménez-Martínez, J., P. d. Anna, H. Tabuteau, R. Turuban, T. L. Borgne, and Y. Méheust (2015), Pore-scale mechanisms for the enhancement of mixing in unsaturated porous media and implications for chemical reactions, *Geophysical Research Letters*, 42(13), 5316–5324.
- Jiménez-Martínez, J., T. Le Borgne, H. Tabuteau, and Y. Méheust (2017), Impact of saturation on dispersion and mixing in porous media: Photobleaching pulse injection experiments and shear-enhanced mixing model, *Water Resources Research*, 53(2), 1457–1472.
- Johnson, D. L., J. Koplik, and L. M. Schwartz (1986), New pore-size parameter characterizing transport in porous media, *Physical Review Letters*, 57(20), 2564.
- Jougnot, D., A. Ghorbani, A. Revil, P. Leroy, and P. Cosenza (2010), Spectral induced polarization of partially saturated clay-rocks: A mechanistic approach, *Geophysical Journal International*, 180(1), 210–224.
- Jougnot, D., J. Jiménez-Martínez, R. Legendre, T. Le Borgne, Y. Méheust, and N. Linde (2018), Impact of small-scale saline tracer heterogeneity on electrical resistivity monitoring in fully and partially saturated porous media: Insights from geoelectrical milli-fluidic experiments, *Advances in Water Resources*, 113, 295–309, doi:10.1016/j.advwatres.2018.01.014.
- Jung, H.-K., D.-J. Min, H. S. Lee, S. Oh, and H. Chung (2009), Negative apparent resistivity in dipole–dipole electrical surveys, *Exploration Geophysics*, 40(1), 33–40.
- Katz, A., and A. Thompson (1986), Quantitative prediction of permeability in porous rock, *Physical Review B*, 34(11), 8179.

- Katz, A., and A. Thompson (1987), Prediction of rock electrical conductivity from mercury injection measurements, *Journal of Geophysical Research: Solid Earth*, 92(B1), 599–607.
- Kaufman, A. (1985), Tutorial distribution of alternating electrical charges in a conducting medium, *Geophysical Prospecting*, 33(2), 171–184.
- Keller, G. V., and F. C. Frischknecht (1966), *Electrical Methods in Geophysical Prospecting*, Pergamon.
- Kemna, A., J. Vanderborght, B. Kulesa, and H. Vereecken (2002), Imaging and characterisation of subsurface solute transport using electrical resistivity tomography (ERT) and equivalent transport models, *Journal of Hydrology*, 267(3-4), 125–146, doi:10.1016/S0022-1694(02)00145-2.
- Kirchner, J. W. (2016), Aggregation in environmental systems—part 1: Seasonal tracer cycles quantify young water fractions, but not mean transit times, in spatially heterogeneous catchments, *Hydrology and Earth System Sciences*, 20(1), 279–297.
- Koestel, J., A. Kemna, M. Javaux, A. Binley, and H. Vereecken (2008), Quantitative imaging of solute transport in an unsaturated and undisturbed soil monolith with 3-D ERT and TDR, *Water Resources Research*, 44(12), doi:10.1029/2007WR006755.
- Koestel, J., J. Vanderborght, M. Javaux, A. Kemna, A. Binley, and H. Vereecken (2009), Non-invasive 3-D transport characterization in a sandy soil using ERT: 1. investigating the validity of ERT-derived transport parameters, *Vadose Zone Journal*, 8(3), 711–722, doi:10.2136/vzj2008.0027.
- Koestel, J., M. Larsbo, and N. Jarvis (2020), Scale and rev analyses for porosity and pore connectivity measures in undisturbed soil, *Geoderma*, 366, 114,206.
- Koponen, A., M. Kataja, and J. v. Timonen (1996), Tortuous flow in porous media, *Physical Review E*, 54(1), 406, doi:10.1103/PhysRevE.54.406.
- Kowalsky, M. B., S. Finsterle, J. Peterson, S. Hubbard, Y. Rubin, E. Majer, A. Ward, and G. Gee (2005), Estimation of field-scale soil hydraulic and dielectric parameters through joint inversion of GPR and hydrological data, *Water Resources Research*, 41(11), doi:10.1029/2005WR004237.
- Kozlov, B., M. Schneider, B. Montaron, M. Lagues, and P. Tabeling (2012), Archie’s law in microsystems, *Transport in Porous Media*, 95(1), 1–20.
- Kraichnan, R. H. (1970), Diffusion by a random velocity field, *The Physics of Fluids*, 13(1), 22–31.
- Kullback, S., and R. A. Leibler (1951), On information and sufficiency, *The Annals of Mathematical Statistics*, 22(1), 79–86, doi:doi:10.1214/aoms/1177729694.
- LaBrecque, D. J., M. Miletto, W. Daily, A. Ramirez, and E. Owen (1996), The effects of noise on occam’s inversion of resistivity tomography data, *Geophysics*, 61(2), 538–548.

- Laloy, E., N. Linde, and J. A. Vrugt (2012), Mass conservative three-dimensional water tracer distribution from Markov chain Monte Carlo inversion of time-lapse ground-penetrating radar data, *Water Resources Research*, 48(7), doi:10.1029/2011WR011238.
- Laloy, E., N. Linde, D. Jacques, and J. A. Vrugt (2015), Probabilistic inference of multi-Gaussian fields from indirect hydrological data using circulant embedding and dimensionality reduction, *Water Resources Research*, 51(6), 4224–4243, doi:10.1002/2014WR016395.
- Le Borgne, T., M. Dentz, D. Bolster, J. Carrera, J.-R. De Dreuzy, and P. Davy (2010), Non-fickian mixing: Temporal evolution of the scalar dissipation rate in heterogeneous porous media, *Advances in Water Resources*, 33(12), 1468–1475.
- Le Borgne, T., M. Dentz, and E. Villiermaux (2015), The lamellar description of mixing in porous media, *Journal of Fluid Mechanics*, 770, 458–498.
- Lesmes, D. P., and S. P. Friedman (2005), Relationships between the electrical and hydrogeological properties of rocks and soils, in *Hydrogeophysics*, pp. 87–128, Springer.
- Li, Y., and D. W. Oldenburg (1991), Aspects of charge accumulation in dc resistivity experiments 1, *Geophysical Prospecting*, 39(6), 803–826, doi:10.1111/j.1365-2478.1991.tb00345.x.
- Li, Y., and D. W. Oldenburg (1992), Approximate inverse mappings in dc resistivity problems, *Geophysical Journal International*, 109(2), 343–362.
- Linde, N., J. Chen, M. B. Kowalsky, and S. Hubbard (2006), Hydrogeophysical parameter estimation approaches for field scale characterization, in *Applied hydrogeophysics*, pp. 9–44, Springer.
- MacAllister, D., M. Jackson, A. Butler, and J. Vinogradov (2018), Remote detection of saline intrusion in a coastal aquifer using borehole measurements of self-potential, *Water Resources Research*, 54(3), 1669–1687.
- Maineult, A., J.-B. Clavaud, and M. Zamora (2016), On the interest of bulk conductivity measurements for hydraulic dispersivity estimation from miscible displacement experiments in rock samples, *Transport in Porous Media*, 115(1), 21–34, doi:10.1007/s11242-016-0749-0.
- Maliva, R. G. (2016), *Aquifer Characterization Techniques*, Springer.
- Matheron, G., and G. De Marsily (1980), Is transport in porous media always diffusive? A counterexample, *Water Resources Research*, 16(5), 901–917.
- Milton, G. W., and A. Sawicki (2003), Theory of Composites. Cambridge Monographs on Applied and Computational Mathematics, *Appl. Mech. Rev.*, 56(2), B27–B28.
- Mosegaard, K., and A. Tarantola (1995), Monte Carlo sampling of solutions to inverse problems, *Journal of Geophysical Research: Solid Earth*, 100(B7), 12,431–12,447, doi:10.1029/94JB03097.
- Moysey, S., K. Singha, and R. Knight (2005a), A framework for inferring field-scale rock physics relationships through numerical simulation, *Geophysical Research Letters*, 32(8).

- Moysey, S., K. Singha, and R. Knight (2005b), A framework for inferring field-scale rock physics relationships through numerical simulation, *Geophysical Research Letters*, 32(8), doi:10.1029/2004GL022152.
- Müller, K., J. Vanderborght, A. Englert, A. Kemna, J. A. Huisman, J. Rings, and H. Vereecken (2010), Imaging and characterization of solute transport during two tracer tests in a shallow aquifer using electrical resistivity tomography and multilevel groundwater samplers, *Water Resources Research*, 46(3), doi:10.1029/2008WR007595.
- Nussbaumer, R., N. Linde, G. Mariethoz, and K. Holliger (2019), Simulation of fine-scale electrical conductivity fields using resolution-limited tomograms and area-to-point kriging, *Geophysical Journal International*, 218(2), 1322–1335, doi:10.1093/gji/ggz185.
- Ogata, A., and R. Banks (1961), *A solution of the differential equation of longitudinal dispersion in porous media: fluid movement in earth materials*, US Government Printing Office, doi: 10.3133/pp411A.
- Oldenburg, D. W., and Y. Li (1994), Inversion of induced polarization data, *Geophysics*, 59(9), 1327–1341.
- Otsu, N. (1979), A threshold selection method from gray-level histograms, *IEEE Transactions on Systems, Man, and Cybernetics*, 9(1), 62–66.
- Pidlisecky, A., R. Knight, and E. Haber (2006), Cone-based electrical resistivity tomography, *Geophysics*, 71(4), G157–G167, doi:10.1190/1.2213205.
- Pollock, D., and O. A. Cirpka (2012), Fully coupled hydrogeophysical inversion of a laboratory salt tracer experiment monitored by electrical resistivity tomography, *Water Resources Research*, 48(1), doi:10.1029/2011WR010779.
- Pope, S. B. (2001), *Turbulent Flows*, Cambridge University Press.
- Renard, P., and D. Allard (2013), Connectivity metrics for subsurface flow and transport, *Advances in Water Resources*, 51, 168–196.
- Renard, P., and G. De Marsily (1997), Calculating equivalent permeability: a review, *Advances in Water Resources*, 20(5-6), 253–278.
- Revil, A., and L. Cathles III (1999), Permeability of shaly sands, *Water Resources Research*, 35(3), 651–662.
- Revil, A., and P. Glover (1998), Nature of surface electrical conductivity in natural sands, sandstones, and clays, *Geophysical Research Letters*, 25(5), 691–694.
- Revil, A., and A. Jardani (2013), *The self-potential method: Theory and applications in environmental geosciences*, Cambridge University Press.
- Revil, A., A. S. Ahmed, and S. Matthai (2018), Transport of water and ions in partially water-saturated porous media. part 3. electrical conductivity, *Advances in Water Resources*, 121, 97–111.

- Rolle, M., and T. Le Borgne (2019), Mixing and reactive fronts in the subsurface, *Reviews in Mineralogy and Geochemistry*, 85(1), 111–142.
- Rubin, Y. (2003), *Applied Stochastic Hydrogeology*, Oxford University Press.
- Rubin, Y., and S. S. Hubbard (2005), *Hydrogeophysics*, vol. 50, Springer Science & Business Media.
- Rubin, Y., M. A. Cushey, and A. Wilson (1997), The moments of the breakthrough curves of instantaneously and kinetically sorbing solutes in heterogeneous geologic media: Prediction and parameter inference from field measurements, *Water Resources Research*, 33(11), 2465–2481.
- Rücker, C., T. Günther, and F. M. Wagner (2017), pyGIMLi: An open-source library for modelling and inversion in geophysics, *Computers & Geosciences*, 109, 106–123.
- Rücker, C., T. Günther, and F. M. Wagner (2017), pyGIMLi: An open-source library for modelling and inversion in geophysics, *Computers and Geosciences*, 109, 106–123, doi:10.1016/j.cageo.2017.07.011.
- Sanchez-Vila, X., A. Guadagnini, and J. Carrera (2006), Representative hydraulic conductivities in saturated groundwater flow, *Reviews of Geophysics*, 44(3), doi:10.1029/2005RG000169.
- Scales, J. A. (1996), Uncertainties in seismic inverse calculations, in *Inverse Methods*, pp. 79–97, Springer.
- Seigel, H. O. (1959), Mathematical formulation and type curves for induced polarization, *Geophysics*, 24(3), 547–565.
- Sen, P., C. Scala, and M. Cohen (1981), A self-similar model for sedimentary rocks with application to the dielectric constant of fused glass beads, *Geophysics*, 46(5), 781–795, doi:10.1190/1.1441215.
- Sen, P. N., and P. A. Goode (1992), Influence of temperature on electrical conductivity on shaly sands, *Geophysics*, 57(1), 89–96, doi:10.1190/1.1443191.
- Shakas, A., and N. Linde (2017), Apparent apertures from ground penetrating radar data and their relation to heterogeneous aperture fields, *Geophysical Journal International*, 209(3), 1418–1430.
- Silverman, B. W. (1986), *Density Estimation for Statistics and Data Analysis*, vol. 26, CRC Press.
- Singha, K., and S. M. Gorelick (2005), Saline tracer visualized with three-dimensional electrical resistivity tomography: Field-scale spatial moment analysis, *Water Resources Research*, 41(5), doi:10.1029/2004WR003460.
- Singha, K., and S. M. Gorelick (2006), Effects of spatially variable resolution on field-scale estimates of tracer concentration from electrical inversions using archie's law spatially variable resolution, *Geophysics*, 71(3), G83–G91.

- Singha, K., F. D. Day-Lewis, and J. W. Lane Jr (2007), Geoelectrical evidence of bicontinuum transport in groundwater, *Geophysical Research Letters*, 34(12), doi:10.1029/2007GL030019.
- Singha, K., F. D. Day-Lewis, T. Johnson, and L. D. Slater (2015), Advances in interpretation of subsurface processes with time-lapse electrical imaging, *Hydrological Processes*, 29(6), 1549–1576, doi:10.1002/hyp.10280.
- Sisson, S., Y. Fan, and M. Beaumont (2018), Overview of abc, *Handbook of Approximate Bayesian Computation*, pp. 3–54.
- Sjöback, R., J. Nygren, and M. Kubista (1995), Absorption and fluorescence properties of fluorescein, *Spectrochimica Acta Part A: Molecular and Biomolecular Spectroscopy*, 51(6), L7–L21.
- Slater, L., A. Binley, W. Daily, and R. Johnson (2000), Cross-hole electrical imaging of a controlled saline tracer injection, *Journal of Applied Geophysics*, 44(2-3), 85–102, doi: 10.1016/S0926-9851(00)00002-1.
- Straface, S., and M. De Biase (2013), Estimation of longitudinal dispersivity in a porous medium using self-potential signals, *Journal of hydrology*, 505, 163–171.
- Swanson, R. D., K. Singha, F. D. Day-Lewis, A. Binley, K. Keating, and R. Haggerty (2012), Direct geoelectrical evidence of mass transfer at the laboratory scale, *Water Resources Research*, 48(10).
- Swanson, R. D., A. Binley, K. Keating, S. France, G. Osterman, F. D. Day-Lewis, and K. Singha (2015), Anomalous solute transport in saturated porous media: Relating transport model parameters to electrical and nuclear magnetic resonance properties, *Water Resources Research*, 51(2), 1264–1283.
- Tarantola, A. ((2005)), *Inverse Problem Theory and Methods for Model Parameter Estimation*, vol. 89, SIAM.
- Torquato, S., and H. Haslach Jr (2002), Random heterogeneous materials: microstructure and macroscopic properties, *Appl. Mech. Rev.*, 55(4), B62–B63.
- Van Genuchten, M. T., and P. Wierenga (1976), Mass transfer studies in sorbing porous media i. analytical solutions, *Soil science society of america journal*, 40(4), 473–480.
- Vanderborght, J., A. Kemna, H. Hardelauf, and H. Vereecken (2005), Potential of electrical resistivity tomography to infer aquifer transport characteristics from tracer studies: A synthetic case study, *Water Resources Research*, 41(6), doi:10.1029/2004WR003774.
- Villermaux, E. (2019), Mixing versus stirring, *Annual Review of Fluid Mechanics*, 51, 245–273.
- Visentini, A. F., N. Linde, T. Le Borgne, and M. Dentz (2020), Inferring geostatistical properties of hydraulic conductivity fields from saline tracer tests and equivalent electrical conductivity time-series, *Advances in Water Resources*, 146, 103,758.

- Visentini, A. E., P. de Anna, D. Jougnot, T. Le Borgne, Y. Méheust, and N. Linde (2021), Electrical signatures of diffusion-limited mixing: Insights from a milli-fluidic tracer experiment, *Transport in Porous Media*, pp. 1–27.
- Wand, M. P., and M. C. Jones (1994), *Kernel Smoothing*, CRC Press.
- Waxman, M. H., and L. Smits (1968), Electrical conductivities in oil-bearing shaly sands, *Society of Petroleum Engineers Journal*, 8(02), 107–122.
- Wen, X.-H., and J. J. Gómez-Hernández (1996), Upscaling hydraulic conductivities in heterogeneous media: An overview, *Journal of Hydrology*, 183(1-2), ix–xxxii.
- Western, A. W., R. B. Grayson, and G. Blöschl (2002), Scaling of soil moisture: A hydrologic perspective, *Annual Review of Earth and Planetary Sciences*, 30(1), 149–180.
- Whitaker, S. (2013), *The Method of Volume Averaging*, vol. 13, Springer Science & Business Media.
- Willingham, T. W., C. J. Werth, and A. J. Valocchi (2008), Evaluation of the effects of porous media structure on mixing-controlled reactions using pore-scale modeling and micromodel experiments, *Environmental Science & Technology*, 42(9), 3185–3193.
- Wood, B. D. (2009), The role of scaling laws in upscaling, *Advances in Water Resources*, 32(5), 723–736.
- Xiong, L., P. Chen, and Q. Zhou (2014), Adhesion promotion between PDMS and glass by oxygen plasma pre-treatment, *Journal of Adhesion Science and Technology*, 28(11), 1046–1054.
- Yeh, T.-C. J., and J. Šimunek (2002), Stochastic fusion of information for characterizing and monitoring the vadose zone, *Vadose Zone Journal*, 1(2), 207–221.
- Zhang, D. (2001), *Stochastic methods for flow in porous media: coping with uncertainties*, Elsevier.
- Zinn, B., and C. F. Harvey (2003), When good statistical models of aquifer heterogeneity go bad: A comparison of flow, dispersion, and mass transfer in connected and multivariate gaussian hydraulic conductivity fields, *Water Resources Research*, 39(3).

Alejandro Fernandez Visentini

+41 78 693 6764 | alejandro.fernandez@unil.ch | dob: 06.07.1990

Education

University of Lausanne

PhD in Environmental Sciences - Institute of Earth Sciences

- Thesis: Geoelectrical Signatures of Spreading and Mixing
Director: Dr. Niklas Linde

Lausanne, Switzerland

2017 – 2021

Paris Institute of Earth Physics

M2 Master of Research in Exploration Geophysics

- Thesis: Covariance matrix spectrum estimation using ambient-noise cross correlation at the Valhall oilfield
Director: Dr. Nicolai Shapiro
Co-Director: Dr. Julien de Rosny

Paris, France

2016 – 2017

National University of La Plata

Master in Geophysics, Faculty of Astronomy, Geophysics and Meteorology

- Thesis: Estimation of the effective elastic thickness of the lithosphere under the Southern Andes
Director: Dr. Claudia Tocho
Co-Director: Dr. Laura Dacal

La Plata, Argentina

2010 – 2016

Conference presentations

Inferring geostatistical properties of hydraulic conductivity fields from equivalent electrical conductivity time-series
December 2020 AGU Fall Meeting (online). San Francisco, United States

Publications

Fernandez Visentini, A., Linde, N. (2021). Generalization of Archie's law to heterogeneous and anisotropic salinity fields. *Manuscript in preparation*.

Fernandez Visentini, A., de Anna, P., Jougnot, D., Le Borgne, T., Méheust, Y., Linde, N. (2021). Electrical Signatures of Diffusion-Limited Mixing: Insights from a Milli-fluidic Tracer Experiment. *Transport in Porous Media*.

Fernandez Visentini, A., Linde, N., Le Borgne, T., Dentz, M. (2020). Inferring geostatistical properties of hydraulic conductivity fields from saline tracer tests and equivalent electrical conductivity time-series. *Advances in Water Resources*.

Fernandez Visentini, A., K.Y. Ke, J. Lartey, V. Abhishikth and C. Delahaye (2017). Seismic and Geomagnetic Survey in an Archaeological Site at Chartres, France - Evidences of Paleo-channel and Remains of a Roman Temple. *Conference paper at the European Association of Geoscientists and Engineers*.

Workshops and summer schools

Hydrogeophysical inversion and data assimilation

VIU Graduate Seminar - Venice International University

June 2019

Venice, Italy

Lifetime Skills

ENIGMA ITN Workshop - University of Lausanne

February 2018

Lausanne, Switzerland

Flow and transport in porous and fractured media

4th Cargèse summer school - L'Institut d'Etudes Scientifiques de Cargèse

June 2018

Cargèse, France

Modelling and upscaling of flow and transport in heterogeneous aquifers

ENIGMA ITN Workshop - University of Lausanne

February 2018

Lausanne, Switzerland

Multi-scale in situ investigation of fractured media: theory and field practice
ENIGMA ITN Workshop

October 2017
Ploemeur, France

Advanced subsurface characterization methods: theory and field practice
ENIGMA ITN Workshop - University of Liège

October 2017
Liège, Belgium

Languages and programming skills

Languages: English, Spanish (mother tongue), French (intermediate)

OS: Linux, Windows

Programming languages: Python, Matlab, Fortran, L^AT_EX

References

Dr. Niklas Linde · Contact information upon request
Institute of Earth Sciences, Faculty of Geosciences and Environment, University of Lausanne, Lausanne,
Switzerland